Transactions of the ASME, Journal of Heat Transfer (ISSN 0022-1481) is published monthly by The American Society of Mechanical Engineers, Three Park Avenue, New York, NY 10016. Periodicals postage paid at New York, NY and additional mailing offices. POSTMASTER: Send address changes to Transactions of the ASME, Journal of Heat Transfer, c/o THE AMERICAN SOCIETY OF MECHANICAL ENGINEERS, 22 Law Drive, Box 2300, Fairfield, NJ 07007-2300. **CHANGES OF ADDRESS** must be received at Society headquarters seven weeks before they are to be effective. Please send old label and new address. **STATEMENT from By-Laws.** The Society shall not be responsible for statements or opinions advanced in papers or ... printed in its publications (B7.1, Para. 3).

Journal of Heat Transfer

Published Monthly by ASME

VOLUME 130 • NUMBER 4 • APRIL 2008

SPECIAL ISSUE ON MICRO/NANOSCALE HEAT TRANSFER

GUEST EDITORIAL

RESEARCH PAPERS

Micro/Nanoscale Heat Transfer

(Contents continued on inside back cover)

This journal is printed on acid-free paper, which exceeds the ANSI Z39.48-1992 specification for permanence of paper and library materials. ♾™
♻ 85% recycled content, including 10% post-consumer fibers.

TECHNICAL BRIEFS

The ASME Journal of Heat Transfer is abstracted and indexed in the following:

Applied Science and Technology Index, Chemical Abstracts, Chemical Engineering and Biotechnology Abstracts (Electronic equivalent of Process and Chemical Engineering), Civil Engineering Abstracts, Compendex (The electronic equivalent of Engineering Index), Corrosion Abstracts, Current Contents, E & P Health, Safety, and Environment, Ei EncompassLit, Engineered Materials Abstracts, Engineering Index, Enviroline (The electronic equivalent of Environment Abstracts), Environment Abstracts, Environmental Engineering Abstracts, Environmental Science and Pollution Management, Fluidex, Fuel and Energy Abstracts, Index to Scientific Reviews, INSPEC, International Building Services Abstracts, Mechanical & Transportation Engineering Abstracts, Mechanical Engineering Abstracts, METADEX (The electronic equivalent of Metals Abstracts and Alloys Index), Petroleum Abstracts, Process and Chemical Engineering, Referativnyi Zhurnal, Science Citation Index, SciSearch (The electronic equivalent of Science Citation Index), Theoretical Chemical Engineering

Journal of Heat Transfer

Guest Editorial

Special Issue on Energy Nanotechnology

It is with great pleasure that we present this special issue of the *Journal of Heat Transfer*, dedicated to Energy Nanotechnology. This focus area is the natural convergence of two subjects of tremendous and lasting importance. The ever-growing global demand for energy in both developing and industrialized nations is widely recognized as one of modern society's greatest challenges. To have a positive worldwide impact, new energy technologies must not only have the potential to be large scale and cost effective but must also address concerns about national security and environmental issues such as global climate change. As we strive to improve all aspects of the energy cycle—from primary production and extraction to storage, transmission, utilization, and mitigation—our attention naturally turns to nanotechnology because its additional degrees of freedom offer great potential for innovative breakthroughs.

In the heat transfer community, interest in research at nanoscale length and time scales has grown steadily over the past two decades, as evidenced, for example, by previous special issues of the *Journal of Heat Transfer* in April 2002 and January 2007. Early nanoscale heat transfer research was largely driven by the manufacturing and microelectronics industries, and it is only relatively recently that major attention has turned to energy applications. At a fundamental level, nanoscale effects can lead to significant changes in the ways that energy is stored and transported in nanostructures compared to macrostructures. Although the details vary, these phenomena are present for all types of energy carriers, including electrons, phonons, molecules, and photons. Thus, there is rich potential to exploit nanoscale phenomena in a wide range of energy technologies, many of which are described in this special issue.

Beginning with energy sources, one paper in this issue presents a model for the photoelectrochemical production of hydrogen at a proton-exchange membrane. Two contributions describe the synthesis of carbon nanotubes and their hybridization with nanoparticles, which may be useful for solar cells, fuel cells, batteries, and hydrogen storage. A related report describes the enhanced thermal conductance of phase change materials loaded with carbon nanotubes, with applications in the thermal management of electronics. Several papers add to the lively discussion about enhanced heat transfer in nanoparticle colloids, known as "nanofluids," which may lead to more efficient heat exchangers in large-scale power plants. Theoretical and experimental efforts detail conduction, convection, and boiling in nanofluids and at nanostructured surfaces, under both transient and steady-state conditions. Related papers describe heat transfer through porous media, narrow gaps, and flow visualization in microchannels, all of which may prove valuable for optimizing heat exchangers on a smaller scale. Finally, two papers can be related to energy scavenging (through nanocomposite thermoelectrics or a waveguide-ballistic device), which "closes the loop" by recovering energy from waste heat to create another energy source.

This special issue is in large part an outcome of the First Energy Nanotechnology International Conference (ENIC), held at the Massachusetts Institute of Technology on June 26–28, 2006. The conference was chaired by one of us (G.C.), and we would like to thank the Program Chair, Yang Shao-Horn, and the Organizing Committee, Arun Majumdar, Samuel Mao, and Ernie Moniz. Their efforts helped make this first-of-its-kind conference a success: there were over 100 technical contributions including talks, tutorials, posters, and panel sessions. This special issue contains papers submitted at ENIC as well as selected additional papers submitted directly to the journal. All have undergone full peer review. We hope that you, the reader, will find this issue both informative and thought provoking.

Chris Dames
University of California, Riverside

Gang Chen
Massachusetts Institute of Technology

Heat Transfer Behavior of Silica Nanoparticles in Pool Boiling Experiment

Denitsa Milanova

Ranganathan Kumar
e-mail: rnkumar@mail.ucf.edu

University of Central Florida,
4000 Central Florida Boulevard,
Orlando, FL 32816

The heat transfer characteristics of silica (SiO_2) *nanofluids at* 0.5 vol % *concentration and particle sizes of* 10 nm *and* 20 nm *in pool boiling with a suspended heating Nichrome wire have been analyzed. The influence of acidity on heat transfer has been studied. The p*H *value of the nanosuspensions is important from the point of view that it determines the stability of the particles and their mutual interactions toward the suspended heated wire. When there is no particle deposition on the wire, the nanofluid increases critical heat flux (CHF) by about 50% within the uncertainty limits regardless of p*H *of the base fluid or particle size. The extent of oxidation on the wire impacts CHF, and is influenced by the chemical composition of nanofluids in buffer solutions. The boiling regime is further extended to higher heat flux when there is agglomeration on the wire. This agglomeration allows high heat transfer through interagglomerate pores, resulting in a nearly threefold increase in burnout heat flux. This deposition occurs for the charged* 10 nm *silica particle. The chemical composition, oxidation, and packing of the particles within the deposition on the wire are shown to be the reasons for the extension of the boiling regime and the net enhancement of the burnout heat flux.*
[DOI: 10.1115/1.2787020]

Keywords: nanofluids, pool boiling, CHF, surface charge

Introduction

Millimeter- and micron-sized particles in suspension tend to form huge agglomerates and settle down quickly, which would increase the pressure drop and deteriorate the heat transfer characteristics of the fluid. However, suspensions of less than 50 nm size particles in fluids, called complex or nanofluids, have been found to significantly increase the thermal conductivity in single phase flows at very low concentrations [1–4] and up to threefold increase in maximum heat flux in pool boiling studies [5–7]. Thus, these nanofluids have potential applications in electronic cooling, reactors, and optical systems. The adopted particle-fluid combinations are usually oxide nanoparticles (Al_2O_3, CuO, SiO_2, TiO_2, and CeO_2), metal nanoparticles (Cu, Au, and Ag), diamond, and carbon nanotubes suspended in water, ethylene glycol, ethanol, and other oils.

In the presence of nanoparticles, particle-particle and particle-molecule interactions play a major role in increasing the thermal conductivity of the nanofluids, which enhances the heat transfer. Two subsequent studies by Masuda et al. [8] and Lee et al. [9] show 30% and 15% increases in thermal conductivity, respectively, for Al_2O_3 nanofluid at 4.3% concentration. The difference in the results was attributed to the particle size with smaller size giving more free surface area and higher conductivity. CuO nanoparticles were dispersed [9] in water and ethylene glycol and showed greater enhancement compared to Al_2O_3 nanofluid in the same base liquids. Experimental data for metallic particles are limited. Copper particle solution has displayed enhanced conductivity by 40% in ethylene glycol at 0.3 vol % with a mean diameter of ~10 nm [3].

The discrepancies in the enhancements achieved by different groups are attributed not only to the particle size and concentration but also to the particle surface treatment and the presence of additives. The preparation of the nanofluids is important from the point of view of stability and good dispersion. Dry nanopowder suspended in a base liquid tends to be unstable and settles over a period of time. The aggregation of nanoparticles and formation of large agglomerates at low concentrations may lead to sedimentation and creation of areas with high thermal resistance. To improve stability, the following techniques have been adopted: (1) change of *p*H by the addition of acid or base to keep the nanoparticles away from their isoelectric point (IEP)—point of zero charge, (2) addition of surfactants/dispersants, and (3) treatment with ultrasonic vibration for better dispersion.

A few possible factors that enhance the thermal conductivity are discussed in the published literature, including the Brownian motion of nanoparticles, ordered arrangement of liquid molecules in the vicinity of nanoparticles, ballistic heat transfer mode in nanoparticles, and clustering and networking of nanoparticles [10–13]. Although it was proposed that Brownian motion and collisions of the particles can influence the heat transport, it has been shown that its effect is minimal [14]. Molecular dynamics simulations propose a formation of an ordered layer (between 1 nm and 3 nm) at the particle-fluid surface interface with higher thermal conductivity than that of the bulk liquid. Such factors are only theoretically postulated at this stage and they do not account for the particle-particle and particle-molecule chemical interactions, and surface charge by breaking the host molecules.

Vassallo et al. [5] and Milanova and Kumar [6] showed 100% and 200% enhancements, respectively, in burnout heat flux of Nichrome wire in silica-water suspension. This tremendous improvement in maximum heat flux was partially attributed to the formation of wire coating and more nucleation sites for bubble initiation [6]. You et al. [7] used Al_2O_3 nanofluid to show a threefold increase in critical heat flux (CHF). They found that the average size of the departing bubbles increases and the bubble frequency decreases for alumina nanofluids.

In the following study, we examine the pool boiling heat transfer characteristics of silica nanoparticles dispersed in water and quantify their enhanced maximum heat flux. Different *p*H of the

Contributed by the Heat Transfer Division of ASME for publication in the JOURNAL OF HEAT TRANSFER. Manuscript received February 11, 2006; final manuscript received March 25, 2007; published online March 17, 2008. Review conducted by Satish G. Kandlikar.

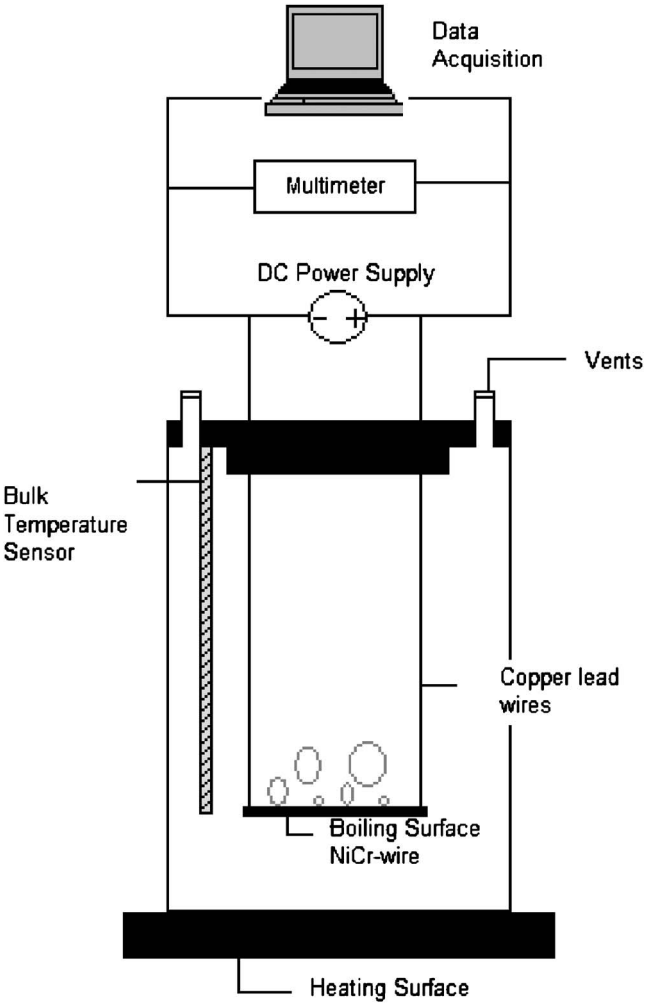

Fig. 1 Experimental setup of nanofluid pool boiling experiment

solution plays a significant role in the heat transferred. The dissociated ions from the suspension and the chemical reactions between them and the silica particles appear to determine the maximum heat flux. The dispersion characteristics of the fluid were experimentally evaluated through the electrostatic potential of nanoparticles, called zeta potential, in order to give insight into particle-particle, particle-liquid, and particle-heating surface interactions. Thus, the chemical structure and motion within the fluid are responsible for a higher burnout heat flux. The objective of this work is to systematically study the effect of the charged silica (SiO_2) nanoparticle suspension in boiling conditions in water for different particle sizes, *p*H, and particle concentrations.

Experimental Procedure

Heat transfer characteristics of nanosilica in water with varying acidity and chemical composition are systematically examined in a pool boiling experiment. The pool boiling experimental setup (Fig. 1) consists of a glass cylindrical test section filled with 250 ml of nanofluid. A Nichrome wire serving as a temperature sensor is horizontally immersed in the pool through tightly attached copper lead wires. The dimensions of the heating element are 46 mm in length, 0.32 mm in diameter, and 0.558 mm in diameter for the lead wires. This particular alloy was chosen for its brittleness. It also breaks at its melting point (1400°C) without any plastic deformation. Melting of the material before failure is undesirable.

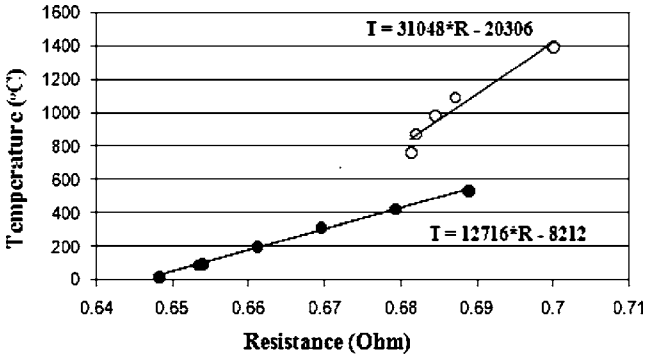

Fig. 2 Temperature-resistance calibration curve

The temperature of the bulk fluid is brought and maintained initially to nearly 100°C and monitored. When current is passed through the heating wire, measurements of the potential drop through the wire at a given current flow are taken. The heat flux from the wire to the saturated liquid is determined using $q = I^2R_w/\pi DL$, where I, R_w, D, and L are current, wire resistance, wire diameter, and length. In order to achieve steady state, each data point is recorded 30 s after reaching the desired heat flux. The wire temperature T_w is determined from the electrical resistance of the uncoated wire available for Nichrome. The ($T_w - R_w$) calibration requires a piecewise interpolation due to the jump in resistance at higher temperatures, as shown in Fig. 2. As this calibration curve shows, from 20°C up to about 550°C and again from 800°C and beyond, the curves were fitted piecewise linearly. Two different linear functions were used, one from 0.656 Ω to 0.69 Ω, and another from 0.69 Ω to 0.71 Ω. The double-value region between 0.69 and 0.70 cannot be avoided since it is an intrinsic property of the Nichrome material near its CHF. Calibration curves are generated for each experiment since temperature, T_w, is plotted as a percentage increase in resistance from the initially recorded resistance. The calibration curve for the temperature change is given as percent increase in resistance by the manufacturer [15] for Nichrome wire for the diameter used in this study. The pool boiling curve is generated by plotting the heat flux q versus the wall superheat ($T_w - T_{sat}$). The experimental system is vented to ensure atmospheric interactions.

Since only the resistance including the lead wires is determined first, the resistance of the copper lead wires is subtracted from that of the whole system to obtain the resistance of the Nichrome wire. The lead wire resistance is not a constant, but increases with current, possibly due to the heat dissipated from copper at high heat fluxes. With increasing power, the heat flux initially increases slowly, but more rapidly as the wire superheat increases further. The total uncertainty in heat flux is determined via propagation of error approach and is calculated to be 5.8% in all the flow regimes. The uncertainty is mainly attributed to variations in wire length and soldering, which affect the resistance. Since the temperature of the wire is interpolated from available data, the error in superheat in the saturated boiling regime where resistance varies linearly with wire temperature is 8.4°C. At CHF, where there is a jump in wire temperature, the uncertainty in temperature is 53°C (3.8–6.3%). With respect to Fig. 2, typically, majority of the data fell below 0.69 Ω, i.e., below CHF. When drastic conditions on the wire are noticed which are usually associated with the temperature jump, the high temperature from the upper linear curve in Fig. 2 is used. The actual deviation of burnout heat flux in different runs is found to be less than the predicted uncertainty. The reliability of the data is ensured by repeating each experiment three times for the same conditions.

Results and Discussion

Characterization of Nanoparticles. Silicon dioxide nanosuspension is a commercial product of Alfa Aesar and is obtained at 15% concentration in water at an initial particle size of 10 nm. A particle size of 20 nm is obtained at 40% concentration in water by the same vendor. The stabilizing agent for both particle sizes is sodium oxide at 0.83% concentration. Silica nanofluids are diluted to 0.5 vol %, which lead to slight agglomeration, and the average particle size increased to 18.8 nm from the initial size of 10 nm, determined by particle size analysis. In pure de-ionized water, 20 nm silica particles slightly increase to an average size of 22.5 nm. The colloidal stability in the presence of salts and electrolyte is further discussed.

Electric double layers (EDLs) form spontaneously on interfaces when colloidal particles are dispersed in a liquid medium depending on the electrolytic concentration. Charge is generally acquired by adsorption or desorption of ions. In the case of oxides, there is a loss or gain of protons from the hydroxyl surface groups, which leads to overall change in the surface charge. The positive or negative charge is electrostatically compensated with diffusively distributed counterions (countercharge). Thus, when there is no strong electrolyte (acid or base), a second layer is formed around a wetting surface such as silica particle, and this layer is called the hydration layer. In water, oxides generally acquire positive charge at low *p*H, negative charge at high *p*H, and zero charge at some point. That point is called point of zero charge (PZC). The real *p*H values used in our experiments for silica are basic (10.2 for 10 nm particles and 9.2 for 20 nm particles). The theoretical PZC value is *p*H 2 for silica. Zeta potential measurement determines the stability characteristics of the nanoparticle suspension by measuring the electrophoretic mobility of particles. Theoretically, zeta potential is computed at the surface of the shear plane, between the solid and diffuse layers where the fluid velocity is zero due to no-slip condition. It determines the net charge on the particles. The measurements are performed with zeta potential analyzer (Nicomp 380/ZLS), which uses the method of electrophoretic light scattering (ELS) to measure the average mobility of the dispersed charged particles subjected to electric field. The zeta potential is obtained by the Smoluchowski equation, which is preferred for high ionic strengths over the one by Huckel used for low ionic strengths. Zeta potential values for the diluted nanosolutions are −17.5 mV and −22 mV for the 10 nm and 20 nm nanosilica, respectively. These values are adequate because the *p*H of the suspensions is far removed from their PZC. These highly negative potentials indicate the surface charge and ensure strong electrostatic repulsion barriers and good stability. The effect of EDLs and *p*H on pool boiling behavior is discussed below.

Effect of *p*H in Pure Buffer Solution. Since particle suspensions are stable at different *p*H solutions depending on the particle characteristics, our initial investigation focused on the effect of *p*H in pure water. Figure 3 is the boiling curve for de-ionized water compared with buffer solutions at *p*H 3, 4, 7, and 10. Acidic buffer solutions are commonly made from a weak acid and one of its salts—often a sodium and/or potassium salt, while basic ones contain mostly weak base salts. For all *p*H, the boiling curve displays the well known flow regimes such as natural convection, nucleate boiling, and CHF before the wire burnout, with some exceptions as given below. As has been noted in the boiling flow literature, as the heat flux is increased, the vapor bubbles form at the nucleation sites and separate from the surface. When the active sites on the wire become numerous, bubbles begin to coalesce. As the heat flux is further raised, vapor generation is so large that the surface is depleted of liquid. Beyond a limiting heat flux called CHF, a slight increase in power input to the wire causes a large rise in the wire temperature as shown by the temperature jump. The few changes caused by *p*H are noted below.

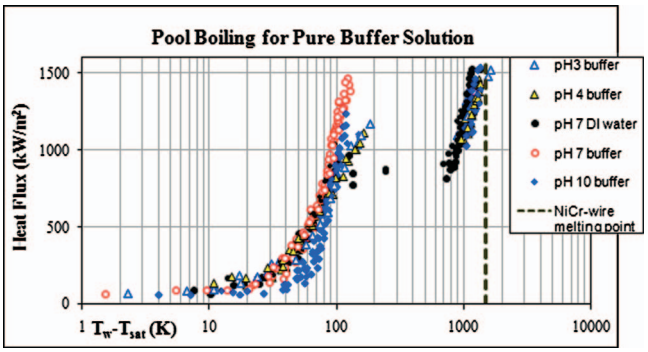

Fig. 3 Pool boiling for pure buffer solution at different acidities

1. Initially, as the current is passed through the wire, the heat transfer mode is natural convection. Figure 3 shows that pure fluids at high *p*H tend to exhibit prolonged natural convection prior to transition to nucleate boiling.
2. With the exception of buffer *p*H 7, all solutions display all the flow regimes including CHF where there is a sudden rise in wire temperature. In particular, boiling curves for *p*H 3 and *p*H 4 are practically the same in all regimes. Due to the delay in transition to boiling, *p*H 10 has a steeper slope in the saturated boiling regime; however, the CHF of 1100 kW/m^2 is nearly the same as that of *p*H 3 and 4, although higher than that for de-ionized (DI) water. Differences in the boiling curve between *p*H 7 buffer and DI water need further explanation.
3. The difference between the buffer solution and DI water for *p*H 7 is in the manner the wire burns out. While the DI water displays the sudden jump in the temperature at CHF associated with wire glowing, such a jump is completely absent for the buffer. Buffers by nature easily recombine their dissociated ions to their original salts, which results in a decrease of the overall number density of free ions. This, in turn, could cause a delay in the sudden increase in wire superheat for the buffer solution or be absent as in the current case. Thus, unlike in DI water, in the case of the buffer solution, dissociated positive and negative ions are limited. This can affect the size of the bubbles around the wire, and restrict wire glowing or altogether eliminate it for buffer *p*H 7.
4. The effect of acidic and basic buffer on CHF is analyzed next. The intensity of the bubbles and vapor formation is high in the nucleate boiling regime. Since buffer solutions are weak electrolytes, they are expected to release free ions at a controlled rate. For *p*H 3 and 4, the wire starts to glow at a higher temperature. The glowing of the wire could be associated with the nature and intensity of the vapor phase. Depending on whether the solution is acidic or basic, hydrogen (H_2) or oxygen (O_2) gas is possibly formed, respectively [6]. Acidic solutions are more reactive than the basic ones because hydrogen molecule is lighter than oxygen molecule in terms of molecular weight. This may have an influence on the intensity of the bubble formation. For acidic buffer, for the same superheat, the heat flux is higher.

Figure 4 represents the pool boiling curves for 10 nm and 20 nm silica nanofluids in pure DI water. The nanofluids were diluted to 0.5 vol % and no other stabilizers were added. Significant differences exist in the burnout characteristics between the two nanofluid solutions. In silica 10 nm nanofluid, the burnout heat flux is 2.67 times that of pure DI water. The deposition on the wire in this case is significant (~0.3 mm) and it is loosely packed, which could be a direct result of its amorphous structure. The saturated boiling regime for this nanofluid extends over two linear

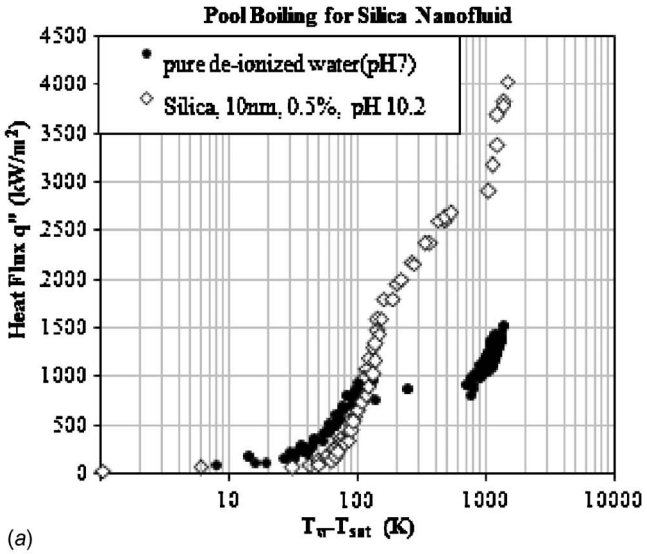

(*a*)

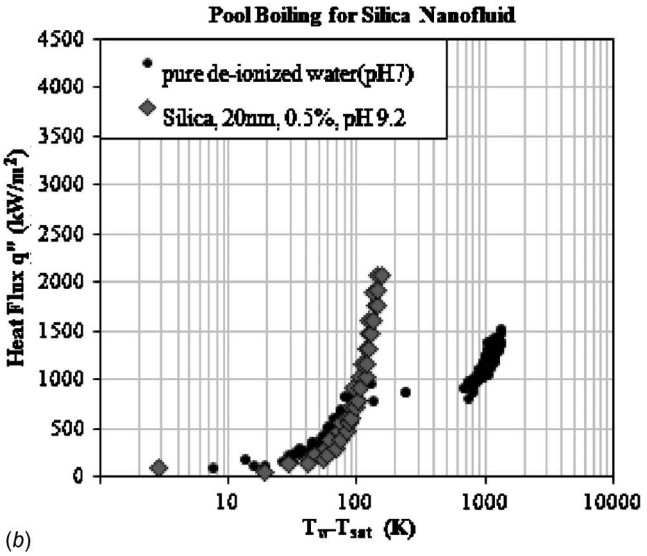

(*b*)

Fig. 4 Pool boiling for (*a*) 10 nm silica in *p*H 10.2 at 0.5 vol % concentration and (*b*) 20 nm silica in *p*H 9.2 at 0.5 vol % concentration

segments well beyond CHF for pure water. It was observed that smaller bubbles nucleated rapidly and departed at higher frequency from the numerous porous sites compared to the pure water case, which could be a possible reason for the extension of the boiling regime. This, in turn, increases CHF. At about 500°C superheat, a sudden rise in resistance (and temperature) takes place, associated with glowing of the wire up to about 1000°C. Despite a strong deposition, the jump occurs at approximately the same resistance (Fig. 2), adding credence to the fact that the resistance and calibration of the deposited wire did not change significantly. This is the CHF regime, which now occurs at a much higher heat flux of 2600–2700 kW/m^2 compared to pure water. Prior to burnout at a heat flux of ~4100 kW/m^2, the boiling curve displays a steep slope again as in pure water. Thus, the porosity and thickness can control the vapor formation and burnout heat flux. Similar phenomenon has been observed [16] for copper micro-sized particles coated on a plain surface.

In contrast, silica (20 nm) at the same concentration (0.5%) shows no significant deposition on the wire and the wire breaks at a lower heat flux compared to that for 10 nm, however, still at 1.47 times higher CHF compared to DI water (Fig. 4(*b*)). Heat flux increases with superheat in nearly the same manner as for the

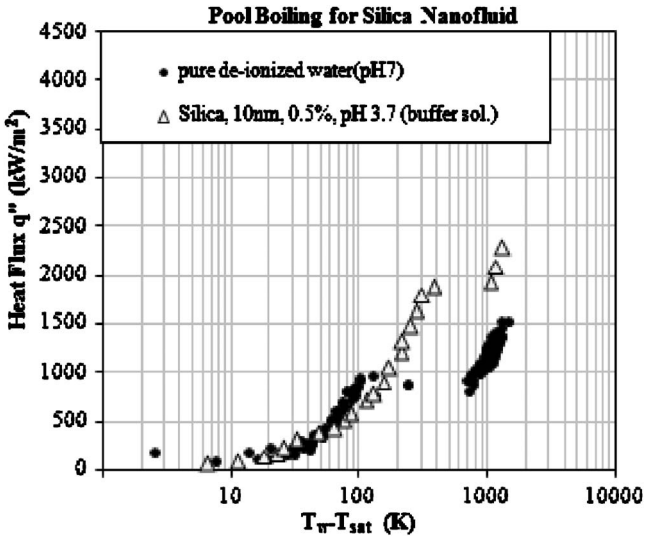

Fig. 5 Pool boiling for 10 nm silica in *p*H 3.7 buffer at 0.5 vol % concentration

10 nm case in the saturated boiling regime until the wire burns out with no visible glowing. No wire deposition was present for the 20 nm solution.

Effect of *p*H in Nanofluids. The *p*H of the nanofluids is important from the point of view that it determines the charge of the particles, their motion in the presence of electric field, and mutual collisions. The lower or higher the *p*H is, the stronger the surface potential that can be expected. Hence, we can expect more vigorous motion and collisions between the individual particles. Higher positive or negative charge of nanoparticles determines the amount of deposition on the wire and electrodes.

The *p*H value of the nanoparticles determines not only the particle movement toward the wire when current is applied but also their mutual interactions and formation of agglomeration and flocculation. In order to delineate the *p*H effect on maximum heat flux, the silica nanofluid was mixed with acidic buffer solution. When silica nanoparticles are added to the *p*H 3 buffer solution, alkaline solutions contain hydroxide ions and the buffer solution removes them in the following manner. The salt, CH_3COOH, present in the acidic buffer solution can combine with the OH^- group to form a water molecule. CH_3COOH dissociates into CH_3COO^- and H^+. Then, the released H^+ ions combine with the OH^- ions in the solution. Thus, the excess OH^- ions from the nanosilica solution are neutralized to maintain a constant *p*H of 3.

For 10 nm and *p*H 3.7 in the buffer solution, the saturation regime extends beyond CHF for pure buffer solution at 3.0 (Fig. 5). Particle aggregation was measured; however, there was no deposition on the wire, and 10 nm silica in acidic buffer provides better performance than pure water.

In Fig. 5, a very interesting trend in the natural convection regime is observed due to the change in *p*H. Comparing this figure with Fig. 4(*a*), silica nanofluid at its original acidity (higher *p*H) exhibits a prolonged natural convection regime. Acidic silica nanofluid enters the nucleate boiling regime earlier compared to the basic silica nanofluid, as shown in Figs. 4(*a*) and 5. Due to the highly basic nature of nanosilica solution, even with a buffer solution of *p*H 3, the dilution of the nanosilica solution at a concentration of 0.5% can only be maintained at *p*H 3.7. The presence of free ions is substantiated by the inability to maintain the nanofluid at lower than *p*H 3.7 even though a buffer solution of *p*H 3 was originally used to make the nanofluid. The excess free ions, which are not neutralized by the buffer solution, may be the reason why nucleation begins earlier on the wire.

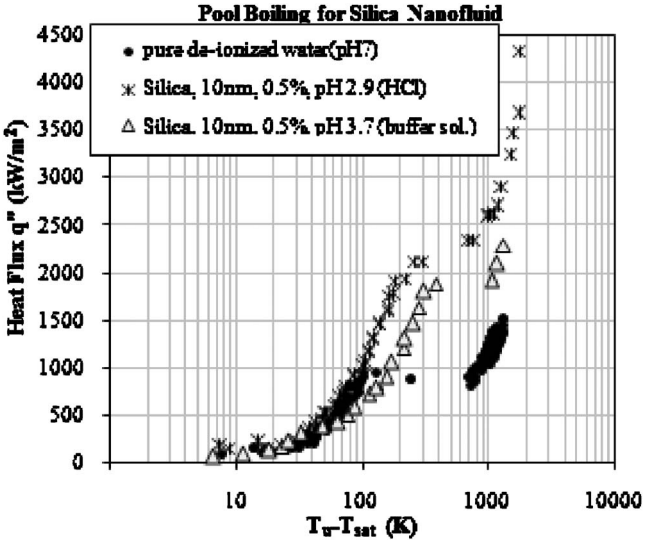

Fig. 6 Pool boiling for 10 nm silica at ~*p*H 3 with HCl and buffer solution

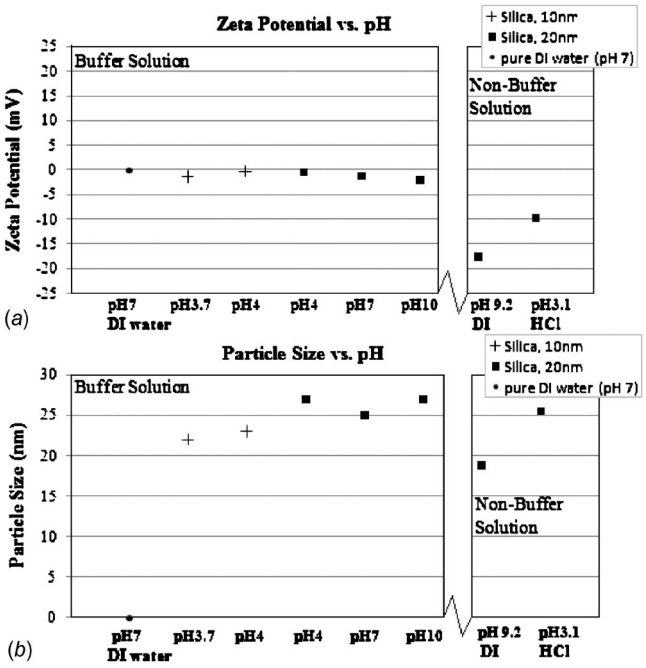

Fig. 7 (*a*) Zeta potential versus *p*H and (*b*) particle size versus *p*H

Comparing Figs. 4(*a*) and 5 near burnout, the burnout heat flux for silica *p*H 3.7 is lower than for *p*H 10.2 where silica is stable. Both exhibit CHF; however, for low *p*H, the CHF regime is pronounced and occurs at about 300–400°C superheat. As in the case of pure water, the sudden jump in temperature in the CHF regime is usually associated with the glowing of the wire for both high and low *p*H. It is important to note that the CHF is enhanced for nanofluids over that for pure DI water or buffer solution even when they are not maintained at their original acidity. The difference in the boiling behavior can be attributed to particle charge and particle deposition on the wire as discussed later. The range of superheat is distinct at CHF for the low *p*H case, and barely noticeable for high *p*H.

The burnout heat flux and the CHF can vary solely because of the chemical solution the nanoparticles are mixed in. Figure 6 shows the differences in the pool boiling curves between two cases for very nearly the same *p*H for 10 nm nanosilica, prepared with hydrochloric acid and buffer solution. Acidic buffer solution was added to silica 10 nm at *p*H 10.2 to make a solution of *p*H 3.7. In the case of silica+HCl, the burnout heat flux is 4400 kW/m^2 compared to 2200 kW/m^2. To understand the differences in burnout, it is important to first understand the basic differences in the types of nanosolutions used, and the particle zeta potential associated with particle size.

There are three types of solutions used in this study: (a) lyophilic, (b) lyophobic, and (c) lyophilic+buffer. Lyophilic dispersion is one that acquires stability by hydration of the wetting silica surface. Lyophilic (hydrophilic in the case of an aqueous solution) dispersions are less sensitive to salt content. These solutions are made by merely adding high *p*H silica particles to DI water. The burnout heat flux of 4100 kW/m^2 obtained in Fig. 4 is for lyophilic dispersion. Second, particles that are electrostatically stabilized by ions (by adding HCl) are termed lyophobic dispersions. In this case, less coagulation (formation of permanent aggregates) takes place. The burnout heat flux of 4400 kW/m^2 obtained earlier is for lyophobic dispersion. A possible reason for the delayed burnout in this case is the presence of dissociated ions, which carry part of the supplied power, diverting them from the wire. The last type of solution is a lyophilic solution but with salts (buffer). This electrolytic solution results in significant coagulation.

In aqueous solution, the ions are separated due to the steric repulsion barriers of water molecules around them. In DI water, the hydrate shell around the ions is usually thick enough so that when oppositely charged ions come to close proximity, the forces due to the kinetic energy is greater than the attractive forces. As a result, those ions bounce on each other upon collision instead of recombining and neutralizing [17]. The addition of hydrochloric acid to the solution ensures the presence of dissociated H^+ and Cl^- ions. Those ions as well as the negatively charged silica nanoparticles acquire hydration layers, which prevent chemical interaction and neutralization when ions approach the particle surface. This is the reason the solution is lyophobic when HCl is added to the nanofluid. However, these ions stay near the surface due to electrical attraction and form the so called diffuse double layer. The overall free ion-nanoparticle system is electrostatically neutral. The concentration of ions near the surface is high and decreases with distance. The zeta potential (Fig. 7(*a*)) for this case is −0.79 mV, which is representative of the fact that the negatively charged silica nanoparticles are balanced with counterions, i.e., there exists an EDL. The particle size (Fig. 7(*b*)) is 23.6 nm, which could be due to surface accumulated ions. Theoretically, EDLs can extend to tens of nanometers depending on the ionic concentration. Since silica was brought to *p*H 2.9, which is close to its PZC, it is reasonable to expect a zeta potential close to zero.

Wire burnout not only depends on lyophilic and lyophobic solutions but also on the amount of deposition of the particles on the wire. To understand whether the increase in the heat transfer is due to the changed morphology of the wire or solely due to the dispersed nanoparticles, burnout heat flux is plotted in Fig. 8 only for those cases where there is no or minimal deposition on the wire. This figure shows that when there is no wire deposition, for the seven cases ranging in *p*H in lyophilic or lyophobic or in buffer for 10 nm and 20 nm particles, the CHF is still increased to ~2200–2300 kW/m^2, an increase of about 50%. This near uniform increase in CHF regardless of the size and chemical characteristics of the particles is a significant finding.

Figures 7 and 8 represent the zeta potential and particle size, and burnout heat flux measurements for seven cases. In all these cases, there was no wire deposition. Five of these cases were measurements taken in buffer solution; hence, some particle agglomeration was seen. These cases were plotted against increasing

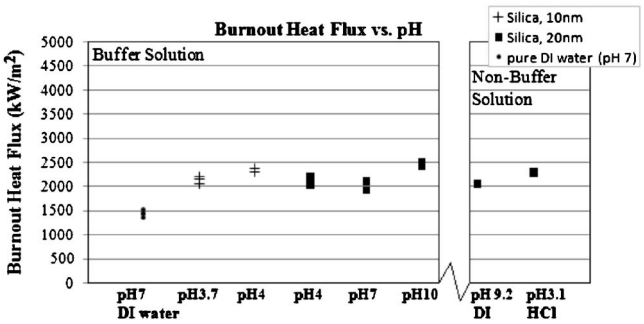

Fig. 8 Burnout heat flux for silica 10 nm and silica 20 nm

*p*H. Two of the cases are provided on the right portion of the figure, and they represent one lyophilic solution and one lyophobic solution.

The particle size in Fig. 7(*b*) shows that the 10 nm silica more than doubled its average size to 22–23 nm (*p*H 3 and 4 buffer) due to aggregation since the potential is low and there is no electrostatic repulsion (buffer solution does not have free ions). This aggregation of particles is inferred from the zeta potential measurement (~0 mV) of silica nanoparticles for all the buffer solutions. This result is in concert with the *p*H value for the PZC. The lack of particle charge hinders their motion toward the wire and electrodes. Therefore, no deposition or significant change of surface roughness was found on the wire for any of the silica buffer solutions.

The surface potential of the nanoparticles determines their movement toward the electrodes and the wire as current flows through the uncoated NiCr wire, which results in the collapse of particles on the surface and the formation of coating. In the case of silica nanofluid with *p*H 10.2, a large amount of oxide coating was found on the wire, whereas for *p*H 9.2 (20 nm) nanofluid, there is no deposition since oxidation of Nichrome seems to have been prevented. Although from a materials point of view, the formation of thick deposition and oxidation of the Nichrome material are detrimental, surface roughness can maintain saturated boiling at higher heat fluxes. This is a result of trapped vapor in the cavities from which numerous bubbles can grow, since nucleation site density is larger for a porous surface compared to a smooth one. In the case of *p*H 9.2 in DI water, there appears to be no agglomeration as the particle size stays constant at 20 nm (Fig. 7(*b*)) and the zeta potential is high at −18 mV. In both cases of lyophilic and lyophobic solutions, the 20 nm particles are charged, do not agglomerate, and burn out at about 2000–2200 kW/m^2. This is in contrast with the 10 nm particles in DI water at high *p*H, and in the presence of HCl at low *p*H, which agglomerated to approximately 20–25 nm particles and increased the burnout heat flux almost threefold. When we eliminate the change in surface roughness and deposition on the wire, the enhancement in burnout heat flux over DI water is uniformly 50%. Hence, the higher heat fluxes are attributed solely to the nanoparticles and not to change in wire thickness and morphology.

Conclusions

In pool boiling of nanofluids, silica particles suspended in water go through different interactions with one another and the wire, and exhibit very different heat transfer behavior due to their crystal structure. Based on the detailed experiments in silica suspensions in the presence of an immersed heated Nichrome wire, the following conclusions may be drawn.

- Silica particles in lyophilic, lyophobic, and in the buffer solution enhance the CHF. When there is no deposition on wire, burnout heat flux is increased by about 50%. This near uniform increase in CHF regardless of the particle size and surface morphology is significant.
- A smaller particle size of silica (10 nm) suspended in solution results in the best CHF performance at high or low *p*H. The Nichrome wire encountered the maximum deposition of silica in the case of 10 nm particle suspension. This suggests that the porosity due to silica deposition and oxidation of the Nichrome material is responsible for the greatest increase in CHF. An enhancement of over 150–200% in burnout heat flux in 10 nm silica solution is consistent with what has been measured in the literature by several researchers.

References

[1] Choi, S. U. S., 1995, *Enhancing Thermal Conductivity of Fluids With Nanoparticles*, ASME, New York, Vol. 66, pp. 99–105.
[2] Das, S. K., Putra, N., Thiesen, P., and Roetzel, W., 2003, "Temperature Dependence of Thermal Conductivity Enhancement for Nanofluids," ASME J. Heat Transfer, **125**, pp. 567–574.
[3] Eastman, J. A., Choi, S. U. S., Li, S., Yu, W., and Thompson, L. J., 2001, "Anomalously Increased Effective Thermal Conductivities of Ethylene Glycol-Based Nanofluids Containing Copper Nanoparticles," Appl. Phys. Lett., **78**, pp. 718–720.
[4] Xuan, Y., and Li, Q., 2000, "Heat Transfer Enhancement in Nanofluids," Int. J. Heat Fluid Flow, **21**, pp. 58–64.
[5] Vassallo, P., Kumar, R., and D'Amico, S., 2004, "Pool Boiling Heat Transfer Experiments in Silica-Water Nano-Fluids," Int. J. Heat Mass Transfer, **47**, pp. 407–411.
[6] Milanova, D., and Kumar, R., 2005, "Role of Ions in Pool Boiling Heat Transfer of Pure and Silica Nanofluids," Appl. Phys. Lett., **87**, p. 233107.
[7] You, S. M., Kim, J. H., and Kim, K. H., 2003, "Effect of Nanoparticles on Critical Heat Flux of Water in Pool Boiling Heat Transfer," Appl. Phys. Lett., **83**, pp. 3374–3376.
[8] Masuda, H., Ebata, A., Teramae, K., and Hishinuma, N., 1993, "Alteration of Thermal Conductivity and Viscosity of Liquid by Dispersing Ultra-Fine Particles (Dispersion of γ-Al_2O_3, SiO_2, and TiO_2 Ultra-Fine Particles)," Netsu Bussei, **4**, pp. 227–233.
[9] Lee, S., Choi, S. U. S., Li, S., and Eastman, J. A., 1999, "Measuring Thermal Conductivity of Fluids Containing Oxide Nanoparticles," ASME J. Heat Transfer, **121**, pp. 280–289.
[10] Bhattacharya, P., Saha, S. K., Yadav, A., Phelan, P. E., and Prasher, R. S., 2004, "Brownian Dynamics Simulation to Determine the Effective Thermal Conductivity of Nanofluids," J. Appl. Phys., **95**, pp. 6492–6494.
[11] Keblinski, P., Phillpot, S. R., Choi, S. U. S., and Eastman, J. A., 2002, "Mechanisms of Heat Flow in Suspensions of Nano-Sized Particles (Nanofluids)," Int. J. Heat Mass Transfer, **45**, pp. 855–863.
[12] Jana, N. R., Chen, Y., and Peng, X., 2004, "Size- and Shape-Controlled Magnetic (Cr, Mn, Fe, Co, Ni) Oxide Nanocrystals via a Simple and General Approach," Chem. Mater., **16**, pp. 3931–3935.
[13] Yu, W., and Choi, S. U. S., 2003, "The Role of Interfacial Layers in the Enhanced Thermal Conductivity of Nanofluids: A Renovated Maxwell Model," J. Nanopart. Res., **5**, pp. 167–171.
[14] Gupta, A., Wu, X., and Kumar, R., 2006, "Possible Mechanisms for Thermal Conductivity Enhancement in Nanofluids," International Conference on Nanochannels, Microchannels and Minichannels, ICNMM2006, Limerick, Ireland, Jun. 19–21.
[15] www.resistancewire.com
[16] Hwang, G.-S., and Kaviany, M., 2006, "Critical Heat Flux in Thin, Uniform Particle Coatings," Int. J. Heat Mass Transfer, **49**(4–5), pp. 844–849.
[17] Lyklema, J., 2000, *Fundamentals of Interface and Colloid Science*, Vol. II, Academic, London, pp. 3.2–3.42.

Carbon Nanotubes, Synthesis, Growth and Orientation Control in Opposed Flow Diffusion Flames

Lawrence A. Kennedy
Department of Mechanical and Industrial Engineering,
University of Illinois at Chicago,
Chicago, IL 60605-7043
e-mail: lkennedy@uic.edu

The combustion synthesis of carbon nanotubes is reviewed, examining their formation and control in diffusion flames. Much of the initial work in this area employed coflow diffusion flames and provided insight into carbon nanotube (CNT) formation. However, the inherent multidimensional nature of such coflow flames made the critical spatial location difficult to maintain. Among this early work, our UIC group demonstrated the superiority of the opposed flow diffusion flame configuration due to its uniform radial distribution that reduces such flow to a one-dimensional process. While a summary of the early coflow flame work is presented, the use of the opposed flow diffusion flame will be the focus of this review. The production of carbon nanostructures in the absence of a catalyst is discussed together with the range of morphology of nanostructures generated when a catalyst is employed. The important aspect of control of the growth and orientation of CNTs and generation of CNT arrays through the use of electric fields is examined as is the use of anodized aluminum oxide templates. Fruitful areas for further research such as the functional coating of CNTs with polymers and the application of these opposed flow flames to synthesis of other materials are discussed.
[DOI: 10.1115/1.2818751]

Keywords: carbon nanotubes, material combustion synthesis, nanotube growth control

Introduction

In 1991 [1], Iijama's discovery of microtubules of graphitic carbon and the subsequent discovery of single-walled carbon nanotubes (CNTs) in 1993 has led to intensive worldwide experimental and theoretical efforts devoted to the investigation of their generation and applications. CNTs possess unique mechanical and electrical properties. Recently, vertically aligned CNT arrays have received much attention due to their potential applications as electrocatalyst supports for use in fuel cells, field emission devices, anodes in lithium-ion batteries, nanoelectronics, biological probes, capacitors, etc.

Until the past few years, three techniques were principally employed to produce CNTs. These are arc discharges [2,3], pulsed laser vaporization (PLV) [4], and chemical vapor deposition (CVD) [5]. All these techniques require the introduction of a catalytic precursor such as cobalt, iron, or nickel for the generation of nanotubes. Arc discharges are a good medium for the production of both multiwalled carbon nanotubes (MWNTs) and single-walled carbon nanotubes (SWNTs) and can yield high quantities of CNTs but with large amounts of undesirable carbonaceous by-products. The growth conditions can be controlled by chamber pressure and arc current. CVD heats a catalyst material to high temperatures and a hydrocarbon gas is introduced as a carbon source. Growth is controlled by the specific hydrocarbon feedstock and the particular catalytic material employed. While CNT synthesis has been dominated by CVD, it contains large amounts of undesirable carbonaceous by-products and requires complex and costly purification. PLV processes evaporate a target carbon composite that is catalytically doped. Its advantage includes high quality CNTs and high accuracy in diameter control. Disadvantages include small production rates and the presence of contaminants such as soot and catalytic metals. All of these methods are subatmospheric processes and have limited abilities for their size to be scaled upwards.

Since 2001–2002, several investigators have shown that flames are an alternate good carbon source and can be employed as a very efficient method for growing multiwalled and single-walled CNTs. Saito and co-workers [6–8] employed coflow methane-air and ethylene-air diffusion flames with the introduction of solid supports for the growth of CNTs. Kennedy's group used opposed flow, flat diffusion flames to generate CNTs with and without catalysts [9,10]. They also demonstrated the effective use of applied electric fields to control their growth and orientation [11]. Vander Wal and co-workers [12] employed coflow diffusion flames using metallocene doped acetylene as fuel to synthesize SWNTs. They have also produced MWNTs with a metal catalyst on TiO_2 [13] and demonstrated that catalytic particle shape, particle elemental composition, and fuel type influences the growth and structure of CNTs and nanofibers [14]. They also report that CNTs can be synthesized in premixed coflow flames [15,16]. Height and co-workers [17] reported the synthesis of CNT as a function of flame position and air-to-fuel ratio. Recently, several authors have successfully reported the application of electric field to control the growth of nanotubes in CVD and in plasma [18–20]. Hurt [21] proposed a three step mechanism for CNT growth in coflow methane flames: (1) methane is pyrolized in the preheat zone to yield hydrocarbon species as a carbon source; (2) catalyst particles form on substrate surface; (3) at appropriate temperatures, catalyst particles absorb the carbon source to produce CNTs.

There is a strong interest in obtaining arrays of CNTs for a variety of applications and such arrays of CNTs have been grown mostly using templates. Typical templates involve aluminum oxide films and mesoporous silicon with catalyst particles embedded in the micropores. The most widely used methods for growing the arrays include metal (Fe, Co, and/or Ni) alumina templates in a microwave plasma, nickel-based layers on glass substrates employing CVD, coating a glass surface with a nickel using a plasma-enhanced hot-filament CVD, etc. Arrays of vertically

Contributed by the Heat Transfer Division of ASME for publication in the JOURNAL OF HEAT TRANSFER. Manuscript received August 21, 2006; final manuscript received March 24, 2007; published online March 17, 2008. Review conducted by Satish G. Kandlikar. Paper presented at the Fourth International Conference on Nanochannels, Microchannels, and Minichannels (ICNMM2006) Limerick, Ireland, June 19–21, 2006.

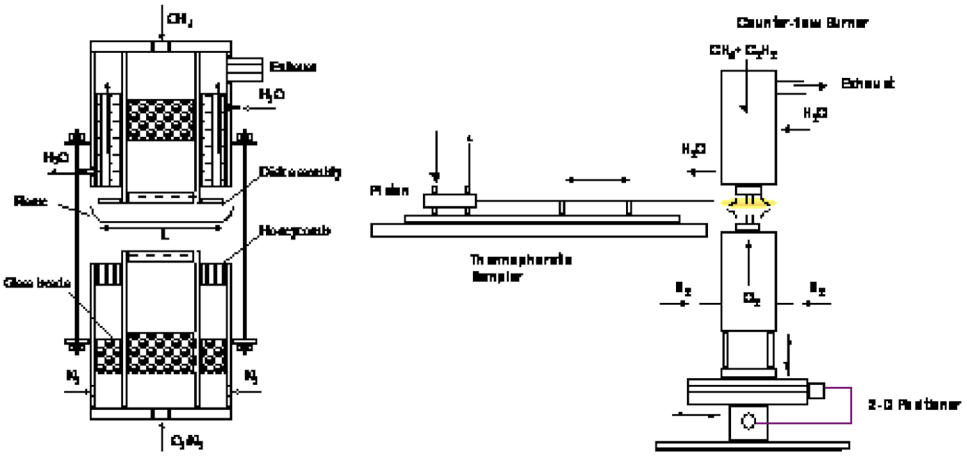

Fig. 1 Schematic of counterflow burner

aligned CNTs have been grown in flames employing a substrate composed of a high number of pore arrays in an anodized aluminum oxide film wherein cobalt catalytic particle are chemical inserted in the pores. This technique yield CNTs in the array with an average outer diameter of 35 nm and nanotube lengths of a few microns. Unfortunately, the small flame volume in coflow flames plus strong flame-substrate interactions make the controlling parameters difficult to delineate. Also, these processes are usually complex and composed of time intensive multistep processes. Saito et al. [22] have recently exploited the opposed flow diffusion flame to provide a larger flame volume, more controlled conditions, and improve sampling to enhance the generation of CNT arrays. Conversely, the formation of CNT arrays using an opposed flow diffusion flame together with electric field control techniques does not require preformed substrates. Therefore, it is a one step process resulting in a simple and inexpensive method for the growth of CNT arrays.

This paper will provide a review of combustion synthesis of CNTs employing opposed flow flames and the control of their growth rates and morphology through the use of electric fields. This paper will also discuss future areas of fruitful research including functionalizing CNTs through coating with polymers and the synthesis of nanostructures of noncarbon materials. Most of this discussion will center on work from our laboratory

Experimental Apparatus

Most early work in the combustion synthesis of CNTs utilized coflowing diffusion flames as noted in the Introduction. One major difficulty with such coflowing approaches is the existence of strong gradients of temperature, species, and velocity in both the radial and axial directions. An alternative configuration is the counterflow diffusion burner, which eliminates the radial gradients resulting in a quasiuniform, one-dimensional flame that fundamentally reduces the spatial complexity associated with sampling. Further, such a configuration is much more susceptible to modeling using such standard codes as "OPPDIFF." [23]

A schematic of such a counterflow burner and associated experimental setup is shown in Fig. 1. The counterflow diffusion flame forms from two opposing streams of gases; the fuel is supplied from the top nozzle, and the oxidizer (O_2/N_2 mixture) is introduced from the bottom nozzle and permits low strain rate oxyfuel operation at atmospheric pressure. The fuel and oxidizer nozzles have inside diameters of 52 mm. Coflowing nitrogen is introduced through a cylindrical annular duct around the outer edge of the oxidizer nozzle, extinguishing the flame near the outer jacket and preventing dissipation into the environment. This creates a test volume separated from the surroundings with no solid boundary. The nitrogen annular duct has inner and outer diameters of 60 mm and 108 mm, respectively. The fuel, oxidizer, and nitrogen flows are initially introduced into chambers in the respective top/bottom sections of the burner. Beds of 3 mm diameter glass beads are used to distribute the flows uniformly across the nozzles. Finally, sets of stainless steel screens are used to stabilize fuel and oxidizer flows directly at the nozzle exits, while a honeycomb plate is used to stabilize the nitrogen flow. The fuel and oxidizer flows impinge against each other to form a stable stagnation plane, with a diffusion flame established from the oxidized side. Technical purity methane (98%, AGA Gas) was used as a fuel. Additional experiments were performed with the addition of 8 carbon percent of acetylene to the methane stream. Mixing flows of oxygen with laboratory dry air controlled the oxygen content in the oxidizer stream. The flows were metered with electronic mass flow controllers providing accuracy within 1.5%. For a more comprehensive discussion of the experimental apparatus, see Ref. [24].

Thermophoretic sampling was used to capture particulates from the flame zone without the presence of a catalyst. The sampler is mounted on a tilted platform, which minimizes flame exposure of the grid and permitted the simultaneous sampling from the fuel to oxidizer sides of the flame. The grid's residence time inside the flame was approximately 30 ms. The grids were copper grids with a thin film of pure carbon deposited on one side. The thickness of the grid was 30 nm with a diameter of approximately 3 mm. Additionally, silicon oxide coated copper grids were utilized to confirm the presence of nanotubes on the carbon free coatings.

Synthesis of Nanostructures Without a Catalyst

Results were the first to demonstrate the formation of CNTs in the absence of a catalysis. Initially a single CNT surrounded by soot aggregate particles was captured in the flame (Fig. 2); its diameter and length are, respectively, approximately 20 and 320 nm. Figure 3 presents a transmission electron microscopy (TEM) image of captured nanoparticles and nanotubes. Here the tubes have diameters and lengths of approximately 20 and 120 nm, respectively, and the captured nanoparticles have an approximate average diameter of 30 nm. Also, it should be noted that evaluation of the nanotubes and nanopartcles from a large number of TEM images showed that the distribution of the species in these samples is essentially bimodal, e.g., numerous small nanoparticles and lengthy nanotubes but very few intermediate lengths. This bimodal distribution implies that nanoparticles and nanotubes probably are derived from the same seeds. If this is true, then once the nanotube reaches a critical length (several diameters of the nanoparticles), it does not close very easily until there is a large fluctuation in the flame. If the tubes are derived from the same seed as the nanoparticles, it may be able to control

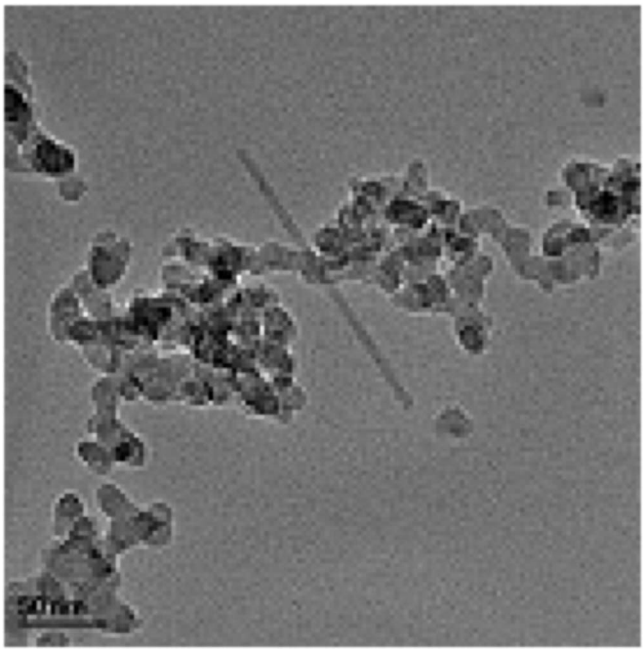

Fig. 2 TEM of single CNT

their production. A phenomenological explanation can be made for the mechanism of CNT formation. Since the CNTs were only observed for oxygen enrichment of greater than 50% and from a region slightly on the fuel rich side of the narrow diffusion flame, the nanotubes may be synthesized through a pyrolysis of the hydrocarbons resulting from an increase of radicals due to oxygen enrichment. Temperature also plays a significant role although delineating its influence in the narrow thickness of the reaction zone will be a challenge. These experiments demonstrated for the first time that CNTs could be formed in counterflow diffusion flames at atmospheric pressure without the introduction of a catalyst. However, a threshold oxygen concentration of approximately 52% appears to be required to synthesize CNTs through the pyrolysis of hydrocarbons resulting from the increase of radicals in oxygen enriched flames and opens the possibility that CNTs can be grown

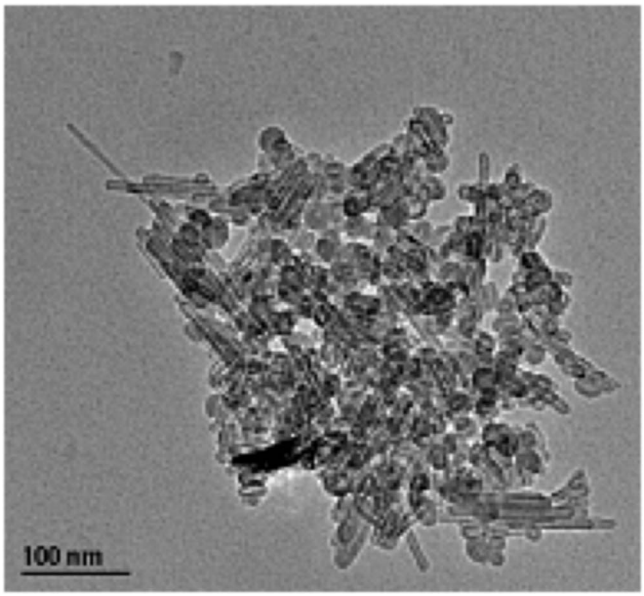

Fig. 3 TEM of captured nanotubes and nanopartcles

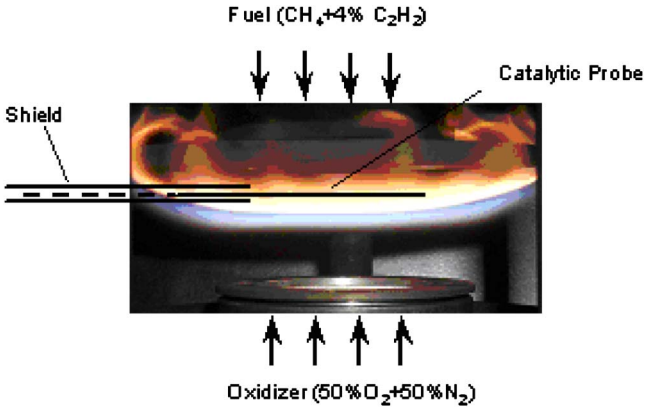

Fig. 4 Schematic of the experimental setup

in simple oxyfuel flames without a catalyst. These flames also exhibit an unusually large concentrations of fullerene [25]. Samples of condensable material from opposed flow diffusion flames and oxygen enriched air at atmospheric pressure were collected and analyzed by high-pressure liquid chromatography (HPLC) to determine the fullerene yield. High-resolution TEM studies revealed the strong presence of fullerenes. The molar ratio of C_{60} and C_{70} is nearly constant along the flame axis and close to 3. The existence of fullerenes may provide the needed nucleation sites for CNT formation.

Synthesis of Nanostructures Using Catalysts

To explore the influence of a catalyst on the generation of carbon nanostructures, the counterflow burner was modified to permit a 40 mm long catalytic probe to be introduced radially through the flame-protecting nitrogen gas shield to the yellow soot-containing region of the flame Fig 4. The central part of the probe (~25 mm) was used to study the structure of deposited materials. The 0.64 mm diameter probe was fabricated from Ni-based alloy with a composition 73%Ni+17%Cu+10%Fe. The axial position of the probe was controlled by a micron accurate positioning system.

The initial optical surface scans of the catalyst probe were performed by a scanning electron microscopy (SEM) with a cold field emission source. The SEM images collected from the location ~8.5 mm from the fuel nozzle show abundance of tubular nanostructures grown on the catalytic substrate (Fig. 5). Most of the formed nanofibers have inhomogeneous shapes containing frequent bends, kinks, and curved segments. The observed diameters vary from 20 nm to 100 nm. Some of the filaments are straight and uniform indicating the presence of regular internal graphitic structure. High densities of formed nanofibers and CNTs completely cover the catalyst surface.

The TEM images of characteristic nanostructures are shown in Figs. 6 and 7. Figure 6 shows carbon nanofibers of tubular structure with varying diameter and wall thickness. Straight sections of uniform diameter are clearly observed. Detailed TEM studies of the multiple tubular fibers reveal the presence of catalytic pearlike particles on the tip of the growing nanofibers, clearly indicating their catalyst-aided mechanism of formation. High-resolution TEM studies show the occurrence of nested carbon layers. Bundle of CNTs (Fig. 7) is another typical configuration observed. The CNTs and nanofibers with diameters from 10 nm to 70 nm form a well-oriented structure with dense tubular packing. Relative stability of the structure allows us to suggest that it forms by simultaneous parallel growth of tightly packed nanotubes. Formation of well-aligned structures of CNTs were reported by Yuan et al. [6] in coflow flames. However, significant separation of the tubes was observed in Yuan's experiments.

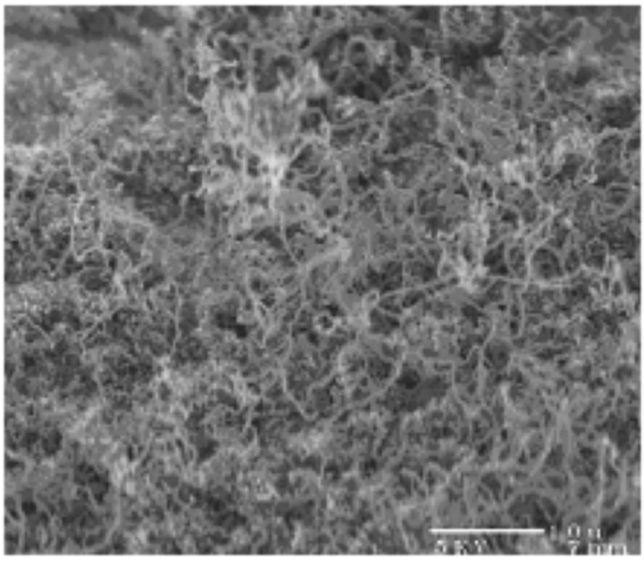

Fig. 5 SEM image showing the catalyst substrate covered with high-density layer of carbon nanofibers and CNTs

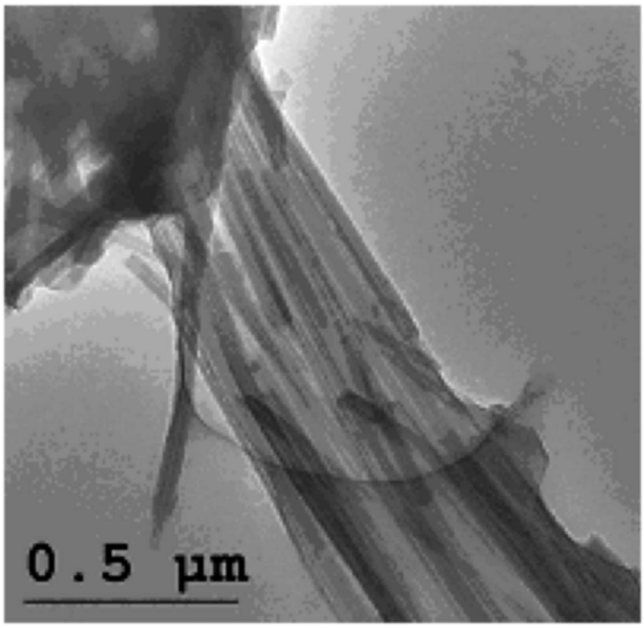

Fig. 7 TEM micrograph of well-aligned MWNT

It is generally accepted [26] that the growth of carbon tubules and nanofibers occurs by the extrusion of carbon dissolved in a metallic catalyst particle and/or an active catalytic site on the metal surface. The carbon constantly precipitates on one side of the particle resulting in a carbon over saturation and diffusion through the particle. As a result, graphene sheets are deposited on the other side of the particle forming a tubule with a diameter close to the particle size. The distinction between "tip growth" and "base growth" mechanisms does not appear to be essential; the dominant mechanism is often defined by the transport of the carbon to the active catalytic site. Puri [27] has developed a model to estimate the precipitation rates of carbon in the growth of CNTs.

The particle geometry and precipitation rate of the carbon on its surface are the main factors controlling the shape and growth rate of produced nanomaterials. In fact, a number of experiments have demonstrated that active particles can be produced by initial dissolving of the carbon in the surface layer of the metal catalyst and subsequent extraction of the particle with predetermined size and geometry. Similarly, particles often change size and geometry during the growth adjusting to the process parameters.

Samples collected closer to the flame front depict structural changes of the formed nanotubular material. SEM images illustrate that spiral coil morphology in this region of the flame. Here the temperature is approximately 950°C. The high concentration of helically coiled carbon nanofibers in carbon lattice is hindered by the essentially three-dimensional form of the studied object (Fig. 8).

Carbon microcoils have also been observed and obtained in CVD experiments. These CVD process studied catalyzed pyrolysis of acetylene as reported by several researches [28,29]. These unique morphology structures are expected to have numerous applications including microsensors, nanomechanical devices, and advanced composite materials. The regularly shaped nanotubular coils are expected to provide excellent properties, combining those of CNTs and solid carbon coils [30,31]. The mechanism of nanotubular coil formation, proposed by the authors, is based on

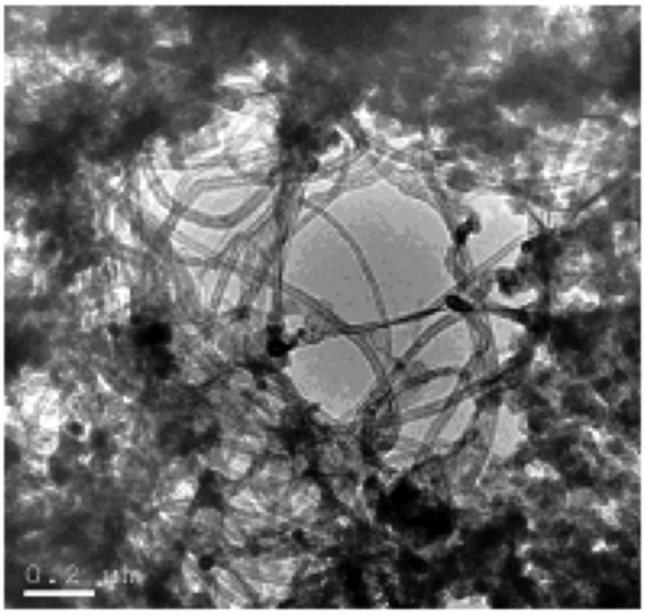

Fig. 6 TEM image of CNTs transferred to the microscope grid

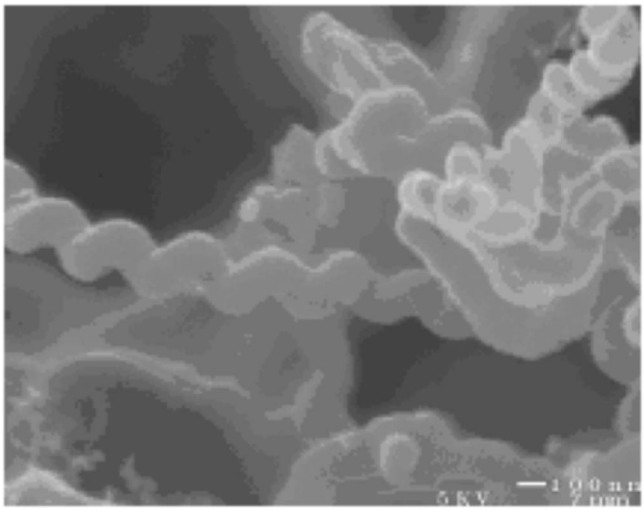

Fig. 8 SEM image of regularly coiled spiral carbon nanofiber

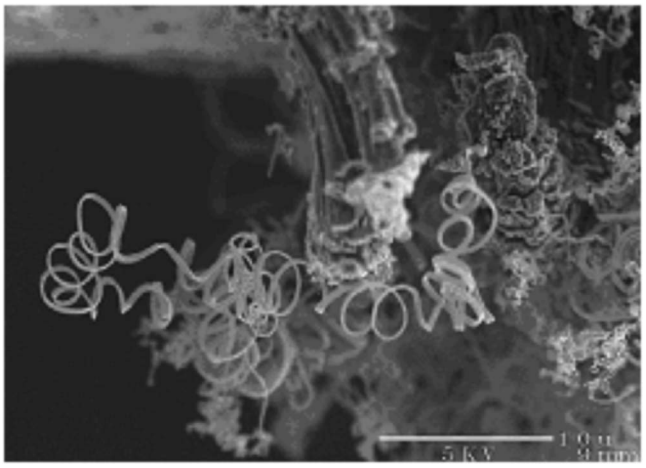

Fig. 9 TEM image of coiled carbon nanofiber. The nanofiber has rectangular cross section with height of 300 nm and thickness of 100 nm.

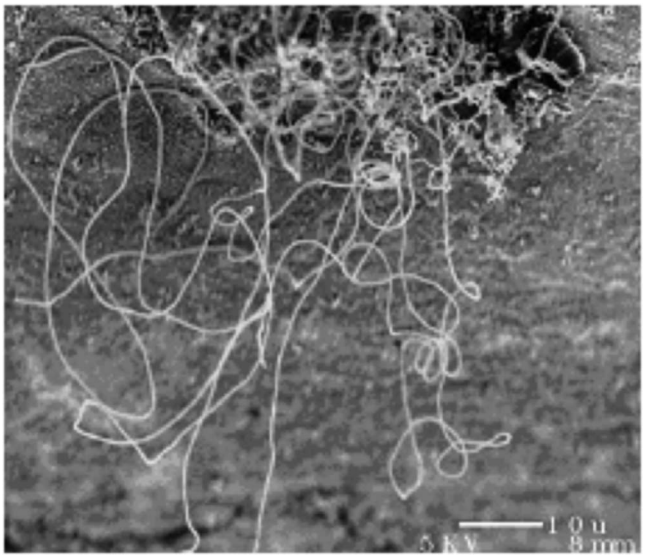

Fig. 10 SEM image of long (~0.2 mm) uniform diameter tubular carbon nanofiber

the variation of carbon deposition rates from adjacent planes of catalytic nanocrystal particles. More general consideration qualitatively describes formation of spiral and helical nanotubes by variation of deposition rates and hence, extrusion velocities along the contact curve between the active catalytic particle and the already formed tube. Detailed consideration shows that this can produce a spiral-shaped tube in the case of a circular contact area and a helix-shaped tube in the case of an elliptical contact area. It is possible to suggest that sharp gradients of temperature and chemical species in the vicinity of the flame zone induce sensible variations of carbon deposition rates providing the condition for the growth of helical structures.

Another distinctive coiled carbon structure revealed by TEM analysis is shown in Fig. 9. These structures are found to be present closer to the fuel nozzle (~8 mm from the fuel nozzle at ~550°C). The nanofiber has a distinctive ribbonlike appearance. The rectangular cross section, measured from TEM images, normally exhibit a height of 300 nm and a thickness of 100 nm. Infrequently, an aspect ratio of 5:1 was also observed. Large carbon deposits can be observed in the background. This image also depicts several similar structures appearing like unwound ribbon rolls, suggesting that formation of these structures occurs by circular growth of the carbon fiber. It was reported previously [32] that growth of this rarely observed ribbonlike filaments could be catalyzed by small iron-containing particles in an atmosphere containing CO at 650–700°C. The numerical simulations performed with the model developed by Beltrame et al. [33] shows that the given flame location are indeed characterized by temperature close to 700°C and the presence of carbon monoxide. Previous studies revealed that stacking of carbon layers in similar objects is not only very ordered but also aligned perpendicular to the ribbon surface providing numerous edges of graphite layers useful for development of catalysts and adsorbents.

In another low temperature region of the flame, long (~0.2 mm) regular carbon nanofibers with diameters from 50 nm to 200 nm were observed (Fig. 10). Relatively low concentration of other carbon deposits can be seen in the background. Higher magnification reveals smooth uniform fiber surface with practically constant diameter. The characteristic length of the fiber suggests relatively high growth rates. High-resolution TEM images of these objects (Fig. 11) depict a texture of well-oriented concentric graphitic cylinders with average interplanar spacing close to 0.34 nm. The small hollow core inside the fiber is surrounded by large numbers (~100) of axiparallel layers. The somewhat similar structured carbon nanofibers, recently reported by Endo et al. [34] were obtained by the pyrolysis of benzene/ferrocene feedstock in CVD experiments. Albeit the characteristic diameters of the obtained nanofibers are relatively large, their internal structure is very similar to the structure of CNTs.

Even though all current experiments were conducted with fixed flame parameters and by applying only a single catalyst material, the synthesized forms of carbon nanomaterials change dramatically. A change in flame position induces significant variations in macromorphology and in the microstructure of the carbon nanomaterials formed. The modification of growth conditions is directly related to the variation of the flame environment pertinent to the specific flame location and temperature. Temperature, radical, and hydrocarbon concentrations are strong functions of axial position in the flame. The presence of specific hydrocarbons and

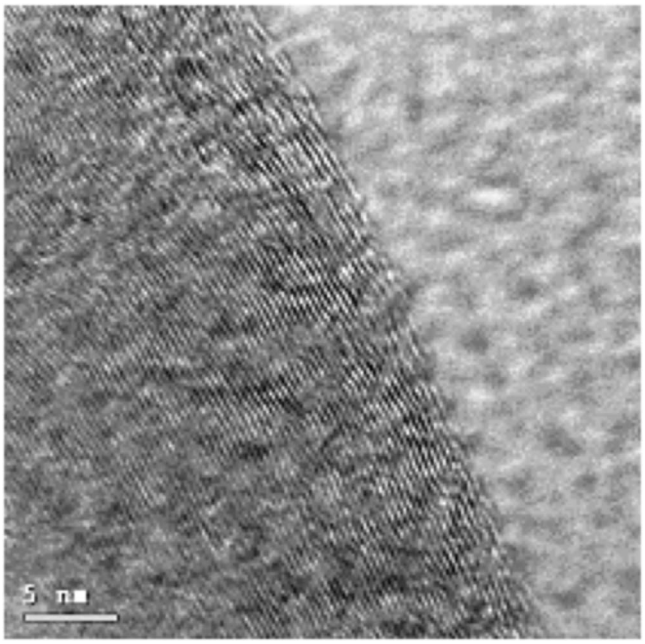

Fig. 11 High-resolution TEM image of the wall of the long uniform diameter tubular carbon nanofiber uniform-diameter carbon nanofiber shown in Fig. 10. Regular structure and orientation of the carbon layers parallel to the fiber axis is observed.

radical species at a given local temperature condition alters the growth mechanism leading to the selective production of various forms of nanostructures.

The variety of the observed nanoforms leads to the conclusion that flames are a very powerful and highly selective tool for generation of carbon structures with varying morphology and structure. The optimal conditions for production of distinctive nanomaterials of interest include optimization of both catalyst and flame parameters. However, the obtained results suggest that even for a given catalytic substrate, a specific nanomorphology can be effectively grown by tailoring the flame environment and/or selective sampling in specific regions of the flame.

Electric Field Control of Nanostructure Growth and Alignment

If compared with CVD and plasma methods, a typical flame is a reacting medium characterized by strong thermal and chemical nonuniformities. It is not surprising that a number of flame studies show a high morphological and growth rate sensitivity of formed carbon nanomaterials to the flame location. For this reason, the opposed flow diffusion flame is superior to the coflow flame since the former is essentially a 1D process. Regardless an efficient control method is required to improve uniformity and productivity of flame based synthesis, utilization of electromagnetic fields as a method of control is one of the promising approaches. The electric field control was successfully tested in CVD and plasma synthesis studies. The first use of electric fields applied to control the growth of CNTs in flames was reported in Ref. [11] wherein the carbon nanostructures formed on a catalytic probe were comparatively analyzed for various probe potentials.

The counterflow burner and 40 mm long catalytic probe in Fig. 4 was modified to establish a radial electric field. To generate radial electric fields on the probe surface, the probe was supported on Teflon® isolators while the burner nozzles were kept at ground potential thus generating a floating potential. In general, this configuration allows the generation of a variety of electric fields to control the probe potential with the external electric source. Due to the small size of the probe relative to size of the burner nozzles, the electric field around the probe can be well approximated as radial. Experiments were conducted with a residence time of 10 min with the probe grounded or at various potentials With a grounded catalytic probe, carbon nanostructures similar to those discussed in the previous section were found. With various floating potentials applied, a significant change occurred. Instead of multiple morphologies, only aligned multiwall CNTs were formed.

Variation of structure and morphology of formed carbon nanomaterials is directly attributed to the strong variation of temperature and chemical composition in the studied flame region. The distributions of several major hydrocarbons (CH_4, C_2H_2, CO, and C_6H_6) that can contribute to the growth of carbon deposits are shown in Fig. 12 along with the temperature profile [33]. All components vary significantly in the flame region of interest.

Thus, concentration of CH_4 and C_2H_2 diminishes below 100 ppm for $Z>10.5$ mm; the concentration of CO grows with Z reaching its maximum at this point; C_6H_6 is present in essential quantities only from 8 nm to 10 mm, maximizing at 9.5 mm ($T \approx 890°C$). The catalytic probe was inserted at the axial flame position of $Z=8.5$ mm ($T \approx 740°C$) with a probe potential −300 mV. The produced carbon deposits were analyzed with SEM (Figs. 13 and 14). Figure 13 shows that controlled electric field growth generates a coat of vertically aligned CNTs (VACNTs).

Low magnification image shows that a layer of VACNT, uniformly coat the catalytic substrate. The generated nanotubes are characterized by high purity and alignment, as shown in Fig. 14. The absence of alternative nanomorphology observed without the E field should be noted as well as the absence of soot. For this

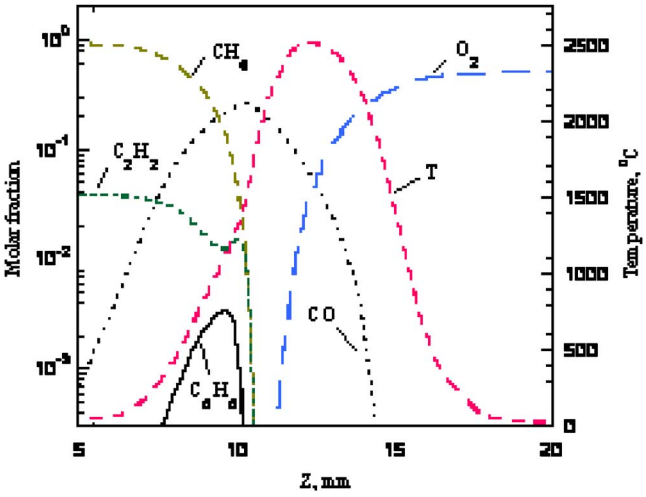

Fig. 12 Temperature and major chemical species in opposed flow oxy-flame as a function of the distance from the fuel nozzle (Z), data of numerical model [24]

axial position, hundreds of nanotube diameters were measured. The results for these multiwalled nanotubes show a very narrow diameter distribution with a mean diameter close to 38 nm. Analysis of SEM images on the synthesized carbon materials on grounded and applied E field catalytic substrates suggests that nanotube growth is greatly enhanced when the electric field is present compared with the case when the probe is grounded and produces only VACNTs. Other interesting aspects, displayed in Figs. 13 and 14, include not only the presence of VACNTs but also the *absence of contaminants* such as soot or other nontubular carbon structures that are often present in the flame synthesis of CNTS. It should be noted that the samples analyzed in this study were never purified by any kind of chemical and/or physical treatment. With electric field stabilization, position in the flame remains the important factor in controlling the thickness of the coat layer of multiwalled nanotubes formed under a floating point potential.

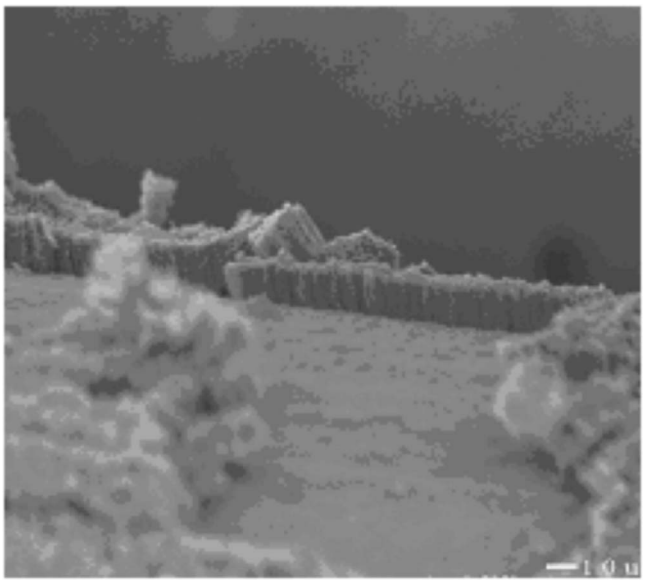

Fig. 13 SEM image of orderly VACNT layer covering the probe surface; floating potential mode, $Z=8.5$ mm, $T \sim 740C$. The layer is partially removed revealing the bare catalytic surface.

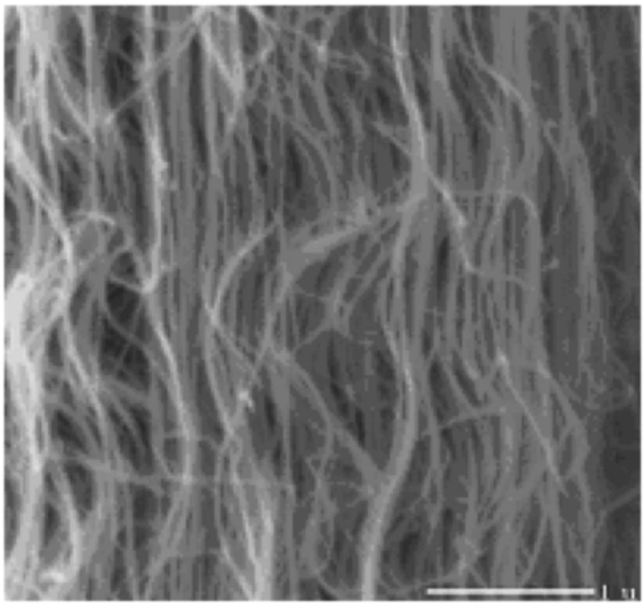

Fig. 14 High-resolution SEM of the wall edge of the layer shown in Fig. 4 displays nanotube purity and alignment

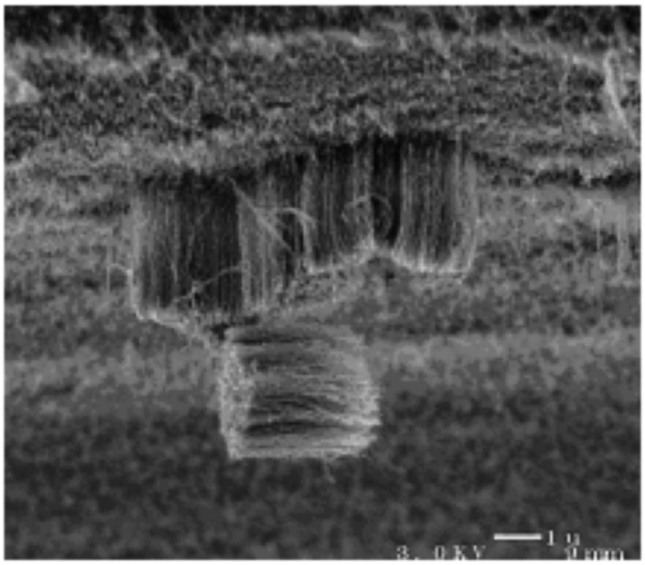

Fig. 16 Higher resolution SEM of a micro area in Fig. 6. The CNT bundle mechanically removed from catalytic surface is re-attached to the top of the originally uniform VACNT layer.

Figures 15 and 16 show the variation of nanotube formation along the burner axis. Figure 15 is a low resolution SEM image of the catalytic substrate inserted in the floating potential mode (FPM) at the axial distance of $Z=9.5$ mm ($T\approx 890°C$). The well defined layer formed here shows highly ordered CNT arrays, similar to those found in the previous position. The application of high-resolution imaging in Fig. 15 reveals a highly dense bundle of nanotubes attached to the tips of the undisturbed nanotube layer, as shown in Fig. 16. High-resolution imaging and an energy dispersive x-ray (EDX) elemental spectrum analysis shows that these nanotube bundles are free of contaminants as well. It is evident by comparing micrographs obtained at the axial position of $Z=8.5$ mm to those obtained at $Z=9.5$ mm that the thickness of the coating layer decreased when the substrate is inserted further down from the edge of the fuel nozzle. Several SEM images were examined from various locations on the probe surface; an average layer thickness of 9 μm was measured for this flame location. Another interesting aspect of these nanotube layers is the strong van der Waals body attraction force existing between the tubes in the self-formed macrobundles [25]. This aspect is unique since it greatly simplifies their harvesting, e.g., micron size arrays of VACNTs can be easily removed.

Figure 17 represents SEM images of arrays of orderly and high purity nanotubes scanned at top, center, and bottom of the probe surface, respectively. For all probe locations considered for microscopic analysis, arrays of nanotubes covered the probe with orientation perpendicular to the probe surface. By inspection of Fig. 18, it is evident that most of the formed material remains attached to the surface. Higher resolution SEM on the walls of this material showed that the bulk material is composed of arrays of nanotubes. The separated material always tends to remains packed like

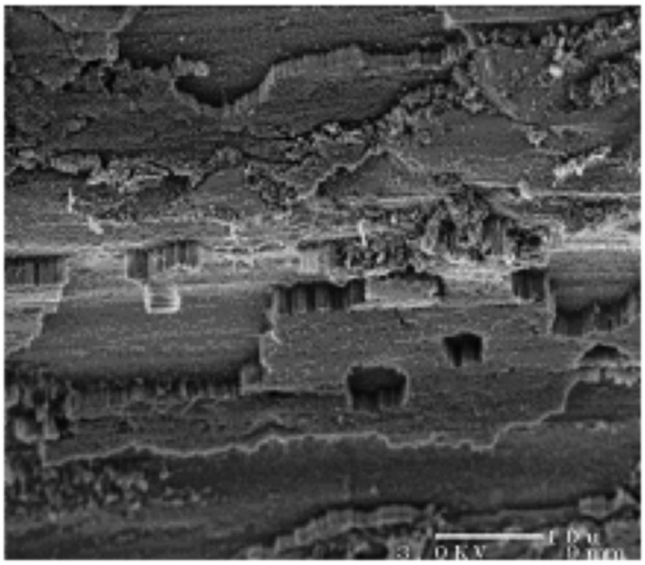

Fig. 15 Low resolution SEM image shows the catalyst substrate coated with a layer of carbon nanotubes (FPM) $Z=9.5$ mm.

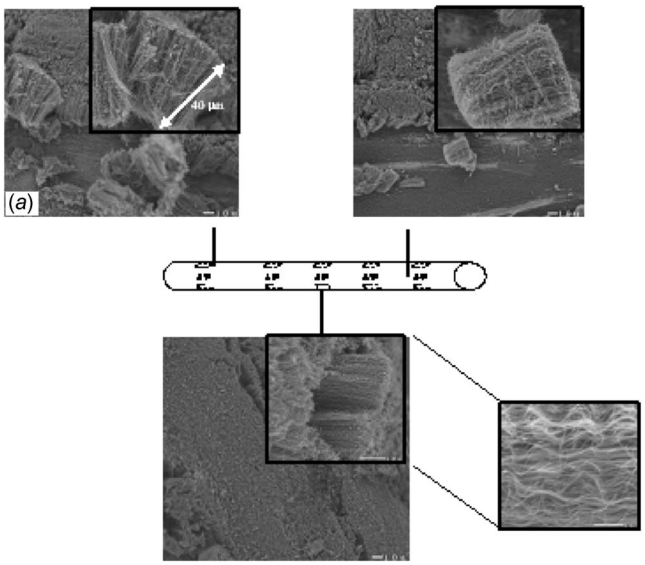

Fig. 17 Low- and high-resolution (inserts) SEM images of scanned probe surface coating layer, showing uniformity of VACNT

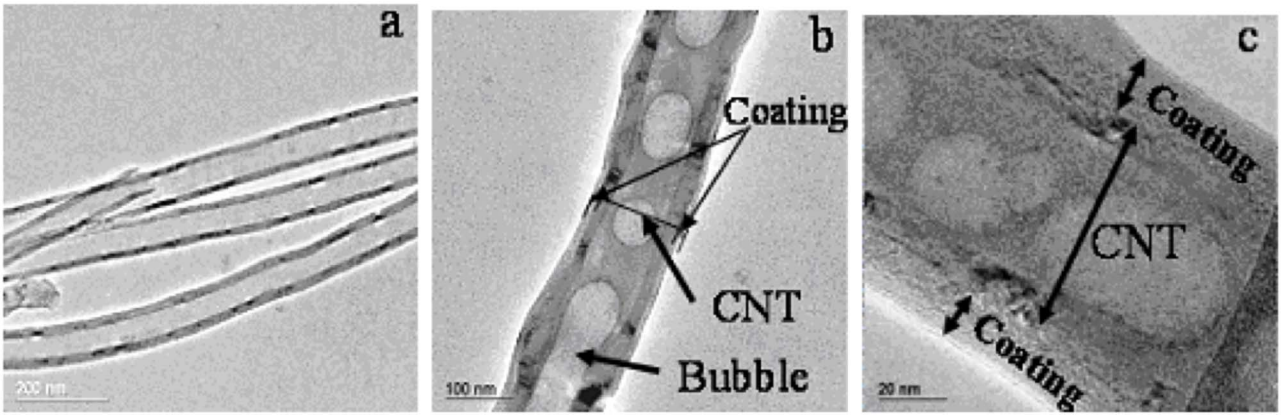

Fig. 18 Coating of the flame generated CNT: (*a*) not treated CNTs; (*b*) CNT coated with polystyrene-fluid bubbles in inner channels; (*c*) polystyrene coating

bundles of hay and always maintains its original length. In the upper right corner of Fig. 17(*b*), a bundle of highly dense nanotubes is observed. This bundle has a cylindrical shape and a length of approximately 40 μm, which coincide with the length of nanotubes in the attached VACNT layer. The material remains packed due to the strong van der Waals forces that exist between the tubes in the bundles. The same sample probe was then rotated 180 deg for further SEM scanning and again, layers of nanotubes were present covering the catalytic substrate surface.

From a number of micrographs, the average diameter of the cylindrical multishells was measured, a monodisperse diameter distribution averaging 38 nm was obtained. The application of high-resolution TEM imaging on these CNTs reveals a texture of well-aligned and highly graphitized concentric graphitic cylinders. The average interplanar distance of the concentric cylindrical graphene sheets was measured to be 0.34 nm. The layer planes appear to be perfectly parallel to the central tube axis.

The experimental results show the strong influence of the electric field on alignment, size distribution, internal structure, and growth rate of carbon nanotubes. The mechanism of alignment is widely discussed in the literature [35]. As an example, employing a plasma discharge, Merkulov et al. [36] successfully demonstrated that the direction of the electric field lines determines the orientation of the carbon nanotubes and nanofibers; electric field alignment of single-walled nanotubes was considered by Zhang et al. [37].

Overall, the electric fields near the tips of growing nanotubes can be extremely high. Even applied potentials as small as few tens of millivolts can develop an electric field exceeding 1000 V/cm at the characteristic nanotube diameter. The experimentally measured field enhancement factors are reaching 800 for multiwalled nanotubes [37] and 3000 for single-walled nanotubes [38]. The enhancement of the electric field at the tip of closed conducting nanotube was calculated by Maiti et al. [39]; the resulting force estimated from the axial stress is in good agreement with Taylor's solution for long rods in an *E* field.

The important aspect of the aligned growth is that the constant orientation of catalytic particles at the tips of the growing nanotubes is preserved by the electric field. The nonsymmetric catalytic particle is polarized in the electric field, and the induced dipole moment tends to be aligned along the electric field lines. The formation of helical and spiral nanotubes requires variation of the particle orientation. As a result, the constant orientation of the catalytic particle stabilizes the linear CNT structures. Finally, the electric field can influence the transport of charged particles in flames that include ions and charged soot particles. In this way, soot entrapment in the growing layer can be controlled by the electric field.

As an alternate approach, Saito et al. [22] recently employed the opposed flow flame configuration together with anodized aluminum oxide (AAO) templates to generate aligned CNTs. The CNT diameters generated were the same as the pores and the CNTs' growth stopped at the AAO surface, which would yield the same lengths for all the CNTs. These CNTs were extracted from the template with a sonication treatment. They also varied the strain rate and their results suggest that its effect was through the carbon source available to diffuse across the stagnation surface rather than the residence time. They also showed that there is a common temperature region (1023–1073 K) for both CVD and their process for synthesizing CNTs. This was the temperature region that also existed in the MWNT synthesis employing electric field control.

Future Areas of Research

Functionalization of Carbon Nanotubes. Once CNTs' growth, orientation, and properties can be controlled, the focus of research efforts is shifted from synthesis to the processing of CNTs for functionalization. This often involves coating and/or filling of the CNTs. While the coating of the outer surface of CNTs can be performed in aqueous and other organic solvents, the inner surface modifications and deposit are challenging. Reported CNT coating methods include coating of single- and multiwalled nanotubes with SiO_2, polymers, proteins, metals, and metal oxides [40–43]. The development of polymer coating of carbon nanotubes is very desirable due to their potential application in composites and electronic devices. A variety of methods are developed for production of CNT composites in epoxy and SiO_2 matrices [44,45]. One promising approach employs the use of supercritical fluids. Various polymers can be dissolved in supercritical CO_2. If the supercritical CO_2 medium contains CNTs, a change in temperature or pressure can result in specific polymers precipitating out of the supercritical state and onto the surface of the CNT. Early experiments coated individual MWNTs using this process. Preliminary results showed the following.

Different synthesis methods employed for preparation of pristine CNTs had important influences on the coating quality. The flame synthesized nanotubes had bamboo shapes and closed tips. Due to the low reaction temperature of 40°C, it is difficult to expect the penetration of supercritical CO_2 and monomer mixtures through the CNT walls. Indeed, inside nanotube cavities were found to be free of any material. However, as shown in Fig. 18, very good and uniform coating was achieved. The thickness of the coating was approximately 11 nm. After encapsulation and single coating of the CNT, they were further processed to obtain a second polymer coating. A grid with the previously polystryrene

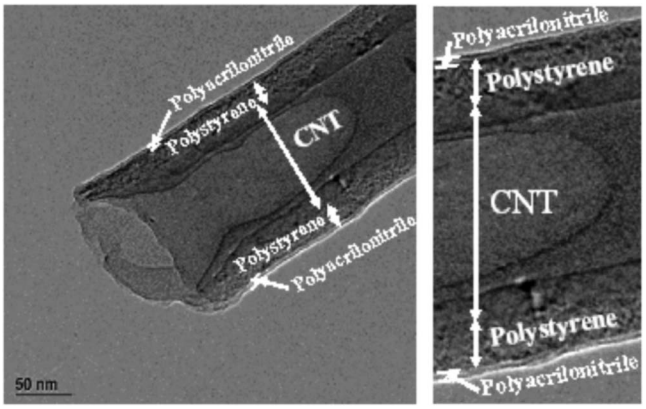

Fig. 19 Double coating of CNT

coated and encapsulated nanotubes was placed in solution of acrylonitrile and BPO and a second coating layer was achieved (Fig. 19). The polyacrylonitrile layer was uniform and had a thickness of 5 nm, which was attributed to the different solubilities of styrene and acrylonitrile in CO_2. In order to ensure a solution, the difference of the solubility parameters of two substances should approach zero. The solubility parameter of CO_2 at 223 K is 8.9 compared to the solubility parameters of acrylonitrile and styrene at 298 K of 10.5 and 9.3, respecively. This means that styrene is much more soluble in CO_2 compared to acrylonitrile. This is expected to be a fruitful area of future study.

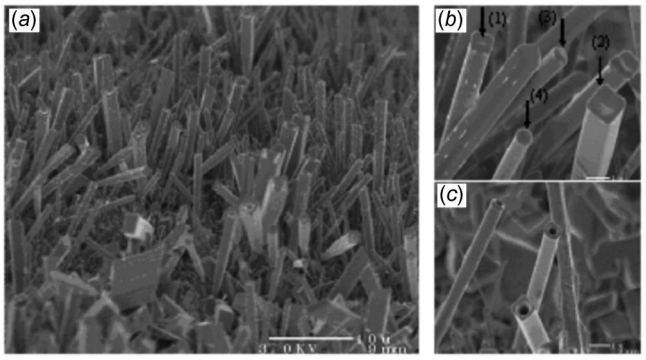

Fig. 20 Representative SEM images collected on the surface of a Mo probe inserted at the flame height of 12 mm for 2 min: (*a*) A low resolution SEM image collected on the Mo surface, (*b*) Higher-resolution imaging analysis shows the presence of rectangular (1), square (2), and circular fiberlike structures (3,4) (*c*) Some tips of the circular and rectangular structures are open showing the inner hollow cavities.

Other Nanomaterials. Flames have been also successfully employed for growth of a variety of other nanomaterials such as carbides and oxides of various metals [46,47]. In recent years, much effort has been devoted to the study of molybdenum oxides and related materials. It has been shown that molybdenum oxides possess unique catalytic and electronic properties and have potential applications in chemical synthesis, petroleum refining, recording media, and sensors [48–51].

Figure 20 represents SEM images collected at different resolutions on the surface of a 1 mm diameter molybdenum probe exposed to the flame at a height of $Z=12.0$ mm (wire temperature $\sim 1200°C$) for a period of 2 min [52]. At this particular flame position, the whiskers of rectangular and square cross section are observed along with the circular ones (Fig. 20). The tips of rectangular structures exhibit small depressions of regular shape suggesting their crystalline structure. The tips of the circular whiskers have a dome-capped shape suggesting the presence of liquid matter during the synthesis (Fig. 20(*b*)). In several areas, SEM analysis also revealed that some rectangular and circular whiskers have open tips (Fig. 20(*c*)) exhibiting their hollow structure. Characteristic sizes of rectangular and circular objects were determined from several SEM images. The rectangular structures have side dimensions ranging from 0.5 μm to 4 μm. The circular structures appear to be much smaller; their diameters are less than 1 μm with the average diameter close to 0.33 μm. Some of the circular whiskers have characteristic nanoscale dimensions. The dominance of circular geometry at submicron and nanoscale range could be related to the small relative surface area and, hence, reduced surface energy. The tip structure also supports the vapor-liquid-solid growth mechanism. Under the influence of the surface tension, a liquid droplet formed on the tip of the growing whisker acquires a semispherical shape that influences the formation of cylindrical whisker body.

The repositioning of the 1 mm probe to the flame height of $Z=11.0$ mm (wire temperature $\sim 1150°C$) led to the essential variation of the synthesized material structures. As in the previous case, the probe was exposed to the flame for a period of 2 min. Performed SEM analysis revealed that the surface of the probe is covered with densely packed micron-size structures that have

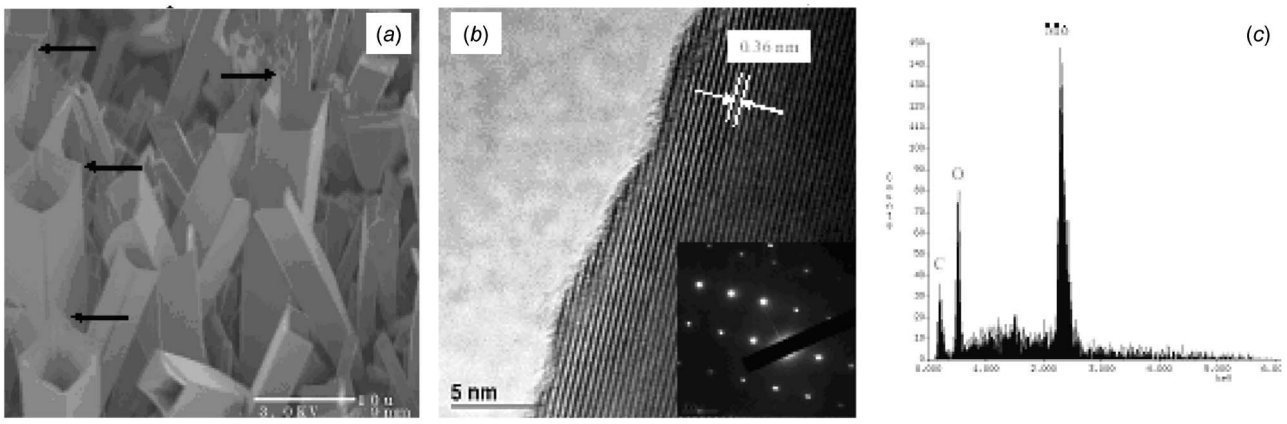

Fig. 21 Representative SEM images collected on a Mo probe inserted at the flame height of 11.0 mm for sampling time of 2 min: (*a*) SEM image shows the presence of channellike structures with rectangular and square morphologies, the structures appear to be completely hollow, and their corners are well defined, with lengths slightly longer at one of the corners, as shown by arrows; (*b*) High-resolution TEM image exhibiting the lattice structure on the edge of the channel with measured lattice distance of 0.36 nm corresponding to 0_111*p* plane of a monoclinic MoO_2; (*c*) EDX of elemental spectrum acquired using SEM.

shape of hollow rectangular channels (Fig. 21(*a*)). It is observed that the slender, prismatic, four face structures are completely hollow, and the inside cavities are very large and devoid of other materials. The unique morphology with large cavities, nanosized walls, sharp edges, and high specific surface gives the structure a significant importance, for example, in medical applications. The large cavities can also be useful for a variety of applications including storage of liquids or nanoparticles, material reinforcements, or as a significant component in the fabrication of microelectromechamical system (MEMS) devices, etc.

Summary

This review examined combustion synthesis processes useful for the generation of carbon nanostructures. Results obtained using of coflow diffusion flames are summarized. The inherent advantages of alternately employing an opposed flow diffusion flame, which includes their one dimensionality and greater flame volume, are discussed. Employing oxygen enriched air in such opposed flow flames, it was found that for the first time that carbon nanotubes and carbon nanoparticles could be synthesized without the use of a catalyst when the oxygen enhancement exceeded 52%. When a catalyst was employed, multiple nanostructures (tubes, spirals, ribbons, fibers) were generated in different temperature regions of this flame process. It suggests that a single such flame could be exploited to yield different carbon nanomorphologies by simply harvesting from different regions of this opposed flow diffusion flame.

The application of *E* fields on the opposed flow diffusion flame lead to a preferred single morphology, CNTs allowing control of their orientation and growth rates. Such *E*-field application also lead to the generation of vertically aligned arrays of CNTs in a simple direct manner without the need for templates. A discussion of the used of AAO templates in these types of flames is also presented together suggestion for areas of future work.

Acknowledgment

This work was partially supported by the National Science Foundation Grant No. CTS-0304528 and the Kaplan Scholar Fund. The author extends special thanks to colleague Dr. A. Saveliev, for input and helpful discussions and to the students who worked on this research, W. Merchan-Merchan, A. Milanese, and E. Lock.

References

[1] Iijima, S., 1991, "Helical Microtubules of Graphitic Carbon," Nature (London), **354**, pp. 56–58.
[2] Shi, Z., Lian, Y., Zhou, X., Gu, Z., Zhang, Y., Iijima, S., Zhiou, L., Yue, K. T., and Zhang, S., 1999, "Mass Production of Single-Wall Carbon Nanotubes by Arc Discharge Method," Carbon, **37**, pp. 1449–1453.
[3] Guo, T., Nikolaev, P., Thess, A., Colbert, D. T., and Smalley, R. E., 1995, "Catalytic Growth of Single-Walled Nanotubes by Laser Vaporization," Chem. Phys. Lett., **243**, pp. 49–54.
[4] Andrews, R., Jacques, D., Rao, A. M., Derbyshire, F., Qian, D., Fan, X., Dickey, E. C., and Chen, J., 1999, "Continuous Production of Aligned Carbon Nanotubes: A Step Closer to Commercial Realization," Chem. Phys. Lett., **303**, pp. 467–474.
[5] Thess, A., Lee, R., Nikolaev, P., Dai, H. J., Petit, P., Robert, J., Xu, C. H., Lee, Y. H., Kim, S. G., Rinzler, A. G., Colbert, D. T., Scuseria, G. E., Tomanek, D., Fischer, J. E., and Smalley, R. E., 1996, "Crystalline ropes of Metallic Carbon Nanotubes," Science, **273**, pp. 483–487.
[6] Yuan, L., Saito, K., Pan, C., Williams, F. A., and Gordon, A. S., 2001, "Nanotubes From Methane Flames," Chem. Phys. Lett., **340**, pp. 217–223.
[7] Yuan, L., Saito, K., Hu, W., and Chen, Z., 2001, "Ethylene Flame Synthesis of Well-Aligned Multi-Walled Carbon Nanotubes," Chem. Phys. Lett. **346**, pp. 23–28.
[8] Yuan, L., Li, T. X., and Saito, K., 2002, "Synthesis of Multiwalled Carbon Nanotubes Using Methane/Air Diffusion Flames," Proc. Combust. Inst., **29**, pp. 1087–1092.
[9] Merchan-Merchan, W., Saveliev, A. V., Kennedy, L. A., and Fridman, A. A., 2002, "Formation of Carbon Nanotubes in Counter-Flow, Oxy-Methane Diffusion Flames Without Catalyst," Chem. Phys. Lett., **354**, pp. 20–24.
[10] Merchan-Merchan, W., Saveliev, A. V., Kennedy, and L. A., 2003, "Carbon Nanostructures in Opposed Flow Methane Oxy Flames," Combust. Sci. Technol., **175**, pp. 2217–2236.
[11] Merchan-Merchan, W., Saveliev, A. V., and Kennedy, L. A., 2004, "High-Rate Flame Synthesis of Vertically Aligned Carbon Nanotubes Using Electric Field Control," Carbon, **42/3**, pp. 599–608.
[12] Vander Wal, R. L., 2000, "Diffusion Flame Synthesis of Single-Walled Carbon Nanotubes," Chem. Phys. Lett., **323**, pp. 217–223.
[13] Vander Wal, R. L., 2000, "Flame Synthesis of Substrate-Supported Metal-Catalyzed Carbon Nanotubes," Chem. Phys. Lett., **324**, pp. 217–223.
[14] Vander Wal, R. L., and Lee, J. H., 2002, "Ferrocene as a Precursor Reagent for Metal-Catalyzed Carbon Nanotubes: Competing Effects," Combust. Flame, **130**, pp. 27–36.
[15] Vander Wal, R. L., 2002, "Fe-Catalyzed Single-Walled Carbon Nanotube Synthesis Within a Flame Environment," Combust. Flame, **130**, pp. 37–47.
[16] Vander Wal, R. L., Hall, L. J., and Berger, G. M., 2002, "Optimization of Flame Synthesis for Carbon Nanotubes Using Supported Catalyst," J. Phys. Chem. B, **106**, pp. 13122–13132.
[17] Height, M. J., Howard, J. B., Tester, J. W., and Vander Sande, J. B., 2004, "Flame Synthesis of Single-Walled Carbon Nanotubes," Carbon, **42**, pp. 2295–2307.
[18] Avigal, Y., and Kalish, R., 2001, "Growth of Aligned Carbon Nanotubes by Biasing During Growth," Appl. Phys. Lett., **78**(16), pp. 2291–2293.
[19] Srivastava, A., Srivastava, A. K., and Srivastava, O. N., 2001, "Curious Aligned of Carbon Nanotubes Under Applied Electric Field," Carbon, **39**, pp. 201–206.
[20] Lee, K. H., Cho, J. M., and Sigmund, W., 2003, "Control of Growth Orientation for Carbon Nanotubes," Appl. Phys. Lett., **82**(3), pp. 448–450.
[21] Hurt, R., 2005, "Synthesis and Destruction of Carbon Materials and Nanoforms in Flames," *Proceedings of the Fourth Joint Meeting U.S. Section of the Combustion Institute*, Plenary Session II.
[22] Li, T. X., Zhang, H. G., Wang, F. J., Chen, Z., and Saito, K., 2007, "Synthesis of Carbon Nanotubes on Ni-Alloy and Si-Substrates Using Counterflow Methane-Air Diffusion Flames," Proc. Combust. Inst., **31**, pp. 1849–1856.
[23] Lutz, A. E., Kee, R. J., Grcar, J. F., and Rupley, F. M., 1996, "OPPDIFF: A Fortran Program for Computing Opposed Flow Diffusion Flames," Sandia National Laboratories Report No. SAND96-8243.
[24] Merchan-Merchan, W., 2004, "Flame Synthesis of Carbon Nanotubes and Related Carbon Nano-Materials," Ph.D. thesis, University Illinois at Chicago.
[25] Silvestrini, M., Merchan-Merchan, W., Richter, H., Saveliev, A., and Kennedy, L. A., 2005, "Fullerenes Formation in Atmospheric Pressure Opposed Flow Oxy-Flames," Proc. Combust. Inst., **30**, pp. 2545–2552.
[26] Baker, R. T. K., 1989, "Catalytic Growth of Carbon Filaments," Carbon, **315**, pp. 315–323.
[27] Naha, S., Sen, S., De, A. K., and Puri, I. K., 2007, "A Detailed Model for the Flame Synthesis of Carbon Nanotubes and Nanofibers," Proc. Combust. Inst., **31**, pp. 1821–1829.
[28] Motojima, S., Hasegawa, I., Kagiya, S., Andoh, H., and Iwanaga, H., 1995, "Vapor Phase Preparation of Micro-Coiled Carbon Fibers by Metal Powder Catalyzed Pyrolysis of Acetylene Containing a Small Amount of Phosphorus Impurity," Carbon, **33**, pp. 1167–1173.
[29] Chen, X., and Motojima, S., 1999, "Morphologies of Carbon Micro-Coils Grown by Chemical Vapor Deposition," J. Mater. Sci., **34**, pp. 5519–5524.
[30] Amelinckx, S., Zhang, X. B., Bernaerts, D., Zhang, X. F., Ivanov, V., and Nagy, J. B., 1994, "A Formation Mechanism for Catalytically Grown Helix-Shaped Graphite Nanotubes," Science, **265**, pp. 635–637.
[31] Wen, Y., and Shen, Z., 2001, "Synthesis of Regular Coiled Carbon Nanotubes by Ni-Catalyzed Pyrolysis of Acetylene and a Growth Mechanism Analysis," Carbon, **39**, pp. 2369–2386.
[32] Murayama, H., and Maeda, M. A., 1990, "A Novel Form of Filamentous Graphite," Nature (London), **345**, pp. 791–793.
[33] Beltrame, A., Porshnev, P., Merchan-Merchan, W., Saveliev, A., Fridman, A., Kennedy, L. A., Petrova, O., Zhdanok, S., Amoury, F., and Charon, O., 2001, "Soot and NO Formation in Methane Oxygen Enriched Diffusion Flames," Combust. Flame, **124**, pp. 295–310.
[34] Endo, M., Kim, Y. A., Takeda, T., Hong, S. H., Matusita, T., Nayashi, T., and Dresselhaus, M. S., 2001, "Structural Characterization of Carbon Nanofibers Obtained by Hydrocarbon Pyrolysis," Carbon, **39**(13), pp. 2003–2010.
[35] Lee, K. H., Cho, J. M., and Sigmund, W., 2002, "Control of Growth Orientation for Carbon Nanotubes," Appl. Phys. Lett., **82**(3), pp. 448–450.
[36] Merkulov, V. I., Melechkov, A. V., Guillorn, M. A., and Simpson, M. L., 2002, "Controlled Alignment of Carbon Nanofibers in a Large-Scale Synthesis Process," Appl. Phys. Lett., **80**(25), pp. 4816–4818.
[37] Zhang, Y., Chang, A., Cao, J., Wang, Q., Kim, W., Li, Y., Morris, N., Yenilmez, E., Kong, J., and Dai, H., 2001, "Electric-Field-Directed Growth of Aligned Single-Walled Carbon Nanotubes," Appl. Phys. Lett., **79**, pp. 3155–3157.
[38] de Heer, W. A., Chatelain, A., and Ugarte, D., 1995, "A Carbon Nanotube Filed-Emission Electron Source," Science, **270**, pp. 1179–1180.
[39] Maiti, A., Brabec, C. J., Roland, C., and Bernholc, J., 1994, "Growth Energetics of Carbon Nanotubes," Phys. Rev. Lett., **73**, pp. 2468–2471.
[40] Balavione, J., Schulz, F., Richard, C., Mallouh, V., Ebessen, T., and Mioskowski, C., 1999, "Helical Crystallization of Proteins on Carbon Nanotubes: A First Step Towards the Development of New Biosensors," Angew. Chem., Int. Ed., **38**, pp. 1912–1915.
[41] Zhang, Y., Franklin, N. W., Chen, R. J., and Dai, H., 2000, "Metal Coating on Suspended Carbon Nanotubes and Its Implication to Metal-Tube Interaction," Chem. Phys. Lett., **331**, pp. 35–41.
[42] Poetschke, P., Bhattacharyya, A., and Janke, A., 2004, "Carbon Nanotube-Filled Polycarbonate Composites Produced by Melt Mixing and Their Use in

Blends With Polyethylene," Carbon, **42**(5–6), pp. 965–969.
[43] Qian, D., Dickey, E. C., Andrews, R., and Rantell, T., 2000, "Load Transfer and Deformation Mechanisms in Carbon Nanotube-Polystyrene Composites," Appl. Phys. Lett., **76**(20), pp. 2868–2870.
[44] Ning, J., Zhang, J., Pan, Y., and Guo, 2004, "Surfactants Assisted Processing of Carbon Nanotube-Reinforced SiO2 Matrix Composites," Ceram. Int., **30**, pp. 63–67.
[45] Wang, X. B., Liu, Z. M., Hu, P. A., Liu, Y. Q., HAn, B. X., and Zhu, D. B., 2005, "Nanofluids in Carbon Nanotubes Using supercritical CO2: A First Step Towards a Nanochemical Reaction," Appl. Phys. A: Mater. Sci. Process., **80**, pp. 637–639.
[46] Suemitsu, M., Abe, T., Na, H.-J., and Yamane, H., 2005, "MoO2 Hollow Fiber With Rectangular Cross Sections," Jpn. J. Appl. Phys., Part 2, **44**, pp. L449–L450.
[47] Abe, T., Suemitsu, M., and Miyamoto, N., 1993, "Formation of Highly Uniform and Dense Diamond Microcrystal Thin Films Using a Combustion Flame Surrounded by an Inert-Gas Flow," J. Appl. Phys., **74**(5), pp. 3531–3537.
[48] Dhas, N. A., and Gedanken, A., 1997, "Sonochemical Synthesis of Molybdenum Oxide- and Molybdenum Carbide-Silica Nanocomposites," Chem. Mtls., **9**, pp. 3144–3154.
[49] Anpo, M., Kondo, M., Kubokawa, Y., Louis, C., and Che, M., 1988, "Dynamic Studies of the Photoinduced Metathesis of C_3H_6 and Photoreduction of Mo and CO on Anchored and Impregnated Mo/SiO_2 Catalysts," J. Chem. Soc., Faraday Trans. 1, **84**(8), pp. 2771–2782.
[50] Liu, Y., Qian, Y., Zhang, M., Chen, Z., and Wang, C., 1996, "Preparation of Nano-Sized Amorphous Molybdenum Dioxide Powders by Use of γ-Ray Radiation Method," Mater. Res. Bull., **31**, pp. 1029–1033.
[51] Zhou, J., Xu, N. S., Deng, S. Z., Chen, J., and She, J. C., 2003, "Synthesis of Large-Scaled MoO_2 Nanowire Arrays," Chem. Phys. Lett., **382**, p. 443.
[52] Merchan-Merchan, W., Saveliev, A. V., and Kennedy, L. A., 2006, "Flame Synthesis of Molybdenum Oxide Whiskers," Chem. Phys. Lett., **422**, pp. 72–77.

Latent Heat Fluxes Through Soft Materials With Microtruss Architectures

Matthew J. Traum
Institute for Soldier Nanotechnologies, Massachusetts Institute of Technology, 77 Massachusetts Avenue, Cambridge, MA 02139; Department of Mechanical Engineering, Massachusetts Institute of Technology, 77 Massachusetts Avenue, Cambridge, MA 02139

Peter Griffith
Department of Mechanical Engineering, Massachusetts Institute of Technology, 77 Massachusetts Avenue, Cambridge, MA 02139

Edwin L. Thomas
Institute for Soldier Nanotechnologies, Massachusetts Institute of Technology, 77 Massachusetts Avenue, Cambridge, MA 02139; Department of Materials Science and Engineering, Massachusetts Institute of Technology, 77 Massachusetts Avenue, Cambridge, MA 02139

William A. Peters[1]
Institute for Soldier Nanotechnologies, Massachusetts Institute of Technology, 77 Massachusetts Avenue, Cambridge, MA 02139
e-mail: peters@mit.edu

Microscale truss architectures provide high mechanical strength, light weight, and open porosity in polymer sheets. Liquid evaporation and transport of the resulting vapor through truss voids cool nearby surfaces. Thus, microtruss materials can simultaneously prevent mechanical and thermal damage. Assessment of promise requires quantitative understanding of vapor transport through microtruss pores for realistic heat loads and latent heat carriers. Pore size may complicate exegesis owing to vapor rarefaction or surface interactions. This paper quantifies the nonboiling evaporative cooling of a flat surface by water vapor transport through two different hydrophobic polymer membranes, 112–119 μm *(or* 113–123 μm*) thick, with microtruss-like architectures, i.e., straight-through pores of average diameter of* 1.0–1.4 μm *(or* 12.6–14.2 μm*) and average overall porosity of 7.6% (or 9.9%). The surface, heated at* 1350 ± 20 W_t/m^2 *to mimic human thermal load in a desert (daytime solar plus metabolic), was the bottom of a* 3.1 cm *inside diameter,* 24.9 cm^3 *cylindrical aluminum chamber capped by the membrane. Steady-state rates of water vapor transport through the membrane pores to ambient were measured by continuously weighing the evaporation chamber. The water vapor concentration at the membrane exit was maintained near zero by a cross flow of dry nitrogen* (velocity=2.8 m/s). *Each truss material enabled* 13–14 °C *evaporative cooling of the surface, roughly 40% of the maximum evaporative cooling attainable, i.e., with an uncapped chamber. Intrinsic pore diffusion coefficients for dilute water vapor* (<10.4 mole %) *in air (P total* ~112,000 Pa*) were deduced from the measured vapor fluxes by mathematically disaggregating the substantial mass transfer resistances of the boundary layers* (~50%) *and correcting for radial variations in upstream water vapor concentration. The diffusion coefficients for the* 1.0–1.4 μm *pores (Knudsen number* ~0.1*) agree with literature for the water vapor-air mutual diffusion coefficient to within* ±20%*, but for the nominally* 12.6–14.2 μm *pores (Kn* ~0.01*), the diffusion coefficient values were smaller, possibly because considerable pore area resides in noncircular, i.e., narrow, wedge-shaped cross sections that impede diffusion owing to enhanced rarefaction. The present data, parameters, and mathematical models support the design and analysis of microtruss materials for thermal or simultaneous thermal-and-mechanical protection of microelectromechanical systems, nanoscale components, humans, and other macrosystems.* [DOI: 10.1115/1.2818760]

Keywords: microtruss, architecture, latent, heat transfer, mass transfer, pore, diffusion, MEMS, nanotechnology, membrane, polymers, soft materials, evaporation, nonboiling, evaporative cooling, phase change, surface, interface, thermal management, systems integration

Introduction

Microtrusses, also known as microframes [1], are polymeric sheetlike structures whose ordered networks of micro- to nanoscale rods, struts, cells, and channels mimic the high strength-to-weight ratio of macroscale trusses used in the construction of bridges, towers, and buildings. Microtrusses provide light weight, high porosity, and extraordinary absorption of mechanical energy without rupture in a single material [2]. Moreover, microtrusses can manipulate heat transmission by modifying the transport of latent heat-carrying vapors. Thus, microtruss architectures have the potential to simultaneously protect humans and inanimate objects from mechanical and thermal damage. Assessment of viability requires that vapor transport within truss pores and the resulting latent heat transmission be quantified for practical thermal loads and latent heat carriers, and be compared with thermal conduction across the truss. There is also a need to determine if smaller pore widths affect vapor transport owing to vapor rarefaction or surface interactions [3–5].

Mass transfer through porous structures has been studied owing, inter alia, to diverse practical applications [6], e.g., catalytic reaction engineering [7], textile comfort [8], fluid permeation of concrete [9], sintered metals and packed beds [10], and separation processes, such as desalination [11] and gas purification [12–14]. Selected examples include measurements of rates of water evaporation into air-filled pores of glass fiber and Teflon™ membranes separating saline and fresh water [11] and studies of drying and cooling with cotton [15]. Johnson et al. [16] studied the potential of polypropylene membranes with 30–100 nm pores to act as multifunctional protective barriers, i.e., to filter bacteria from water and then cool indoor air by evaporating the resulting decontaminated liquid. Gibson et al. [17] studied transport in porous

[1]Corresponding author.

Contributed by the Heat Transfer Division of ASME for publication in the JOURNAL OF HEAT TRANSFER. Manuscript received July 31, 2006; final manuscript received June 20, 2007; published online March 17, 2008. Review conducted by Gang Chen. Paper presented at the ASME 2006 Energy Nanotechnology International Conference (ENIC2006), Boston, MA, June 26–28, 2006.

Table 1 Operating parameters and structural properties of the various barrier materials used in measurements of latent heat transmission

Overlay	Porosity (%)	Av. pore diameter (μm)	Thickness (μm)	Av. T_3 (K)	Av. T_2 (K)	Av. ρ_2 (kg/m^3)	Mole % H_2O vapor (%)	$\Delta m/\Delta t$ (kg/s)
Nucrel®, Sample A	7.6 ± 2.5	1.0 ± 0.2	112 ± 3	302.7	316.1	0.059	8.531	$5.07E-07$
Nucrel®, Sample B	7.5 ± 3.3	1.4 ± 0.2	119 ± 4	301.9	315.0	0.056	8.049	$5.98E-07$
Hytrel®, Sample A	11.2 ± 3.1	14.2 ± 1.6	113 ± 3	302.1	313.3	0.052	7.363	$5.97E-07$
Hytrel®, Sample B	8.6 ± 2.7	12.6 ± 1.5	123 ± 3	305.8	314.7	0.055	7.907	$4.62E-07$
Nonporous latex	0	N/A	141 ± 3	316.8	334.4	0.127	19.292	0
No Membrane	100	N/A	N/A	N/A	N/A	N/A	N/A	$(1.26\pm0.08)E-06$

membranes fabricated from electrospun nylon 6,6 nanofibers to integrate hazardous substance protection with improved human thermal comfort by evaporation of sweat.

Complications may arise if length scales in a porous medium, e.g., pore width, are comparable to or less than the mean free path, de Broglie wavelength, etc. [18]. Physical transport of molecules may be impacted by fluid rarefaction [3,5,19,20], surface curvature [4,21], wetting [4], fluctuations in species concentration at interfaces [22], or surface topography, as seen in superheat requirements for boiling [23,24]. Such effects must be understood because they can give rise to heat and mass transfer behaviors dramatically different from those of macrosystems [18,25]. For example, unprecedented increases in flux densities of liquids and gases through channels with nanoscale widths have been measured [26,27]. The ability to sculpt and image highly reproducible micron and nanometer scale geometric features in hard and soft materials opens new opportunities for experiments to study effects of tiny length scales on heat and mass transfer in well-defined micro- and nanomedia. Progress in the theoretical understanding of heat transfer [18] and mass transfer [7,18,25,28] in condensed phase and micro-nanoscale flow systems over the last two decades facilitates interpretation of the resulting observations.

The above and other prior studies are valuable contributions but do not duplicate the present study of nonboiling latent heat transmission through soft materials with well-defined microtruss architectures. In particular, this paper quantifies water vapor transport rates through the pores of two different hydrophobic polymeric membranes with microtruss features and the resulting evaporative cooling of a nearby flat surface, heated at a flux density representative of the metabolic plus daytime desert solar load on a human. Heat balances close to within $\pm12\%$ and thermal conduction across each microtruss were measured. To facilitate engineering design, an intrinsic (apparatus-independent) coefficient for pore diffusion of latent heat carrier was deduced for each microtruss simulant.

Characterization of Microtruss Simulants and Other Barrier Materials

Zero-porosity latex was the negative control barrier material. Lacking actual microtrusses [29] of sufficient facial area, we studied two microtruss stand-ins prepared by the DuPont Company using DuPont proprietary technology: $112-119\ \mu$m (or $113-123\ \mu$m) thick Nucrel® (or Hytrel®) hydrophobic membranes with straight-through pores of equivalent average diameter of $1.0-1.4\ \mu$m (or $12.6-14.2\ \mu$m) and average overall porosity of 7.6% (or 9.9%). Nucrel® is a random copolymer of ethylene and methacrylic acid (12 wt %). Hytrel® is a random polyether-ester copolymer formed by the condensation of terephthalic acid, tetramethylene glycol, and polytetramethylene glycol. Pore diameters and total porosity (Table 1) were determined by image analysis using an open source software (IMAGEJ from NIH) of 400–500 scanning electron micrographs (SEMs) (Fig. 1). Each microtruss was cleaned before every imaging (or evaporation) run by flushing each face for 30 s with clean, dry nitrogen gas. Each specimen was divided into a grid of ~500 equally spaced nodes. The squares thus defined were systematically examined by tracking left to right and then right to left along adjoining rows. By examining different numbers of randomly selected images, it was shown that 400 micrographs is at least four times the number required to obtain repeatable, statistically significant values for pore diameter and total porosity. The Nucrel® microtruss pores were approximately circular in cross section (Fig. 1), and we defined the equivalent average pore diameter as the arithmetic mean of the diameters measured for 288,450 pores in 455 micrographs. For the appreciably distorted, i.e., noncircular, cross section (Fig. 1) Hytrel® pores, we defined an average equivalent diameter by approximating the pore area as circular, i.e., $d_e=[4A/\pi]^{0.5}$. The area A was the arithmetic mean measured for 167,937 pores in 480 micrographs. As discussed below, more explicit accounting for Hytrel® pore shape may explain the intrinsic pore diffusion coefficients deduced for this truss. SEM images of edges exposed by microtoming (Fig. 1) show that the pores run "straight-through" and normal to the truss faces.

Experimental Apparatus and Performance Validation

The apparatus (Fig. 2) measures rates and extents of surface cooling by liquid evaporation through porous coverings under conditions that are practically relevant. The experiments are sufficiently controlled to allow good closure of heat balances for equipment this small ($\pm12\%$), deduction of quantitative data including intrinsic pore diffusion coefficients, and differentiation of heat transfer mechanisms, i.e., conduction and nonboiling evaporation. The evaporation chamber was a 33.0 mm outside diameter $\times$33.0 mm deep aluminum cylinder with a 3 mm thick flat

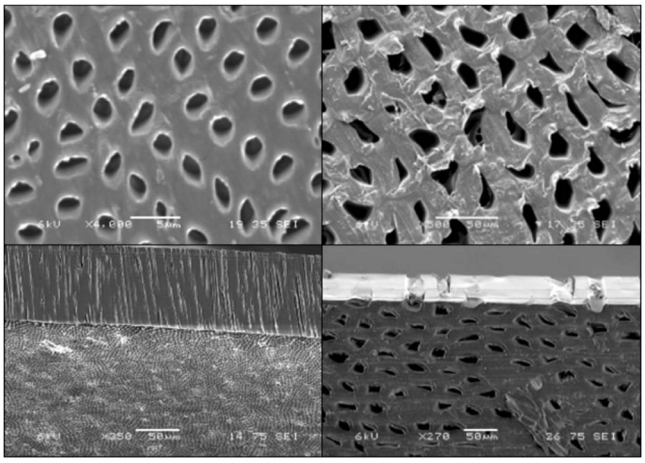

Fig. 1 SEMs of microtruss simulant surfaces (top panels) and edges exposed by microtoming (bottom panels). Left hand side panels: Nucrel®; right hand side panels: Hytrel®. Magnifications: top left panel, 4000×; top right panel, 500×.

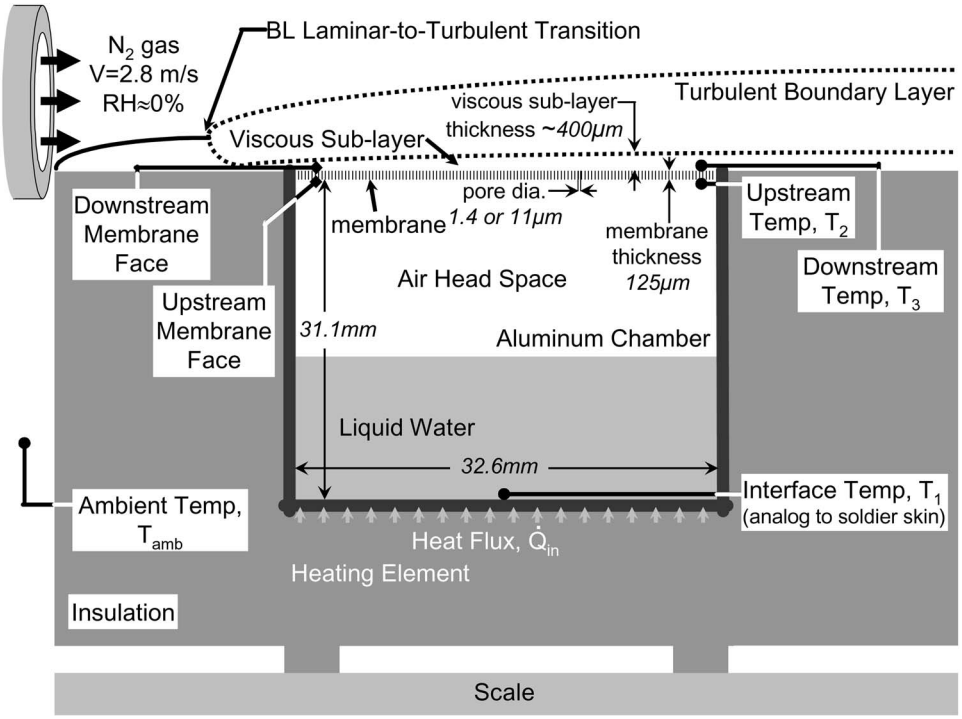

Fig. 2 Schematic (not to scale) of apparatus for quantitative study of evaporative cooling of surfaces by modulation of latent heat carrier flow using barrier materials with microtruss and nanotruss architectures. Dotted BLs represent an average location because turbulence agitates the fluid boundaries.

bottom—the evaporation surface. The outside wall of the cylinder was thermally insulated with a packing foam and a Styrofoam collar. The chamber was continuously weighed using a Mettler-Toledo 8001 series electronic balance (stated sensitivity of ± 0.1 g). The temperatures of the evaporation surface (T_1) and the entrance (upstream, T_2) and exit (downstream, T_3) faces of the barrier material were each measured using Omega 5SC-TT-T-40-36 *T*-type thermocouples (0.076 mm bead outside diameter) connected to Omega HH2001LTC thermocouple readers. A continuous flow of dry nitrogen gas at 30°C temperature was directed over the top of the apparatus (Fig. 2) from a tube at an average exit velocity of 2.8 ± 0.25 m/s (measured using a VWR Enviro-Meter digital anemometer) to match the sweep gas rate of the ASTM upright cup method for determining vapor transmission rates through textiles [30]. The bottom face of the aluminum surface was heated by direct contact with an 85.55 mm outside diameter ProvoCraft® Candlsense™ electrical hot plate (stated maximum heat flux density of 3600 W_t/m^2).

In a typical experiment, T_1, T_2, and T_3 (Fig. 2) and the weight of liquid in the chamber were measured at approximately 2 min intervals for a known input heat load. Thermocouple T_1 was soldered to the center of the inside bottom wall of the evaporation chamber with generic rosin core (electrical) solder to provide good thermal contact. The beads of thermocouples T_2 and T_3 were attached to the upstream and downstream faces of the microtruss with a high-thermal-conductivity epoxy cement, OmegaBond® 101. Calibration experiments [31] showed that this method of bonding a tiny metal thermocouple sensor to soft (polymeric) materials gives reliable steady-state temperature measurements. All three thermocouples were approximately 14 mm from the chamber inside wall. We performed four negative control runs by capping the chamber with a nonporous latex membrane, four positive control runs (maximum water vapor transport rates) by leaving the chamber uncapped, and two runs each with replicate samples of the Nucrel® and Hytrel® microtruss.

Water vapor mass concentrations at the entrance and exit faces of the barriers were calculated from corresponding truss surface temperatures using the ideal gas law, the literature data on the saturation pressure of steam [32], and the assumption of 100% relative humidity (RH) and 0% *absolute* humidity (AH), respectively at the upstream and downstream faces of the barrier. The RH of the sweep gas at the nozzle exit measured with a Kestrel 4000 portable data-logging weather station (stated accuracy $\pm 3.0\%$ RH with a specified range of 5.0–95.0% RH) was 1.4–4.6%, which justifies the assumption of 0% AH owing to the very low water vapor content in the sweep gas. The assumption of a 100% RH at the upstream face of the microtruss simulant is reasonable because T_2 was intentionally kept below the temperature of the liquid water-air interface (i.e., the evaporation front). Consequently, some condensation of liquid water was observed on the entrance face of the polymer barrier. The inside walls of the evaporation chamber between the evaporation front and the microtruss entrance were kept above the temperature of the liquid water-air interface to prevent liquid water from condensing prematurely. Table 1 summarizes experimental conditions for runs with the various barrier materials.

A transient heat balance on the entire apparatus gives

$$\frac{d(C_p M T_1)}{dt} = \dot{Q}_{\text{in}} - Ah(T_1 - T_{\text{amb}}) - \dot{m}\Delta \text{H}_{fg}^{\text{H}_2\text{O}} \tag{1}$$

The overall thermal mass of the apparatus, C_pM, was obtained from the slope of the early stage heat-up curve (Fig. 3) for closed chamber (latex membrane) runs where evaporative transport is prevented ($\dot{m}=0$), and it is a reasonable approximation to neglect convective cooling owing to the relatively low values of $T_1 - T_{\text{amb}}$. Using this C_pM value, the overall convective heat transfer coefficient h was determined by fitting a lumped Newtonian cooling model to the cool-down curve for closed chamber runs (Fig. 3), recognizing that $\dot{Q}_{\text{in}}=0$ (heater off). The resulting h

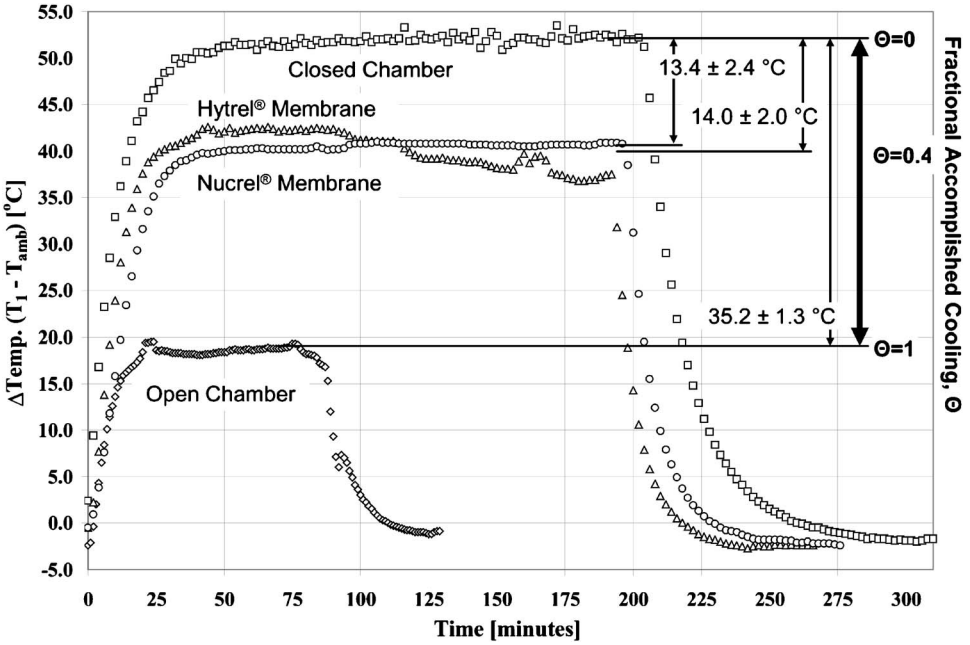

Fig. 3 Typical temperature-time histories (corrected for ambient temperature) for evaporative cooling of an aluminum surface using a closed chamber (negative control), an open chamber (positive control), or microtruss simulant materials. The absolute latent and fractional accomplished cooling (defined in the text) are also shown.

(192 ± 25 W/m^2 K) and C_pM (131 ± 19 J/K) determinations showed good repeatability for the four closed chamber runs. The mean h value was within a typical range for forced convective heat transfer with air, i.e., 30–300 W/m^2 K [33], and the mean C_pM result was within 15% of a value estimated from known masses and tabulated heat capacities of apparatus components [34]. Using these experimentally derived parameters in a steady-state, closed chamber heat balance (i.e., $d(MT_1)/dt=0$ and $\dot{m}\Delta H_{fg}^{H_2O}=0$ in Eq. (1)), the first two terms on the right hand side of Eq. (1) accounted for all thermal flows within +8.6% to −0.2%. For a steady-state heat balance with these C_pM and h values for the barrier runs (latent heat transfer from the chamber enabled), the three terms on the right hand side of Eq. (1) accounted for all thermal flows within +12.4% to +3.3%. These heat balance closures are good considering the small apparatus size and the use of lumped thermal physical parameters derived from transient heat-up and cool-down stages of the experiments.

Thermal buoyancy in the liquid water, conduction through the liquid water, and conduction along the aluminum walls were calculated to respectively account for 69.3%, 3.8%, and 26.7% of the axial heat flow in the evaporation chamber. Neglecting radial heat transfer, this implies that up to 73% of the heat input flowed through the water and, in principle, could have escaped the chamber via the latent heat carrier. In the present experiments, the maximum net latent heat transfer *from the chamber*, which occurred with an open, i.e., uncapped chamber, was 37.7% of the total heat input.

Procedure for Evaporative Cooling Experiments

To thermally equilibrate it with ambient temperature, deionized water was stored overnight in a covered graduated cylinder on the laboratory bench. The evaporation chamber was weighed, charged to a depth of about 11 mm with equilibrated water (~7 gm), and then reweighed to more precisely determine the water weight by difference. The top of the evaporation chamber was then completely covered with a barrier material sealed taut by folding it over and binding its edges to the chamber outside the wall with an elastic band. Positive control runs (open chamber) omitted the barrier. The insulation collar was then placed around the chamber, and the chamber bottom was placed on the heater plate. A continuous flow of 30°C dry nitrogen gas was directed over the top of the apparatus (Fig. 2) from a tube at a linear velocity of 2.8 ± 0.25 m/s, measured at that temperature. The chamber bottom was then heated at 1350 ± 20 W$_t$/m^2 by manually adjusting a 110 V input variable transformer (Variac™) to a predetermined point. The chamber weight and temperatures of the chamber bottom and the membrane sample entrance and exit faces, T_1, T_2, and T_3, respectively, (Fig. 2) were each measured at 2 min intervals. Upon reaching steady state, these measurements were continued for approximately 150 min at the stated constant heat input. Steady state was defined as the condition in which measured values of T_1 and the rates of water removal from the chamber (the slopes of the curves in Fig. 4) were constant to within ±10%. Temperature-time histories of the aluminum surface throughout cool-down (Fig. 3), initiated by turning off the heater, were measured in all runs, providing data on evaporative cooling under transient conditions (not analyzed in this paper).

Experimental Results

Figure 3 displays typical temperature-time histories for the Hytrel® and Nucrel® microtruss simulants and the closed chamber and open chamber control runs. To compare the evaporative cooling potency of different materials, Fig. 3 shows the absolute cooling owing to the latent heat transfer in °C and a corresponding nondimensional, fractional accomplished cooling Θ_a defined in Eq. (3). To correct for variations in room temperature from run to run, absolute latent cooling was defined as the difference, for the negative control, between the average steady-state temperature of the aluminum surface, T_1 (the plateau in Fig. 3), and room temperature T_{amb} (measured at the beginning of the steady-state period), less this same difference when water vapor can exit the chamber through an overlaid membrane sample,

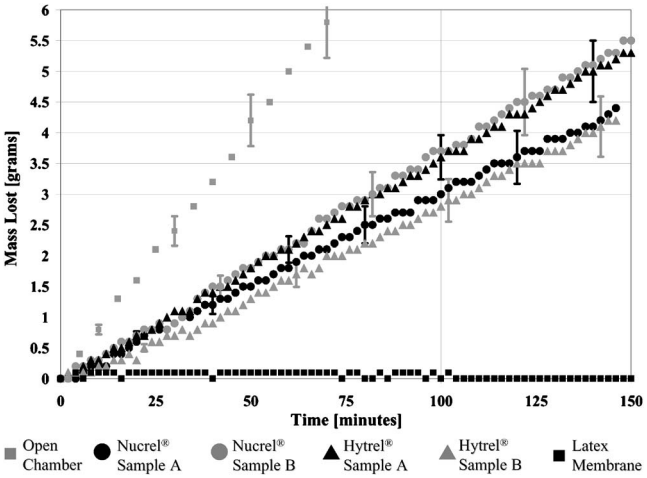

Fig. 4 Cumulative mass of water vapor transported from the evaporation chamber as affected by time. The instantaneous flux of coolant vapor through the microtruss simulant pores is obtained from the first derivative of the curves shown.

$$\text{Absolute latent cooling} = (T_{1,\text{closed}} - T_{\text{amb,closed}}) - (T_{1,\text{membrane}} - T_{\text{amb,membrane}}) \quad (2)$$

We defined Θ_a as the ratio of the absolute cooling with a truss on the chamber to the maximum evaporative cooling at the same heater power with the chamber uncovered,

$$\Theta_a = \frac{(T_{1,\text{closed}} - T_{\text{amb,closed}}) - (T_{1,\text{membrane}} - T_{\text{amb,membrane}})}{(T_{1,\text{closed}} - T_{\text{amb,closed}}) - (T_{1,\text{open}} - T_{\text{amb,open}})} \quad (3)$$

Thus, evaporative cooling approaches its maximum as Θ_a approaches unity, and a small Θ_a implies vapor transport limitations that strongly curtail latent heat removal from the chamber. Table 2 summarizes the average absolute cooling and corresponding Θ_a's and steady-state temperatures deduced for the 12 runs. The Nucrel® and Hytrel® microtruss simulants respectively resulted in $14.0 \pm 2.0\,^\circ\text{C}$ and $13.4 \pm 2.4\,^\circ\text{C}$ absolute latent cooling of the aluminum surface, corresponding to Θ_a values of about 0.4, i.e., a substantial fraction of the maximum possible evaporative cooling.

Figure 4 shows cumulative weight loss of the evaporation chamber, i.e., the aggregate weight of water evaporated from the aluminum surface from the time its temperature first attained steady state to time specified on the abscissa. The derivative of each curve at any time denotes the instantaneous steady-state rate of water mass transfer from the chamber at that time. Each curve is essentially linear over the steady-state period, implying that the corresponding mass flux of water vapor was constant. Accordingly, we defined the average rate of water vapor mass transfer from the apparatus $\dot{m}_{\text{av}}$ as the quotient of the cumulative steady-state weight loss and the cumulative time over which that weight loss occurred, i.e., as the average slopes of the curves in Fig. 4. Table 1 presents the measured $\dot{m}_{\text{av}}$ values for each microtruss simulant run and the average value for the four positive control runs. The uncertainty in $\dot{m}_{\text{av}}$ ($\pm 1.72 \times 10^{-8}$ kg/s, Table 1) was estimated by propagating the experimental uncertainties in the weight measurement ± 0.1 g (in ~ 5 g) owing to the sensitivity of the balance and ± 0.1 g owing to the drift of 0.1 g in the balance zero over a typical 9000 s run time and ± 20 s owing to the uncertainty in the time measurement over the ~ 9000 s period, and then multiplying the result by the largest measured value of $\dot{m}_{\text{av}}$ (about 6.0×10^{-7} kg/s). The constancy of $\dot{m}_{\text{av}}$ and T_1 for 90 min shows that the continuous depletion of liquid water did not undermine the stability of the experiment, e.g., because of reduced thermal convection in the water as its depth decreased or of the buildup of water droplets at the microtruss entrance.

Table 2 Steady state temperatures, fractional accomplished cooling, and absolute latent cooling for evaporative cooling of an aluminum surface using a closed chamber (negative control), an open chamber (positive control), or microtruss simulant materials

Membrane {Number of runs}	Av. T_{amb} (°C)	Av. T_1 (°C)	Fractional accomplished cooling	Absolute latent cooling (°C)
Closed chamber {4}	27.2 ± 0.2	80.1 ± 0.7	0.00	N/A
Open chamber {4}	26.9 ± 0.2	44.6 ± 0.4	1.00	35.2 ± 1.3
Nucrel® {2}	27.5 ± 0.2	66.4 ± 1.0	0.40 ± 0.06	14.0 ± 2.0
Hytrel® {2}	27.5 ± 0.2	67.0 ± 1.4	0.38 ± 0.07	13.4 ± 2.4

Mathematical Modeling

Intrinsic coefficients for pore diffusion of water vapor can be deduced from the present measurements (Fig. 4) by using a mathematical model to decouple the appreciable ($\sim 50\%$) contributions of the boundary layers (BLs) to the overall rate of water vapor mass transfer from the chamber and by determining the contributions of Stefan flow (convection caused by diffusion) and Knudsen flow (molecule-wall versus molecule-molecule collisions) to pore transport. Calculations show that Stefan flow contributes less than 13.0% enhancement, and this transport mode was ignored. For pores of circular cross section, Knudsen effects can be estimated from an engineering correlation relating the Knudsen impacted diffusion coefficient D_{eff} for a pore of radius r_e (here in meters) to the coefficient for diffusion in a continuum fluid ($\text{Kn} < 0.01$), D [34],

$$\frac{1}{D_{\text{eff}}} = \frac{\tau}{\varepsilon_v}\left(\frac{1}{D} + \frac{1}{97 r_e \sqrt{T/m}}\right) \quad (4)$$

Here, T is in Kelvins, m is in g/(g mole), and the dimensionless tortuosity τ is an adjustable parameter to account for variability in pore axis orientation and pore cross sectional area [35]. Our SEM measurements found that the Nucrel® pores have approximately uniform circular cross sections and run straight through the microtruss with their axis essentially normal to the truss face (Fig. 1), making $\tau = 1$ a reasonable approximation. Using this value and porosities (ε_v) from Table 1, Eq. (4) predicts that D_{eff} should be 10.5% less than D for Nucrel®. The Hytrel® pores also run straight through, but have noncircular cross sections with considerable variability in width from pore to pore (Fig. 1). Thus, without detailed information on the tortuosity of these pores, the quantitative applicability of Eq. (4) for the Hytrel® is suspect. Nevertheless, to allow a qualitative comparison with Nucrel®, we approximated the Hytrel® pores as circular in cross section and τ as 1. Using ε_v from Table 1, Eq. (4) then predicts that Knudsen effects reduce D_{eff}, about 1.3% below D for the Hytrel® pores.

To assess the apparatus performance and determine the intrinsic coefficient for diffusion of dilute water vapor (10.4 mole %) in air at about 1 atm total pressure in the microtruss pores, we derived (Appendix) and solved a predictive mathematical model for the rates of water vapor mass transfer $\dot{m}_{\text{av}}$ from the apparatus of Fig. 1,

$$\dot{m}_{\text{av}} = \int_{r_o}^{r=0} \frac{2\pi r}{R_{\text{BL,downstream}} + R_{\text{mem}}} \left\{ \int_{r_o}^{r=0} \frac{1}{\delta(r) v(r)} \left[\frac{\rho_{\text{chamber}} - \rho(r)}{R_{\text{BL,upstream}}} - \frac{\rho(r)}{R_{\text{mem}} + R_{\text{BL,downstream}}} \right] dr - \rho_{\text{ambient}} \right\} dr \quad (5)$$

Equation (5) was developed by modeling effects of (1) BL mass transfer and radial gradients of water vapor concentration at the

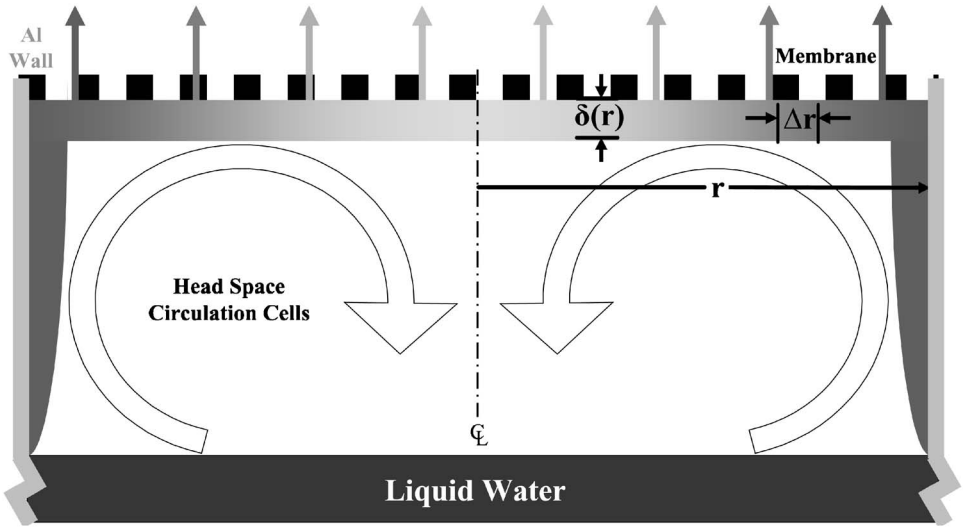

Fig. 5 Schematic cross section of the evaporation chamber to illustrate chirality of the thermal buoyancy driven flows and the radial concentration gradient across the upstream face of the microtruss

microtruss entrance (impacting $R_{BL,upstream}$ and $\rho(r)$) and (2) BL mass transfer at the truss exit (impacting $R_{BL,downstream}$). At the truss exit, the flow of dry nitrogen creates low AH, so $\rho_{ambient} \approx 0$ for all r. The mass transfer resistance of the microtruss itself, R_{mem}, is obtained from

$$R_{mem} = \frac{L}{\varepsilon_v D_{eff}} \tag{6}$$

if D_{eff} is known, e.g., from the literature. Alternatively, Eq. (5) can be solved for R_{mem} using experimental values of $\dot{m}_{av}$, and D_{eff} can then be obtained from Eq. (6). Both approaches were used here.

Tracer measurements found that thermal-buoyancy-induced convection in the chamber headspace caused a radial inward flow of water vapor-air mixture. This creates a BL along the microtruss entrance face, from which diffusion of water vapor through the microtruss pores to the ambient (Fig. 5) causes a radial water vapor concentration gradient at the microtruss entrance. Mass continuity for a fluid element adjacent the microtruss gives

$$\frac{d\rho(r)}{dr} = \frac{1}{\delta(r)v(r)}\left[\frac{\rho_{chamber} - \rho(r)}{R_{BL,upstream}} - \frac{\rho(r) - \rho_{ambient}}{R_{mem} + R_{BL,downstream}}\right] \tag{7}$$

The boundary condition for Eq. (7) is the mass concentration of water vapor at the evaporation chamber wall ($r = r_o$), which is obtained from the temperature of the microtruss entrance face (T_2), the ideal gas law, and the properties of steam assuming saturation. The radial inward velocity of the air-water vapor mixture across the microtruss at the chamber wall was calculated from a correlation in Deen [36] and was within about a factor of 2 of experimental values of this velocity we obtained from tracer studies.

Tracer studies also revealed a laminar-to-turbulent transition in the downstream BL ahead of the leading edge of the microtruss face. However, the Reynolds number based on plate length at this location was only about 12,000, which is far below the 300,000 threshold for the transition to turbulence expected for flat plate flow. We believe that the observed turbulent flow is caused by surface roughness. The "beads" on the Styrofoam collar protruded about 1 mm above the collar surface in a roughly hexagonal pattern, a substantial incursion into the roughly 3 mm thick laminar sublayer (as calculated from Blasius' solution for flow over a flat plate). Since the membrane sample itself was smooth, $R_{BL,downstream}$ was estimated from a correlation of the Sherwood number for turbulent flow over a smooth horizontal flat plate [34]. However, the use of the resulting $R_{BL,downstream}$ values in Eq. (5) badly underestimated the observed $\dot{m}_{av}$ values, leading us to conclude that either the correlation considerably overestimated $R_{BL,downstream}$ or $R_{BL,downstream}$ was determined by the mass transfer resistance of the viscous sublayer beneath the turbulent BL. We assumed the latter and thus that the concentration envelope where $\rho(r)$ first decreases to ~ 0 is the outer edge of the viscous sublayer. The thickness of this sublayer was estimated using Prandtl's "law of the wall" [37],

$$u^+(x) = \frac{U}{u_\tau(x)} = \frac{\delta(x)u_\tau(x)}{\nu} = y^+(x) \tag{8}$$

The exit faces of the microtrusses were very smooth compared to the surface of the Styrofoam collar. Thus, the friction velocity $u_\tau(x)$ was determined from the sheer stress on the wall using a correlation for skin friction from turbulent flow over a *smooth* surface [38] that accounts for the presence of a viscous sublayer

$$u_\tau(x) = U\left(\frac{0.0592\,\mathrm{Re}_x^{-1/5}}{\rho}\right)^{1/2} \tag{9}$$

This correlation is valid for $10^5 < \mathrm{Re}_x < 10^7$ but was used here for $\mathrm{Re}_x = 1.2 \times 10^4$. To find the average thickness of the viscous sublayer over the barrier, we averaged $\delta(x)$ from Eq. (8) over the sample diameter using Eq. (9) for $u_\tau(x)$ and the fact that the dimensionless thickness of the viscous sublayer y^+ is roughly 5 [37],

$$\bar{\delta} = \frac{1}{2r_o}\int_0^{2r_o} \frac{5\nu}{U(0.0592\,\mathrm{Re}_x^{-1/5}/\rho)^{1/2}}dx \tag{10}$$

Dividing the resulting average viscous sublayer height by the diffusion coefficient of water vapor in nitrogen gives the mass transfer resistance for the downstream BL:

$$R_{BL,downstream} = \frac{\bar{\delta}}{D_{H_2O,nitrogen}} \tag{11}$$

Using values of $R_{BL,downstream}$ from Eq. (11), we solved Eq. (5) numerically for $\dot{m}_{av}$. Values of $\rho(r)$ were calculated by numerically integrating Eq. (7) using measured values of T_2 and values of R_{mem} calculated from Eq. (6) using literature data for $D_{H_2O,air}$ [34]. Figure 6 shows that the $\dot{m}_{av}$ predictions became increasingly close to the experimental data, as the model was steadily improved to more realistically capture the mass transport details of

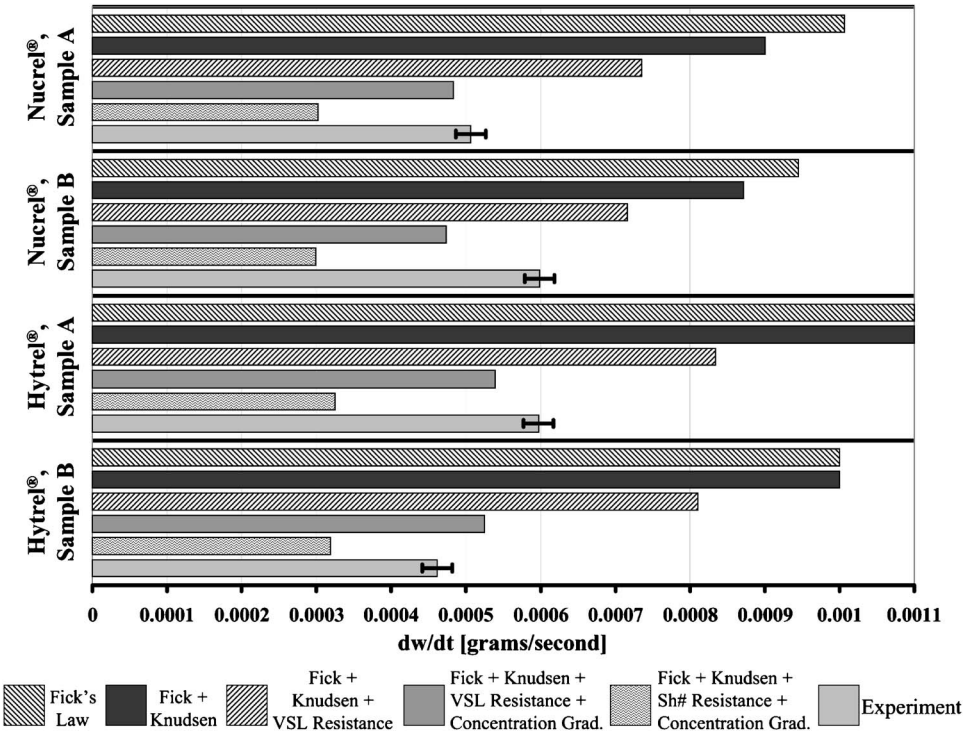

Fig. 6 Comparison of experimental (light gray) rates of water vapor mass transport from the evaporation chamber for the four experiments with microtruss stimulant barriers, with rates predicted by increasingly refined mass transfer models (various fills)

the apparatus of Fig. 1, i.e., from simple 1D continuum diffusion to correcting for (1) slight rarefaction (Knudsen effects) on the pore diffusion coefficient, (2) radial gradients in water vapor concentration at the microtruss entrance, (3) upstream BL mass transfer resistance, and (4) downstream BL mass transfer resistance. The inclusion of all four refinements gave $\dot{m}_{av}$ predictions that agree with experiment to within +14% to −21%, building confidence in the reliability of the apparatus and in the physical assumptions of the modeling.

To compare the latent heat transmission capabilities of different microtruss simulants on a consistent basis, and thus provide a reliable foundation for engineering design, we deduced an intrinsic, i.e., apparatus-independent, pore diffusion coefficient D_{eff} for (dilute) water vapor in atmospheric pressure air for each truss sample. The approach was to numerically solve Eqs. (5) and (7) simultaneously for $\rho(r)$ and R_{mem} using MATLAB. The resulting R_{mem} values were then used in Eq. (6) to calculate D_{eff}. The results (Table 3) agree to within 35% of the experimental bulk diffusion value, 2.59×10^{-5} m^2/s, reported by Deen [36], for continuum regime diffusion of water vapor in molecular nitrogen (N_2) at 308 K.

Discussion

Despite low total porosity (<12%, Table 1), barrier materials with microtruss architectures (Fig. 1) provide substantial evaporative cooling of strongly heated surfaces (Fig. 3, Table 2) by transport of latent heat-carrying vapor through the truss voids. Up to 25% of input heat energy was carried away by latent heat transfer through porous membranes, and the ratio of conductive to latent heat transport across the porous membranes ranged between 3:1 and 5:1. Water vaporization and transport through two different polymer sheets with microtruss features cooled a surface heated at ~1.4 kW/m^2 by about 13°C, about 40% of the maximum evaporative cooling attainable with water for the same heat load with the evaporation chamber uncapped (Table 2, Fig. 3). Because microtruss architectures show promise to provide high mechanical strength, light weight, and breatheability in soft materials, docu-

Table 3 Comparison of intrinsic (i.e., apparatus-independent) coefficients for diffusion of dilute water vapor in air (total pressure, 1 atm) through the microtruss pores with values predicted for mutual diffusion of water vapor in air for continuum conditions and with correction for the onset of fluid rarefaction (Eq. (4) in the text)

Overlay	Knudsen number	Rarified theory $D_{H_2O,air}$ (m^2/s)	Apparatus-independent experimental D_{eff} (m^2/s)	% Difference rarified versus experiment (%)
Nucrel®, Sample A	0.099	2.12*E*−05	1.95*E*−05	−9
Nucrel®, Sample B	0.071	2.18*E*−05	2.68*E*−05	19
Hytrel®, Sample A	0.007	2.33*E*−05	1.68*E*−05	−38
Hytrel®, Sample B	0.008	2.36*E*−05	1.68*E*−05	−40

mentation of latent heat flux densities this high under practically realistic conditions supports the idea that microtruss materials can protect humans and inanimate objects from mechanical and thermal damage simultaneously.

Further assessing this proposition requires latent heat transmission information unencumbered by the idiosyncrasies of apparatus or experimental conditions. BLs at the microtruss entrance and exit accounted for roughly half of the total resistance to cooling vapor mass transfer from the present evaporation chamber (Fig. 2). Mathematical modeling (described above) allowed the apparatus-independent mass transfer resistance for the microtruss, $R_{\text{mem}}=L/[D_{\text{eff}}\varepsilon_v]$ and the intrinsic diffusion coefficient D_{eff} to be disaggregated from the measured rates of water vapor transport from the chamber. The resulting D_{eff} values (Table 3) for the Nucrel® and Hytrel® microtruss simulants are in reasonable agreement with predictions for mutual diffusion of dilute water vapor in air in the continuum regime ($\text{Kn}<0.01$) and with literature values for mutual diffusion of dilute water vapor in N_2 gas under continuum conditions [36]. The differences in the experimentally derived D_{eff} values for the two microtruss simulants are discussed below.

For engineering designs incorporating other microtrusses with straight-through pores, comparable pore widths and geometries, and known thickness, the present D_{eff} values allow an initial estimate of the water vapor/air diffusion resistance in the truss pores. The *steady state* latent heat flux density through the microtruss can then be estimated for various operating conditions by formulating the total mass transfer resistance of the system as a series combination of the mass transfer resistances intrinsic for the truss itself and for the upstream and downstream BLs, then calculating $\dot{m}_{\text{av}}$ from Eq. (5), or its equivalent, for the particular evaporator, and then multiplying $\dot{m}_{\text{av}}$ by the average latent heat of vaporization of water for the temperature regime of interest.

To further benchmark the efficacy of the microtruss simulants for latent heat transmission, it is instructive to estimate what level of convective cooling would be needed to provide equivalent rates of heat removal from the surface. One approach is to assume a constant driving temperature gradient, ΔT, for convection and to calculate the required magnitude of the heat transfer coefficient, h_c. Alternatively, one could assume a constant value for h_c and calculate the required ΔT. Here, we do the former by taking ΔT as the difference between the evaporation chamber surface temperature at steady state, T_1, and a reasonable lower temperature, T_a, i.e., temperature at standard conditions: 298.2 K. Two cases of interest are (1) the convective heat transfer coefficient $h_{c,\text{app}}$ corresponding to the rate of latent heat removal experimentally measured with the present apparatus and operating conditions, $\dot{Q}_{L,\text{app}}$ and (2) an upper bound convective heat transfer coefficient $h_{c,\text{mem}}$ corresponding to the idealized case of latent heat removal, $\dot{Q}_{L,\text{mem}}$, which would be possible at the same operating conditions if the only mass transfer resistance to water vapor removal from the chamber were the intrinsic resistance of the microtruss pores. Thus,

$$h_{c,\text{app}}=\frac{\dot{Q}_{L,\text{app}}}{A(T_1-T_a)} \quad \text{and} \quad h_{c,\text{mem}}=\frac{\dot{Q}_{L,\text{mem}}}{A(T_1-T_a)} \tag{12}$$

where $\dot{Q}_{L,\text{mem}}=\dot{m}_{\text{mem}}\Delta H_{\text{vap}}^{\text{H}_2\text{O}}$, $\dot{m}_{\text{mem}}=D_{\text{eff}}\varepsilon_v(\rho_i-\rho_o)/L$, and ρ_o and ρ_i for this case are respectively taken as zero and at the vapor pressure of water at T_1. The magnitudes of the resulting convective heat transfer coefficients (Table 4) are comparable to those typical of forced convection heat transfer with air near ambient temperatures (298.2 K) [33].

Assuming pores of circular cross section, Eq. (4) predicted that rarefaction (Knudsen) effects reduce the continuum regime diffusion coefficient for the Hytrel® and Nucrel® pores by 1.3% and 10.5%, respectively (Table 3) owing to the smaller average width and thus larger Kn of the Nucrel® ($\sim 1.2\ \mu$m, $\text{Kn}\sim 0.1$) versus the Hytrel® pores ($\sim 13\ \mu$m, $\text{Kn}\sim 0.01$). However, the D_{eff} values derived for the Hytrel® pore from the experimental data were about 27% smaller than those for the Nucrel® pores (Table 3, column 5). A possible explanation is Knudsen-inhibited diffusion in the significant fraction of the Hytrel® pore volume that is not present in a circular cross section but rather in pinched down shapes that approximate narrow rectangles or isosceles triangles of small apex angle (Fig. 1). In qualitative support of this proposal, we calculated that if 40% of the Hytrel® pore volume was sufficiently distorted to reduce the continuum diffusion coefficient tenfold, then the D_{eff} values derived from the Hytrel® measurements would be about 35% lower than those for Nucrel®. A more in-depth assessment of pore shape effects would require reliable measurements of the tortuosity of the Hytrel® pores and/or a large number of SEM measurements to quantify the distortions in pore cross section, ideally as affected by pore depth. Such studies are beyond the scope of the present work.

Table 4 Apparent average and intrinsic convective heat transfer coefficients that would give rates of heat removal from surfaces equal to those obtained by NBEC (1) as measured with the present apparatus and (2) as would be possible if the only mass transfer resistance to water vapor removal from the evaporation chamber arose from the membrane pores. See Eq. (12) and accompanying narrative in the text.

Overlay	(T_1-T_a)[a] (K)	$h_{c,\text{app}}$ ($\text{w/m}^2\,\text{K}$)	$h_{c,\text{mem}}$ ($\text{w/m}^2\,\text{K}$)
Nucrel®, Sample A	39.8	39	61
Nucrel®, Sample B	43.0	43	68
Hytrel®, Sample A	42.5	42	62
Hytrel®, Sample B	41.3	35	48

[a]Assumed driving force for thermal convection.

Despite differences in their pore width and geometry, we observed no significant difference in the fractional accomplished cooling Θ_a between Nucrel® and Hytrel® (Fig. 3, Table 2), putatively because (1) the effect of variations in intratruss mass transfer resistance is tempered by the sizable ($\sim$50% of the total) contribution from the upstream and downstream BLs; (2) the intrinsic diffusion coefficients for the two microtruss simulants are not that different (1.7×10^{-5} versus $2.7\times10^{-5}\ \text{m}^2/\text{s}$ in the worst case, Table 3); and (3) the D_{eff} determinations reflect experimental uncertainty of $\pm 6.6\%$.

The present apparatus and operating procedures are useful tools for a quantitative characterization of the latent heat transfer capabilities of various porous media including materials with microtruss architectures. The equipment provides steady state heat balance closures to within $\pm 12\%$ for practically realistic heat loads, temperatures, and working fluid (water). The method of continuously weighing the entire evaporation chamber requires some care, but enables direct measurement of the mass fluxes of latent heat carrier responsible for latent heat transmission. Moreover, intrinsic, i.e., free of apparatus artifacts, coefficients for the diffusion of latent heat carrier through the microtruss voids can be deduced from these mass fluxes by mathematical modeling to disaggregate BL and other mass transfer resistances dictated by the apparatus geometry and operating conditions. Design and operation to sustain thermal buoyancy in the coolant liquid and the coolant vapor headspace simplify this mathematical modeling.

Conclusions

Latent Heat Transfer. Thin ($\sim 120\ \mu$m) sheets of soft materials with microtruss architectures, including pore widths of $\sim 1-15\ \mu$m, enable substantial evaporative cooling of surfaces, *without boiling*. At appreciable surface heat flux densities ($1.4\ \text{kW}_t/\text{m}^2$) and despite their low overall porosity (7.5–11.2%), the present microtruss structures provided evaporative cooling of

13–14 °C (about 40% of the maximum attainable, i.e., with an uncovered evaporation chamber). The cooling mechanism is latent heat transfer enabled by diffusion of evaporated coolant through the microtruss voids (pores). Thus, the efficacy of microtrusses for evaporative cooling of a nearby surface can be quantified in terms of a pore diffusion coefficient, microtruss thickness, and coolant heat of vaporization. The present rates of latent heat lift can be benchmarked by estimating the equivalent thermal convection that would be needed to provide identical surface cooling rates. For example, equivalent convective heat transfer coefficients as high as 43 W/m^2 K, i.e., comparable to those typical of forced convective cooling with air, were calculated for the Nucrel® microtruss simulant by assuming a ΔT equal to the difference between the surface temperature and standard temperature (298.2 K).

Pore Width and Shape. Effects of width and shape of microtruss pores must be understood to interpret experimental observations and design reliable evaporative cooling systems. Here, apparent average pore width was varied from about 15 μm (Kn $\sim$0.01) to 1 μm (Kn $\sim$0.1), and no impact on measured cooling was observed. This result is consistent with small estimated effects of rarefaction in this range of Knudsen numbers (<10% reduction for the smaller pores), together with similar overall porosities and substantial ($\sim$50%) contributions from the BLs on either microtruss external face. However, intrinsic coefficients for mutual diffusion of dilute water vapor in air deduced for the microtruss pores exhibited a contrarian variation, i.e., smaller values for the pores of *larger* width. This may be caused by rarefaction-impeded diffusion owing to the distortion of pore cross section, considerably reducing the effective pore width. Further testing of this hypothesis by measurements of tortuosity and characterization of pore shapes and sections was beyond the scope of this work.

Apparatus Performance and Utility. The present apparatus design and operating procedures simultaneously quantify the latent heat transmission, thermal conduction, and coolant vapor mass transfer characteristics of materials with microtruss architectures under practical heat loads with good reliability. Heat balances close to within ±12% and intrinsic pore diffusion coefficients deduced from measured water vapor mass flow rates are in satisfying agreement with the literature. Thus, the present experimental approach and mathematical modeling show promise for quantifying pore mass transfer, latent heat transfer (evaporative cooling and condensation heating), and thermal conduction characteristics of other microtruss materials, and indeed other porous materials and media more generally, for diverse practical working fluids, surfaces, heat loads, and temperature differences.

Applications. Soft materials with microtruss (and nanotruss, i.e., pore widths of 10–1000 nm) architectures show promise for providing high mechanical strength and light weight in sheetlike structures. The present results support the proposition that microtrusses can simultaneously protect against mechanical and thermal damage. More generally, microtrusses have the potential to integrate mechanical protection, breathability and cooling in shapeable, and barrier materials to protect, inter alia, humans, microelectromechanical systems (MEMS), nanocomponents (e.g., electronics), and larger structures such as turbine blades and space vehicle heat shields. This paper provides latent heat and mass transfer data, pore diffusion coefficients, and mathematical modeling methods for the design, operation, and performance assessment of materials and devices that exploit microtruss architectures for thermal management, mechanical protection, vapor separations, and combinations thereof. One application is *nonboiling* evaporative cooling (NBEC), which is of interest when boiling temperatures at the prevailing pressure would be intolerable, e.g., cooling humans, sensitive electronics, biological specimens, archeological samples, etc. NBEC provides reasonably high heat flux densities at lower temperatures. Integration with microfluidic channel networks can enable controlled delivery of latent heat carriers to tiny or difficult-to-access components.

Acknowledgment

This research was supported by the U.S. Army through the Institute for Soldier Nanotechnologies under Contract No. DAAD-19-02-D-0002 with the U.S. Army Research Office. The content does not necessarily reflect the position of the Government, and no official endorsement should be inferred. We thank Professor Ludovic Noels for valuable guidance on numerical modeling, Dr. Catherine Byrne for assistance in developing the experimental apparatus, Dr. Vahik Krikorian for expert guidance on SEM measurements and interpretation, and Dr. Vivek Kapur and Dr. Wayne Marsh of DuPont for supplying Hytrel® and Nucrel® sheets that we used as microtruss simulants. Hytrel® and Nucrel® are registered trademarks of the DuPont Company.

Nomenclature

A = area
C_p = specific heat at constant pressure
D = continuum diffusion coefficient
d_e = equivalent diameter
D_{eff} = Knudsen impacted diffusion coefficient
$D_{\text{H}_2\text{O,air}}$ = continuum diffusion coefficient of water vapor in air
h = convection coefficient
$h_{c,\text{app}}$ = experimentally measured latent heat transfer coefficient
$h_{c,\text{mem}}$ = upper bound convective heat transfer coefficient
M = mass
m = molecular mass
$\dot{m}$ = mass transfer rate
$\dot{m}_{\text{mem}}$ = intrinsic mass transfer rate across the microtruss
$\dot{m}_{\text{av}}$ = average water vapor mass transfer rate from the apparatus
$\dot{Q}_{\text{in}}$ = heat input
$\dot{Q}_{L,\text{app}}$ = rate of latent heat removal experimentally measured with the apparatus
$\dot{Q}_{L,\text{mem}}$ = idealized latent heat removal rate for the microtruss only
r = radial coordinate
$R_{\text{BL,downstream}}$ = downstream membrane mass transport resistance owing to a BL
$R_{\text{BL,upstream}}$ = upstream membrane mass transport resistance owing to a BL
Re_x = Reynolds number at coordinate x along a flat plate
R_{mem} = mass transport resistance of the membrane
r_o = outer radius of the evaporation chamber
T = temperature
T_1 = evaporation chamber bottom surface temperature
T_2 = upstream membrane surface temperature
T_3 = downstream membrane surface temperature
T_a = temperature at standard conditions (298.2 K, 1 atm)
T_{amb} = ambient temperature
U = free stream velocity
$u^+(x)$ = dimensionless velocity
u_τ = friction velocity
$v(r)$ = velocity
W_t = watts, thermal
$y^+(x)$ = dimensionless BL thickness
δ (x or r) = BL thickness at coordinate x or r

$\bar{\delta}$ = average viscous sublayer thickness
$\Delta H_{fg}^{H_2O}$ = latent heat of vaporization
ΔT = driving temperature gradient
ε_v = void fraction (porosity)
Θ_a = fractional accomplished cooling
ν = kinematic viscosity
$\rho(r)$ = mass concentration
ρ_{ambient} = mass concentration in the ambient environment
ρ_{chamber} = mass concentration in the evaporation chamber
τ = tortuosity

Appendix

Here, we derive Eqs. (5) and (7) from a mass continuity balance on a fluid element in the vicinity of the upstream microtruss face (Fig. 5). The element is a cylindrical shell of radius r, width Δr, and height $\delta(r)$, approximated as the BL thickness. The top surface of the element is the upstream truss face, and the element follows the fluid flow from the outer radius of the evaporation chamber, r_o, toward the chamber center, $r=0$ through incremental reductions in its radius by Δr (Fig. 5). By mass continuity, the water vapor contained within the element must equal the mass entering minus the mass leaving the element,

$$\frac{d\rho(r)}{dt} dA(r)\,\delta(r) = \frac{dm_{\text{in}}}{dt} - \frac{dm_{\text{out}}}{dt} \tag{13}$$

By expanding the left hand side of Eq. (13) in a Taylor series and canceling like terms,

$$\frac{d\rho(r)}{dr} \Delta r dA(r)\,\delta(r) = \frac{dm_{\text{in}}}{dt}\Delta t - \frac{dm_{\text{out}}}{dt}\Delta t \tag{14}$$

To put the fluid element in a Lagrangian reference frame, a substitution is made for Δt to give

$$\frac{d\rho(r)}{dr} \Delta r dA(r)\,\delta(r) = \frac{dm_{\text{in}}}{dt}\frac{\Delta r}{v(r)} - \frac{dm_{\text{out}}}{dt}\frac{\Delta r}{v(r)} \tag{15}$$

Recognizing that the mass flows in and out of the fluid element are governed respectively by diffusion (in) through the BL on the upstream barrier face and diffusion (out) through the barrier and downstream BL, the following substitutions are made:

$$\frac{dm_{\text{in}}}{dt} = \frac{\rho_{\text{chamber}} - \rho(r)}{R_{BL,\text{upstream}}} dA(r) \quad \text{and}$$

$$\frac{dm_{\text{out}}}{dt} = \frac{\rho(r) - \rho_{\text{ambient}}}{R_{\text{mem}} + R_{BL,\text{downstream}}} dA(r) \tag{16}$$

where $\rho_{\text{amblent}} \approx 0$ due to a cross flow of dry nitrogen. Finally, substituting the expressions of Eq. (16) into Eq. (15) and cancelling like terms, the desired result Eq. (7) is obtained,

$$\frac{d\rho(r)}{dr} = \frac{1}{\delta(r)v(r)}\left[\frac{\rho_{\text{chamber}} - \rho(r)}{R_{BL,\text{upstream}}} - \frac{\rho(r) - \rho_{\text{ambient}}}{R_{\text{mem}} + R_{BL,\text{downstream}}}\right] \tag{7'}$$

Both BL resistances are calculated in the main text, and Eq. (7) is combined with Eq. (17), an integral representation of Fick's law for diffusion, to create the complete apparatus transport model (Eq. (5)),

$$\dot{m}_{\text{av}} = \int_{r_o}^{r=0} \frac{2\pi r}{R_{BL,\text{downstream}} + R_{\text{membrane}}} [\rho(r) - \rho_{\text{ambient}}] dr \tag{17}$$

$$\dot{m}_{\text{av}} = \int_{r_o}^{r=0} \frac{2\pi r}{R_{BL,\text{downstream}} + R_{\text{mem}}} \left\{ \int_{r_o}^{r=0} \frac{1}{\delta(r)v(r)} \times \left[\frac{\rho_{\text{chamber}} - \rho(r)}{R_{BL,\text{upstream}}} - \frac{\rho(r)}{R_{\text{mem}} + R_{BL,\text{downstream}}}\right] dr - \rho_{\text{ambient}} \right\} dr \tag{5'}$$

which was solved numerically via MATLAB for the unique combination of R_{mem} and $\rho(r)$ that satisfies the boundary condition.

References

[1] Jang, J.-H., Ullal, C. K., Choi, T. Y., LeMieux, M. C., Tsukruk, V. V., and Thomas, E. L., 2006, "3D Polymer Microframes That Exploit Length-Scale-Dependent Mechanical Behavior," Adv. Mater. (Weinheim, Ger.), **18**(16), pp. 2123–2127.
[2] Choi, T., Jang, J.-H., Ullal, C. K., LeMieux, M. C., Tsukruk, V. V., and Thomas, E. L., 2006, "The Elastic Properties and Plastic Behavior of Two-Dimensional Polymer Structures Fabricated by Laser Interference Lithography," Adv. Funct. Mater., **16**, pp. 1324–1330.
[3] Karniadakis, G., and Beskök, A., 2002, *Micro Flows: Fundamentals and Simulation*, Springer, New York.
[4] de Gennes, P., Brochard-Wyart, F., and Quere, D., 2004, *Capillarity and Wetting Phenomena: Drops, Bubbles, Pearls, Waves*, Springer, New York.
[5] Cercignani, C., 2000, *Rarefied Gas Dynamics: From Basic Concepts to Actual Calculations*, Cambridge University Press, New York.
[6] Kärger, J., and Ruthven, D. M., 1992, *Diffusion in Zeolites and Other Microporous Solids*, Wiley, New York.
[7] Cussler, E. L., 1997, *Diffusion: Mass Transfer in Fluid Systems*, 2nd ed., Cambridge University Press, New York.
[8] McCullough, E. A., Kwon, M., and Shim, H., 2003, "A Comparison of Standard Methods for Measuring Water Vapour Permeability of Fabrics," Meas. Sci. Technol., **14**(8), pp. 1402–1408.
[9] Mantle, M. D., Reis, N. C., Griffiths, R. F., and Gladden, L. F., 2003, "MRI Studies of the Evaporation of a Single Liquid Droplet From Porous Surfaces," Magn. Reson. Imaging, **21**(3–4), pp. 293–297.
[10] Manz, B., Chow, P. S., and Gladden, L. F., 1999, "Echo-Planar Imaging of Porous Media With Spatial Resolution Below 100 μm," J. Magn. Reson., **136**(2), pp. 226–230.
[11] Findley, M. E., Tanna, V. V., Rao, Y. B., and Yeh, C. L., 1969, "Mass and Heat Transfer Relations in Evaporation through Porous Membranes," AIChE J., **15**(4), pp. 483–489.
[12] Pietrass, T., 2006, "Carbon-Based Membranes," MRS Bull., **31**(10), pp. 765–769.
[13] Sholl, D. S., and Ma, Y. H., 2006, "Dense Metal Membranes for the Production of High-Purity Hydrogen," MRS Bull., **31**(10), pp. 770–773.
[14] Perry, J. D., Nagai, K., and Koros, W. J., 2006, "Polymer Membranes for Hydrogen Separations," MRS Bull., **31**(10), pp. 745–749.
[15] Ghali, K., Ghaddar, N., and Jones, B., 2002, "Empirical Evaluation of Convective Heat and Moisture Transport Coefficients in Porous Cotton Medium," ASME Trans. J. Heat Transfer, **124**(3), pp. 530–537.
[16] Johnson, D. W., Yavuzturk, C., and Pruis, J., 2003, "Analysis of Heat and Mass Transfer Phenomena in Hollow Fiber Membranes Used for Evaporative Cooling," J. Membr. Sci., **227**(1–2), pp. 159–171.
[17] Gibson, P., Schreuder-Gibson, H., and Rivin, D., 2001, "Transport Properties of Porous Membranes Based on Electrospun Nanofibers," Colloids Surf., A, **187**, pp. 469–481.
[18] Chen, G., 2005, *Nanoscale Energy Transport and Conversion: A Parallel Treatment of Electrons, Molecules, Phonons, and Photons*, Oxford University Press, New York.
[19] Pollard, W. G., and Present, R. D., 1948, "On Gaseous Self-Diffusion in Long Capillary Tubes," Phys. Rev., **73**(7), pp. 762–774.
[20] Present, R. D., 1958, *Kinetic Theory of Gases*, McGraw-Hill, New York.
[21] Churaev, N. V., and Galwey, A. K., 2000, *Liquid and Vapor Flows in Porous Bodies: Surface Phenomena*, Gordon and Breach, Amsterdam.
[22] Luo, G., Malkova, S., Yoon, J., Schultz, D. G., Lin, B., Meron, M., Benjamin, I., Vanysek, P., and Schlossman, M. L., 2006, "Ion Distributions Near a Liquid-Liquid Interface," Science, **311**(5758), pp. 216–218.
[23] Collier, J. G., and Thome, J. R., 1994, *Convective Boiling and Condensation*, 3rd ed., Oxford University Press, New York.
[24] Lock, G. S. H., 1994, *Latent Heat Transfer: An Introduction to Fundamentals*, Oxford University Press, New York.
[25] Sholl, D. S., 2006, "Understanding Macroscopic Diffusion of Adsorbed Molecules in Crystalline Nanoporous Materials Via Atomistic Simulations," Acc. Chem. Res., **39**(6), pp. 403–411.
[26] Holt, J. K., Park, H. G., Wang, Y., Stadermann, M., Artyukhin, A. B., Grigoropoulos, C. P., Noy, A., and Bakajin, O., 2006, "Fast Mass Transport Through Sub-2-Nanometer Carbon Nanotubes," Science, **312**(5776), pp. 1034–1037.
[27] Eijkel, J. C. T., Dan, B., Reemeijer, H. W., Hermes, D. C., Bomer, J. G., and van den Berg, A., 2005, "Strongly Accelerated and Humidity-Independent Drying of Nanochannels Induced by Sharp Corners," Phys. Rev. Lett., **95**(25), p. 256107.

[28] Heitjans, P., and Kärger, J., 2005, *Diffusion in Condensed Matter: Methods, Materials, Models*, Springer, New York.
[29] Ullal, C. K., Maldovan, M., Thomas, E. L., Chen, G., Han, Y. J., and Yang, S., 2004, "Photonic Crystals Through Holographic Lithography: Simple Cubic, Diamond-Like, and Gyroid-Like Structures," Appl. Phys. Lett., **84**(26), pp. 5434–5436.
[30] ASTM, 1999, "Standard Test Methods for Water Vapor Transmission of Materials: Upright Cup Method," American Society for Testing and Materials Annual Book of ASTM Standards, Part 3.01, ASTM E, 96, Procedure B, Conshohocken, PA.
[31] Traum, M. J., 2007, "Latent Heat Fluxes Through Nano-Engineered Porous Materials," Ph.D. thesis, Massachusetts Institute of Technology, Cambridge, MA.
[32] Cravalho, E. G., and Smith, J. L., 1981, *Engineering Thermodynamics*, Pitman, Boston, pp. 522.
[33] Whitaker, S., 1977, *Fundamental Principles of Heat Transfer*, Pergamon, New York.
[34] Mills, A. F., 1999, *Basic Heat and Mass Transfer*, 2nd ed., Prentice-Hall, Englewood Cliffs, NJ.
[35] Satterfield, C. N., 1991, *Heterogeneous Catalysis in Industrial Practice*, 2nd ed., McGraw-Hill, New York.
[36] Deen, W. M., 1998, *Analysis of Transport Phenomena*, Oxford University Press, New York.
[37] Mills, A. F., 1999, *Basic Heat Transfer*, 2nd ed., Prentice-Hall, Englewood Cliffs, NJ.
[38] Tritton, D. J., 1977, *Physical Fluid Dynamics*, Van Nostrand Reinhold, New York.

Effect of Rarefaction, Dissipation, and Accommodation Coefficients on Heat Transfer in Microcylindrical Couette Flow

Latif M. Jiji
Department of Mechanical Engineering,
The City College of the City University
of New York,
New York, NY 10031
e-mail: jiji@ccny.cuny.edu

This paper examines the effects of rarefaction, dissipation, curvature, and accommodation coefficients on flow and heat transfer characteristics in rotating microdevices. The problem is modeled as a cylindrical Couette flow with a rotating shaft and stationary housing. The housing is maintained at uniform temperature while the rotating shaft is insulated. Thus, heat transfer is due to viscous dissipation only. An analytic solution is obtained for the temperature distribution in the gas filled concentric clearance between the rotating shaft and its stationary housing. The solution is valid in the slip flow and temperature jump domain defined by the Knudsen number range of $0.001 < \mathrm{Kn} < 0.1$. *The important effect of the momentum accommodation coefficient on velocity reversal and its impact on heat transfer is determined. The Nusselt number was found to depend on four parameters: the momentum accommodation coefficient of the stationary surface* σ_{uo}, *Knudsen number Kn, ratio of housing to shaft radius* r_o/r_i, *and the dimensionless group* $[\gamma/(\gamma+1)](2\sigma_{to}-1)/(\sigma_{to}\mathrm{Pr})$. *Results indicate that curvature, Knudsen number, and the accommodation coefficients have significant effects on temperature distribution, heat transfer, and Nusselt number.* [DOI: 10.1115/1.2818763]

Keywords: heat transfer, microchannels, momentum, and energy accommodation coefficients

1 Introduction

Temperature distribution and heat transfer in the clearance of rotating microdevices such as microturbines, pumps, and microbearings have not been investigated. The effect of velocity slip, temperature jump, curvature, and viscous dissipation on heat transfer characteristics is unknown. Although extensive work on the related problem of convection in straight microchannels and tubes has been carried out, few studies examined the effect of viscous dissipation on heat transfer. Tunc and Bayazitoglu [1] obtained analytic solutions to heat transfer characteristics of gas flow in the entrance and fully developed regions of tubes at uniform surface temperature and uniform surface heat flux. They examined the effects of Knudsen number and Brinkman number on heat transfer and Nusselt number. Temperature jump was found to increase with Knudsen number while the Nusselt number increases with increasing Brinkman number. Hadjiconstantinou [2] analytically examined Poiseuille gas flow between parallel plates at uniform surface flux. Attention was focused on the effect of boundary shear work on the Nusselt number. In an earlier study, Zhang and Bogy [3] obtained analytical solutions to Couette and Poiseuille flow between parallel plates taking into consideration dissipation, velocity slip, and temperature jump. They used a continuum model to solve the simplified Navier–Stokes equations and energy equation.

Aside from the effects of rarefaction, temperature jump, and dissipation, the clearance between a rotating shaft and its housing in microdevices may not be small compared to shaft radius. Thus, curvature effect is important and consequently hydrodynamic and heat transfer analysis of such devices cannot be modeled as Couette flow between parallel plates.

Studies on rotating flows in cylindrical microchannels are limited to hydrodynamic effects in the clearance of gas lubricated microbearings. Maureau et al. [4] obtained an exact flow field solution for incompressible gas flow in the clearance of microbearings taking into consideration eccentricity and velocity slip. They also presented the solution to the limiting case of flow in the clearance between concentric cylinders. Lee et al. [5] examined the effect of slip velocity on gas lubricated journal bearings. Their analysis showed that slip flow effects become more significant as gas temperature is increased. The general case of rotating concentric inner and outer cylinders was investigated by Yuhong et al. [6]. They focused attention on the effect of the momentum accommodation coefficients on the velocity distribution. Their solution shows that at low values of the accommodation coefficient, a velocity inversion takes place.

In this paper, we consider the case of a microshaft rotating concentrically inside stationary housing. Specifically, we examine temperature distribution and heat transfer in the gas filled gap. The analysis takes into consideration rarefaction, temperature jump, viscous dissipation, and curvature effects. Particular attention is given to the effect of the momentum and energy accommodation coefficients on temperature distribution, heat transfer, and Nusselt number.

2 Analysis

Figure 1 shows a shaft of radius r_i concentrically positioned inside a stationary housing of radius r_o. The shaft rotates with angular velocity ω and the housing is maintained at uniform temperature T_0. We assume steady state and neglect axial variation. Since all angular derivatives vanish due to concentricity and surface uniformity conditions, the problem simplifies to one-

Contributed by the Heat Transfer Division of ASME for publication in the JOURNAL OF HEAT TRANSFER. Manuscript received July 31, 2006; final manuscript received April 4, 2007; published online March 17, 2008. Review conducted by Gang Chen.

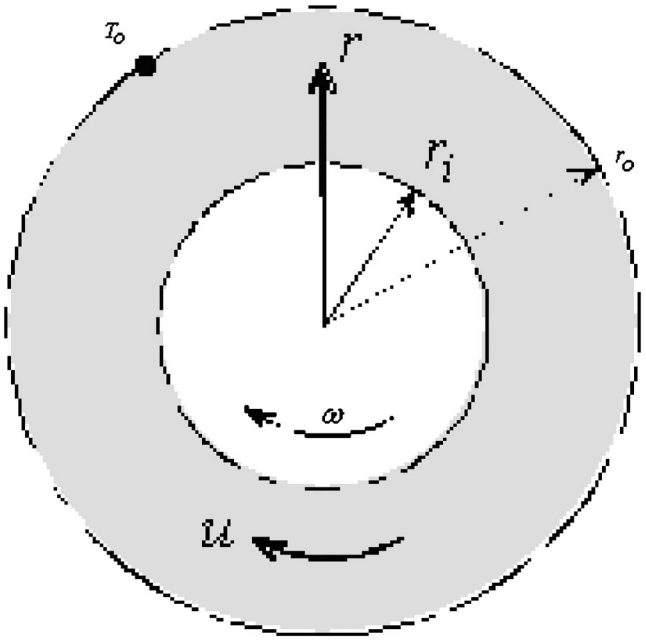

Fig. 1 Cylindrical Couette flow

dimensional flow and heat transfer. We limit the analysis to continuum, gaseous slip flow domain, defined in terms of the Knudsen number Kn as [7]

$$0.001 < \mathrm{Kn} < 0.1 \tag{1}$$

where Kn is the dimensionless mean free path λ defined as

$$\mathrm{Kn} = \frac{\lambda}{r_o - r_i}$$

Expecting r_o/r_i to be one of the governing parameters, the above definition is rewritten as

$$\mathrm{Kn} = \frac{\lambda/r_i}{(r_o/r_i) - 1} \tag{2}$$

2.1 Previous Results: Velocity Distribution. Because fluid velocity is central to temperature distribution, and because of the velocity anomalies associated with slip and curvature, the flow field solution detailed in Ref. [6] is summarized here.

Assuming constant properties, the Navier–Stokes equation in the tangential direction simplifies to

$$\frac{d^2u}{dr^2} + \frac{1}{r}\frac{du}{dr} - \frac{u}{r^2} = 0 \tag{3}$$

where u is the tangential velocity. Using the Maxwell slip model, the velocity boundary condition at the moving surface $r=r_i$ is given by [6]

$$u(r_i) = \omega r_i + \frac{2-\sigma_{ui}}{\sigma_{ui}}(r_o - r_i)\mathrm{Kn}\left[\frac{du(r_i)}{dr} - \frac{u(r_i)}{r_i}\right] \tag{4}$$

where σ_{ui} is the tangential momentum accommodation coefficient of the inner surface. Similarly, at the stationary surface $r=r_o$, the boundary condition is

$$u(r_o) = -\frac{2-\sigma_{uo}}{\sigma_{uo}}(r_o - r_i)\mathrm{Kn}\left[\frac{du(r_o)}{dr} - \frac{u(r_o)}{r_o}\right] \tag{5}$$

where σ_{uo} is the tangential momentum accommodation coefficient of the outer surface.

Integration of Eq. (3) and using Eqs. (4) and (5) gives the solution to the velocity

$$\frac{u(r)}{\omega r_i} = \left\{1 - \frac{r_i^2}{r_o^2} + 2\mathrm{Kn}\left(\frac{r_o}{r_i} - 1\right)\left[\frac{2-\sigma_{ui}}{\sigma_{ui}} + \frac{2-\sigma_{uo}}{\sigma_{uo}}\frac{r_i^3}{r_o^3}\right]\right\}^{-1} \times \left\{\frac{r_i^2}{r_o^2}\left[2\mathrm{Kn}\left(1 - \frac{r_i}{r_o}\right)\frac{2-\sigma_{uo}}{\sigma_{uo}} - 1\right]\frac{r}{r_i} + \frac{r_i}{r}\right\} \tag{6}$$

2.2 Temperature Field

2.2.1 Governing Equation, Boundary Conditions, and Solution. Taking into consideration viscous dissipation, the energy equation reduces to

$$\frac{k}{r}\frac{d}{dr}\left[r\frac{dT}{dr}\right] + \mu\left[\frac{du}{dr} - \frac{u}{r}\right]^2 = 0 \tag{7}$$

where T is the temperature, k is the thermal conductivity, and μ is the viscosity. Since the moving surface is thermally insulated, the boundary condition at $r=r_i$ is

$$\frac{dT(r_i)}{dr} = 0 \tag{8}$$

Accounting for temperature jump, the fluid temperature at the stationary surface $r=r_o$ is [7]

$$T(r_o) = T_0 - \frac{2-\sigma_{to}}{\sigma_{to}}\frac{2\gamma}{1+\gamma}(r_o - r_i)\frac{\mathrm{Kn}}{\mathrm{Pr}}\frac{dT(r_o)}{dr} \tag{9}$$

where Pr is the Prandtl number, γ is the specific heat ratio, and σ_{to} is the energy accommodation coefficient of the outer surface. The coefficients σ_{ui}, σ_{uo}, and σ_{to} are empirical factors that reflect the interaction between gas molecules and a surface. They depend on the gas as well as the geometry and surface nature. Their values range from zero (perfectly smooth) to unity. Although they are difficult to determine, there is general agreement that their values for various gases flowing over several surfaces are close to unity [8].

Substituting flow field solution (6) into energy equation (7), integrating, and using boundary conditions (8) and (9) give the temperature distribution

$$\frac{T(r) - T_0}{\mu\omega^2 r_i^2/k} = \frac{(r_i^2/r_o^2) - (r_i^2/r^2) - 2\ln(r_i/r_o)(r/r_i) - [4\gamma/(\gamma+1)][(2-\sigma_{to})/\sigma_{to}](1 - (r_i/r_o))((r_i^2/r_o^2) - 1)\mathrm{Kn/Pr}}{\{1 - (r_i^2/r_o^2) + 2\mathrm{Kn}((r_o/r_i) - 1)[[(2-\sigma_u)/\sigma_{ui}] + [(2-\sigma_{uo})/\sigma_{uo}](r_i^3/r_o^3)]\}^2} \tag{10}$$

2.2.2 Nusselt Number. Examination of energy equation (7) shows that it does not include convective terms. This is traced to the assumption of concentricity and circumferential uniformity of surface conditions. Thus, despite the dependence of temperature on velocity distribution, the mechanism for heat transfer is conduction. Nevertheless, it is useful to determine the Nusselt number for this case to provide a limiting value for more general problems involving eccentricity and surface nonuniformity. The Nusselt

number for this configuration is defined as

$$\mathrm{Nu} = \frac{2(r_o - r_i)h}{k} \tag{11}$$

where $2(r_o - r_i)$ is the equivalent diameter of the clearance and h is the heat transfer coefficient obtained by equating Newton's law of cooling and Fourier's conduction law

$$h = -k\frac{dT(r_o)/dr}{T_m - T_0} \tag{12}$$

Here, T_m is the mean channel temperature given by

$$T_m = \frac{\int_{r_i}^{r_o} uT dr}{\int_{r_i}^{r_o} u dr} \tag{13}$$

Combining Eqs. (11) and (12) gives

$$\mathrm{Nu} = -2(r_o - r_i)\frac{dT(r_o)/dr}{T_m - T_0} \tag{14}$$

The integrals in Eq. (13) are evaluated using Eqs. (6) and (10) to determine the mean temperature T_m. Substituting T_m and Eq. (10) into Eq. (14) gives the Nusselt number

$$\mathrm{Nu} = \frac{8}{[(A+B)/C] + D} \tag{15}$$

where

$$A = \left[2\mathrm{Kn}\frac{2-\sigma_{uo}}{\sigma_{uo}}\left(1 - \frac{r_i}{r_o}\right) - 1\right]\left[\frac{r_o^2}{r_i^2} - \frac{r_i^2}{r_o^2} - 4\ln\frac{r_o}{r_i}\right] \tag{16}$$

$$B = 1 - \frac{r_o^2}{r_i^2} + 2\ln\frac{r_o}{r_i} + 2\frac{r_o^2}{r_i^2}\left(\ln\frac{r_o}{r_i}\right)^2 \tag{17}$$

$$C = \left(1 - \frac{r_i}{r_o}\right)\left(\frac{r_o^2}{r_i^2} - 1\right)\left\{\left[\mathrm{Kn}\frac{2-\sigma_{uo}}{\sigma_{uo}}\left(1 - \frac{r_i}{r_o}\right) - \frac{1}{2}\right]\left(1 - \frac{r_i^2}{r_o^2}\right) + \ln(r_o/r_i)\right\} \tag{18}$$

and

$$D = \frac{8\gamma}{\gamma+1}\frac{2-\sigma_{to}}{\sigma_{to}}\frac{\mathrm{Kn}}{\mathrm{Pr}} \tag{19}$$

The Nusselt number for the corresponding macrocase is obtained by letting $\mathrm{Kn} \to 0$ in Eq. (15)

$$\mathrm{Nu}_{\mathrm{macro}} = 8\frac{1/2(1 - (r_i/r_o))((r_o^2/r_i^2) - 1)[(r_i^2/r_o^2) - 1 + 2\ln(r_o/r_i)]}{1 + (r_i^2/r_o^2) - 2(r_o^2/r_i^2) + 6\ln(r_o/r_i) + 2(r_o^2/r_i^2)(\ln(r_o/r_i))^2} \tag{20}$$

2.2.3 Fluid Temperature Rise. $T(r_i) - T(r_o)$. Application of solution (10) at the inner and outer radii gives fluid temperature rise due to dissipation

$$\frac{T(r_i) - T(r_o)}{\mu\omega^2 r_i^2/k} = \frac{(r_i^2/r_o^2) + 2\ln(r_o/r_i) - 1}{\{1 - (r_i^2/r_o^2) + 2\mathrm{Kn}((r_o/r_i) - 1)[[(2-\sigma_{ui})/\sigma_{ui}] + [(2-\sigma_{uo})/\sigma_{uo}](r_i^3/r_o^3)]\}^2} \tag{21}$$

2.2.4 Surface Heat Flux. Heat flux at the outer surface is obtained by substituting Eq. (10) into Fourier's law to give

$$\frac{q''}{\mu\omega^2 r_i} = 2\frac{(r_i/r_o) - (r_i^3/r_o^3)}{\{1 - (r_i^2/r_o^2) + 2\mathrm{Kn}((r_o/r_i) - 1)[[(2-\sigma_{ui})/\sigma_{ui}] + [(2-\sigma_{uo})/\sigma_{uo}](r_i^3/r_o^3)]\}^2} \tag{22}$$

3 Results

3.1 Velocity Distribution. Since temperature distribution and heat transfer characteristics depend on the flow field, it is helpful to examine the effect of various parameters on the velocity distribution. Although the tangential velocity in the macroscale cylindrical Couette flow decreases monotonically with distance from the rotating inner surface, this is not always the case under rarefied conditions [6]. It is instructive to determine how this anomalous velocity behavior affects temperature distribution and Nusselt number. Depending on the value of the momentum accommodation coefficient, a velocity inversion can occur. Yuhong et al. [6] identify three cases: a fully inverted profile in which the velocity increases monotonically with radial distance, a partially inverted profile where the velocity decreases and then increases, and no inversion where the velocity decreases monotonically. Full inversion occurs if

$$\sigma_{uo} < 2\left[1 + \frac{1}{2\mathrm{Kn}}\frac{1 + (r_o^2/r_i^2)}{1 - (r_i/r_o)}\right]^{-1} \tag{23}$$

The condition for partial inversion is

$$2\left[1 + \frac{1}{2\mathrm{Kn}}\frac{1 + (r_o^2/r_i^2)}{1 - (r_i/r_o)}\right]^{-1} < \sigma_{uo} < 2\left[1 + \frac{1}{\mathrm{Kn}}\frac{1}{1 - (r_i/r_o)}\right]^{-1} \tag{24}$$

The no inversion case holds if

$$\sigma_{uo} > 2\left[1 + \frac{1}{\mathrm{Kn}}\frac{1}{1 - (r_i/r_o)}\right]^{-1} \tag{25}$$

According to Eq. (23), in the slip flow domain defined by Eq. (1), full velocity inversion takes place at very small values of σ_{uo}. For example, at $\mathrm{Kn}=0.1$ and $r_o/r_i=1.5$, full inversion occurs at values of σ_{uo} smaller than 0.04. Figure 2 gives the velocity distribution for various values of the Knudsen number for $\sigma_{ui}=\sigma_{uo}=0.03$ and $r_o/r_i=1.5$. Equation (23) is satisfied at $\mathrm{Kn}=0.1$ giving a fully inverted profile. At $\mathrm{Kn}=0.05$, Eq. (24) is satisfied and thus the profile is partially inverted. According to Eq. (25), the velocity decreases monotonically for $\mathrm{Kn} \leq 0.0457$, as indicated in Fig. 2. Partial inversion is also shown in Fig. 3 for $\sigma_{ui}=\sigma_{uo}=0.1$, $r_o/r_i=3$, and $\mathrm{Kn}=0.1$. Velocity profiles corresponding to other combinations of σ_{ui} and σ_{uo} are shown in Figs. 4(*a*)–4(*c*) for r_o/r_i

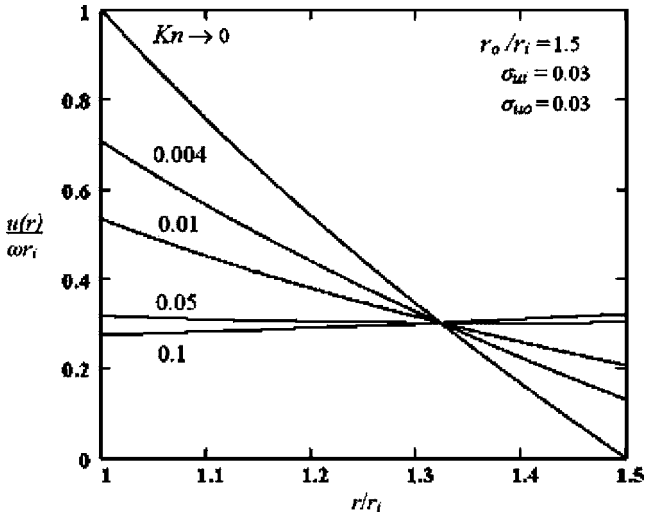

Fig. 2 Velocity distribution showing partial inversion at Kn =0.05 and total inversion at Kn=0.1

=1.5. These graphs illustrate the significant impact of σ_{ui} and σ_{uo} on velocity. As might be expected, σ_{ui} and σ_{uo} affect slip velocities at their respective surfaces. Decreasing values of the accommodation coefficients result in increasing the slip velocity and a general flattening of the velocity profiles. Increasing the Knudsen number has the same effect on the profiles, progressing toward uniform velocity distribution, as shown in Figs. 2–4. Examination of these results shows that solutions for all values of the Knudsen number intersect at a common location r^*/r_i. This location can be determined analytically for all values of r_o/r_i, σ_{ui}, and σ_{uo} by differentiating Eq. (6) with respect to Kn, setting the result equal to zero and solving for r^*/r_i to obtain

$$\frac{r}{r_i} = \left\{ \frac{(r_o^3/r_i^3) + \{[\sigma_{ui}(2-\sigma_{uo})]/[\sigma_{uo}(2-\sigma_{ui})]\}}{(r_o/r_i) + [\sigma_{ui}(2-\sigma_{uo})]/[\sigma_{uo}(2-\sigma_{ui})]} \right\}^{1/2} \quad (26a)$$

For the special case of $\sigma_{ui}=\sigma_{uo}=\sigma$, Eq. (26*a*) simplifies to

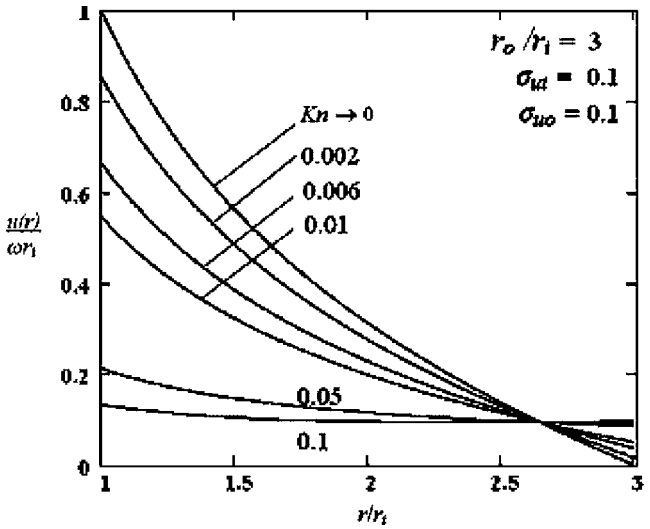

Fig. 3 Velocity distribution showing partial inversion at Kn =0.1

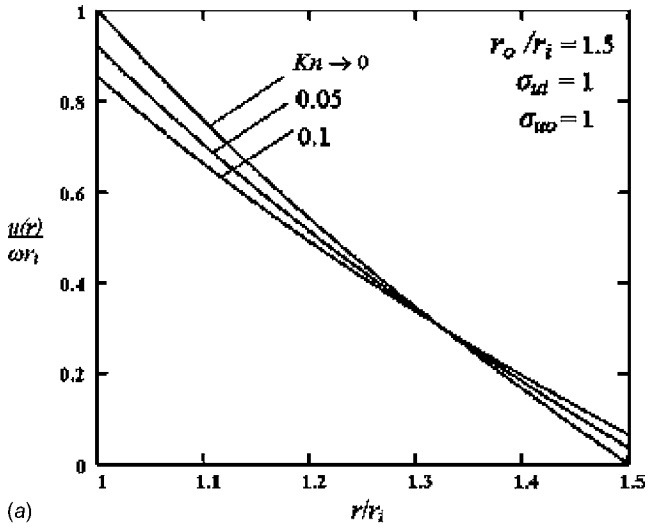

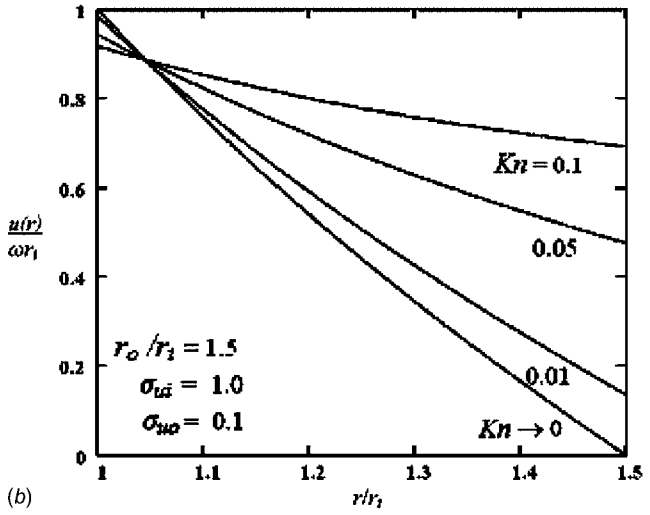

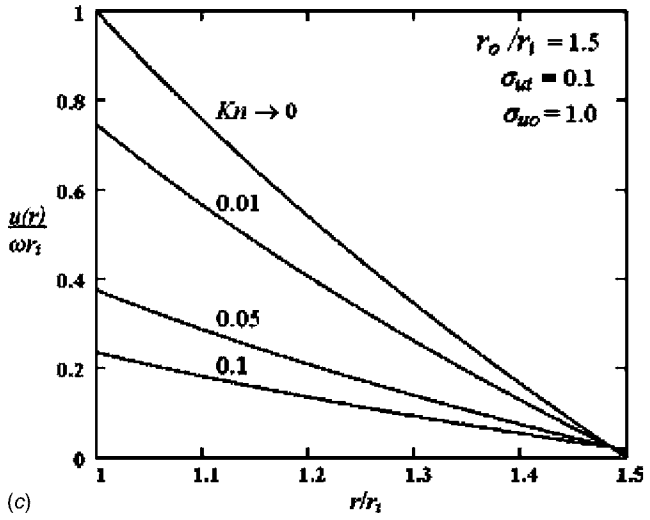

Fig. 4 Effect of σ_{ui} and σ_{uo} on the intersection point of velocity profiles

$$\frac{r}{r_i} = \left[\frac{(r_o/r_i)^3 + 1}{(r_o/r_i) + 1} \right]^{1/2} \quad (26b)$$

This special case is presented in Ref. [6]. However, according to Eq. (26*a*), the family of velocity profiles intersect at a common location regardless of the values σ_{ui} and σ_{uo}, and for all values of

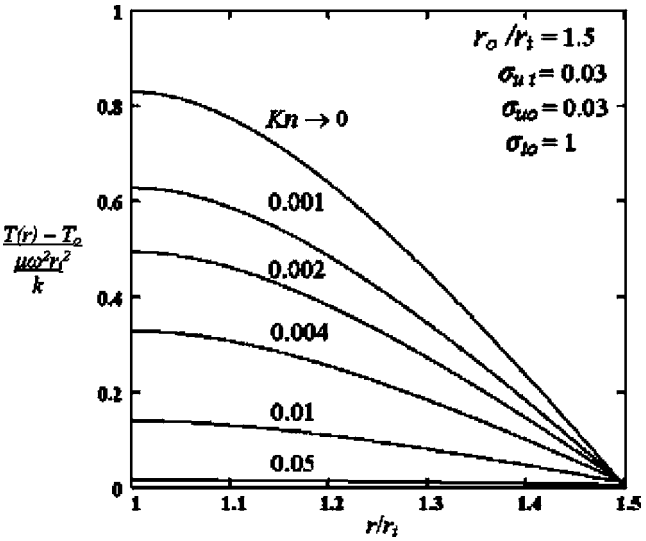

Fig. 5 Full, partial, and no velocity inversion effect on temperature distribution

the Knudsen numbers. This location shifts as values of the accommodation coefficients are changed, as shown in Figs. 2–4. Reference [6] compares analytical predictions of the tangential velocity with the DSME data of Ref. [9] for Kn=0.5. Although this value of the Knudsen number is outside the validity of the continuum model, results show that the two solutions exhibit similar behavior.

It is important to note that the effect of Knudsen number on velocity reverses direction for $r/r_i > r^*/r_i$. Changes in the values of σ_{ui} and σ_{uo} shift the location of r^*/r_i between the two surfaces. This is evident in Figs. 4(*a*)–4(*c*) where three combinations of σ_{ui} and σ_{uo} are used. These results show that a decrease in σ_{ui} or σ_{uo} shifts the intersection location away from their respective surfaces. In Fig. 4(*a*), the intersection location is $r^*/r_i = 1.323$ for $\sigma_{ui} = \sigma_{uo} = 1.0$. Decreasing σ_{uo} from 1.0 to 0.1 shifts the intersection point close to the inner surface to $r^*/r_i = 1.045$, as shown in Fig. 4(*b*). Consequently, the velocity increases with increasing Knudsen number throughout much of the channel. In addition, velocity slip diminishes at the inner surface and increases at the outer surface. On the other hand, decreasing σ_{ui} to 0.1 has the opposite effect. For this case, the intersection point moves close to the outer surface to $r^*/r_i = 1.486$, as indicated in Fig. 4(*c*). Here, the velocity decreases with increasing Knudsen number for $1.0 < r/r_i < 1.486$. Furthermore, comparing Fig. 4(*a*) with Fig. 4(*c*) shows that velocity slip diminishes at the outer surface and increases at the inner surface with increased Knudsen number. This holds for all values of Kn examined.

3.2 Temperature Distribution. Of particular interest is the influence of velocity distribution on temperature and heat transfer characteristics. Examination of solution (10) shows that temperature distribution depends on Kn, σ_{ui}, σ_{uo}, σ_{to}, r_o/r_i, and gas properties. Figure 5 gives the temperature distribution for air corresponding to the velocity profiles of Fig. 2. Full velocity inversion at Kn=0.1 results in very low, and nearly uniform, temperature throughout the channel. For partial inversion at Kn=0.05, temperature level increases but remains nearly uniform. In the no inversion range, $Kn < 0.0457$, the temperature continues to increase with decreasing Kn, departing progressively from uniform distribution. Temperature jump at the outer surface is negligible due to the high energy accommodation coefficient and low Kn, as indicated in boundary condition (9).

Figure 6 shows the temperature distribution for the three cases of Fig. 4 for $\sigma_{to} = 1$. Temperature profiles for $\sigma_{ui} = \sigma_{uo} = 1.0$, shown

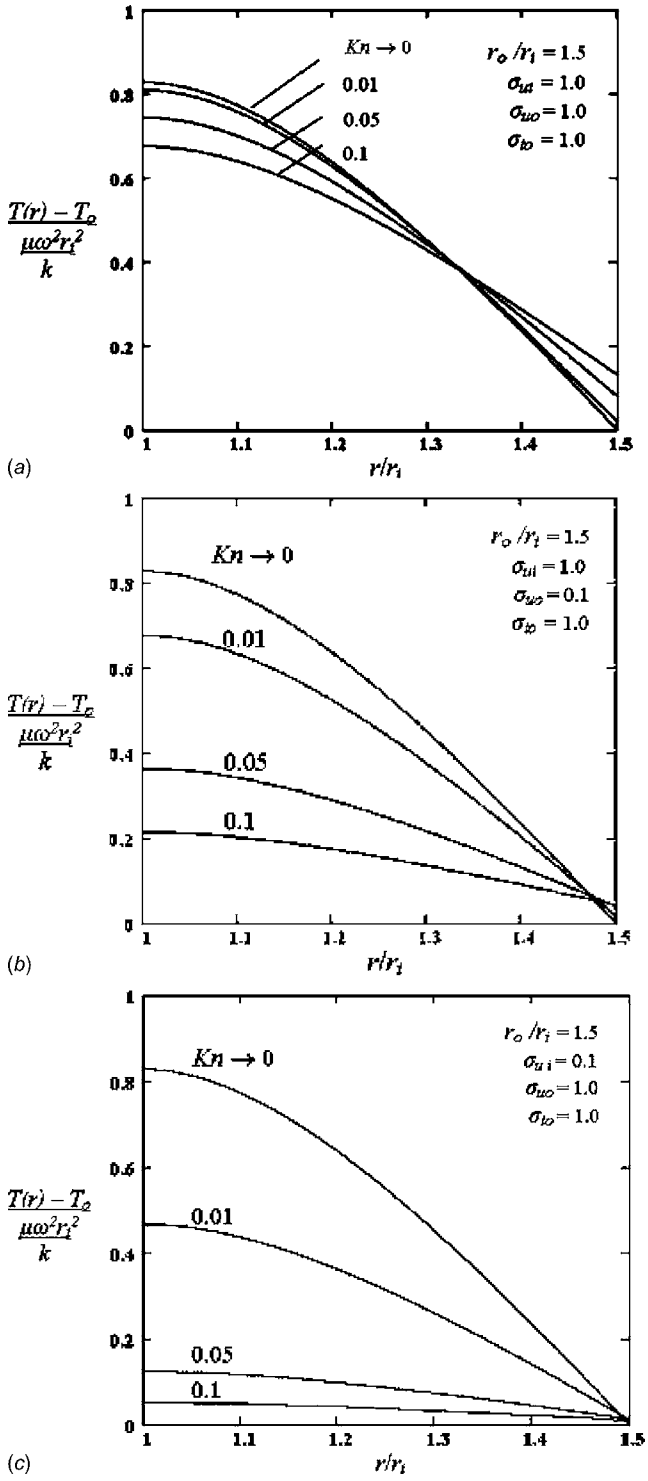

Fig. 6 Effect of Knudsen number, σ_{ui}, and σ_{uo} on temperature distribution in air, γ=1.4, Pr=0.7

in Fig. 6(*a*), follow their corresponding velocity profiles in Fig. 4(*a*). However, unlike the velocity case, temperature profiles for various values of Kn do not intersect at a common location. Nevertheless, in some cases, they appear to intersect over a narrow range of r/r_i. This has important implications since, as with the velocity case, the effect of Knudsen number on temperature reverses direction as this region is traversed. Decreasing σ_{ui} or σ_{uo} to 0.1 shifts the intersection region toward the outer surface and

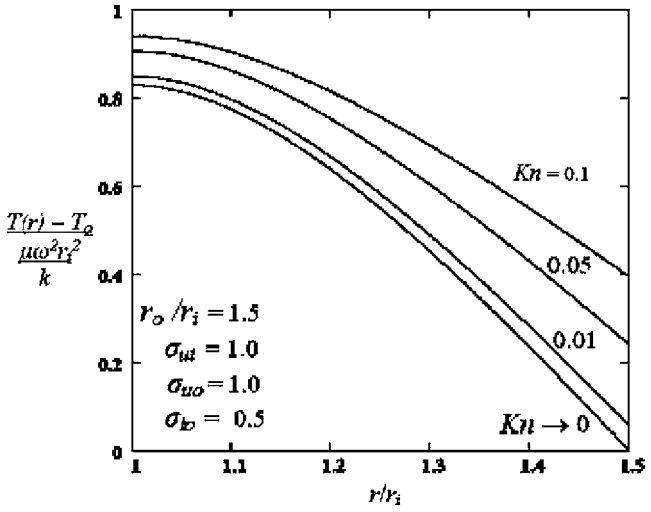

Fig. 7 Inversion of Knudsen number effect as σ_{to} is reduced from 1.0 (Fig. 6(*c*)) to 0.5 for air, γ=1.4, Pr=0.7

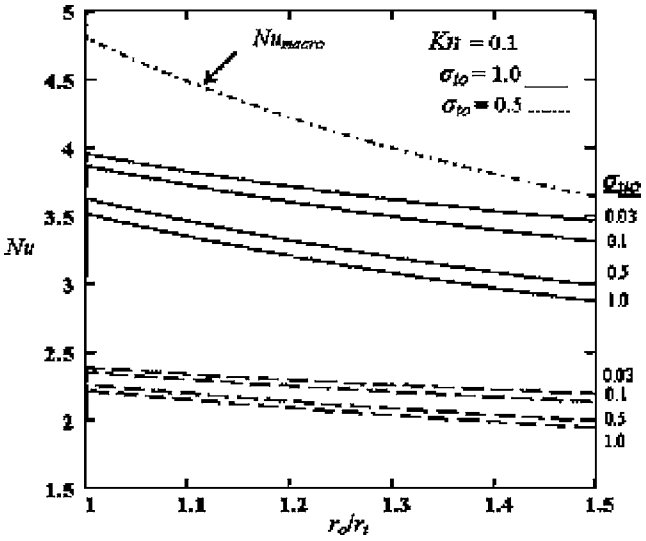

Fig. 9 Effect of σ_{uo} and curvature on Nusselt number for Kn =0.1 in air, γ=1.4, Pr=0.7

significantly lowers fluid temperature at the inner surface, as shown in Figs. 6(*b*) and 6(*c*). In contrast, the effect of σ_{uo} on velocity is more pronounced at the outer surface.

The role of energy accommodation coefficient,σ_{to}, is examined in Figs. 6–8 for the special case of r_o/r_i=1.5. Comparing Fig. 6 with Fig. 7 shows that important changes in temperature distribution occur as σ_{to} is reduced from 1.0 to 0.5. First, constant Knudsen number curves do not intersect in Fig. 7. In fact, gradually decreasing σ_{to} from unity shifts the intersection region toward the inner surface and vanishes for σ_{to}=0.5. Second, an increase in Knudsen number is accompanied by an increase in temperature throughout the channel. This is not the case in Fig. 6. Third, significant increase in temperature follows a reduction in σ_{to} from 1.0 to 0.5. For example, at r/r_i=1.25 for $\sigma_{ui}=\sigma_{uo}$=1.0 and Kn =0.1, the dimensionless temperature increases by 53%, and temperature jump at the outer surface increases by 200%. To further evaluate the effect of the energy coefficient on temperature, results were obtained for various values of σ_{to}. Figure 8 examines the case of $\sigma_{ui}=\sigma_{uo}$=1.0, r_o/r_i=1.5, and Kn=0.1 with σ_{to} varied from 0.25 to 1.0. This result shows that temperature increases monotonically with decreasing σ_{to} throughout the channel. Furthermore, temperature gradient at a given location is independent of σ_{to}, as indicated in solution (10).

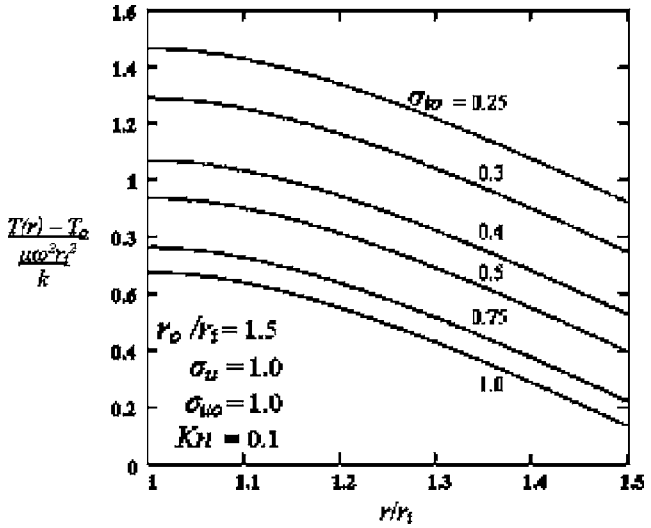

Fig. 8 Effect of the energy accommodation coefficient on temperature distribution in air, γ=1.4, Pr=0.7

3.3 Nusselt Number. According to solution (15), the Nusselt number depends on Kn, σ_{uo}, σ_{to}, r_o/r_i, and gas properties. However, it is independent of σ_{ui}. This follows from the definition of Nu in Eq. (14) where both numerator and denominator are directly proportional to σ_{ui}. Figure 9 examines the effects of σ_{uo}, σ_{to}, and curvature on the Nusselt number for air at Kn=0.1. For σ_{uo} =0.03, the velocity profile is fully inverted, as shown in Fig. 2. As σ_{uo} is increased, velocity profiles move progressively to no inversion. This trend results in a decrease in the Nusselt number for a given r_o/r_i. For example, at r_o/r_i=1.5 and Kn=0.1, the Nusselt number decreases by 17% as σ_{uo} is increased from 0.03 to 1.0. To explain this behavior, we return to the definition of the Nusselt number in Eq. (14). According to boundary condition (5), velocity slip at the outer surface decreases as σ_{uo} is increased. This results in an increase in dissipation, surface flux, and T_m-T_0. Although both numerator and denominator in Eq. (14) increase, the net effect is a drop in Nusselt number.

Turning to the energy accommodation coefficient, Fig. 9 shows that reducing σ_{to} results in a significant decrease in the Nusselt number. For example, at σ_{uo}=1, r_o/r_i=1.5, and Kn=0.1, the Nusselt number decreases by 32% as σ_{to} is reduced from 1.0 to 0.5. To explain this, we note that since properties are assumed constant, a change in σ_{to} does not affect the flow field. Thus, dissipation, surface heat flux, and flow rate are independent of σ_{to}. However, a decrease in σ_{to} is accompanied by an increase in temperature jump. This leads to an increase in T_m-T_0 and consequently a decrease in Nusselt number.

The Nusselt number for Kn$\rightarrow$0, $\mathrm{Nu}_{\mathrm{macro}}$, is shown in Fig. 9. For the parameters considered in this figure, the effect of rarefaction is to decrease the Nusselt number. This is consistent with results observed in microchannels such as parallel plates and tubes [10–12]. However, departure from the $\mathrm{Nu}_{\mathrm{macro}}$ diminishes as r_o/r_i increases. In Fig. 10, curvature is extended to r_o/r_i=3. The behavior of the Nusselt number with regard to σ_{uo} and σ_{to} is similar to Fig. 9. However, in Fig. 10, values of the Nusselt number begin to rise about $\mathrm{Nu}_{\mathrm{macro}}$ as r_o/r_i is increased. This is due to the effects of velocity slip and temperature jump, which tend to flatten the Nusselt number curves.

In Fig. 11, the Knudsen number is reduced to 0.01 with σ_{to} =0.5 and r_o/r_i=3. Comparing Fig. 10 with Fig. 11 shows that the

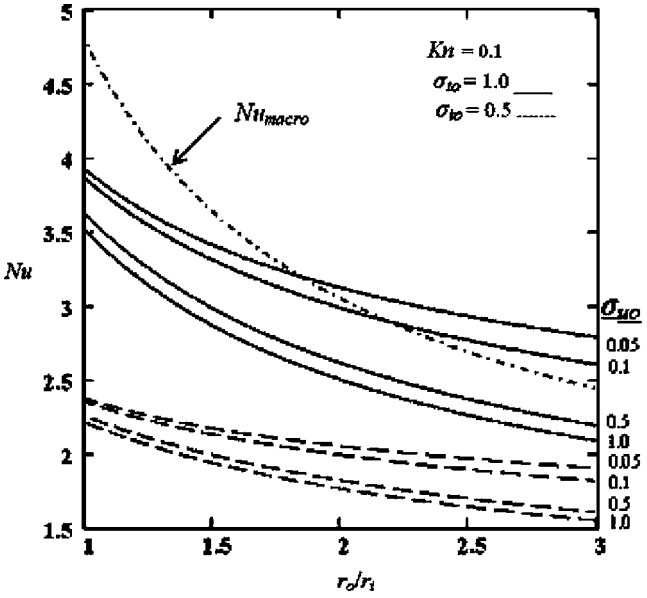

Fig. 10 Effect of σ_{uo}, σ_{to}, and curvature on Nusselt number for Kn=0.1 in air, γ=1.4, Pr=0.7

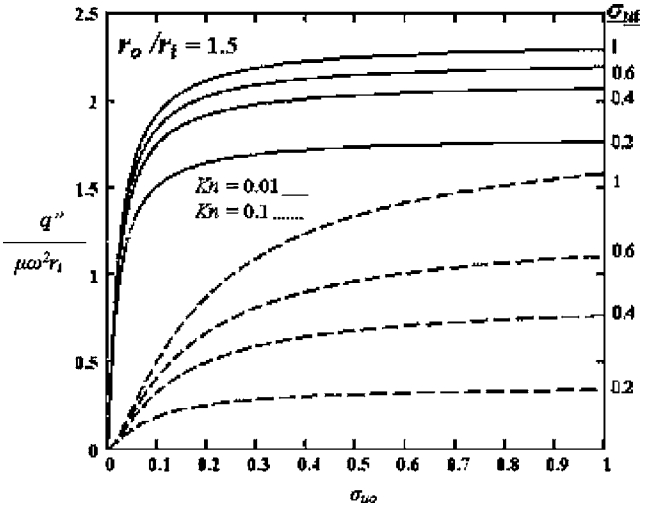

Fig. 12 Surface heat flux variation with σ_{ui} and σ_{uo}

Nusselt number decreases with increasing Knudsen number. For example, for σ_{uo}=1, σ_{to}=0.5, and r_o/r_i=1.5, the Nusselt number decreases by 42% as the Knudsen number is increased from 0.01 to 0.1.

3.4 Curvature. Solutions (6), (10), and (15), show that velocity, temperature, and Nusselt number depend on the curvature parameter r_o/r_i. The limiting case of $r_o/r_i \rightarrow 1$ represents parallel plates. Figures 9–11 show the effect of curvature on the Nusselt number. Increasing the curvature results in a decrease in the Nusselt number for various combinations of the parameters Kn, σ_{uo}, and σ_{to}. In interpreting curvature influence in Figs. 9–11, special attention should be given to the definition of the Knudsen number in Eq. (2) and the Nusselt number in Eq. (14). Equation (2) shows that Kn depends on r_o/r_i. Thus, for constant λ and Kn, an increase in r_o/r_i must be accompanied by a decrease in both r_i and r_o such that r_o-r_i remains constant. It follows that a constant Kn curve defines concentric cylinders having a fixed gap, r_o-r_i. The definition of Kn in Eq. (2) and the parameter r_o/r_i specify the radii r_i and r_o as

$$r_i = \frac{\lambda}{\mathrm{Kn}[\, r_o/r_i) - 1]} \quad r_o = r_i \frac{r_o}{r_i} \tag{27}$$

The reduction in Nusselt number with increasing r_o/r_i can be explained by examining the effect of r_o/r_i on $dT(r_o)/dr$ and $T_m - T_0$ in Eq. (14). An increase in r_o/r_i is accompanied by a reduction in r_i, r_o, u, and T, and an increase in velocity slip at r_i. This results in a decrease in dissipation and heat flux at the outer surface. The effect on T_m-T_0 is evaluated using the definition of T_m in Eq. (13). Since both u and T decrease, their effect on T_m-T_0 cannot be predicted qualitatively. For the values of σ_{uo}, σ_{to}, and Kn used in this example, the net effect is a decrease in the Nusselt number. Figure 11 examines the effect of σ_{uo} and r_o/r_i on the Nusselt number for Kn=0.01 and σ_{to}=0.5. It shows a decrease in the Nusselt number as σ_{uo} is increased for a given r_o/r_i. To explain this behavior, we return to the definition of the Nusselt number in Eq. (14). According to boundary condition (5), velocity slip at the outer surface decreases as σ_{uo} is increased. This results in an increase in dissipation, surface flux, and T_m-T_0. Although both numerator and denominator in Eq. (14) increase, the net effect is a drop in Nusselt number.

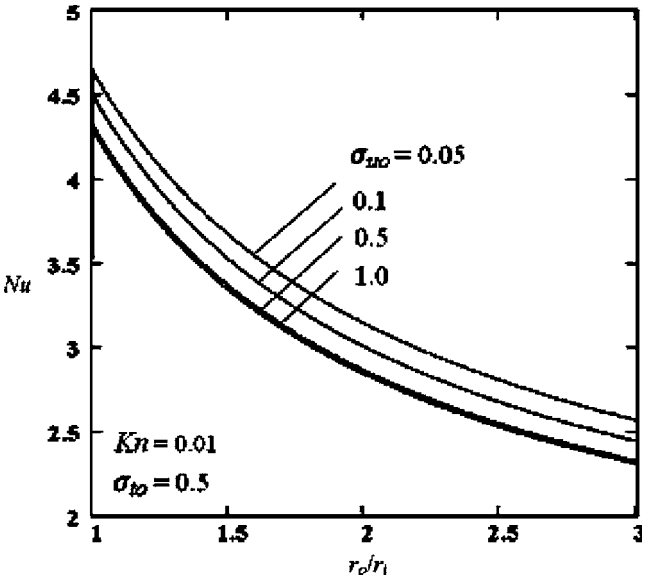

Fig. 11 Effect of σ_{uo} and curvature on Nusselt number for Kn=0.01 in air, γ=1.4, Pr=0.7

3.5 Surface Heat Transfer. Under steady state conditions, dissipated frictional energy leaves the channel through the outer surface. Based on solution (22), surface heat flux is a function of Kn, σ_{ui}, σ_{uo}, and r_o/r_i. However, it is independent of the energy accommodation coefficient σ_{to}. Examination of the temperature distribution (10) shows that σ_{to} affects the temperature level uniformly throughout the channel. Figure 12 gives the variation of heat flux with σ_{ui} and σ_{uo} for r_o/r_i=1.5, and Kn=0.01 and 0.1. Since dissipation is inversely proportional to velocity slip, it follows that surface flux increases as σ_{ui} and σ_{uo} are increased. Changes in σ_{ui} and σ_{uo} near the highest value of unity have considerably less impact on surface flux than changes at low values. Since values σ_{ui} and σ_{uo} for gas flow over several surfaces are close to unity [8], uncertainty in σ_{ui} and σ_{uo} does not result in large errors in determining surface heat flux. Since velocity slip is also proportional to Kn, Fig. 12 shows an increase in heat flux as Kn is decreased from 0.1 to 0.01.

3.6 Examples. To examine the magnitude of temperature rise due to dissipation, solution (21) is applied to the following cases.

Case 1: Air at 20°C, $r_i=10\ \mu$m, $r_o=20\ \mu$m, Kn=0.0063, $\omega=10^6$ rpm, and $\sigma_{ui}=\sigma_{uo}=1.0$. Equation (21) gives $T(r_i)-T(r_o)=8.5\times10^{-4}$°C. This temperature rise is indeed insignificant. The tangential velocity of the inner cylinder for this case is 1.05 m/s. Thus, dissipation at this low velocity is negligible and consequently fluid temperature rise is very small.

Case 2: Air at 20°C, $r_i=1000\ \mu$m, $r_o=1010\ \mu$m, Kn=0.0065, $\sigma_{ui}=\sigma_{uo}=1.0$, and $\omega=10^6$ rpm. Equation (21) gives $T(r_i)-T(r_o)=3.84$°C. The tangential velocity of the inner cylinder is 105 m/s.

4 Conclusions

In this investigation, the microcylindrical Couette flow and heat transfer problem is solved analytically. The solution is used to carry out a parametric study of the effects of rarefaction, dissipation, curvature, and momentum and energy accommodation coefficients on flow and heat transfer characteristics. Key findings are the following.

(1) Velocity profiles for all Knudsen numbers intersect at a common location, r^*/r_i, regardless of the values of σ_{ui} and σ_{uo}. This location is predicted analytically. It shifts between the inner and outer surfaces as the values of σ_{ui} and σ_{uo} are changed.
(2) The momentum and energy accommodation coefficients have major impact on temperature distribution, heat transfer, and Nusselt number. Under certain conditions, but not always, temperature profiles for all values of Knudsen number intersect over a narrow range of r/r_i. Knudsen number effect on temperature reverses direction as this region is traversed. For all cases, fluid temperature rise across the channel, $T(r_i)-T(r_o)$, decreases as the Knudsen number increases. However, it is independent of the energy accommodation coefficient σ_{to}.
(3) Decreasing σ_{ui} and/or σ_{uo} increases velocity slip, leading to a reduction in dissipation, temperature, and surface heat flux.
(4) The Nusselt number decreases with increasing Knudsen number, the momentum accommodation coefficient of the outer surface, and curvature. However, the energy accommodation coefficient has the opposite effect and the momentum accommodation coefficient of the inner surface, σ_{ui}, plays no role.
(5) Curvature, as measured by r_o/r_i, affects velocity, temperature, surface heat flux, and Nusselt number. For the special case of $r_o/r_i\rightarrow1$, the cylindrical geometry approaches parallel plate Couette flow. Depending on the value of r_o/r_i, using parallel plates to model cylindrical Couette flow can result in large errors.
(6) Surface flux is independent of the energy accommodation coefficient.

Acknowledgment

This work was supported by NSF Grant No. 525413 and PSC-CUNY Award No. 68098-0037. The author would like to thank Professor Jason Reese of the University of Strathclyde and Dr. Robert Barber and Dr. David Emerson of Daresbury Laboratory for their helpful discussion on the flow field and for bringing to his attention the velocity inversion phenomenon associated with the momentum accommodation coefficient. The assistance of Luis Bravo in the preparation of graphs is appreciated.

Nomenclature

h = heat transfer coefficient, W/m^2°C
k = thermal conductivity, W/m°C
Kn = Knudsen number
Nu = Nusselt number
Pr = Prandtl number
q'' = surface heat flux, W/m^2
r = radial coordinate, m
r^* = intersection location of velocity profiles, m
T = temperature, °C
T_m = mean temperature, °C

Greek

γ = specific heat ratio
λ = mean free path, m
μ = viscosity, kg/m s
σ_t = energy accommodation coefficient
σ_u = momentum accommodation coefficient
ω = angular velocity, rad/s

Subscripts

i = inner surface
macro = corresponding to Kn$\rightarrow$0
o = outer surface
t = temperature

References

[1] Tunc, G., and Bayazitoglu, Y., 2001, "Heat Transfer in Microtubes With Viscous Dissipation," Int. J. Heat Mass Transfer, **44**, pp. 2395–2403.
[2] Hadjiconstantinou, N. G., 2003, "Dissipation in Small Scale Gaseous Flows," ASME J. Heat Transfer, **125**, pp. 944–947.
[3] Zhang, S., and Bogy, D. B., 1999, "A Heat Transfer Model for Thermal Fluctuations in a Thin Slide/Disk Air Bearing," Int. J. Heat Mass Transfer, **42**, pp. 1791–1800.
[4] Maureau, J., Sharatchandra, M. C., Sen, M., and Gad-el-Hak, M., 1997, "Flow and Load Characteristics of Microbearings With Slip," J. Micromech. Microeng., **7**, pp. 55–64.
[5] Lee, Y.-B., Kwak, H.-D., Kim, C.-H., and Lee, N.-S., 2005, "Numerical Prediction of Slip Flow Effect on Gas-Lubricated Journal Bearings for MEMS/MST-Based Micro-Rotating Machinery," Tribol. Int., **38**, pp. 89–96.
[6] Yuhong, S., Barber, R. W., and Emerson, D. R., 2005, "Inverted Velocity Profiles in Rarefied Cylindrical Couette Gas Flow and the Impact of the Accommodation Coefficients," Phys. Fluids, **17**, p. 047102–1.
[7] Gad-el-Hak, M., 2005, "Flow Physics," *The MEMS Handbook*, M. Gad-el-Hak, ed., CRC, Boca Raton, FL.
[8] Zohar, Y., 2003, *Heat Convection in Micro Ducts*, Kluwer Academic, Norwell, MA.
[9] Tibbs, K. W., Baras, F., and Garcia, A. L., 1997, "Anomalous Flow Profile Due to the Curvature Effect on Slip Length," Phys. Rev. E, **56**, pp. 2282–2283.
[10] Hadjiconstantinou, N. G., and Simek, O., 2002, "Constant-Wall-Temperature Nusselt Number in Micro and Nano-Channels," ASME J. Heat Transfer, **124**, pp. 356–364.
[11] Hadjiconstantinou, N. G., 2000, "Convective Heat Transfer and Nano Channels: Nusselt Number Beyond Slip Flow," *Proceedings of the 2000 IMECE, HTD* Vol. 366-2, pp. 13–22.
[12] Arkilic, E. B., Schmidt, M. A., and Breuer, K. S., 1995, "Gaseous Slip Flow in Micro-Channels," *Rarefied Gas Dynamics: Proceedings of the 19th International Symposium*, J. Harvey and G. Lord, eds., Oxford, pp. 347–353.

Randy D. Weinstein[1]
e-mail: randy.weinstein@villanova.edu

Thomas C. Kopec
e-mail: thomas.kopec@villanova.edu

Amy S. Fleischer
e-mail: amy.fleischer@villanova.edu

Elizabeth D'Addio
e-mail: elizabeth.daddio@villanova.edu

Carol A. Bessel
e-mail: carol.bessel@villanova.edu

Center for Advanced Communications,
Villanova University,
800 Lancaster Avenue,
Villanova, PA 19085

The Experimental Exploration of Embedding Phase Change Materials With Graphite Nanofibers for the Thermal Management of Electronics

To improve the thermal performance of phase change materials (PCMs), graphite nanofibers were embedded into a paraffin PCM. The thermal effects of graphite fiber loading levels (0–5 wt %) *and graphite fiber type (herringbone, ribbon, or platelet) during the melting process were examined for a* 131 cm^3 *volume system with power loads between* 3 W *and* 7 W (1160–2710 W/m^2). *It was found that the maximum system temperature decreased as graphite fiber loading levels increased and that the results were fiber-structure dependent.* [DOI: 10.1115/1.2818764]

Keywords: paraffin, graphite nanofiber, phase change material (PCM), thermal management

Introduction

Phase change materials (PCMs) are materials that undergo a phase transformation, typically the solid-liquid phase transformation, at a temperature within the operating range of the thermal application. The latent heat absorption inherent in the phase change process results in the maintenance of a constant operating temperature during the melt process. In transient applications, PCMs can thus be used to absorb heat and maintain operation at a specified temperature. PCMs have been shown to be effective in transient thermal abatement by slowing the rate of temperature increase during transient operation [1].

While basic PCM systems have proven to be effective in low volume applications [2–12], in larger volumes, the low thermal conductivity of the PCM (for example, 0.2 W/m K for tricosane) impedes the thermal performance. The low thermal conductivity creates a high conductive thermal resistance and leads to the isolation of the melt process near the heat source. Pal and Joshi [13] numerically analyzed the melting of PCM using a uniformly dissipating flush mounted heat source in a rectangular enclosure and established that for low thermal conductivity PCMs, melting is localized near the heat source, whereas for higher conductivity, heat is more effectively distributed throughout the mass. Krishnan et al. [14] studied a hybrid heat sink/paraffin combination for use in electronics cooling applications, finding that paraffin alone is unsuitable for transient heating applications due to its low thermal diffusivity. Therefore, for high power applications the design must be adapted to facilitate more effective heat flow into the PCM.

The PCM is typically contained within a sealed container (module) located adjacent to the heat source. The PCM can melt as it absorbs heat and then resolidify at the end of a power cycle within this container module. In some cases, embedded finned heat sinks [15–19] or metallic foams [20–22] have been used to facilitate the heat penetration from the module walls into the contained PCM by providing a heat flow path to the module center and thus ensuring effective heat absorption through an even melt process. However, the use of embedded heat sinks and metallic foams has several significant disadvantages, including added weight, displaced PCM, and the difficulty of manufacturing foams in thick enough layers for larger modules. This project investigates the use of graphite nanofibers suspended within the PCM to increase thermal performance without significantly increasing module weight or size.

One of the most commonly studied PCMs is paraffin wax. Paraffin waxes in general are inexpensive, thermally and chemically stable, and have a low vapor pressure in the melt [23]. In this project, graphite nanofibers are mixed uniformly into a paraffin wax blend with a melt temperature of 56 °C and the thermal performance of the system is quantified.

Graphite nanofibers (GNFs) generally have diameters of 2–100 nm and lengths of up to 100 μm [24]. The advantage of using GNF as the conductivity enhancer is that they exhibit high surface area [25] and possess thermal properties, which are of the same order of magnitude of carbon nanotubes [24], but with a significantly easier and less expensive production process [25]. The suspension of graphite nanofibers in the PCM is expected to improve the thermal diffusivity and thus the thermal performance by reducing the bottlenecking of heat flux at the source. The embedding of graphite nanofibers will accomplish this through increased conductivity of the composite material and possibly through an additional nanofluid-type enhancement effect through Brownian motion of the particles when suspended in the liquid phase. This will be accomplished with low fiber loading levels, thus preserving a maximum volume for PCM and maximizing the possible heat absorption and duration of melt process.

The GNFs used in this study are grown through the catalytic deposition of hydrocarbons and/or carbon monoxide over metal catalysts in a reducing atmosphere using a process previously described [25], which will be thus only covered in summary here. The carbon precipitates as graphite, which initially encapsulates the metal particle. The catalyst particle is "squeezed" through, leaving a perfectly formed graphite plane. As each graphite plane is formed, the fiber grows longer along an axis extending outwards from the metal catalyst particle. Through precise management of the deposition process, the resulting orientation of these

[1]Corresponding author.

Contributed by the Heat Transfer Division of ASME for publication in the JOURNAL OF HEAT TRANSFER. Manuscript received October 10, 2006; final manuscript received May 1, 2007; published online March 18, 2008. Review conducted by Suresh V. Garimella.

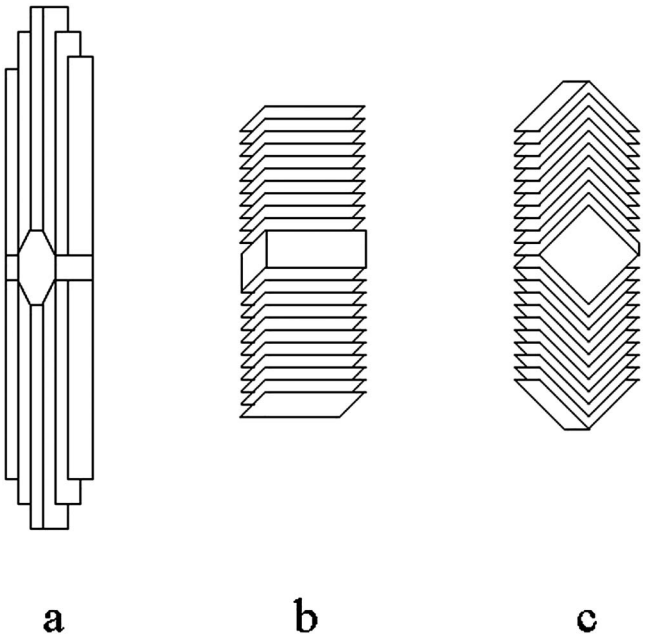

Fig. 1 Styles of graphite nanofibers (*a*) ribbon, (*b*) platelet, and (*c*) herringbone [25]

graphite planes can be controlled. The standard forms, which are accurately created in our laboratory, include the ribbon, platelet, and herringbone styles depicted in Fig. 1. As seen in Fig. 1, the orientation of the graphitic basal plane is distinctly different in each case, which may lead to differences in their thermal performance. This will be investigated as part of this study. The solid particles shown in the middle of each fiber in Fig. 1 are the metallic catalysts upon which the fibers were grown. It is possible to strip the catalyst particle from the fiber after it is grown, but this was not done for this study. During the growth process, the herringbone fibers exhibit a strong tendency to interlink, often creating a spongy agglomeration of particles. This characteristic may be particularly effective in creating a network of linked fibers thus creating a percolation network to effectively spread the heat throughout the PCM. This is the first study, which investigates the use of GNFs with controlled orientation graphite layers to improve PCM performance for application in transient thermal management.

The closest previous studies include that of Py [26], which explored the use of amorphously shaped graphite powders embedded in PCMs in which with high carbon loading in the solid graphite-PCM matrix achieved the same thermal conductivity of the sole graphite matrix and that of Lafdi et al. [27], which explored the response of PCMs embedded with carbon nanofibers of unreported orientation and surface area during the solidification process only. To the best knowledge of the authors, to date no studies have been performed on the use of GNFs with precisely controlled graphite plane orientation to enhance the thermal performance of PCMs during the melting phase.

In this study, the thermal performance of unique PCM/GNF mixtures created using each of the three types of graphite nanofibers shown in Fig. 1 is quantified as a function of fiber loading levels for power loads of 3–7 W in transient operation. The performance of the PCM/GNF mixture in both the solid and liquid phases as well as the interaction of the moving boundary between the two phases is examined to understand the heat transfer fundamentals of this nanoenhanced material

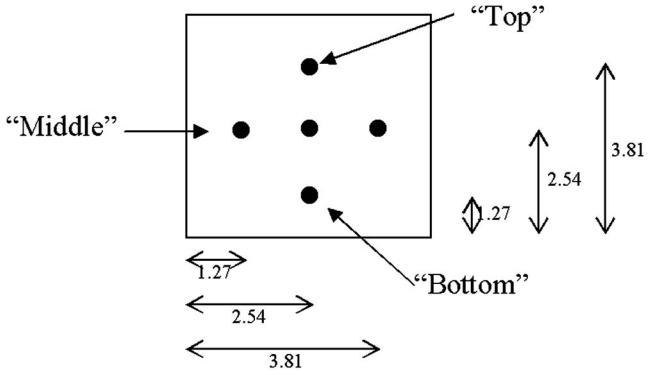

Fig. 2 PCM module illustrating thermocouple hole spacing. The spacing is in centimeters.

Experimental Equipment

The PCM module is a cube with an internal sidewall dimension of 5.08 cm and a total internal volume of 131 cm^3. The cube sidewalls are fabricated from 4.76 mm thick Kydex T Acrylic/PVC with a thermal conductivity of 0.15 W/m K. The bottom of the cube is fabricated from 1.58 mm thick copper 110 alloy with a thermal conductivity of 391 W/m K.

A constant flux is applied to the bottom surface using a 5.08 $\times$ 5.08 cm^2 Kapton resistance heater secured with high temperature metallic tape and centered directly below the internal volume of the cube. The top surface of the cube is an isothermal cold plate maintained at 5 °C using a 50/50 mixture of water and antifreeze supplied from a constant temperature bath. The entire cube is insulated from the environment using fiberglass insulation. This cold plate temperature will remain unchanged throughout the heat absorption process (presented in this paper) and the resolidification process (with the heater turned off). In the situation studied here, it is desired to minimize the recharge time and the soldification occurs faster with the cold plate in place. The choice of cold plate temperature is lower than ambient for this reason, but the choice of cold plate temperature will not affect the fundamental behavior of the nanoenhanced PCM.

Five Type T thermocouples (1/16 in OD, stainless steal sheathed) extend into the PCM module through one sidewall to record the transient temperature response of the PCM at several locations and depths (Fig. 2). These thermocouples were held securely in place using external clamps and did not move during the test run. Thermocouple "bottom" was 1.27 cm from the bottom surface and 2.54 cm from either side, along the centerline of the module. Thermocouple "top" was 3.81 cm from the bottom surface and also along the centerline of the module. Three "middle" thermocouples were placed 2.54 cm from the bottom surface, with one on the centerline of the module, one 1.27 cm from the left side, and the third 1.27 cm from the right side. An additional surface mount Type T thermocouple was located between the heater and the bottom surface of the PCM module to record base temperature. Heat losses from the thermocouples were quantified [1] and were less than 2%.

The PCM module was designed to establish heat flow from the bottom heater to the top surface to best analyze the effects of the embedded nanofibers on the PCM in a controlled environment. As a zero flux boundary along the sidewalls is not physically achievable, the walls were fabricated from low conductivity material and further insulated to minimize sidewall heat losses. The applied temperature difference from top to bottom forces most of the heat flux to travel vertically from bottom to top of the container and not out through the sidewalls. Using the thermocouple measurements, it is observed that large temperature differences are found from bottom to top, while the measurements along the same horizontal plane consistently measured within 1-2 °C of each other,

confirming that heat conduction in the vertical direction is the dominant path while losses out the insulated sides are small in comparison. However, as the PCM changes phase, under certain circumstances, the critical Rayleigh number of the problem is exceeded and convection currents are initiated within the module, creating a more complex heat flow field.

It is noted that as the sidewall conductivity (0.15 W/m K) is of the same order as the base PCM conductivity (0.25 W/m K), a small proportion of applied power is conducted directly along the wall height to the cold plate. This proportion decreases as the PCM conductivity increases with the embedded nanofibers creating a lower thermal resistance through the GNF/PCM than through the walls.

Experimental Procedures

The PCM module must be filled with the PCM in its liquid phase. This is because the density is larger in the solid phase so as the PCM solidifies it contracts leaving an ullage space at the top of the module. To completely fill the module, 105 g of solid paraffin wax is melted completely at 56°C and carefully transferred to the module for pure PCM baseline testing. In the solid phase, the base PCM material has a thermal conductivity of 0.25 W/m K, a heat capacity of 2.1 kJ/kg K, and a latent heat of fusion of 34 kJ/kg.

For the GNF/PCM blends, 105 g of paraffin wax is melted and an appropriate weight of the selected style of graphite nanofiber is carefully added to the liquid paraffin wax to create the proper weight percentage (wt %). The graphite nanofibers are added to the PCM to create weight percentages (wt %) of 0.25%, 0.5%, 1.0%, and 5% for each of the selected types: ribbon, platelet, and herringbone (see Fig. 1). The graphite nanofibers were manufactured by the catalytic decomposition of various hydrocarbons as discussed in the Introduction and as well described in a previous paper [25]. Representative samples of nanofibers were measured by transmission electron microscopy and ranged in diameter from 4 nm to 10 nm with nominal lengths of 1 μm.

The liquid PCM/GNF mixture is then sonicated for 4 h using a SONICS VC505 Ultrasonic Processor with a 0.635 cm stepped microtip to ensure thorough mixing and even distribution of the GNF throughout the PCM. Following sonication, the liquid mixture is poured gently into the module with the thermocouples already in place, completely filling it. The sonication results in the random and uniform dispersion of fibers within the PCM. However, as they are suspended, and not anchored in any way to the PCM, the fibers will move randomly. They stay uniformly distributed during this time. When left in the liquid phase to observe any settling effects, the GNF remained uniformly distributed for the duration of each test, which lasted a minimum of 24 h. The mixture is cooled completely to room temperature before the testing takes place so that each test begins with the PCM in the solid phase with a consistent initial condition of $T_{\text{initial}}=22°\text{C}$. A volume decrease takes place upon phase transition from liquid to solid, creating a concave ullage space at the top of the module.

After each experiment the PCM/GNF mixture is resonicated if the test is to be repeated. If resonficiation is not completed, significant settling of the GNF is observed by the third melting/solidification cycle. It appears to be the volume expansion/contraction, which drives the settling process. Additives, which can prevent fiber settling, are being investigated, but those are not addressed in this paper.

The heat capacity and thermal conductivity of the PCM/GNF blends in the solid phase were measured experimentally and results are presented in Table 1. Heat capacity was measured by a differential scanning calorimeter (TA Instruments, model DSC 2010). The thermal conductivity of the fiber-PCM matrix was measured for the solid phase using a 100 cm^3 sample. The sample was prepared by filling the 131 cm^3 PCM module with the liquid GNF/PCM mixture. This mixture was allowed to cool and solidify, contracting in volume with the phase change. The resulting solid with a concave ullage space was removed from the module and cut into a perfect 100 cm^3 sample. This sample was insulated with fiberglass insulation and instrumented with thermocouples at precisely known locations along its height (along the centerline). A known amount of low power was applied using resistance heating placed in the exact center of the cube and the system was allowed to reach steady state. The power load was selected to allow the cube to always stay below the melt temperature. With the known power load and separation distance of the thermocouples, the thermal conductivity of the solid could be calculated using Fourier's law. It can bee seen that the addition of the GNF has a strong influence on thermal conductivity, increasing it two orders of magnitude, while not adversely affecting the heat capacity.

Table 1 Thermal properties (C_p=heat capacity, k=thermal conductivity, and α=thermal diffusivity) of PCM and PCM/GNF composites

Material	C_p (kJ/kg K)	k (W/m K)	α^*10^6 (m^2/s)
Base PCM	2.1	0.25	0.14
PCM/0.25 wt % Herringbone GNF	2.1	3.5	1.9
PCM/0.25 wt % Platelet GNF	2.2	2.9	1.5
PCM/0.25 wt % Ribbon GNF	2.1	2.1	1.1
PCM/5 wt % Herringbone GNF	1.9	17.2	10.0
PCM/5 wt % Platelet GNF	2.0	25.3	13.9
PCM/5 wt % Ribbon GNF	2.1	29.8	15.6

At the start of each test run, the sample solid in the module is at a consistent initial condition of 22°C. In order to avoid dealing with two transient conditions simultaneously, the cooling water flow is first initiated to the cold plate and the module temperatures are allowed to stabilize before power is supplied to the heater. This develops a known temperature profile in the solid matrix. The heater is then turned on and the transient response of the PCM blend is recorded using the five embedded thermocouples and the base thermocouple. The thermocouple responses are recorded every 5 s to properly capture the nature of the transient response over the 10 h it takes to establish steady-state conditions. However, the shear volume of data over this duration necessitates that for clarity the temperature response be reported only every 20 min on the graphical representation of the data in this paper. The full data set has been analyzed and no discontinuities are seen between presented data points. The applied power is varied from 3 W to 7 W. 3 W allows the study of the thermal response of the material without a complete phase transition, while 7 W is enough power to trigger the phase transformation.

Results and Discussion

This project investigates the use of suspended graphite nanofibers to improve the transient thermal response of PCM systems. The thermal performance of paraffin PCM/GNF mixtures created using each of the three types of graphite nanofibers shown in Fig. 1 is quantified as a function of fiber loading level for weight percentages (wt %) of 0.25%, 0.5%, 1.0%, and 5% and power loads of 3–7 W in transient operation. The performance of the PCM/GNF mixture in both the solid and liquid phase as well as the interaction of the moving boundary between the two phases is examined.

Figure 3 shows the transient response of the pure paraffin PCM with 7 W of applied power. The primary temperature difference is seen to be from bottom to top with a temperate gradient of 10–35°C. The primary heat flow path is designed to be from bottom to top and consistent with this design; the three middle thermocouples were found to consistently record temperatures within 1–2°C of each other. Thus for clarity of the graphs, the average value of the three middle thermocouples is presented.

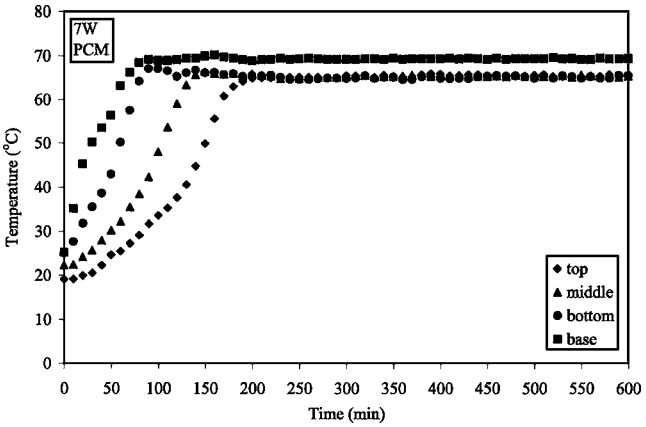

Fig. 3 Transient thermal response of pure paraffin PCM module with 7 W applied power

Additionally, although data were collected every 5 s, for clarity over the long time scale of the experiment the temperature response is reported only every 20 min. The full data set has been analyzed and no discontinuities are seen between presented data points. The graphical representation of the data begins at the time the heater is turned on. At this point, the cold plate has already been initiated and the initial condition of ambient temperature throughout the PCM has been affected by the cold plate, establishing the temperature profile shown at time represented as $t=0$ on Fig. 3.

The difference in the transient response of the thermocouples at the different distances from the heat source is clearly evident, indicating a strong effect of the low thermal conductivity of the PCM material. The bottom thermocouple, which in the PCM is closest to the heater, closely follows the transient temperature trend of the base heater. This location does exhibit a slight temperature overshoot of about 4 °C before settling to steady state, which is attributed to the stratification of temperatures occurring before the establishment of Rayleigh–Benard convection currents even out the temperature distribution in the liquid.

A significant temperature differential between the top and bottom thermocouples is established and reaches as high as 35 °C about 90 min into the test. At this point, the module features a heated liquid layer at the bottom with solid PCM toward the top. The bottom thermocouple records the heating of the liquid layer while the top thermocouple remains firmly embedded in the solid layer until the melt front reaches the top of the module. Once the entire volume is in the liquid state, the internal Rayleigh–Benard convection currents act to mix the volume and lead to a temperature equilibration, which occurs 8 °C above the melting temperature of the PCM. The thermal response, as expected, creates a Stefan problem with the melt front progressing until the entire mass transitions from solid to liquid.

It can be seen in Fig. 3 that there is no point at which the temperature remains steady at the melt temperature for an extended period of time. This is due to the nature of the heating process and the measurement techniques used in this low conductivity solid. As the PCM is heated, as seen in Fig. 3, a significant temperature difference develops between the bottom and top of the module. As discussed, this leads to a heated liquid layer at the bottom with a solid layer of PCM floating above. As the melt front slowly progresses from bottom to top, each embedded thermocouple transitions in turn from being embedded in solid PCM to being exposed to the heated liquid layer. The entire mass of PCM did not heat up uniformly to the melt temperature and maintain operation at this point for an extended period, as is often desired in phase change thermal management systems. Instead, we see a variation on the Stefan problem with a slow progression of the melt front through the module from bottom to top.

The top thermocouple reached steady state and bulk of the PCM was entirely melted 1.3 h after the bottom thermocouple first reaches the steady-state temperature and this temporal lag between two thermocouples located only 2.54 cm apart is related to the reduced ability of the heat to penetrate the PCM mass. It is clear that the low thermal conductivity and thermal diffusivity of the PCM (see Table 1) limit the effectiveness of the PCM. If a system is exposed to a discrete thermal load as is the case here, the low-conductivity PCM may not be able to absorb and suppress the transient heat loads quickly enough. Instead, the response will be isolated near the heat source and the volume of PCM farthest away will not respond to the applied heat load or contribute to the thermal management. This may limit the effectiveness of this technique for high power and fast transient heat loads. The remainder of this paper explores the use of GNFs as additives to the PCM to enhance the thermal response. This can be done using small fiber loadings, displacing very little of the PCM in the module and thus maximizing the available thermal storage. By improving the thermal diffusivity and thus the response time to an applied heat load, the effectiveness of the PCM as a transient thermal abatement technique is improved.

Under ideal conditions, the PCM with embedded GNFs will heat quickly and all locations within the module will reach the melt temperature without significant temporal delays, avoiding thermal bottlenecks at the heat source. Once the melt temperature is reached, it would be desirable for the GNF/PCM mixture to remain at this temperature for a long transient as the PCM melts before finally obtaining a low steady-state temperature. The steady-state temperature of the PCM and heat source must always be maintained below the design temperature limit of the source. If the final steady-state temperature falls below the melt temperature, the PCM will remain in the solid phase. In this case, the PCM acts simply as a heat spreader. Although this would accomplish the ultimate goal of maintaining a heat source below a desired operating temperature, this arrangement would not take full advantage of the natural heat storage capabilities of the PCM. In the case where the PCM remains solid, it will be possible to provide more power to the device while still remaining below desired operating temperature. Typically a PCM module would be designed for a particular application to provide a long transient period of effectiveness during which the PCM melts completely at which time the source is turned off and the PCM allowed to resolidify.

The transient response of GNF/PCM mixtures in various wt % for each of the fiber types is analyzed. The thermal situations, which occur in these tests, are extremely complex and involve physical interaction between several distinct states. Initially, the entire mass is in the solid phase. As the heat penetrates the mass, the melt temperature is reached first at the bottom of the module and the progression of the melt front can be observed through the module. During this time, the module features first a stable liquid layer with a solid layer above, and conduction is the dominant heat transfer mechanism in each phase. However, as the temperature in the liquid layer continues to rise, Rayleigh–Benard convection currents are induced in the liquid, while the solid phase remains stable above this convective environment, leading to convection-conduction interaction at the melt front. Finally, once the entire mass has melted, the module contains a fully liquid phase with convection and the steady-state temperature is obtained with minimal thermal gradients throughout the module. This behavior is made more complex by the addition of the GNF, which increase the viscosity of the mixture at high wt % and thus influence and even suppress the development of Rayleigh–Benard convection in the liquid phase.

The thermal responses of 0.25 wt % mixtures of each GNF style with 7 W of applied power are shown in Figs. 4–6. It is seen that there is a significant difference in the thermal response between the pure PCM (Fig. 3) and the response of each of the 0.25% GNF/PCM mixtures (Figs. 4–6). The pure PCM module

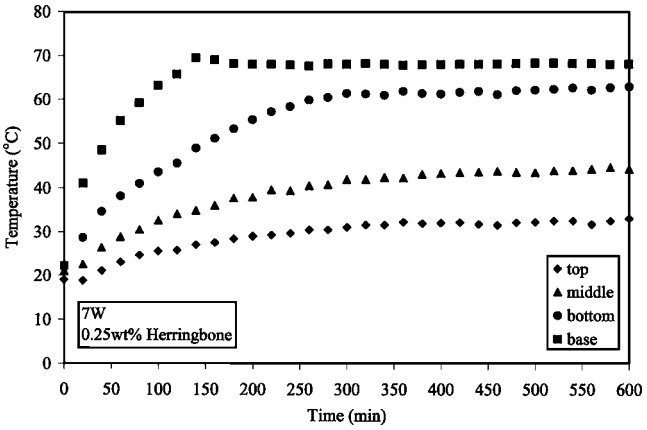

Fig. 4 Transient thermal response of 0.25% herringbone GNF/PCM mixture with 7 W applied power

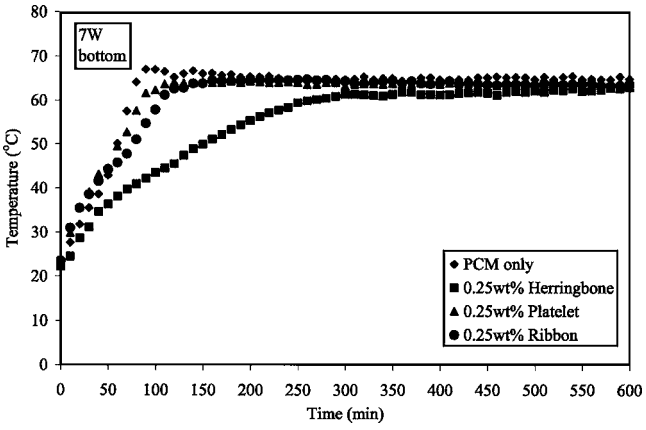

Fig. 7 Transient response of the bottom thermocouple for the 0.25% PCM/GNF module with 7 W applied power compared to the pure PCM module

featured complete melting of the PCM mass and establishment of Rayleigh–Benard convection currents, which equalized the temperature throughout the module at steady state. However, with the addition of 0.25 wt % GNF, only the mixture using ribbon style fibers exhibited complete melting. A significant delay to steady state is seen when compared to the pure PCM case. It took 10 h for the melt front to reach the top thermocouple in the 0.25 wt % ribbon GNF/PCM mixture as compared to 2.5 h for the pure PCM. The temperature response in Fig. 5 indicates that the movement of the melt front stalls between the middle and top thermocouple locations for the 0.25% platelet GNF/PCM mixture, while Fig. 4 shows that the melt front remains isolated below the midplane of the module for the 0.25% herringbone GNF/PCM mixture.

Although the thermal response is distinctly different for each fiber style, even at this low weight percentage, none of the fiber styles was able to significantly impact the thermal diffusivity enough to effect a change in the temperature stratification between thermocouples during the progression of the melt front. With both the herringbone and platelet fibers, large temperature differences persisted throughout the module both during the transient and at steady states, since complete melting was not achieved. Figure 6 shows that the GNF/PCM mixture with ribbon fibers most effectively conducted the heat throughout the PCM module and complete melting was achieved, the ribbon GNF/PCM mixture did not exhibit a significantly lower overall steady-state temperature when compared to the pure PCM. However, the delay to steady state is advantageous, leading to a longer transient effectiveness of the PCM module without significant reduction in the available latent heat of fusion for thermal energy storage.

Comparisons of the thermal response at the top and bottom thermocouples for each mixture are shown in Figs. 7 and 8. The thermal diffusivity of the ribbon and platelet GNF/PCM mixtures was improved when compared to that of the pure PCM when in the solid phase, due to enhanced effective thermal conductivity

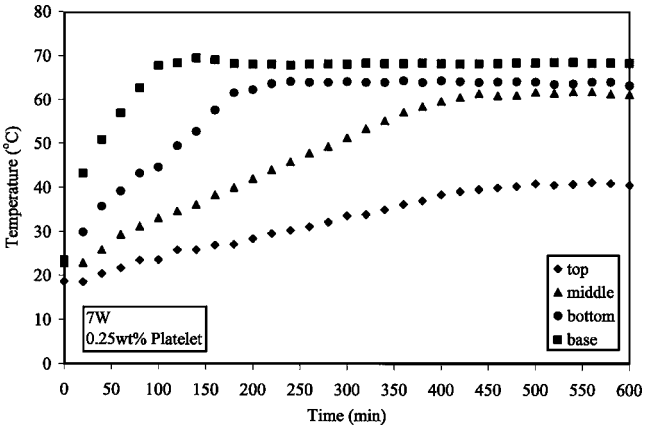

Fig. 5 Transient thermal response of 0.25% platelet GNF/PCM mixture with 7 W applied power

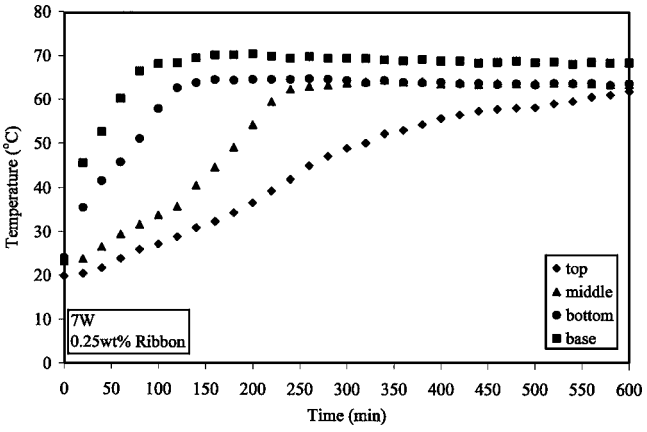

Fig. 6 Transient thermal response of 0.25% ribbon GNF/PCM mixture with 7 W applied power

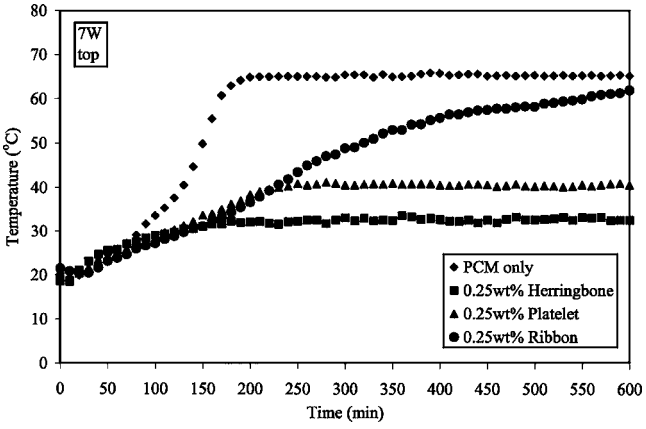

Fig. 8 Transient response of the top thermocouple for the 0.25% PCM/GNF module with 7 W applied power compared to the pure PCM module

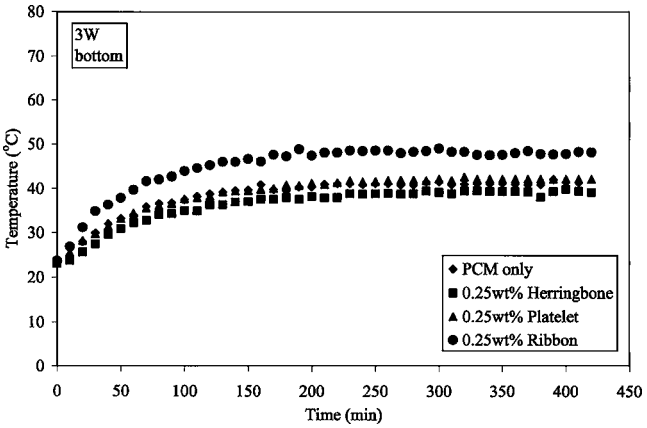

Fig. 9 Transient response of the bottom thermocouple for the 0.25% PCM/GNF module with 3 W applied power compared to the pure PCM module

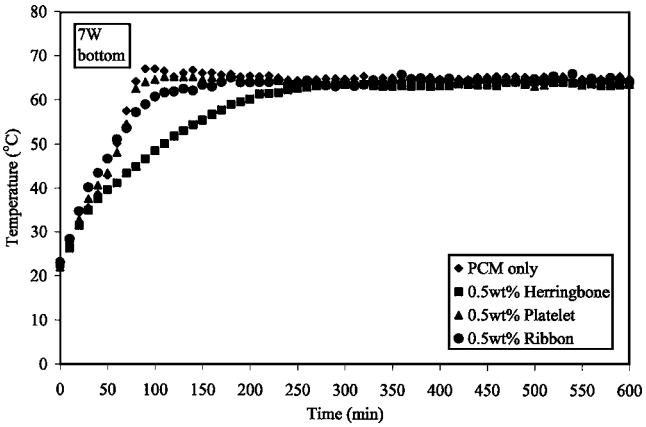

Fig. 10 Transient response of the bottom thermocouple for the 0.5% PCM/GNF module with 7 W applied power compared to the pure PCM module

(see Table 1). However, as the mixture approaches the melting point, the thermal response of the mixture slows as exhibited by the change in slope. Once the melting temperature is reached and Rayleigh–Bernard convection currents develop in the liquid phase the GNF acts to spread the heat effectively through the liquid and at the melt front. This thermal response is desirable, as it is desirable for the PCM to conduct heat effectively in the solid phase to reduce high thermal resistances and then upon melting, continue to effectively transfer heat at the melt front into the solid phase above.

The herringbone fibers had the lowest operating temperatures at this loading level, indicating better heat conduction throughout the module and leading to the observation that this GNF/PCM mixture could handle the dissipation of much higher heat loads. The thermal response of the herringbone GNF/PCM mixture was significantly different from that of the platelet or ribbon mixtures and may be rated to the different physical characteristics of the fiber styles. The herringbone fibers exhibit greater clumping and agglomeration than either of the other two fiber types and this clumping leads to greater fiber-fiber interaction, enhancing heat conduction along fiber-fiber paths.

To more closely examine the influence of the GNFs on heat conduction in solid PCM, the same modules were exposed to 3 W applied power. For this power loading, all mixtures remained in the solid phase throughout the duration of the test. The thermal response of the bottom thermocouple is shown in Fig. 9. The ribbon fiber mixture reached the highest temperature with a steady-state temperature of 7 °C above that of the pure PCM. The herringbone GNF/PCM mixture has a lower temperature than the pure PCM while the platelet fibers exhibit minimal effect. These results show that the herringbone fibers are more effective at transferring heat from the heat source throughout the solid PCM/GNF composite at a loading of 0.25% than the other two types of fibers. The herringbone's effectiveness is perhaps due to the greater fiber linkage, leading to a lower temperature at the bottom thermocouple. This translates into improved thermal conductivity and thermal diffusivity of the herringbone fiber matrix at this fiber loading level when compared to the other types (see Table 1).

The change in thermal response with an increase in wt % to 0.5% is seen in Figs. 10 and 11 for the same power level as before (7 W). The response is similar to that seen for the 0.25 wt % in Figs. 7 and 8. The primary change is that now the ribbon and the platelet GNF/PCM mixtures exhibit more complete melting. Both the platelet and ribbon fiber mixtures exhibit melting at the top thermocouple at roughly 325 min and both delay steady state as compared to the pure PCM. The ribbon fibers show an overshoot in the final steady-state temperature of the top thermocouple, which is corrected once complete mixing occurs. The heat is seen to conduct more efficiently with the slightly higher wt %. The thermal response of the herringbone GNF/PCM mixture is very similar to that seen with the 0.25 wt % loading albeit with a slightly reduced steady-state temperature and a longer time to steady state due to more efficient heat conduction. Once again, although complete melting was not achieved, the herringbone fibers again spread the heat most effectively in the sold phase, reducing the temperature gradients throughout the module.

The change in thermal response with a further increase in wt % to 1.0% is seen in Figs. 12 and 13 for the same power level as before (7 W). The primary change in the physical response is seen in Fig. 13 where it is clear that all of the 1% GNF/PCM mixtures feature both melting of the entire mass, a delay to steady state and a slightly reduced steady-state temperature when compared to the pure PCM. The herringbone and platelet GNF/PCM mixtures delayed time to steady state by about 100 min and the ribbon mixture by about 350 min. The 1% ribbon GNF/PCM mixture delayed steady state by 350 min, slightly longer than with 0.5% loading, but only achieved a 4 °C reduction in the steady-state temperature at the top thermocouple, while the 0.5% loading featured a 9 °C reduction. These results are related to the complex interactions of fiber loading, viscosity in the liquid phase, and the establishment of Rayleigh–Benard convection. It appears that the increased viscosity due to the higher fiber loadings acts to suppress the motion of the liquid and the establishment of Rayleigh–Benard convection. This is particularly seen at this loading level with the ribbon fibers. The thermal response of the bottom ther-

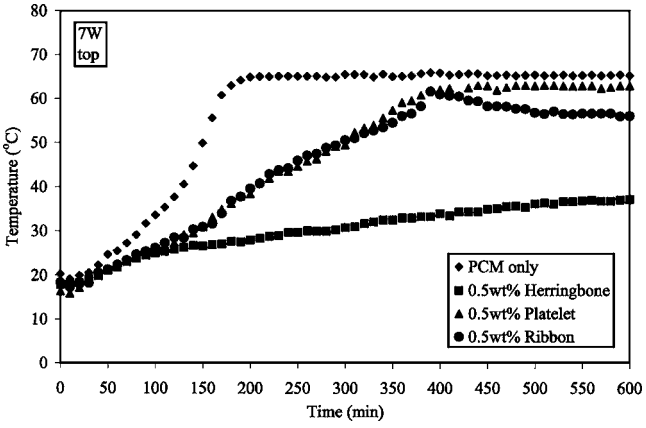

Fig. 11 Transient response of the top thermocouple for the 0.5% PCM/GNF module with 7 W applied power

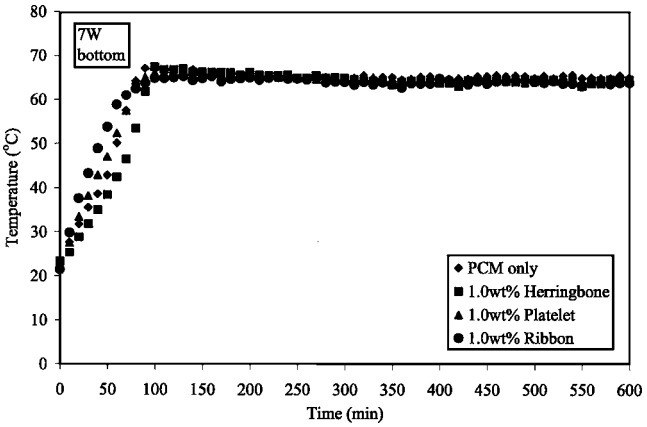

Fig. 12 Transient response of the bottom thermocouple for the 1.0% GNF/PCM module with 7 W applied power

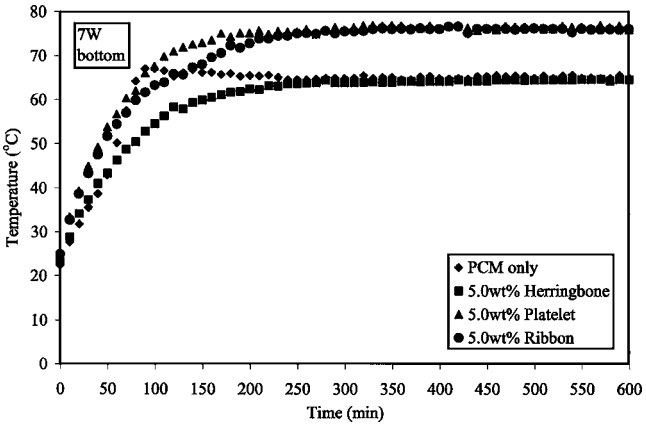

Fig. 14 Transient response of the bottom thermocouple for the 5.0% PCM/GNF module with 7 W applied power

mocouple (Fig. 12) shows that the ribbon GNF/CM mixture heats up much faster in both the solid and liquid phases than the pure PCM. This is different than the results seen for the 0.25% and 0.5%, which showed a change in slope as the material transitioned to liquid. In this case, convection is suppressed, the heat transfer to the solid layer above is reduced, and the more viscous mixture continues to heat up rapidly at the module bottom. With the suppression of convection in the liquid layer below, the solid layer above now heats up more slowly, as seen in Fig. 13 for the ribbon fibers.

With an even further increase in fiber loading levels to 5 wt %, the effects of suppressed convection become more significant and expand to the platelet mixture. The bottom thermocouple's response to 7 W of power is shown in Fig. 14 while the top thermocouple's response is shown in Fig. 15. The ribbon and platelet GNF/PCM mixtures now exhibit temperatures higher than that of even the pure PCM with a steady-state temperature 12°C above that of the pure PCM. However, the herringbone GNF/PCM mixture has the most uniform temperature gradient throughout the module of any case examined to date.

The high fiber loading levels improved conduction in the solid phase and the viscous liquid phase, leading to overheating of the bottom liquid layer for the platelet and ribbon cases. However, because Rayleigh–Benard convection was not established, the built-up heat in the viscous liquid layer failed to penetrate as effectively as before into the solid PCM above. Therefore, the module exhibits the highest temperatures of any case near the bottom and the lowest near the top, leading to the highest temperature gradients and least effective thermal performance. These results indicate that there may be a fiber loading level that will allow for optimized performance, which would feature improved thermal spreading throughout the PCM, a delay to steady state, complete melting of the PCM, a reduced base temperature, and a reduction in overall module steady-state temperature.

To examine the possibility of an optimal fiber loading point, the herringbone GNF/PCM was examined with increasing weight percentages. The herringbone fiber style was selected because of its strong performance in reducing thermal gradients in the previous studies. Starting with the 1% mixture, herringbone fibers were added to increase the weight percentage in increments of 0.25%. It was found that a 3.75% herringbone GNF/PCM mixture improved heat penetration throughout the PCM, delayed the onset of steady state of the module, and reduced the overall steady-state temperature of the module (Fig. 16). The steady-state temperature in this case occurred at the melting point of the PCM. Steady state at the melt points leads to increased temporal effectiveness of the PCM as it remains in thermal equilibrium at the melting/solidifcation interface. This finding shows that GNF can be used to effectively enhance PCMs and improve their transient thermal abatement characteristics, but that their effect is complex and higher fiber loading levels do not necessarily lead to improved thermal characteristics.

Conclusions

The low thermal conductivity of PCMs limits their effectiveness in the transient thermal management of larger volume sys-

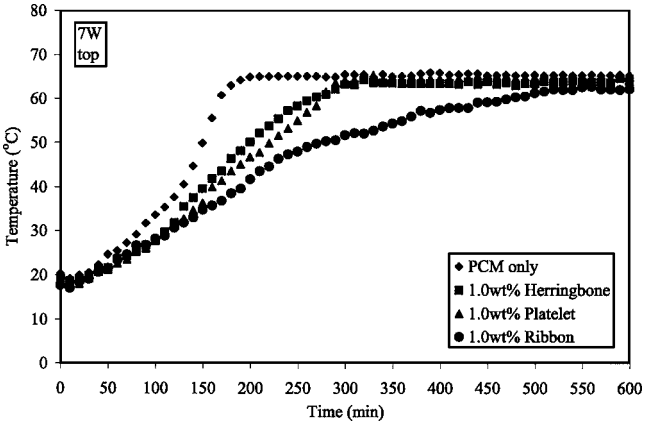

Fig. 13 Transient response of the top thermocouple for the 1.0% GNF/PCM module with 7 W applied power

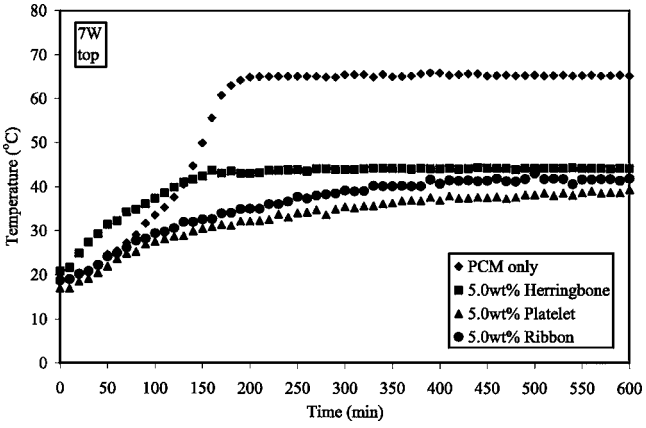

Fig. 15 Transient response of the top thermocouple for the 5.0% PCM/GNF module with 7 W applied power

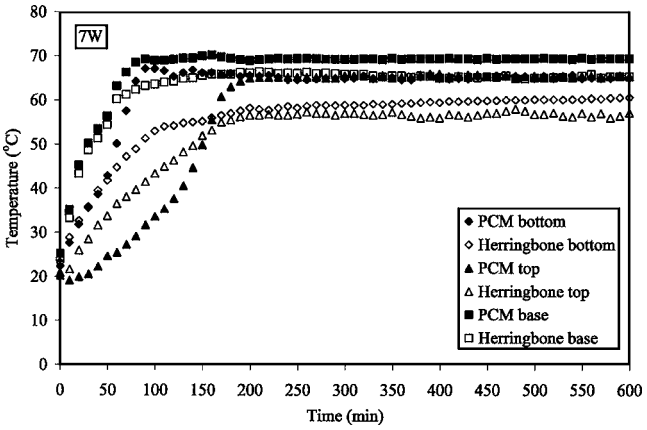

Fig. 16 Transient response of the pure PCM and a 3.75% herringbone GNF/PCM mixture with 7 W applied power

tems by creating large thermal differences throughout the PCM. To improve the performance of a paraffin PCM, GNFs were embedded into the PCM. Under the properly selected conditions, the GNFs were able to delay steady state, reduce thermal differences throughout the PCM, improve the thermal response close to the heat source, and lower the source temperature.

Even at low fiber loading levels, the GNF/PCM mixtures were able to more effectively conduct heat and delay steady state, but a significant portion of the PCM did not undergo phase change and hence the large latent heat of melting available in the PCM for transient thermal management was not fully utilized.

Thermal performance was found to be fiber style dependent. As the GNF weight percentage increased, initially the thermal response improved, but at significantly high GNF loadings, Rayleigh–Benard convection is suppressed and the PCM becomes overheated near the heat source. An optimal fiber loading level was found to prevent overheating, delay steady state, and reduce steady-state temperature.

Acknowledgment

We would like to gratefully acknowledge the support of the Office of Naval Research (ONR), which supported this project under Grant No. N00014-05-1-0863. This material is also based upon work supported by the National Science Foundation (NSF) under Grant No. 0416040. Any opinion, finding, and conclusions or recommendations expressed in this material are those of the authors and do not necessarily reflect the views of ONR or the NSF. We would also like to acknowledge G. F. Jones, whose comments on the work were valuable to us.

References

[1] Hodes, M., Weinstein, R. D., Pence, S. J., Piccini, J. M., Manzione, L., and Chen, C., 2002, "Transient Thermal Management of a Handset Using Phase Change Material (PCM)," ASME J. Electron. Packag., **124**, pp. 419–426.

[2] Yoo, D. W., and Joshi, Y. K., 2001, "Smart Thermal Management Systems Based on Solid Liquid Phase Change Materials (PCM)," *Proceedings of Interpack'01, The Pacific Rim/ASME International Electronic Packaging Technical Conference and Exhibition*, Kaui, HI, Paper No. IPACK2001-15506, pp. 601–607.

[3] Pal, D., and Joshi, Y., 1996, "Application of Phase Change Materials for Passive Thermal Control of Plastic Quad Flat Packages: A Computational Study," Numer. Heat Transfer, Part A, **30**, pp. 19–34.

[4] Evans, A. G., He, M. Y., Hutchinson, J. W., and Shaw, M., 2001, "Temperature Distribution in Advanced Power Electronics Systems and the Effect of Phase Change Materials on Temperature Suppression During Power Pulses," ASME J. Electron. Packag., **123**, pp. 211–217.

[5] Fleischer, A. S., Weinstein, R. D., and Kopec, T., 2006, "Analysis of Transient Thermal Management Characteristics of PCM With an Embedded Carbon Fiber Heat Sink," Itherm Conference, San Diego, CA.

[6] Weinstein, R. D., Hodes, M., and Piccini, J. M., 2001, "Improved Static and Thermal Management of Handsets Using Heat Spreaders and Phase Change Materials (PCMS)," *ASME Proceedings of the 35th National Heat Transfer Conference*, Anaheim, CA.

[7] Vesligaj, M. J., and Amon, C. H., 1999, "Transient Thermal Management of Temperature Fluctuations During Time Varying Workloads on Portable Electronics," IEEE Trans. Compon. Packag. Technol., **22**, pp. 541–550.

[8] Marongiu, M. J., Berhe, M. K., Fallon, G. S., 2001, "Thermal Management of IC'S Using Heat Sinks Incorporating Phase Change Materials (PCM)," *International Conference on High-Density Interconnect and Systems Packaging*, pp. 60–65.

[9] Yoo, D., and Joshi, Y., 2002, "Energy Efficient Thermal Management of Electronic Components Using Solid-Liquid Phase Change Materials," *Proceedings of the InterSociety Conference on Thermal Phenomena*, pp. 800–807.

[10] Alawadhi, E. M., and Amon, C. H., 2002, "Thermal Analysis of a PCM Thermal Control Unit for Portable Electronic Devices: Experimental and Numerical Studies," *Proceedings of the InterSociety Conference on Thermal Phenomena*, pp. 466–475.

[11] Leoni, N., and Amon, C. H., 1997, "Transient Thermal Design of Wearable Computers With Embedded Electronics Using Phase Change Materials," *ASME Proceedings of the 32nd National Heat Transfer Conference*, Baltimore, MD, Aug. 8–12, ASME HTD Vol. 343, Vol. 5, pp. 49–56.

[12] Egan, E., and Amon, C. H., 2000, "Thermal Management Strategies for Embedded Electronic Components of Wearable Computers," ASME J. Electron. Packag., **122**, pp. 98–106.

[13] Pal, D., and Joshi, Y. K., 1997, "Application of Phase Change Materials to Thermal Control of Electronic Modules: A Computational Study," ASME J. Electron. Packag., **119**, pp. 40–50.

[14] Krishnan, S., Garimella, S. V., and Kang, S. S., 2005, "A Novel Hybrid Heat Sink Using Phase Change Material for Transient Thermal Management of Electronics," IEEE Trans. Compon. Packag. Technol., **28**, pp. 281–289.

[15] Baker, K. W., Jang, J. H., and Yu, J. S., 1995, "Thermal Control of Phase Change Package with Periodic Pulse Heating—a Case Study," *Proceedings of ASME/JSME Joint Thermal Engineering Conference*, Vol. 4, pp. 463–469.

[16] Leland, J. M., 2002, "Numerical Optimization of a Phase Change Heat Sink," MS Thesis, Portland State University.

[17] Alawadhi, E. M., and Amon, C. H., 2000, "Performance Analysis of an Enhanced PCM Thermal Control Unit," *Proceedings of the 2000 InterSociety Conference on Thermal Phenomena*, pp. 283–289.

[18] Leland, J., and Recktenwald, G., 2003 "Optimization of a Phase Change Heat Sink for Extreme Environments," *Proceedings of the 19th IEEE SEMI-THERM (Semiconductor Thermal Measurement and Management Symposium*, San Jose, CA, Mar. 11–13.

[19] Marongiu, M. J., Berhe, M. K., Fallon, G. S., Solomon, K. H., and Trinh, D., 1999, "Thermal Management of IC'S and Microprocessor Using Heat Sinks (Pin Fin and Channel) Incorporating Phase Change Materials (PCM) for Transient Operation," *Proceedings of the 1999 International Symposium in Microelectronics*, Chicago, IL, pp. 789–794.

[20] Krishnan, S., Murthy, J. Y., and Garimella, S. V., 2004, "A Two-Temperature Model for the Analysis of Passive Thermal Control Systems," ASME J. Heat Transfer, **126**, pp. 628–637.

[21] Krishnan, S., and Garimella, S., 2003, "Thermal Analysis of Transient Power Spikes in Electronics—Phase Change Energy Storage Or Copper Heat Sinks?" *Proceedings of the 2003 International Electonic Packaging Technical Conference and Exhibition*, Paper No. IPACK2003-35169, pp. 1–12.

[22] Alawadhi, E. M., and Amon, C. H., 2003, "PCM Thermal Control Unit for Portable Electronic Devices: Experimental and Numerical Studies," IEEE Trans. Compon. Packag. Technol., **26**, pp. 116–125.

[23] Hasnain, S. M., 1998, "Review of Sustainable Thermal Energy Storage Technologies, Part I: Heat Storage Materials and Techniques," Energy Convers. Manage., **39**, pp. 1127–1138.

[24] Kuriger, R. J., Alam, M. K., and Jacobson, R. L., 2001, "Transport Properties of Vapor Grown Carbon Nanofiber Composites," *Proceedings of the 35th ASME National Heat Transfer Conference*, pp. 1901–1906.

[25] Bessel, C. A., Laubernds, K., Rodriguez, N. M., Baker, R., and Terry, K., 2001, "Graphite Nanofibers as an Electrode for Fuel Cell Applications," J. Phys. Chem., **105**, pp. 1115–1118.

[26] Py, X., Olives, R., and Mauran, S., 2001, "Paraffin/Porous-Graphite-Matrix Composite as a High and Constant Power Thermal Storage Material," Int. J. Heat Mass Transfer, **44**, pp. 2727–2737.

[27] Elgfy, A., and Lafdi, K., 2005, "Effect of Carbon Nanofiber Additives on Thermal Behavior of Phase Change Materials," Carbon, **43**, pp. 3067–3074.

Effect of Brownian Motion on Thermal Conductivity of Nanofluids

Ratnesh K. Shukla

Vijay K. Dhir
e-mail: vdhir@seas.ucla.edu

Mechanical and Aerospace Engineering Department,
Henry Samueli School of Engineering and Applied Science,
University of California,
Los Angeles, CA 90095

Nanofluids, i.e., liquids containing nanometer sized metallic or nonmetallic solid particles, show an increase in thermal conductivity compared to that of the pure liquid. In this paper, a simple model for predicting thermal conductivity of nanofluids based on Brownian motion of nanoparticles in the liquid is developed. A general expression for the effective thermal conductivity of a colloidal suspension is derived by using ensemble averaging under the assumption of small departures from equilibrium and the presence of pairwise additive interaction potential between the nanoparticles. The resulting expression for thermal conductivity enhancement is applied to the nanofluids with a polar base fluid, such as water or ethylene glycol, by assuming an effective double layer repulsive potential between pairs of nanoparticles. It is shown that the model predicts a particle size and temperature dependent thermal conductivity enhancement. The results of the calculation are compared with the experimental data for various nanofluids containing metallic and nonmetallic nanoparticles. [DOI: 10.1115/1.2818768]

Keywords: nanofluid, Brownian motion, thermal conductivity

1 Introduction

Nanofluids are liquids which contain nanometer sized metallic or nonmetallic particles suspended in them. Compared to ordinary fluids containing microsized particles, nanofluids are more stable, do not clog flow channels, and also show a considerable increase in thermal conductivity for very small volume fraction of solid particles [1–8]. Due to their improved heat transfer characteristics, nanofluids have potential application in many heat transfer areas. Conventional theories employing continuum models underpredict the relative increase in thermal conductivity obtained by addition of nanoparticles. This failure has been attributed to the lack of particle size as a parameter in the continuum models and as a consequence, other possible mechanisms, namely, Brownian motion, clustering of nanoparticles liquid layering close to nanoparticles, and nature of heat transport in nanoparticles, have been suggested [9–11]. Recent experiments [6,7] have established the importance of Brownian motion as the dominant mechanism behind the enhanced thermal conductivity of nanofluids. It has been found that smaller nanoparticles contribute more to thermal conductivity at elevated temperatures.

Various models focusing on either Brownian motion or liquid layering as the dominant mechanism have been proposed in the literature. Jang and Choi [12] analyzed Brownian motion of nanoparticles as a possible mechanism for explanation of high thermal conductivity of nanofluids and developed a model based on the assumption that ordered layers of liquid atoms close to the nanoparticle surface act as a hydrodynamic boundary layer. Unlike conventional Hamilton–Crosser model [13], their model was able to predict a particle size and temperature dependent thermal conductivity of nanofluids. However, their assumption of this hydrodynamic boundary layer being 3 atomic diameters thick seems highly unrealistic. Bhattacharya et al. [14] used Brownian dynamics simulation to calculate the thermal conductivity of nanofluids. Two unknown parameters in the potential function between two nanoparticles were chosen to reproduce two experimental data points for thermal conductivity of a given nanofluid system. Using this empirical potential, good agreement was reported between calculated and experimental values of thermal conductivity. Xuan et al. [15] developed a theoretical model for predicting thermal conductivity of nanofluids by taking into account physical properties of both fluid and solid nanoparticle and the structure of nanoparticle clusters. Xue [16] developed a theoretical model based on Maxwell and average polarization theory for predicting thermal conductivities of nanofluids by taking into account the presence of a thin liquid layer around nanoparticles. The thermal conductivity of the liquid layer was assumed to be higher than the thermal conductivity of the bulk liquid. Good agreement with the experimental data was reported for nanotube/oil and alumina/water mixtures; however, the choice of thickness and thermal conductivity of the liquid layer remained empirical. Xue et al. [17] used molecular dynamics simulations to analyze the effect of liquid layering on thermal conductivity of a thin liquid film confined between solid walls. Wang et al. [18] developed a theoretical model for estimating thermal conductivity of nanofluids based on effective medium approximation and fractal theory for the description of a nanoparticle cluster and its radial distribution. Kumar et al. [19] developed a model based on kinetic theory, which assumes an unrealistic mean free path of 0.01 m for nanoparticles in liquid. Prasher et al. [20,21] modeled the effect of Brownian motion through a convective heat transfer coefficient for flow around a sphere. However, use of such an approach involving macrorelations at length scales of 10–20 nm is difficult to justify. Recently, Wang et al. [22] emphasized the role played by interparticle potential in the enhanced heat transfer in nanofluids. Vadasz [23] suggested transient heat conduction process as one of the possible reasons behind the experimentally observed increased thermal conductivity of nanofluids. Xuan and Li [24] reported an increase in the convective heat transfer coefficient of copper/water nanofluid suspension when compared to that of water at the same Reynolds number. The importance of Brownian diffusion and thermophoresis as the primary slip mechanisms in nanofluids was highlighted in Ref. 25 through a detailed analysis of the convective heat transfer coefficient enhancement.

In the past, a significant research effort has gone into analyzing the effect of Brownian motion on viscosity and diffusion coefficient of a suspension (see Refs. 26 and 27). In comparison, how-

Contributed by the Heat Transfer Division of ASME for publication in the JOURNAL OF HEAT TRANSFER. Manuscript received December 13, 2006; final manuscript received May 1, 2007; published online March 18, 2008. Review conducted by Ranga Pitchumani.

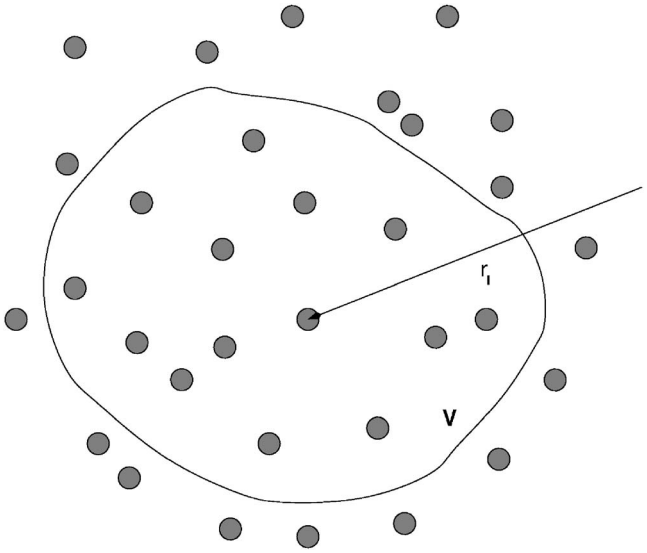

Fig. 1 Schematic showing coordinate system for *N* identical spheres in a volume *V*

ever, there is limited work on the study of thermal conductivity of colloidal nanofluid suspensions. Our objective in this work is to deduce macroscale thermal conductivity from the nanofluid suspension microstructure and to accomplish this, we employ appropriate averaging techniques and determine the suspension thermal conductivity as a function of nanoparticle characteristics (size, volume fraction, interparticle potential) and liquid properties (viscosity, temperature).

This paper is organized as follows. The details of the model along with elaborate theoretical analysis of the effect of Brownian motion on thermal conductivity of nanofluids using a microscopic approach similar to Refs. 28 and 29 for motion of particles in the presence of temperature gradients are described in Secs. 2 and 3. In Sec. 4, an expression for the effective thermal conductivity enhancement of a nanofluid is derived in terms of various particle characteristics and fluid properties. Detailed comparison between theoretical predictions and the available experimental data is made in Sec. 5. Conclusions and future work are then discussed.

2 Model

In the model, we assume a nanofluid to be comprised of monodispersed spherical nanoparticles of radius a and thermal conductivity λ_p, suspended in a liquid of thermal conductivity λ_f. The liquid medium is assumed to be of infinite extent with a mean temperature $T(\mathbf{r})$, where $\mathbf{r}$ denotes position in the medium, and an average temperature gradient $\mathbf{G}$, which is given by

$$\mathbf{G} = \lim_{V\to\infty} \frac{1}{V}\int_V \nabla T dV = \frac{\int \nabla T(\mathbf{r}) d\mathbf{r}}{\int d\mathbf{r}} \tag{1}$$

The volume V is assumed to be a very large volume consisting of N nanoparticles, which are determined by their positions $\mathbf{r}_i$ and velocities $\mathbf{u}_i$ with $i=1,\ldots,N$, as shown in Fig. 1. The volume fraction of the nanoparticles ϕ is related to the number density n through their radius a as $\phi=\frac{4}{3}\pi n a^3$, where $n=N/V$. The resulting average heat flux $\mathbf{F}$ in the system due to the presence of temperature gradient is given by

$$\mathbf{F} = \lim_{V\to\infty} \frac{1}{V}\int_V \mathbf{J} dV \tag{2}$$

where $\mathbf{J}(\mathbf{r})$ is the heat flux at position $\mathbf{r}$. This expression is converted into an integral over the volume occupied by spherical nanoparticles V_p and the remaining liquid volume $V-V_p$ [30,31] as

$$\mathbf{F} = \lim_{V\to\infty} \frac{1}{V}\left(\int_{V_p} \mathbf{J}_p dV + \int_{V-V_p} \mathbf{J}_f dV\right) \tag{3}$$

For the heat flux in the liquid $\mathbf{J}_f$, we use regular Fourier's law to obtain

$$\mathbf{J}_f(\mathbf{r}) = -\lambda_f \nabla T(\mathbf{r}) \tag{4}$$

The expression for the heat flux inside the spherical nanoparticle is modified in order to account for both conduction through the solid, which is modeled using Fourier's law, and a Brownian motion contribution. Thus, we have the following expression [32,33]:

$$\mathbf{J}_p(r) = -\lambda_p \nabla T(\mathbf{r}) + \mathcal{U}(\mathbf{r})\mathbf{u}(\mathbf{r}) \tag{5}$$

The first term in the above expression corresponds to the contribution due to the intrinsic thermal conductivity of nanoparticles, whereas the second accounts for the contribution from their motion. The contribution from the Brownian motion of the nanoparticle stationed at $\mathbf{r}$ and having energy $\mathcal{U}(\mathbf{r})$ and velocity $\mathbf{u}(\mathbf{r})$ is specified through the flux of energy density, $\mathcal{U}(\mathbf{r})\mathbf{u}(\mathbf{r})$, convected by it. With the above expressions for local heat flux, we obtain the following for the average heat flux in the system:

$$\mathbf{F} = -\lambda_f \mathbf{G} + \lim_{V\to\infty} \frac{1}{V}\int_{V_p} (\lambda_f - \lambda_p) \nabla T dV + \lim_{V\to\infty} \frac{1}{V}\int_{V_p} \mathcal{U}\mathbf{u} dV \tag{6}$$

In the above expression, the first two terms represent macroscopic contribution to the average heat flux simply due to the presence of higher thermal conductivity nanoparticles, whereas the third term represents the contribution due to Brownian motion of nanoparticles. In the present work, we are concerned with dilute nanofluid suspensions so that the volume fraction of nanoparticles $\phi \ll 1$ and contributions of $O(\phi^2)$ or higher to thermal conductivity are ignored. Various models have been developed in the literature for calculation of macroscopic contribution and we choose Hamilton–Crosser model [13] due to its wide range of applicability with which the expression for the average heat flux becomes

$$\mathbf{F} = \mathbf{F}_M + \mathbf{F}_B$$

$$\mathbf{F}_M = -\lambda_f \left\{ \frac{\lambda_p + 2\lambda_f + 2\phi(\lambda_p - \lambda_f)}{\lambda_p + 2\lambda_f - \phi(\lambda_p - \lambda_f)} \right\} \mathbf{G}$$

$$\mathbf{F}_B = \lim_{V\to\infty} \frac{1}{V}\int_{V_p} \mathcal{U}\mathbf{u} dV \tag{7}$$

where $\mathbf{F}_M$ represents macroscopic contribution (given by Hamilton–Crosser model) and $\mathbf{F}_B$ represents contribution from Brownian motion.

3 Brownian Motion in Presence of Temperature Gradient

Before we can make further progress in identifying the heat flux due to Brownian motion $\mathbf{F}_B$, we need to find an expression relating $\mathbf{u}(\mathbf{r})$ to the local temperature gradient $\nabla T(\mathbf{r})$. Dhont [28,29] presented a general framework for theoretical analysis of motion of a Brownian particle in the presence of small temperature gradients using a statistical and microscopic approach, respectively. In the present work, we use the same approach and assume that the particles interact with each other through a direct pair poten-

tial, $\Psi(r_{ij}|T)$, and through hydrodynamic interactions, which are assumed to be given by the Stokes flow response of the solvent fluid to the motion of the suspended nanoparticles in the limit of zero inertia. Note that the dependence of the interparticle potential on temperature, which is usually observed in studies on colloids [26], is also accounted for in the model. The microstructure of the nanofluid suspension is specified by the function $P_N^{(N)}(\mathbf{r}^N)$, which gives the probability of finding spheres centered simultaneously at $\mathbf{r}^N=(\mathbf{r}_1,\ldots,\mathbf{r}_N)$. The translational velocity $\mathbf{u}_i$ of the nanoparticle i is then related to the forces $\mathbf{f}_j^h$ that the fluid exerts on the spheres j as

$$\mathbf{u}_i = -\frac{1}{6\pi\mu a}\sum_{j=1}^{N}\mathbf{M}_{ij}\mathbf{f}_j^h \tag{8}$$

$\mathbf{M}_{ij}$ in the above expression represents elements of the generalized friction tensor, which determines the force on the nanoparticle i at $\mathbf{r}_i$ due to nanoparticle j centered at $\mathbf{r}_j$. Thus, the fact that a moving sphere induces a flow field in the solvent which in turn affects the motion of other particles is accounted for. In the present analysis, we assume that the nanoparticles are well separated and move independently so that the hydrodynamic interactions amongst particles are negligible. With this assumption, there is no coupling between $\mathbf{u}_i$ and $\mathbf{f}_j^h$ for $i\neq j$, and Stokes law holds for each nanoparticle

$$\mathbf{f}_i^h = -6\pi\mu a\mathbf{u}_i \tag{9}$$

A force balance on each spherical nanoparticle implies an equilibrium between the hydrodynamic force $\mathbf{f}_i^h$, interaction force $\mathbf{f}_i^I$ from the potential between nanoparticles, and the Brownian force $\mathbf{f}_i^B$ which when combined with Eq. (9) yields

$$\mathbf{u}_i = -\frac{1}{6\pi\mu a}\mathbf{f}_i^h = \frac{1}{6\pi\mu a}(\mathbf{f}_i^I + \mathbf{f}_i^B) \tag{10}$$

Following Ref. [29], we assume small temperature gradients so that the local temperature can be expanded as

$$T\left(\frac{\mathbf{r}_i+\mathbf{r}_j}{2}\right) = T(\mathbf{r}_i) + \frac{1}{2}\mathbf{r}_{ij}\cdot\boldsymbol{\nabla}_i T(\mathbf{r}_i) \tag{11}$$

Assuming small local deviations $\delta T(\mathbf{r})=T(\mathbf{r})-T$ from the mean temperature T, the interaction force is given by

$$\begin{aligned}\mathbf{f}_i^I &= -\boldsymbol{\nabla}_i\sum_{j\neq i}\Psi(r_{ji}|T)\\ &= -\sum_{j\neq i}\boldsymbol{\nabla}_i\Psi(r_{ji}|T) - \sum_{j\neq i}\left\{\delta T(\mathbf{r}_i) + \frac{1}{2}\mathbf{r}_{ji}\cdot\boldsymbol{\nabla}_i T(\mathbf{r}_i)\right\}\frac{\partial}{\partial T}\boldsymbol{\nabla}_i\Psi(r_{ji}|T)\end{aligned} \tag{12}$$

where $\Psi(r_{ij}|T)$ is the interparticle potential assumed to be pairwise additive. In a similar way, it follows that, to leading order in deviations of temperature $\delta T(\mathbf{r})$, the Brownian force is given by

$$\mathbf{f}_i^B = -k_B T(\mathbf{r}_i)\boldsymbol{\nabla}_i\ln\{P_N^{(N)}(\mathbf{r}^N)T(\mathbf{r}_i)\} \tag{13}$$

Substitution of Eqs. (12) and (13) into Eq. (10) gives the expression for velocity of nanoparticle i in the presence of temperature gradient as

$$\begin{aligned}\mathbf{u}_i = -\frac{1}{\gamma}\Bigg\{&\sum_{j\neq i}\boldsymbol{\nabla}_i\Psi(r_{ji}|T) + \sum_{j\neq i}\Bigg(\delta T(\mathbf{r}_i)\\ &+\frac{1}{2}\mathbf{r}_{ji}\cdot\boldsymbol{\nabla}_i T(\mathbf{r}_i)\Bigg)\frac{\partial}{\partial T}\boldsymbol{\nabla}_i\Psi(r_{ji}|T) + k_B T(\mathbf{r}_i)\boldsymbol{\nabla}_i\ln(P_N^{(N)}(\mathbf{r}^N)T(\mathbf{r}_i))\Bigg\}\end{aligned} \tag{14}$$

where $\gamma=6\pi\mu a$. More detailed derivation of these results can be found in Ref. [29], where analytical expressions for the diffusion and thermodiffusion coefficient have also been derived.

4 Effective Thermal Conductivity of a Nanofluid Suspension

It follows from Eq. (14) that the velocity of the nanoparticle, in the presence of small temperature gradient, comprises of a hydrodynamic part and a potential interaction term. From Eq. (7), the Brownian contribution to the average heat flux is given by

$$\mathbf{F}_B = \lim_{V\to\infty}\frac{1}{V}\int_{V_p}\mathcal{U}\mathbf{u}dV = \frac{1}{V}\sum_{i=1}^{N}\int_{V_i}\mathcal{U}\mathbf{u}dV \tag{15}$$

where V_i denotes the volume of a nanoparticle with center at $\mathbf{r}_i$. Assuming ergodicity, the summation in Eq. (15) over a large number of identical particles in volume V is equivalent to N times an average of $\mathcal{U}\mathbf{u}$ over all configurations of the surrounding particles. Thus, we have

$$\mathbf{F}_B = \frac{1}{V}\sum_{i=1}^{N}\int_{V_i}\mathcal{U}\mathbf{u}dV = \int\left(\sum_{i=1}^{N}\mathcal{U}_i\mathbf{u}_i\right)P_N^{(N)}(\mathbf{r}^N)d\mathbf{r}^N \tag{16}$$

for the Brownian contribution to the average heat flux. In a similar way, the expression for average temperature gradient in the system, given by Eq. (1), is transformed into an integral over configuration $\mathbf{r}^N$ as

$$\mathbf{G} = \int\boldsymbol{\nabla}T(\mathbf{r})P_N^{(N)}(\mathbf{r}^N)d\mathbf{r}^N \tag{17}$$

The energy carried by the particle for a particular configuration $\mathbf{r}^N$ is given by the sum of its kinetic, internal, and potential energies as

$$E_i = \mathcal{U}_i V = \frac{1}{2}m|\mathbf{u}_i|^2 + \hat{C}T(\mathbf{r}_i) + \frac{1}{2}\sum_{j\neq i,j=1}^{N}\Psi(r_{ij}|T) \tag{18}$$

where $\hat{C}$ denotes the heat capacity of a single nanoparticle of mass m. Therefore, the expression for $\mathbf{F}_B$ reduces to

$$\begin{aligned}\mathbf{F}_B = \frac{1}{V}\int\Bigg\{&\sum_{i=1}^{N}\frac{1}{2}m|\mathbf{u}_i|^2\mathbf{u}_i + \hat{C}\sum_{i=1}^{N}T(\mathbf{r}_i)\mathbf{u}_i\\ &+\frac{1}{2}\sum_{i=1}^{N}\sum_{j=1,j\neq i}^{N}\Psi(r_{ij}|T)\mathbf{u}_i\Bigg\}P_N^{(N)}d\mathbf{r}^N\end{aligned} \tag{19}$$

Next, we split the net heat flux due to Brownian motion into a kinetic (hydrodynamic, when the generalized friction tensor $\mathbf{M}_{ij}$ accounts for the hydrodynamic interactions) part and an interaction part using Eq. (14) as shown below

$$\mathbf{F}_B^H = -\frac{k_B\hat{C}}{V\gamma}\int\sum_{i=1}^{N}\{T^2(\mathbf{r}_i)\boldsymbol{\nabla}_i\ln(T(\mathbf{r}_i)P_N^{(N)})\}P_N^{(N)}d\mathbf{r}^N$$

$$\begin{aligned}\mathbf{F}_B^I = \frac{\hat{C}}{V}\int\sum_{i=1}^{N}&\left\{T(\mathbf{r}_i)\left(\mathbf{u}_i + \frac{k_B T(\mathbf{r}_i)}{\gamma}\boldsymbol{\nabla}_i\ln(T(\mathbf{r}_i)P_N^{(N)})\right)\right\}P_N^{(N)}d\mathbf{r}^N\\ &+\frac{1}{2V}\int\left\{\sum_{i=1}^{N}\sum_{j\neq i}\Psi(r_{ij}|T)P_N^{(N)}\mathbf{u}_i\right\}d\mathbf{r}^N\end{aligned} \tag{20}$$

Note that the contribution of the kinetic energy term in Eq. (19) is neglected since it gives rise to terms that are of the order of $O(\boldsymbol{\nabla}_i T)^3$. In order to make further analytical progress, we evaluate the above expressions under the assumption that the nanoparticles are uniformly distributed in the liquid so that their number density is independent of the position in the liquid. This results in the following relationship:

$$P_N^{(1)}(\mathbf{r}) = \int P_N^N(\mathbf{r}^N) d\mathbf{r}^{N-1} \equiv \frac{1}{V} \tag{21}$$

Note that the inclusion of nanoparticle density variations within the liquid in the above analysis would yield Dufour coefficient. However, in the present work, we ignore density variations and obtain the following expression for the kinetic contribution to the heat flux:

$$\mathbf{F}_B^H = -\frac{k_B \hat{C}}{V\gamma} \int \sum_{i=1}^{N} T(\mathbf{r}_i) \nabla_i \{T(\mathbf{r}_i) P_N^{(N)}\} d\mathbf{r}^N \tag{22}$$

Evaluation of this expression to a first order in temperature gradient $\nabla T(\mathbf{r})$ yields

$$\mathbf{F}_B^H = -\frac{N k_B \hat{C} T}{V\gamma} \mathbf{G} = -\frac{n \hat{C} k_B T}{\gamma} \mathbf{G} \tag{23}$$

We note that the expression for thermal conductivity of an ideal gas derived using Boltzmann transport equation in the relaxation time approximation [34] is given by

$$\lambda_{\text{ideal}} = \frac{5 n k_B^2 T \tau_c}{m} \tag{24}$$

where τ_c is the relaxation time. Our final expression for kinetic contribution to the thermal conductivity enhancement, applicable in the limit of a very dilute noninteracting suspension of "colloidal gas," also has the same final form with a characteristic time $\tau_c = m/\gamma$ and particle specific heat capacity equal to k_B.

Next, we evaluate the contribution of the interaction terms to the average heat flux by taking into account all the binary particle pair interactions. The details of the calculations are presented in Appendix A and here, we only report the final expression

$$\mathbf{F}_B^I = \left\{ -\frac{\pi n^2 k_B}{\gamma} \left(\int_0^\infty r^2 g^{\text{eq}}(r) \Psi(r|T) dr \right) + \frac{\pi n^2 \hat{C} T}{\gamma} \left(\int_0^\infty r^3 g^{\text{eq}}(r) \frac{\partial^2 \Psi(r|T)}{\partial T \partial r} dr \right) + \frac{\pi n^2 \hat{C}}{\gamma k_B T} \left(\int_0^\infty r^3 g^{\text{eq}}(r) \Psi(r|T) \frac{\partial \Psi(r|T)}{\partial r} dr \right) \right\} \mathbf{G} \tag{25}$$

Hence, the expression for the average heat flux in the nanofluid suspension reduces to

$$\mathbf{F} = -\left\{ \lambda_f \left\{ \frac{\lambda_p + 2\lambda_f + 2\phi(\lambda_p - \lambda_f)}{\lambda_p + 2\lambda_f + 2\phi(\lambda_p - \lambda_f)} \right\} + \frac{n k_B \hat{C} T}{\gamma} + \frac{\pi n^2 k_B}{\gamma} \left(\int_0^\infty r^2 g^{\text{eq}}(r) \Psi(r|T) dr \right) - \frac{\pi n^2 \hat{C} T}{\gamma} \left(\int_0^\infty r^3 g^{\text{eq}}(r) \frac{\partial^2 \Psi(r|T)}{\partial T \partial r} dr \right) - \frac{\pi n^2 \hat{C}}{\gamma k_B T} \left(\int_0^\infty r^3 g^{\text{eq}}(r) \Psi(r|T) \frac{\partial \Psi(r|T)}{\partial r} dr \right) \right\} \mathbf{G} \tag{26}$$

From Eq. (26), we obtain the expression for the effective thermal conductivity enhancement of nanofluid as

$$\frac{\lambda_{\text{eff}}}{\lambda_f} = -\frac{\mathbf{F}}{\lambda_f \mathbf{G}} = \left\{ \frac{\lambda_p + 2\lambda_f + 2\phi(\lambda_p - \lambda_f)}{\lambda_p + 2\lambda_f - \phi(\lambda_p - \lambda_f)} \right\} + \frac{n k_B \hat{C} T}{\lambda_f \gamma} + \frac{\pi n^2 k_B}{\lambda_f \gamma} \left(\int_0^\infty r^2 g^{\text{eq}}(r) \Psi(r|T) dr \right) - \frac{\pi n^2 \hat{C} T}{\lambda_f \gamma} \left(\int_0^\infty r^3 g^{\text{eq}}(r) \frac{\partial^2 \Psi(r|T)}{\partial T \partial r} dr \right) - \frac{\pi n^2 \hat{C}}{\lambda_f \gamma k_B T} \left(\int_0^\infty r^3 g^{\text{eq}}(r) \Psi(r|T) \frac{\partial \Psi(r|T)}{\partial r} dr \right) \tag{27}$$

The function $g^{\text{eq}}(r)$ in the above expressions represents the local equilibrium pair distribution function, which determines the distribution of the neighboring nanoparticles surrounding a tagged nanoparticle. For large distances from a tagged nanoparticle or for very dilute suspension of nanoparticles, $g^{\text{eq}}(r)$ has a value close to 1. We also note that repulsive long range potentials give a positive contribution to the net effective thermal conductivity, whereas an attractive potential will actually lead to a negative contribution from interparticle potential term. Previous research [26,35] has revealed that the presence of repulsive potential stabilizes a colloidal suspension by preventing agglomeration. Hence, our current findings are consistent with this observation in the sense that stable nanofluid suspensions actually do show enhanced thermal conductivity.

5 Comparison With Experiments

An evaluation of the effective thermal conductivity enhancement in the nanofluid given by Eq. (27) requires prior knowledge of the interparticle potential between various nanoparticles. Unfortunately, to the best of our knowledge, the experiments concerning nanofluids have focused solely on the thermal conductivity measurements and not on the measurements of the interparticle potential. Nevertheless, previous investigations in colloidal science (see Refs. [26,35,36]) have established that the existence of a repulsive interparticle potential, electrostatic or steric, is essential in preventing flocculation and eventual gravitational settling in a colloidal suspension. In fact, an interface immersed in a polar solvent with high dielectric constant always gains some charge depending on the surface potential. The various charging mechanisms (such as specific ion adsorption, ionization of surface groups, etc.) are well described in Refs. [26,35,36]. The fact that alumina (corundum) particles do acquire positive charge in a neutral aqueous solution at pH 7 (with H^+ and OH^- as the potential determining ions) has been observed in the streaming potential measurements reported in Ref. [37]. The presence of a repulsive electrostatic potential between two alumina surfaces immersed in an aqueous solution was observed in Ref. [38]. Experimental studies on gold in aqueous solution, conducted in Ref. [39], revealed the role played by H^+ and OH^- ions in determining the interaction potential. Ionization of surface hydroxyl groups was identified as the primary mechanism behind the surface charge development in this study. Streaming potential measurements on gold films [40] provide additional support to the fact that pH controls the electric charge on a gold surface immersed in an aqueous solution. In addition to these studies, there is experimental evidence suggesting that the chemical and surface properties of liquids and nanoparticles play an important role in the thermal conductivity enhancement of nanofluids [3,7]. Bearing these facts in mind, we assume that the nanofluid is an electrostatically stabilized suspension in which the interparticle forces between various nanoparticles are sufficiently well described by the repulsive part of the Derjaguin, Landau, Verwey, and Overbeek (DLVO) potential [26].

This choice of potential prevents us from making meaningful comparisons with the experiments utilizing organic or oil based nanofluids, such as the gold/toluene nanofluid in Ref. [7]. Nevertheless, this is not a serious concern since majority of the experimental studies have focused on nanofluids with water and ethylene glycol as base liquids, which are both polar.

In order to model the interparticle interaction between various nanoparticles, we choose a specific form of the repulsive DLVO potential, which accounts for the electrostatic repulsion between charged spherical nanoparticles when the distance between centers of the spherical particles is comparable to the range of the potential. The potential is given by the following expression [26]:

$$\Psi(r|T) = \frac{1}{2}\epsilon a \psi_s^2 \ln\{1 + \exp(-\kappa_D(r-2a))\} \quad r > 2a \tag{28}$$

where ψ_s is the surface potential, ϵ is the permittivity of the liquid, and κ_D^{-1} is the Debye length, which determines the range of the potential. The surface potential ψ_s is related to the net effective charge on the nanoparticle surface through the following relationship:

$$\psi_s = \frac{Ze}{\epsilon(a + a^2\kappa_D)} \tag{29}$$

The overall charge electroneutrality condition leads to the following expression for the inverse Debye length [26]:

$$\kappa_D = \left(\frac{4\pi l_B(\rho_i + nZ)}{1-\phi}\right)^{1/2} \tag{30}$$

where ρ_i is the number density of ionic charge in the bulk liquid and nZ accounts for the contribution of charged nanoparticles through the number of counterions. The Bjerrum length l_B is defined as $l_B = e^2/(4\pi\epsilon k_B T)$. For water at room temperature, $l_B = 7$ Å. The factor $(1-\phi)$ accounts for the reduced volume of the liquid due to the presence of nanoparticles. As evident from Eq. (30), the nondimensional inverse Debye length $a\kappa_D$ depends on both the nanoparticle charge Ze and the nanoparticle number density n (or equivalently volume fraction ϕ).

The nanoparticle charge Ze is a critical parameter in the determination of the effective strength of the repulsive potential given by Eq. (28). The use of the potential given by Eq. (28) involves a priori assumption of small enough surface potential ψ_s and low ionic strengths so that the linearized Poisson–Boltzmann theory can be applied. In the case of highly charged nanoparticles, strong accumulation of counterions in the vicinity of nanoparticle surface leads to a significant reduction in the net effective charge on the nanoparticle. In such cases, it is postulated that the interparticle potential given by Eq. (28) can still be used provided the effective charge Ze is renormalized appropriately [41,42]. The basic premise behind this approach is that the combined system of nanoparticle and surrounding counterions can be effectively separated into two distinct zones: a spherical region encompassing the nanoparticle and strongly adsorbed counterions where nonlinear effects cannot be ignored, and a diffuse layer away from this spherical region where the linearized Poisson–Boltzmann theory can still be applied. The effective charge is generally an adjustable parameter in a fit of experimental data with analytical or computational models and cannot always be determined theoretically. In the following, we shall assume that Ze is an effective charge that is determined from a fit of the thermal conductivity data for nanofluids.

An estimation of the thermal conductivity enhancement of nanofluid through Eq. (27) requires knowledge of the equilibrium pair distribution function $g^{\text{eq}}(r)$. Following previous investigations [26,27,32], in our present work, we consider a simple approximation of $g^{\text{eq}}(r) = H(r-2a)$, where H represents the Heaviside step function, applicable in the limit of infinitely dilute colloidal systems. As demonstrated through the molecular dynamics simulations of a typical nanofluid, presented later in this section, this approximation is fairly reasonable in the present context of a dilute colloidal suspension. The approximation is especially attractive since it allows us to compute an explicit analytical expression for the net thermal conductivity enhancement in terms of other relevant parameters. We note that since moderate amount of clustering is observed in a nanofluid suspension, such an approximation will lead to a conservative estimate for the final thermal conductivity enhancement.

We use Eq. (27), along with the approximation $g^{\text{eq}}(r) = H(r-2a)$, to obtain the effective thermal conductivity of the nanofluid suspension as

$$\begin{aligned}\lambda_{\text{eff}} = \lambda_f &\left\{\frac{\lambda_p + 2\lambda_f + 2\phi(\lambda_p - \lambda_f)}{\lambda_p + 2\lambda_f - \phi(\lambda_p - \lambda_f)}\right\} + \phi\frac{\rho C k_B T}{\gamma} + \left\{\frac{n k_B^2 T}{\gamma}\right\} \\ &\times\left\{\frac{(1-\phi)Z}{8(1+(\rho_i/nZ))}\right\}\left\{\frac{3.29(a\kappa_D)^2 + 3.61 a\kappa_D + 1.89}{a\kappa_D(1+a\kappa_D)^2}\right\} \\ &+ \phi\left\{\frac{\rho C k_B T}{\gamma}\right\}\left\{\frac{(1-\phi)Z}{16(1+(\rho_i/nZ))}\right\} \\ &\times\left\{\frac{9.87(a\kappa_D)^2 + 21.64 a\kappa_D + 17.05}{a\kappa_D(1+a\kappa_D)^2}\right\} + \left\{\frac{\rho C k_B T}{\gamma}\right\} \\ &\times\left\{\frac{(1-\phi)^2 Z^2}{48(1+(\rho_i/nZ))^2}\right\} \\ &\times\left\{\frac{1.92(a\kappa_D)^4 + 1.80(a\kappa_D)^3 + 1.05(a\kappa_D)^2 + 0.29 a\kappa_D}{(1+a\kappa_D)^4}\right\}\end{aligned} \tag{31}$$

where ρ and C denote the density and specific heat capacity of the solid, which makes up the nanoparticle, respectively. The heat capacity of a single nanoparticle is related to its specific heat capacity as $n\hat{C} = \phi\rho C$. The first term in Eq. (31) represents contribution due to macroscopic Hamilton–Crosser model [13], the second, the contribution from the kinetic part of the Brownian motion, and the remaining three terms represent contributions from the two-body interactions between various nanoparticles. The particle size and temperature dependence of the effective thermal conductivity are accounted for in the model explicitly through the parameters γ and $k_B T$ and implicitly through $a\kappa_D$. Since the viscosity of the liquids used in the thermal conductivity experiments decreases with rising temperature, in the range of interest, the model predicts an increased contribution of the Brownian motion to the net thermal conductivity enhancement with rising liquid temperature and decreasing particle size.

In order to get an estimate on the individual contribution of each of the last four terms corresponding to the Brownian motion in Eq. (31), we consider a typical nanofluid system containing 10 nm sized nanoparticles at a volume fraction of $\phi = 0.01$ in water at a temperature of 300 K. Assuming that the solid which makes up the nanoparticles has $\rho C \approx 3 \times 10^6$ J/m^3 K, we obtain the following:

$$\phi\frac{\rho C k_B T}{\gamma} = 1.32 \times 10^{-6} \quad \text{and} \quad \frac{n k_B^2 T}{\gamma} = 1.45 \times 10^{-13} \tag{32}$$

These numerical values clearly demonstrate that the kinetic contribution to the effective thermal conductivity remains negligible for practical nanofluids ($\lambda_f = 0.611$ W/m K for water at 300 K). This result is consistent with the previous study of Ref. [9] where a dimensional analysis revealed that a noninteracting nanoparticle, acted on by Brownian forces alone, moves much slower than heat. However, the last two terms in Eq. (31) can give significant contributions to the effective thermal conductivity when $10^2 < |Z| < 10^3$; these values of effective charge are typically observed in experimental studies of charge stabilized colloidal systems [43–46].

Having successfully made reasonable qualitative comparisons with some general observations from the experiments concerning nanofluids, we now proceed to make quantitative comparisons with the available data in the literature. Note that the value of the solid nanoparticle thermal conductivity λ_p appearing in Eq. (31) should be chosen such that it accounts for the reduced size effects that are important when the size of the nanoparticle is of the order of the phonon mean free path length in the solid. In addition, the expression for contribution from macroscopic part should also account for the finite interfacial thermal resistance between solid nanoparticle surface and the liquid, which, in general, will be a function of bonding between the nanoparticle surface and the liquid molecules [47–49]. In the presence of an interface thermal resistance, the expression for thermal conductivity enhancement resulting from the macroscopic theory takes the following modified form [50] (when compared with Eq. (7)):

$$\frac{\lambda_{\text{eff}}^{M}}{\lambda_f} = -\frac{\mathbf{F}_M}{\mathbf{G}} = \frac{((1/\lambda_f)+(2/\lambda_p)+(2/a\sigma_b))+2\phi((1/\lambda_f)-(1/\lambda_p)-(1/a\sigma_b))}{((1/\lambda_f)+(2/\lambda_f)+(2/a\sigma_{BD}))-\phi((1/\lambda_f)-(1/\lambda_p)-(1/a\sigma_b))} \tag{33}$$

where λ_{eff}^{M} represents macroscopic contribution to the effective thermal conductivity and σ_b denotes the interfacial conductance at the nanoparticle-liquid boundary. If we further assume $\lambda_p \gg \lambda_f$, the above expression simplifies to the following:

$$\frac{\lambda_{\text{eff}}^{M}}{\lambda_f} = \frac{(a\sigma_b+2\lambda_f)+2\phi(a\sigma_b-\lambda_f)}{(a\sigma_b+2\lambda_f)-\phi(a\sigma_b-\lambda_f)} \tag{34}$$

The exact value of interface thermal resistance has been found to be strongly dependent on the solid-liquid combination under consideration. For example, in the case of gold-water interface, the conductance values in Ref. [49] were found to decrease from $\sigma_b \sim 100$ MW m^{-2} K^{-1} to $\sigma_b \sim 50$ MW m^{-2} K^{-1} as the nature of the interface changed from hydrophilic to hydrophobic. Similar measurements conducted for aluminum-water interface yielded conductance values of approximately 180 MW m^{-2} K^{-1} and 60 MW m^{-2} K^{-1} for hydrophilic and hydrophobic interfaces, respectively. In view of these studies, we next estimate the effect for a typical nanoparticle suspended in water. For the case of a hydrophobic interface, if the conductance is set equal to a 50 MW m^{-2} K^{-1}, we find that nanoparticles with radius a less than 12 nm give a negative contribution to the effective thermal conductivity. On the other hand, if the interface conductance value is set equal to 100 MW m^{-2} K^{-1} corresponding to a hydrophilic interface, only nanoparticles with radius greater than 6 nm give a positive contribution to the effective thermal conductivity. Thus, we find that the contribution from the high thermal conductivity particles is strongly counteracted by the presence of an interfacial resistance. Since an exact value of σ_b, which accounts for the interfacial resistance, has not been reported in the experiments concerning thermal conductivity measurements, we set $\lambda_p \approx \lambda_f$ in all our future calculations. We note that such an approximation gives us a lower estimate of thermal conductivity enhancement of nanofluids and does not affect our results drastically, since the volume fraction of nanoparticles added to the liquid is usually quite low ($<5\%$).

Additionally, for nanofluids based on water as base liquid, ρ_i is set equal to the value corresponding to a neutral aqueous solution with pH=7 ($\rho_i = 2\times10^{-7}M = 1.2044\times10^{20}$ m^{-3} from the dissociation product of water at 300 K). The temperature dependence of the thermal conductivity and the viscosity of the base liquid (water/ethylene glycol) is taken into account for the calculation of the effective thermal conductivity enhancement. The values of ρ and C are taken to be the bulk values corresponding to the solid of which the nanoparticle is composed.

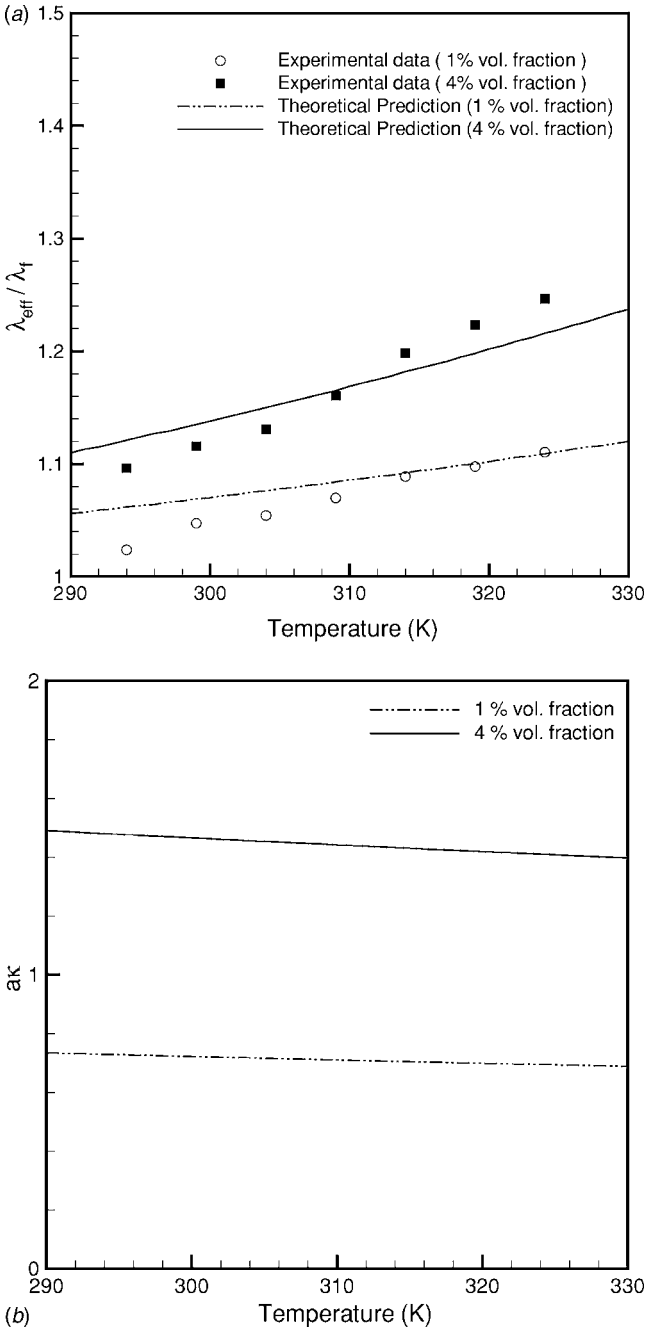

Fig. 2 (*a*) Comparison of the theoretical predictions with the experimental data for alumina (*a*=19.2 nm)/water nanofluid, *Z* =475. (*b*) Corresponding nondimensional inverse Debye length used in the calculations.

Figures 2(*a*) and 3(*a*) show a comparison of the theoretical predictions with the experimental data concerning the thermal conductivity enhancement ratio (effective thermal conductivity of the nanofluid to thermal conductivity of the base fluid) for two sets of calculations involving alumina (19.2 nm) and copper oxide (12.1 nm) nanoparticles suspended in water [6], respectively. We observe reasonable agreement between the theoretical predictions and experimental data for these two nanofluids for a choice of Z =475. The most probable cause for the discrepancy between the theoretical predictions and the experimental data (especially in the case of copper oxide nanoparticles suspended in water at 1% volume fraction) is the presence of clustering in nanofluid suspensions. As also mentioned in previous works (see Ref. [9]), mod-

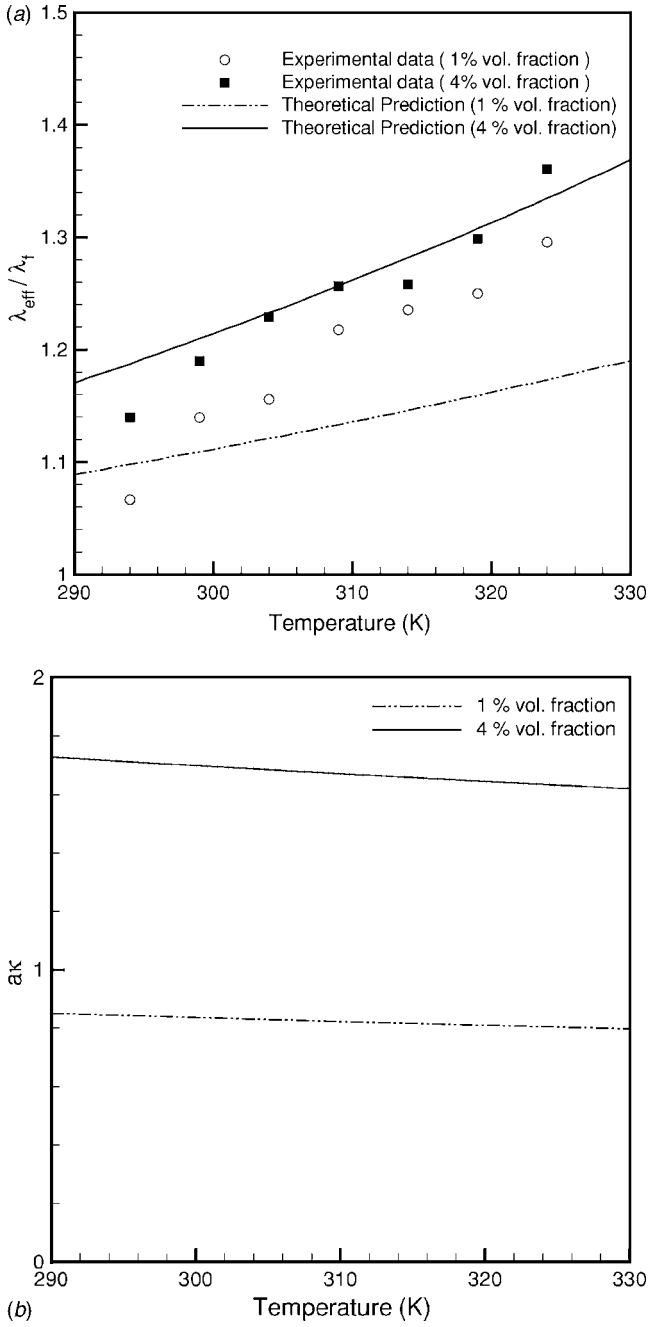

Fig. 3 (*a*) Comparison of the theoretical predictions with the experimental data for copper oxide (*a*=12.1 nm)/water nanofluid, *Z*=475. (*b*) Corresponding nondimensional inverse Debye length used in the calculations.

erate clustering in stable nanofluids can play an important role in determining the effective thermal conductivity. In principle, the clustering mechanism is incorporated in our current model through the pair distribution function. However, information regarding the pair distribution function can only be obtained through a detailed knowledge of microstructure of the suspension. Additionally, other factors such as polydispersity of the nanoparticles and the finite interface thermal conductance can also have a significant effect on the effective thermal conductivity. Figures 2(*b*) and 3(*b*) show the variation of inverse Debye length (κ_D), nondimensionalized with respect to the inverse of the particle radius a. For the present case of water as the base liquid with $\epsilon = 8.9 \times 10^{-9}$ C^2/N m^2, we have

$$a\kappa_D = 9.375 \times 10^{-5} \left\{ \frac{1.2044 \times 10^{20} a^2}{1-\phi} + \frac{3\phi Z}{4\pi a(1-\phi)} \right\}^{1/2} \tag{35}$$

We observe that the Debye length shows a significant decrease when nanoparticle volume fraction is increased from 0.01% to 0.04%. This is accompanied by a slight decrease with the rising liquid temperature when the volume fraction is kept constant.

The evaluation of the effective thermal conductivity of a nanofluid given by Eq. (27) involves an implicit assumption of $g^{eq}(r) = H(r-2a)$. In order to test the validity of this assumption, we next present results from the molecular dynamics simulations with parameters chosen to approximately model the experimental system under consideration. Note that we are interested in the equilibrium pair distribution function, which is a static property of a given system, and the choice of simulation technique (molecular dynamics or Brownian dynamics) is expected to have no significant effect on the final results.

We consider simulation of a nanofluid system with colloidal nanoparticles interacting with each other through the interparticle potential given by Eq. (28). Previous molecular dynamics studies of similar colloidal systems (see Refs. [43,51]) have established that at equilibrium, the thermodynamic and static properties of the system depend only on two nondimensional parameters $\lambda^* = \kappa_D n^{-1/3}$ and $T^* = k_B T / U_a$, where

$$U_a = \frac{Z^2 e^2 \ln(1 + e^{\kappa_D(2a - n^{-1/3})})}{2\epsilon a(1 + a\kappa_D)^2} \tag{36}$$

represents interaction energy at interparticle separation. We choose the parameters λ^* and T^* in order to closely match the alumina/water nanofluid system with alumina nanoparticles of size 19.2 nm. For brevity, equilibrium pair distribution function for only two sets of computations for volume fractions of 1% and 4% at a system temperature of T=300 K is reported. The choices of simulation parameters for these test cases are $\lambda^*=5.417$, $T^*=3.462\times10^{-2}$ for $\phi=0.01$, and $\lambda^*=6.934$, $T^*=7.272\times10^{-2}$ for $\phi=0.04$. Details of the setup and implementation of the molecular dynamics simulation along with a validation test case from Ref. [51] are given in Appendix B. Figure 4 depicts the equilibrium pair distribution function as a function of the nondimensional radial distance (nondimensionalized using characteristic interparticle spacing of $n^{-1/3}$) for two volume fractions of 1% and 4%. It is observed that the equilibrium radial distribution function attains a value close to unity for distances beyond interparticle spacing; this certifies our assumption of radial distribution of unity employed in the derivation of the final expression for effective thermal conductivity enhancement. We also note that the peak value of the radial distribution function is lower (corresponding to a less ordered state) for the suspension at a volume fraction of $\phi=0.04$ when compared to the suspension at $\phi=0.01$. The reason for the above observation is that the Debye length decreases by approximately a factor of 2 when the volume fraction of nanoparticles is increased by a factor of 4 (Fig. 2(*b*)). This decrease in Debye length causes the interaction potential to decay much more rapidly in the case of higher concentration so that the interaction energy at the interparticle spacing is lower for $\phi=0.04$. This lower interaction energy in the case of $\phi=0.04$ leads to a smaller peak in $g(r)$ when compared to the suspension at a volume fraction of $\phi=0.01$.

Figures 5(*a*) and 5(*b*) show a comparison of the theoretical predictions with the experimental data for 4 nm copper nanoparticles suspended in ethylene glycol [3] and the corresponding nondimensional inverse Debye length used in the calculations. The concentration of the ionic charge in the bulk liquid ρ_i is set equal to the value corresponding to pK_a for dissociation of ethylene glycol (15.56 at 300 K). We observe a reasonable agreement between theoretical predictions and experimental data for a choice of Z=475 corresponding to the case in which no stabilizing agent

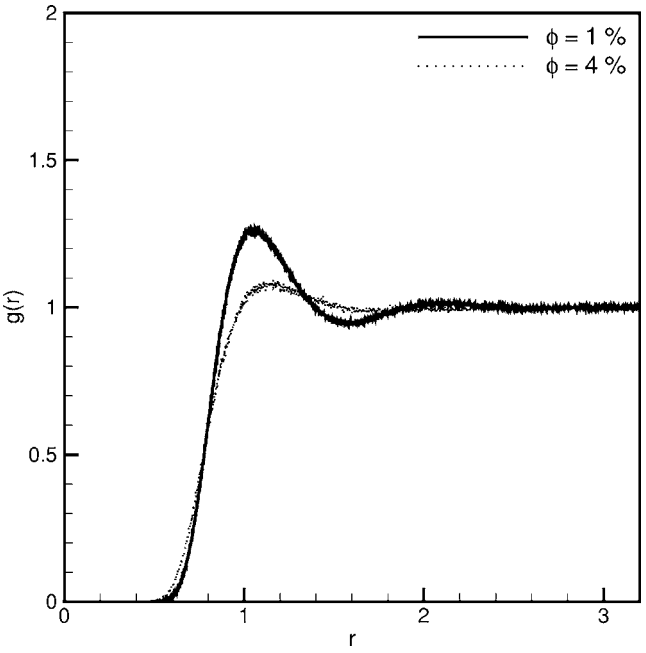

Fig. 4 Pair distribution function $g(r)$ as a function of nondimensional distance r for computations using (a) $\lambda^*=5.417$, $T^*=3.462\times10^{-2}$ and (b) $\lambda^*=6.934$, $T^*=7.272\times10^{-2}$, corresponding to alumina/water nanofluid at 300 K with nanoparticle volume fractions of 1% and 4%, respectively

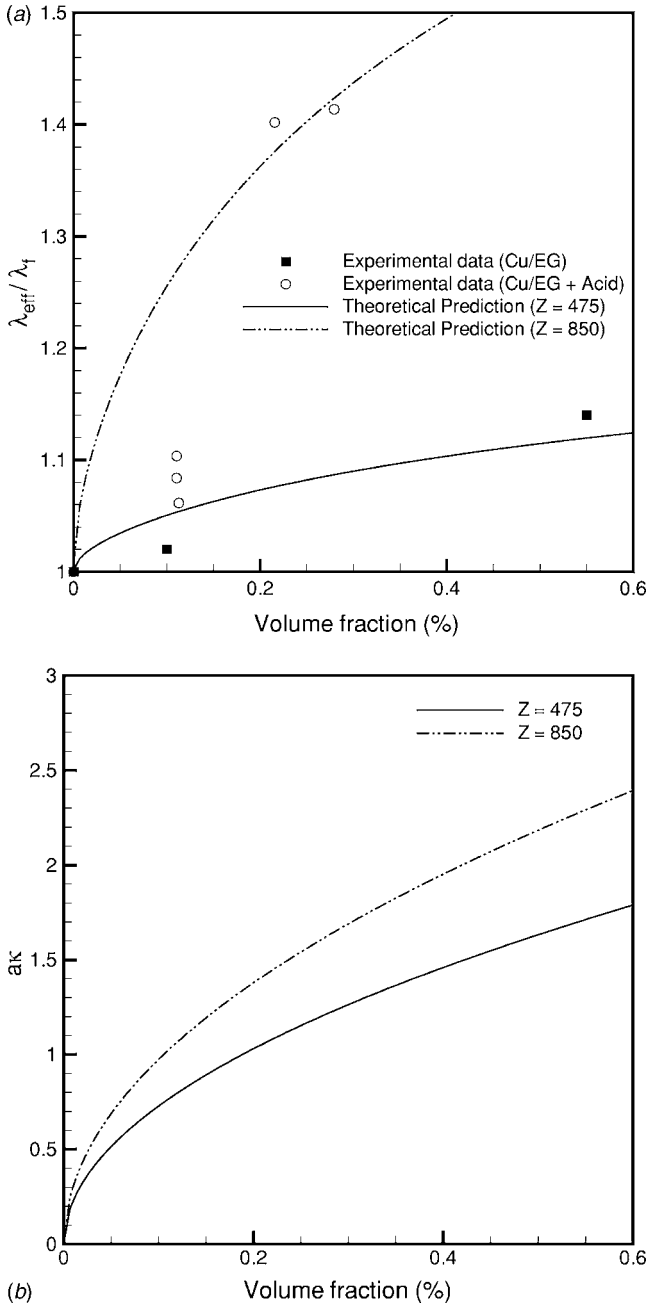

Fig. 5 (a) Comparison of the theoretical predictions with the experimental data for copper (a=4 nm)/ethylene glycol nanofluid. (b) Corresponding nondimensional inverse Debye length used in the calculations.

is added to the nanofluid. For the case when thioglycolic acid is added in order to improve the overall dispersion of nanoparticles within the suspension we had to use a higher value of $Z=850$ in order to predict the experimental data closely. Nevertheless, this higher value of Z is not totally unexpected given that a stabilizing agent (thioglycolic acid in this case) stabilizes the suspension by increasing repulsion between particles, and the way this increased repulsion is incorporated in our present model is through an increase in value of nondimensional effective surface charge Z.

Next, we compare our theoretical predictions with the experimental data for the variation of thermal conductivity enhancement ratio with the temperature for 8.5 nm gold/water nanofluid [7]. As shown in Fig. 6, good agreement is found between the predicted values and experimental data for both the particle volume fractions of 0.00013% and 0.00026%, when the value of nondimensional charge on the nanoparticle Z is set equal to 1150. We believe that the higher value of nondimensional charge on the nanoparticle Z (1150 versus 475 in previous cases) required in this case is due to the presence of citrate ions in the solution. The experimental studies in Ref. [7] emphasized the effect of volume fraction and temperature on the effective thermal conductivity, and the other factors which affect thermal conductivity in our model (surface charge, Debye length) were not reported. The surface charge present on the nanoparticle surface has a strong dependence on not only the available site density on the nanoparticle surface but also the concentration of potential determining ions. The nanoparticles which made up the suspension in these studies were coated with citrate ions [7], and possibly for this reason, the value of nondimensional charge Z is relatively high. The experimental measurements conducted in Ref. [40] provide evidence in favor of this argument and it was found that citrate ions adsorb strongly to the gold surface and remain adhered in spite of extensive dialysis. It is also noted that since the volume fraction of solid nanoparticles in the liquid is extremely low ($\sim10^{-4}\%$), macroscopic Hamilton–Crosser model predicts no change in conductivity enhancement with increasing temperature. Figure 7 shows a comparison between theoretical predictions and experimental data for 30 nm silver/water nanofluid [7] for the same choice of value of $Z=1150$. Reasonable agreement is observed between the experimental data and theoretical predictions for this case.

Overall, we observe good agreement between the theoretical predictions and the experimental data in all the cases for physically realistic choices of constant Z for nanofluids: $Z=475$ at relatively higher particle volume fractions ($\phi\sim1\%$) and $Z=1150$ at relatively lower particle volume fractions ($\phi\sim0.001\%$), when the nanoparticles were coated with citrate ions. The choices of the effective charge on nanoparticle Z and the Debye length (κ_D^{-1}) employed in various cases are physically realistic and are consistent with several previous studies, some of which are discussed next. The phase diagram of charged polystyrene spherical nano-

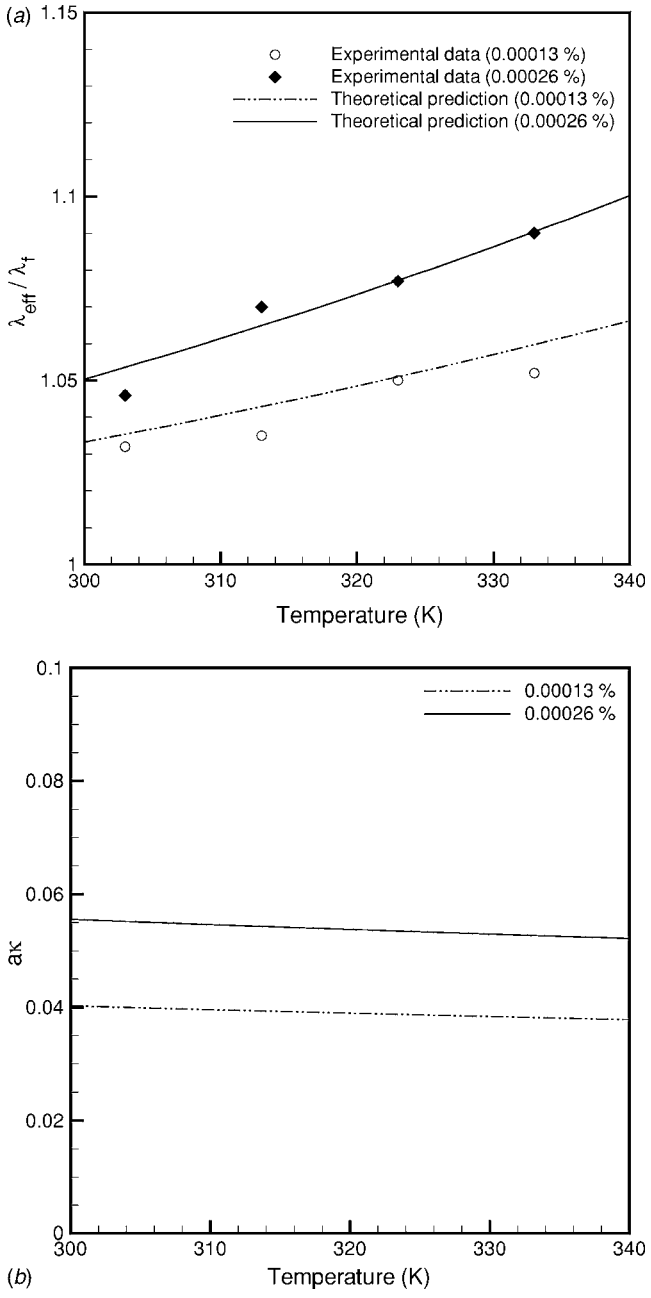

Fig. 6 (*a*) Comparison of the theoretical predictions with the experimental data for gold (*a*=8.5 nm)/water nanofluid, *Z* =1150. (*b*) Corresponding nondimensional inverse Debye length used in the calculations.

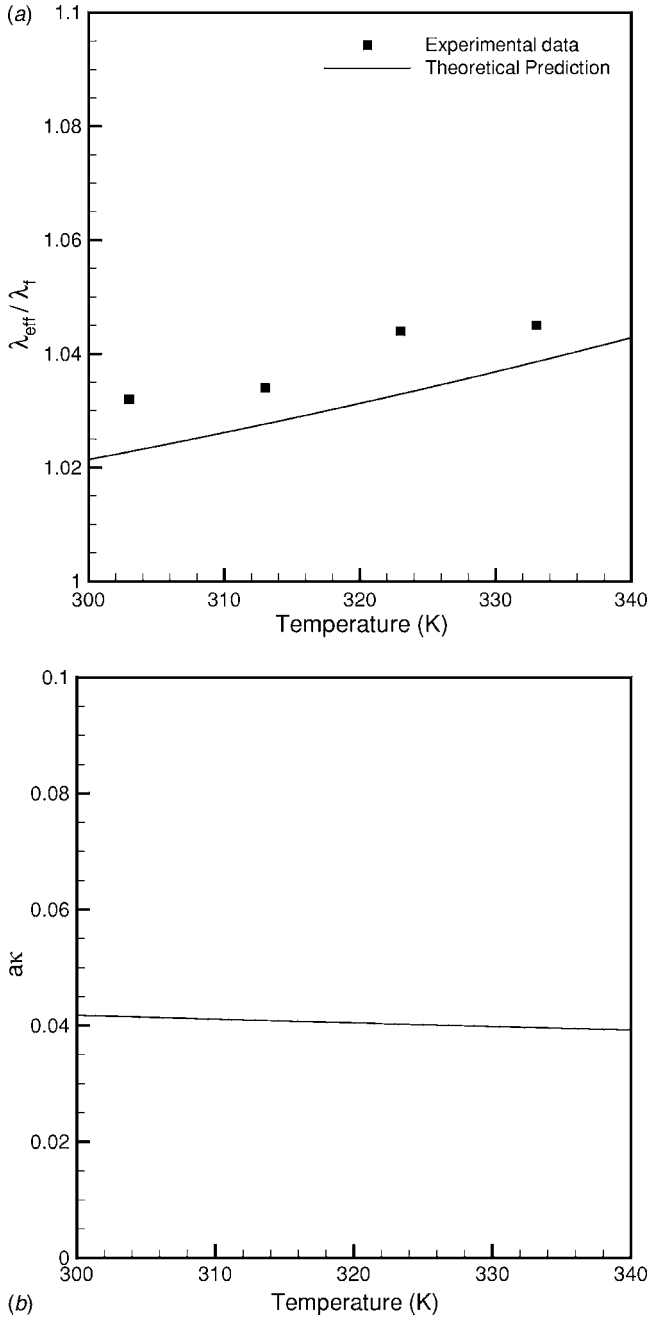

Fig. 7 (*a*) Comparison of the theoretical predictions with the experimental data for silver (*a*=30 nm)/water nanofluid, *Z* =1150. (*b*) Corresponding nondimensional inverse Debye length used in the calculations.

particles of radius 66 nm suspended in an aqueous medium was investigated experimentally in Ref. [43]. The experimental results were found to compare favorably with the numerical simulations for a choice of effective charge of $Z=880$. The conductivity measurements gave an effective charge of $Z=1200$. Mallamace et al. [44] conducted shear viscosity measurements on polystyrene nanoparticles suspended in de-ionized water for a range of particle radii from 33.5 nm to 107.5 nm. The corresponding effective charges were found to vary from 980 to 2700. Wette et al. [45] carried out effective charge measurements for polymer latex particles suspended in de-ionized water through experimental determination of suspension shear modulus and conductivity. As the radius of particles varied from 34 nm to 78 nm, the effective charge Z, measured from conductivity, was found to vary from 450 to 945. In Ref. [46], experimental measurements of the collective diffusion coefficient and electrophoretic mobility of latex nanoparticles of mean radius of 20 nm suspended in an aqueous solution yielded effective surface charges of the order of few hundreds of electrons per particle. Härtl et al. [52] studied the effect of addition of NaOH and NaCl to an otherwise neutral aqueous suspension comprised of 45.5 nm radius polystyrene nanoparticles. Under the assumption that the interparticle potential could be adequately described using screened Coulomb repulsive potential, the theoretical predictions of the structure factor were compared with the experimental data for a range of ionic concentrations starting from a neutral solution. It was observed that as the concentration of NaCl was increased from zero to $9.2\times10^{-6}M$,

the effective charge and the corresponding Debye length required to fit the experimental data varied from $Z=504$ and $\kappa_D^{-1}=433$ nm to $Z=469$ and $\kappa_D^{-1}=111$ nm. Additionally, the much reduced influence of concentration of NaOH on structure factor when compared to concentration of NaCl was attributed to an ion exchange mechanism, which is present in the case of NaOH but not NaCl. The microscopic measurement of interaction potential between charged polystyrene sulfate spheres of 320 nm radius was found to agree well with a screened Coulomb potential for a choice of $Z=1991$ and $\kappa_D^{-1}=161$ nm in Ref. [53].

It is clear from the studies reported above that the effective charges of the order of a few hundreds of electrons have been successfully employed in order to fit several experimental measurements concerning conductivity, order-disorder transition, and viscoelastic properties of colloids. This experimental evidence leads us to believe that the values of Z used to fit the thermal conductivity data in our present study are reasonable. The value of Debye screening length used in all the calculations is below the upper limit of 960 nm for a neutral aqueous solution at pH 7 [36]. At present, we do not have an established way of predicting the effective surface charge Z in our model. The true surface charge achieved in the experimental conditions depends strongly on the surface site density and the adsorption and desorption of potential/charge determining ions thereby leading to a net electrostatic potential difference between nanoparticle surface and the bulk liquid. This potential difference influences the charge adsorption/desorption so that the two processes are interdependent. The interparticle potential used in our current model is a highly simplified expression that results from the linearized Derjaguin approximation for low surface potentials [26,35] and is open to question in the present context of highly charged spherical nanoparticles. Besides, our model assumes nanoparticles to be perfect monodispere spheres. The analysis that we carried out accounts for only two-body interactions and ignores the effect of higher multi-body interactions. In addition, a detailed knowledge of the microstructure of the nanofluid suspension is absolutely essential for the prediction of the effective thermal conductivity since it can play a very important role through clustering. We attribute the discrepancies between our theoretical predictions and the experimental data to these aforementioned factors. To the best of our knowledge, the available experiments have emphasized the effect of volume fraction, temperature, and particle size on the effective thermal conductivity, and several other crucial factors that affect our predictions on conductivity, such as the surface potential and the Debye length, were not reported. We hope that we have provided a better understanding of the effect of the Brownian motion of interacting nanoparticles on the effective thermal conductivity and that future experimental measurements will allow more rigorous tests on the validity of the model. The main strength of the model lies in the fact that it can be used to estimate thermal conductivity of nanofluid suspensions with different nanoparticles (suspended in a base liquid), which may interact with each other through a specified interparticle potential (e.g., DLVO, steric, van der Waals forces, etc.). However, we note that the applicability of the model is restricted to relatively large nanoparticles whose size is significantly higher than the molecular dimensions so that the Stokes law for the drag on a sphere can be utilized successfully. Our future work aims at extending the present derivation to account for the hydrodynamic interactions between various nanoparticles of arbitrary shapes.

6 Conclusions

In this paper, a microscopic model which takes into account the dependence of size of nanoparticles and temperature on the effective thermal conductivity of nanofluids is proposed based on the theory of Brownian motion of nanoparticles in a fluid. A general theoretical framework is presented for the derivation of the effective thermal conductivity of a nanofluid suspension by accounting for the Brownian motion and pairwise additive interparticle potential between various nanoparticles. For a typical nanofluid, the kinetic contribution to the effective thermal conductivity is shown to be negligible. The contribution from the interparticle potential is analyzed through calculations involving DLVO interaction between the electric double layers on spherical nanoparticles. A comparison between the theoretical predictions and the experimental data establishes the importance of long range repulsive potentials in the enhancement of thermal conductivity of nanofluids. It is shown that the model predicts an increase in the effective thermal conductivity enhancement with the volume fraction of solid nanoparticles and liquid temperature.

Acknowledgment

The authors gratefully acknowledge the support this research received from NASA under the Microgravity Fluid Physics Program.

Nomenclature

ϵ = permittivity of the liquid
$\hat{C}$ = heat capacity of a nanoparticle
$\kappa_{D_*}^{-1}$ = Debye length
λ^* = Nondimensional inverse Debye length
λ_f = thermal conductivity of the liquid
λ_p = thermal conductivity of the nanoparticle
λ_{eff} = effective thermal conductivity of the suspension
λ_{eff}^M = effective conductivity from macroscopic part
$\mathbf{F}$ = volume averaged heat flux
$\mathbf{f}_i^B$ = Brownian force on ith nanoparticle
$\mathbf{f}_i^h$ = hydrodynamic force on ith nanoparticle
$\mathbf{f}_i^I$ = interaction force on ith nanoparticle
$\mathbf{F}_B$ = heat flux due to Brownian motion
$\mathbf{F}_M$ = macroscopic heat flux
$\mathbf{G}$ = volume averaged temperature gradient
$\mathbf{J}$ = heat flux vector
$\mathbf{J}_f$ = heat flux vector in the liquid
$\mathbf{J}_p$ = heat flux vector in the nanoparticle
$\mathbf{M}$ = generalized friction tensor
$\mathbf{r}$ = position vector of an arbitrary point
$\mathbf{r}_i$ = position vector of the center of ith nanoparticle
$\mathbf{u}_i$ = velocity of ith nanoparticle
$\mathcal{U}$ = energy density
μ = viscosity of the liquid
ϕ = volume fraction of nanoparticles
Ψ = interparticle potential
ψ_s = surface potential
ρ = density of the nanoparticle
ρ_i = number density of bulk ionic charge
σ_b = interface thermal conductance
a = radius of the nanoparticle
$\mathcal{C}$ = heat capacity of the solid
e = unit charge (1.602×10^{-19} C)
g^{eq} = equilibrium pair distribution function
k_B = Boltzmann constant (1.381×10^{-23} J/K)
l_B = Bjerrum length
m = mass of a nanoparticle
N = number of nanoparticles in V
n = number density of nanoparticles
$P_N^{(N)}$ = nanoparticle position probability distribution function
T = temperature
T^* = nondimensional temperature
U_a = interaction energy at interparticle separation
V = total volume
V_p = volume occupied by N nanoparticles
Ze = total charge on a nanoparticle

Appendix A

In this appendix, we show the calculation steps for manipulation of the terms arising out of Eq. (20) for $\mathbf{F}_B^I$:

$$\mathbf{F}_B^I = \frac{\hat{C}}{V}\int \sum_{i=1}^{N}\left\{T(\mathbf{r}_i)\left(\mathbf{u}_i + \frac{k_B T(\mathbf{r}_i)}{\gamma}\boldsymbol{\nabla}_i \ln(T(\mathbf{r}_i)P_N^{(N)})\right)\right\}P_N^{(N)}d\mathbf{r}^N + \frac{1}{2V}\int\left\{\sum_{i=1}^{N}\sum_{j\neq i}\Psi(r_{ij}|T)P_N^{(N)}\mathbf{u}_i\right\}d\mathbf{r}^N \tag{A1}$$

Each of the individual terms arising from the above expression is considered next. We have

$$\mathbf{F}_B^I = \mathbf{F}_{B,1}^I + \mathbf{F}_{B,2}^I + \mathbf{F}_{B,3}^I \tag{A2}$$

where

$$\mathbf{F}_{B,1}^I = -\frac{\hat{C}}{\gamma V}\int \sum_{i=1}^{N}\sum_{j\neq i}\{T(\mathbf{r}_i)\boldsymbol{\nabla}_i\Psi(r_{ji}|T)\}P_N^{(N)}d\mathbf{r}^N$$

$$\mathbf{F}_{B,2}^I = -\frac{\hat{C}}{\gamma V}\int \sum_{i=1}^{N}\sum_{j\neq i}\left\{T(\mathbf{r}_i)\left(\delta T(\mathbf{r}_i) + \frac{1}{2}\mathbf{r}_{ji}\cdot\boldsymbol{\nabla}_i T(\mathbf{r}_i)\right)\frac{\partial}{\partial T}\boldsymbol{\nabla}_i\Psi(r_{ji}|T)\right\}P_N^{(N)}d\mathbf{r}^N$$

$$\mathbf{F}_{B,3}^I = \frac{1}{2V}\int \sum_{i=1}^{N}\sum_{j=1,j\neq i}^{N}\{\Psi(r_{ij}|T)P_N^{(N)}\mathbf{u}_i\}d\mathbf{r}^N \tag{A3}$$

Next taking $i=1$, $j=2$ as representative values, we obtain the following for $\mathbf{F}_{B,1}^I$:

$$\mathbf{F}_{B,1}^I = -\frac{\hat{C}}{V\gamma}\frac{N(N-1)}{2V^2}\int T(\mathbf{r}_1)\boldsymbol{\nabla}_1\boldsymbol{\Psi}(r_{12}|T)g(\mathbf{r}_1,\mathbf{r}_2)d\mathbf{r}_1 d\mathbf{r}_2 \tag{A4}$$

Using the expansion of the local pair distribution function $g(\mathbf{r}_1,\mathbf{r}_2)$ as in Ref. [29], we find

$$\mathbf{F}_{B,1}^I = -\frac{\hat{C}}{V\gamma}\frac{N(N-1)}{2V^2}\int T(\mathbf{r}_1)\boldsymbol{\nabla}_1\Psi(r_{12}|T)\left\{g^{\mathrm{eq}}(r_{12}) + \frac{1}{2}\mathbf{r}_{21}\cdot\boldsymbol{\nabla}_1 T\frac{dg^{\mathrm{eq}}}{dT}\right\}d\mathbf{r}_1 d\mathbf{r}_{21} \tag{A5}$$

Proceeding further, we note that [29]

$$\boldsymbol{\nabla}_1\Psi(r_{12}|T) = \frac{\mathbf{r}_{12}}{r_{12}}\frac{d\Psi(r_{12}|T)}{dr_{12}} \tag{A6}$$

is an odd function of $\mathbf{r}_{12}$, due to which the first term in Eq. (A5) evaluates to zero. Thus, we obtain the following final expression for $\mathbf{F}_{B,1}^I$ to a first order in temperature gradient:

$$\mathbf{F}_{B,1}^I = \frac{n^2\hat{C}T}{4\gamma}\left(\frac{\int\boldsymbol{\nabla}_1 T d\mathbf{r}_1}{V}\right)\left(\int r_{12}\frac{dg^{\mathrm{eq}}(r_{12}|T)}{dT}\frac{d\Psi(r_{12}|T)}{dr_{12}}d\mathbf{r}_{12}\right) = \frac{\pi n^2\hat{C}T}{\gamma}\left(\int_0^\infty r^3\frac{dg^{\mathrm{eq}}}{dT}\frac{d\Psi(r|T)}{dr}dr\right)\mathbf{G} \tag{A7}$$

Proceeding in a similar way, it is possible to show that to a first order in temperature gradient, $\mathbf{F}_{B,2}^I$ is given by

$$\mathbf{F}_{B,2}^I = -\frac{\hat{C}}{V\gamma}\frac{N(N-1)}{2V^2}\int T(\mathbf{r}_1)\left\{\delta T(\mathbf{r}_1) + \frac{1}{2}\mathbf{r}_{21}\cdot\boldsymbol{\nabla}_1 T\right\}\frac{\partial}{\partial T}\boldsymbol{\nabla}_1\Psi(r_{12}|T)d\mathbf{r}_1 d\mathbf{r}_{21} = \frac{n^2\hat{C}T}{4\gamma}\left(\frac{\int\boldsymbol{\nabla}_1 T d\mathbf{r}_1}{V}\right)\left(\int r_{12}g^{\mathrm{eq}}(r_{12}|T)\frac{\partial^2\Psi(r_{12}|T)}{\partial r_{12}\partial T}d\mathbf{r}_{12}\right) = \frac{\pi n^2\hat{C}T}{\gamma}\left(\int_0^\infty r^3 g^{\mathrm{eq}}\frac{\partial^2\Psi(r|T)}{\partial r\partial T}dr\right)\mathbf{G} \tag{A8}$$

where the term corresponding to $\delta T(\mathbf{r}_1)$ evaluates to zero since $\boldsymbol{\nabla}_1\Psi$ is an odd function of $\mathbf{r}_1$. Finally, we evaluate a simplified expression for $\mathbf{F}_{B,3}^I$. In this case, a rather straightforward calculation is performed to a first order in temperature gradient as shown below

$$\mathbf{F}_{B,3}^I = -\frac{k_B}{2V\gamma}\int\sum_{i=1}^{N}\sum_{j\neq i}\Psi(r_{ij}|T)T(\mathbf{r}_i)P_N^{(N)}\boldsymbol{\nabla}_i\ln(T(\mathbf{r}_i)P_N^{(N)})d\mathbf{r}^N = -\frac{k_B}{2V\gamma}\frac{N(N-1)}{2V^2}\int\Psi(r_{12}|T)g(r_{12})\boldsymbol{\nabla}_1 T(\mathbf{r}_1)d\mathbf{r}_1 d\mathbf{r}_{12} = -\frac{k_B n^2}{4\gamma}\left(\frac{\int\boldsymbol{\nabla}_1 T(\mathbf{r}_1)d\mathbf{r}_1}{V}\right)\left(4\pi\int r_{12}^2 g(r_{12})\Psi(r_{12}|T)dr_{12}\right) = -\frac{\pi n^2 k_B}{\gamma}\left(\int_0^\infty r^2 g(r)\Psi(r)dr\right)\mathbf{G} \tag{A9}$$

The remaining terms involve three-body interactions and hence are ignored. Thus, we have the following final expression for the interparticle interaction contribution to the heat flux:

$$\mathbf{F}_B^I = \left\{-\frac{\pi n^2 k_B}{\gamma}\left(\int_0^\infty r^2 g^{\mathrm{eq}}(r)\Psi(r|T)dr\right) + \frac{\pi n^2\hat{C}T}{\gamma}\left(\int_0^\infty r^3 g^{\mathrm{eq}}(r)\frac{\partial^2\Psi(r|T)}{\partial T\partial r}dr\right) + \frac{\pi n^2\hat{C}T}{\gamma}\left(\int_0^\infty r^3\frac{\partial g^{\mathrm{eq}}(r)}{\partial T}\frac{\partial\Psi(r|T)}{\partial r}dr\right)\right\}\mathbf{G} \tag{A10}$$

The presence of dg^{eq}/dT term in the above expression can cause complications in the full analytical treatment of the problem. Fortunately, the temperature dependence of $g^{\mathrm{eq}}(r)$ can be obtained from the following expression derived in Refs. [26,32] for the limiting case of $n\to 0$:

$$g^{\mathrm{eq}}(r) = y(r)\exp\left(-\frac{\Psi(r)}{k_B T}\right) \tag{A11}$$

where the function $y(r)$ depends only on the local position in the liquid. Use of this expression along with Eq. (A10) then yields Eq. (25) for $\mathbf{F}_B^I$.

Appendix B

Here, we present the details of the molecular dynamics simulation in order to calculate the equilibrium pair distribution function $g^{\mathrm{eq}}(r)$. The calculations are performed in a constant volume microcanonical ensemble. The colloidal system comprises of 2048 nanoparticles in a three dimensional periodic cell whose size is chosen in order to correspond to a fixed number density of n. Nanoparticle trajectories are computed using Beeman algorithm

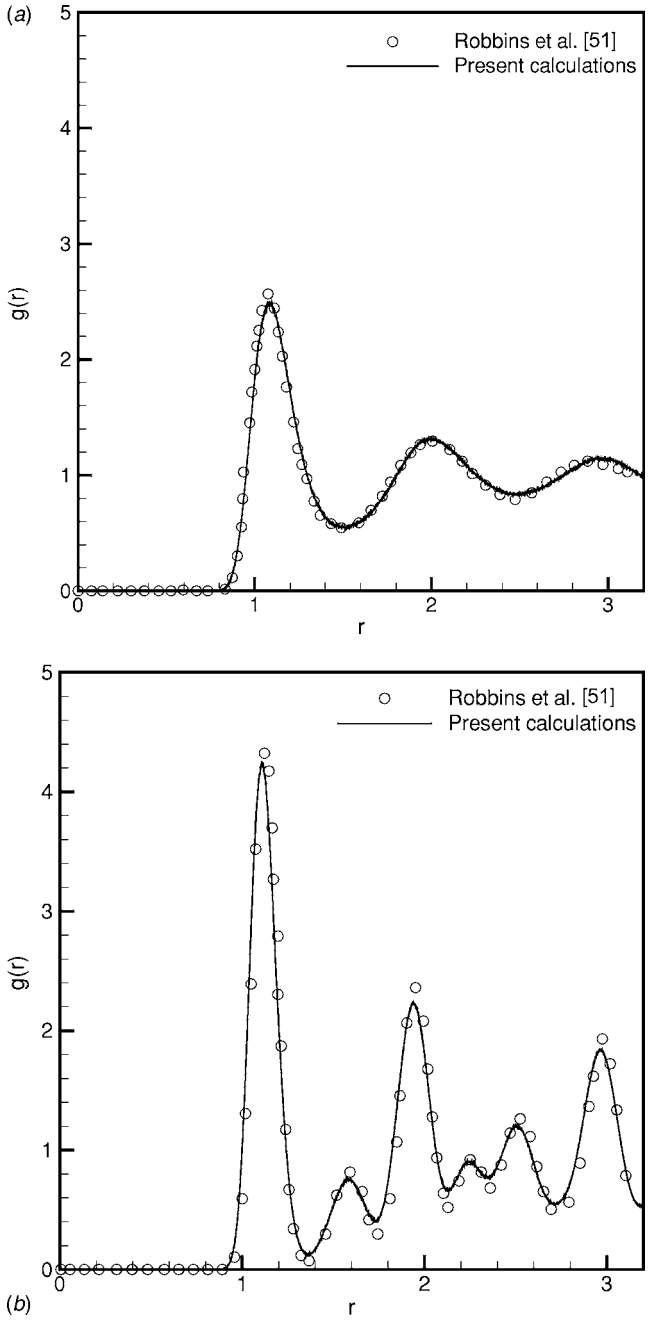

Fig. 8 Pair distribution function $g(r)$ calculations using $\lambda^* = 3.74$ and nondimensional temperatures of (*a*) $T^* = 3.23 \times 10^{-3}$ and (*b*) $T^* = 1.61 \times 10^{-3}$

[54] with a nondimensional time step size of $\Delta t^* = 0.005$ and the forces are computed using neighbor list method with a cutoff radius of 3.5. The system is initially equilibrated at the desired temperature for the first 50,000 time steps using Berendsen's thermostat [55] and then next 50,000 time steps of nonthermostat equilibration. Sampling is performed every ten time steps for the next 1×10^6 time steps in order to compute equilibrium pair distribution function using

$$g(r) = \frac{1}{N}\left\langle \sum_{i \neq j} \delta(\mathbf{r} - \mathbf{r}_i + \mathbf{r}_j) \right\rangle \tag{B1}$$

where N denotes the number of nanoparticles. In order to attest the accuracy of the computational code the model system used in Ref. [51] is simulated with the nondimensional parameters chosen from the data for Figs. 23(a) and 23(b) of Ref. [51]. A good comparison between the pair distribution function obtained in our work and that presented in Ref. [51], as depicted in Figs. 8(*a*) and 8(*b*) for two sets of computations, establishes the accuracy of our numerical technique.

References

[1] Eastman, J. A., Choi, S. U. S., Li, S., Thompson, L. J., and Lee, S., 1997, "Enhanced Thermal Conductivity Through the Development of Nanofluids," *Proceedings of the Symposium on Nanophase and Nanocomposite Materials II*, Vol. 457, pp. 3–11.

[2] Lee, S., Choi, S. U. S., Lu, S., and Eastman, J. A., 1999, "Measuring Thermal Conductivity of Fluids Containing Oxide Nanoparticles," ASME J. Heat Transfer, **121**, pp. 280–289.

[3] Eastman, J. A., Choi, S. U. S., Yu, W., and Thompson, L. J., 2001, "Anomalously Increased Effective Thermal Conductivities of Ethylene Glycol-Based Nanofluids Containing Copper Nanoparticles," Appl. Phys. Lett., **78**, pp. 718–720.

[4] Choi, S. U. S., Zhang, Z. G., Yu, W., Lockwood, F. E., and Grulke, E. A., 2001, "Anomalous Thermal Conductivity Enhancement in Nanotube Suspensions," Appl. Phys. Lett., **79**, pp. 2252–2254.

[5] Xie, H., Wang, J., Xi, T., Liu, Y., Ai, F., and Wu, Q., 2002, "Thermal Conductivity Enhancement of Suspensions Containing Nanosized Alumina Particles," J. Appl. Phys., **91**, pp. 4568–4572.

[6] Das, S. K., Putra, N., Thiesen, P., and Roetzel, W., 2003, "Temperature Dependence of Thermal Conductivity Enhancement for Nanofluids," ASME J. Heat Transfer, **125**, pp. 567–574.

[7] Patel, H. E., Das, S. K., Sundararajan, T., Nair, A. S., George, B., and Pradeep, T., 2003, "Thermal Conductivities of Naked and Monolayer Protected Metal Nanoparticle Based Nanofluids: Manifestation of Anomalous Enhancement and Chemical Effects," Appl. Phys. Lett., **83**, pp. 2931–2933.

[8] Xie, H., Lee, H., Youn, W., and Choi, M., 2003, "Nanofluids Containing Multiwalled Carbon Nanotubes and Their Enhanced Thermal Conductivities," J. Appl. Phys., **94**, pp. 4967–4971.

[9] Keblinski, P., Phillpot, S. R., Choi, S. U. S., and Eastman, J. A., 2002, "Mechanisms of Heat Flow in Suspensions of Nano-Sized Particles (Nanofluids)," Int. J. Heat Mass Transfer, **45**, pp. 855–863.

[10] Eastman, J. A., Phillpot, S. R., Choi, S. U. S., and Keblinski, P., 2004, "Thermal Transport in Nanofluids," Annu. Rev. Mater. Res., **34**, pp. 219–246.

[11] Keblinski, P., Eastman, J. A., and Cahill, D. A., 2005, "Nanofluids for Thermal Transport," Mater. Today, **8**, pp. 36–44.

[12] Jang, S. P., and Choi, S. U. S., 2004, "Role of Brownian Motion in the Enhanced Thermal Conductivity of Nanofluids," Appl. Phys. Lett., **84**, pp. 4316–4318.

[13] Hamilton, R. L., and Crosser, O. K., 1962, "Thermal Conductivity of Heterogeneous Two-Component Systems," Ind. Eng. Chem. Fundam., **1**, pp. 187–191.

[14] Bhattacharya, P., Saha, S. K., Yadav, A., and Phelan, P. E., 2004, "Brownian Dynamics Simulation to Determine the Effective Thermal Conductivity of Nanofluids," J. Appl. Phys., **95**, pp. 6492–6494.

[15] Xuan, Y., Li, Q., and Hu, W., 2003, "Aggregation Structure and Thermal Conductivity of Nanofluids," AIChE J., **49**, pp. 1038–1043.

[16] Xue, Q., 2003, "Model for Effective Thermal Conductivity of Nanofluids," Phys. Lett. A, **307**, pp. 313–317.

[17] Xue, L., Keblinski, P., Phillpot, S. R., Choi, S. U. S., and Eastman, J. A., 2004, "Effect of Liquid Layering at the Liquid-Solid Interface on Thermal Transport," Int. J. Heat Mass Transfer, **47**, pp. 4277–4284.

[18] Wang, B. X., Zhou, L. P., and Peng, X. F., 2003, "A Fractal Model for Predicting the Effective Thermal Conductivity of Liquid With Suspensions of Nanoparticles," Int. J. Heat Mass Transfer, **46**, pp. 2665–2672.

[19] Kumar, D. H., Patel, H. E., Kumar, V. R. R., Sundararajan, T., Pradeep, T., and Das, S. K., 2004, "Model for Heat Conduction in Nanofluids," Phys. Rev. Lett., **93**, p. 144301.

[20] Prasher, R., Bhattacharya, P., and Phelan, P. E., 2005, "Thermal Conductivity of Nanoscale Colloidal Solutions (nanofluids)," Phys. Rev. Lett., **94**, p. 025901.

[21] Prasher, R., Bhattacharya, P., and Phelan, P. E., 2006, "Brownian-Motion-Based Convective-Conductive Model for the Effective Thermal Conductivity of Nanofluids," ASME J. Heat Transfer, **128**, pp. 588–595.

[22] Wang, J., Chen, G., and Zhang, Z., 2005, "A Model of Nanofluids Thermal Conductivity," *Proceedings of 2005 ASME Summer Heat Transfer Conference*, Jul. 17–22.

[23] Vadasz, P., 2006, "Heat Conduction in Nanofluid Suspensions," ASME J. Heat Transfer, **128**, pp. 465–477.

[24] Xuan, Y., and Li, Q., 2003, "Investigation on Convective Heat Transfer and Flow Features of Nanofluids," ASME J. Heat Transfer, **125**, pp. 151–155.

[25] Buongiorno, J., 2006, "Convective Transport in Nanofluids," ASME J. Heat Transfer, **128**, pp. 240–250.

[26] Russel, W. B., Saville, D. A., and Schowalter, W. R., 1989, *Colloidal Dispersions*, Cambridge University Press, Cambridge.

[27] Batchelor, G. K., 1976, "Brownian Diffusion of Particles With Hydrodynamic Interaction," J. Fluid Mech., **74**, pp. 1–29.

[28] Dhont, J. K. G., 2004, "Thermodiffusion of Interacting Colloids. I. A Statistical Thermodynamics Approach," J. Chem. Phys., **120**, pp. 1632–1641.

[29] Dhont, J. K. G., 2004, "Thermodiffusion of Interacting Colloids. II. A Microscopic Approach," J. Chem. Phys., **120**, pp. 1642–1653.
[30] Jeffrey, D. J., 1973, "Conduction Through a Random Suspension of Spheres," Proc. R. Soc. London, Ser. A, **335**, pp. 355–367.
[31] Batchelor, G. K., and O'Brien, R. W., 1977, "Thermal or Electrical Conduction Through a Granular Material," Proc. R. Soc. London, Ser. A, **355**, pp. 313–333.
[32] Hansen, J. P., and McDonald, I. R., 1976, *Theory of Simple Liquids*, Academic, New York.
[33] Landau, L. D., and Lifshitz, E. M., 1959, *Fluid Mechanics*, Pergamon, New York.
[34] Zwanzig, R., 2001, *Nonequilibrium Statistical Mechanics*, Oxford University Press, New York.
[35] Hunter, R. J., 1981, *Zeta Potential in Colloid Science*, Academic New York.
[36] Israelachvili, J., 1991, *Intermolecular and Surface Forces*, Academic, New York.
[37] Modi, H. J., and Fuerstenau, D. W., 1957, "Streaming Potential Studies on Corundum in Aqueous Solutions of Inorganic Electrolytes," J. Phys. Chem., **61**, pp. 640–643.
[38] Karaman, M. E., Pashley, R. M., Waite, T. D., Hatch, S. J., and Bustamante, H., 1997, "A Comparison of the Interaction Forces Between Model Alumina Surfaces and Their Colloidal Properties," Colloids Surf., A, **129–130**, pp. 239–255.
[39] Thompson, D. W., and Collins, I. R., 1992, "Electrical Properties of the Gold-Aqueous Solution Interface," J. Colloid Interface Sci., **152**, pp. 197–204.
[40] Giesbers, M., Kleijn, J. M., and Cohen Stuart, M. A., 2002, "The Electrical Double Layer on Gold Probed by Electrokinetic and Surface Force Measurements," J. Colloid Interface Sci., **248**, pp. 88–95.
[41] Alexander, S., Chaikin, P. M., Grant, P., Morales, G. J., Pincus, P., and Hone, D., 1984, "Charge Renormalization, Osmotic Pressure, and Bulk Modulus of Colloidal Crystals: Theory," J. Chem. Phys., **80**, pp. 5776–5781.
[42] Hansen, J. P., and Lowen, H., 2000, "Effective Interactions Between Electric Double Layers," Annu. Rev. Phys. Chem., **51**, pp. 209–242.
[43] Monovoukas, Y., and Ghast, A. P., 1989, "The Experimental Phase Diagram of Charged Colloidal Suspensions," J. Colloid Interface Sci., **128**, pp. 533–548.
[44] Mallamace, F., Micali, N., and Vasi, C., 1990, "Viscoelastic Properties of Charged Colloids, Polystyrene, and Silica-Water Suspensions," Phys. Rev. A, **42**, pp. 7304–7311.
[45] Wette, P., Schöpe, H. J., and Palberg, T., 2002, "Comparison of Colloidal Effective Charges From Different Experiments," J. Chem. Phys., **116**, pp. 10981–10988.
[46] Tirado-Miranda, M., Hiro-Pérez, C., Quesada-Pérez, M., Callejas-Fernández, J., and Hidalgo-Álvarez, R., 2003, "Effective Charges of Colloidal Particles Obtained From Collective Diffusion Experiments," J. Colloid Interface Sci., **263**, pp. 74–79.
[47] Wilson, O. M., Hu, X., Cahill, D. G., and Braun, P. V., 2002, "Colloidal Metal Particles as Probes of Nanoscale Thermal Transport in Fluids," Phys. Rev. B, **66**, p. 224301.
[48] Ghe, Z., Cahill, D. G., and Braun, P. V., 2004, "AuPd Metal Particles as Probes of Nanoscale Thermal Transport in Aqueous Solution," J. Phys. Chem. B, **108**, pp. 18870–18875 (2004).
[49] Ghe, Z., Cahill, D. G., and Braun, P. V., 2006, "Thermal Conductance of Hydrophilic and Hydrophobic Interfaces," Phys. Rev. Lett., **96**, p. 186101.
[50] Hasselman, D. P. H., and Johnson, L. F., 1987, "Effective Thermal Conductivity of Composites With Interfacial Thermal Barrier Resistance," J. Compos. Mater., **21**, pp. 508–515.
[51] Robbins, M. O., Kremer, K., and Grest, G. S., 1988, "Phase Diagram and Dynamics of Yukawa Systems," J. Chem. Phys., **88**, pp. 3286–3312.
[52] Härtl, W., Versmold, H., and Vittig, U., 1992, "Fluidlike Ordered Colloidal Suspensions: The Influence of Electrolytes on the Structure Factor $S(Q)$," Langmuir, **8**, pp. 2885–2888.
[53] Crocker, J. C., and Grier, D. G., 1994, "Microscopic Measurement of the Pair Potential of Charge-Stabilized Colloid," Phys. Rev. Lett., **73**, pp. 352–355.
[54] Hockney, R. W., and Eastwood, J. W., 1988, *Computer Simulation Using Particles*, IOP, Bristol.
[55] Berendsen, H. J. C., Postma, J. P. M., van Gunsteren, W. F., DiNola, A., and Haak, J. R., 1984, "Molecular Dynamics With Coupling to an External Bath," J. Chem. Phys., **81**, pp. 3684–3690.

Transient and Steady-State Experimental Comparison Study of Effective Thermal Conductivity of Al_2O_3/Water Nanofluids

Calvin H. Li[1]
Department of Mechanical, Industrial, and Manufacturing Engineering,
University of Toledo,
Toledo, OH 12180

Wesley Williams

Jacopo Buongiorno

Department of Nuclear Science and Engineering,
Massachusetts Institute of Technology,
Cambridge, MA 02139

Lin-Wen Hu
Nuclear Reactor Laboratory,
Massachusetts Institute of Technology,
Cambridge, MA 02139

G. P. Peterson
Department of Mechanical Engineering,
University of Colorado,
Boulder, CO 80309-0017
e-mail: bud.peterson@colorado.edu

Nanofluids are being studied for their potential to enhance heat transfer, which could have a significant impact on energy generation and storage systems. However, only limited experimental data on metal and metal-oxide based nanofluids, showing enhancement of the thermal conductivity, are currently available. Moreover, the majority of the data currently available have been obtained using transient methods. Some controversy exists as to the validity of the measured enhancement and the possibility that this enhancement may be an artifact of the experimental methodology. In the current investigation, Al_2O_3*/water nanofluids with normal diameters of* 47 nm *at different volume fractions (0.5%, 2%, 4%, and 6%) have been investigated, using two different methodologies: a transient hot-wire method and a steady-state cut-bar method. The comparison of the measured data obtained using these two different experimental systems at room temperature was conducted and the experimental data at higher temperatures were obtained with steady-state cut-bar method and compared with previously reported data obtained using a transient hot-wire method. The arguments that the methodology is the cause of the observed enhancement of nanofluids effective thermal conductivity are evaluated and resolved. It is clear from the results that at room temperature, both the steady-state cut-bar and transient hot-wire methods result in nearly identical values for the effective thermal conductivity of the nanofluids tested, while at higher temperatures, the onset of natural convection results in larger measured effective thermal conductivities for the hot-wire method than those obtained using the steady-state cut-bar method. The experimental data at room temperature were also compared with previously reported data at room temperature and current available theoretical models, and the deviations of experimental data from the predicted values are presented and discussed.*
[DOI: 10.1115/1.2789719]

Keywords: effective thermal conductivity, nanoparticle suspensions, nanofluids, transient hot-wire method, steady state cut-bar method

Introduction

There are two principal experimental methods typically used to measure the effective thermal conductivity of nanoparticle suspensions: transient methods and the steady-state methods. The most commonly used transient method utilized for the measurement of the effective thermal conductivity of nanoparticle suspensions, nanofluids, is the transient hot-wire method. Nagasaka and Nagashima [1] first applied this method to measure the thermophysical properties of electrically conducting liquids. In this approach, an electrically insulating coated platinum hot wire is suspended symmetrically in a liquid contained within a vertical cylindrical container. This hot wire serves as both a heating element, through electrical resistance heating, and as a thermometer, by measuring the temperature dependent change in the electrical resistance of the platinum wire. The thermal conductivity can be calculated from the relationship between the electrical and thermal conductivity as

$$T(t) - T_{\text{ref}} = q/4\pi k \ln\left(\frac{4K}{a^2 C}t\right) \tag{1}$$

where $T(t)$ is the temperature of the platinum hot wire in the fluid at time t, T_{ref} is the temperature of the test cell, q is the applied electric power applied to the hot wire, k is the thermal conductivity, K is the thermal diffusivity of the test fluid, a is the radius of the platinum hot wire, and $\ln C = g$, where g is Euler's constant. This relationship between δT and $\ln(t)$ is linear. The data of δT were valid only over a valid range of $\ln(t)$, namely, between time t_1 and time t_2, the thermal conductivity of the fluid can be calculated as

$$k = \frac{q}{4\pi(T_2 - T_1)} \ln\left(\frac{t_2}{t_1}\right) \tag{2}$$

where $T_2 - T_1$ is the temperature difference of the platinum hot wire between times t_1 and t_2. Recently, a number of investigators have utilized the transient hot-wire method to measure the effective thermal conductivity of a number of different nanoparticle suspensions. These investigations included those of Choi [2], Eastman et al. [3], Lee et al. [4], Eastman et al. [5], Xuan and Li [6,7], and Xie et al. [8,9] and involve the effective thermal conductivities of a wide range of different nanofluids. However, the effective thermal conductivities of nanofluids obtained supported by steady-state methods are quite limited. The most widely refer-

[1]Corresponding author.

Contributed by the Heat Transfer Division of ASME for publication in the JOURNAL OF HEAT TRANSFER. Manuscript received January 22, 2007; final manuscript received March 5, 2007; published online March 18, 2008. Review conducted by Christopher Dames. Paper presented at the ASME 2006 Energy Nanotechnology International Conference (ENIC2006), Boston, MA, June 26–28, 2006.

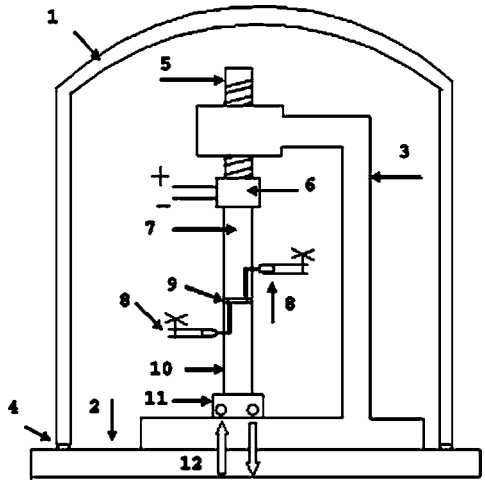

Fig. 1 Steady-state cut-bar facility; (1) stainless steel bell cover; (2) aluminum plain base stage; (3) sustaining rig; (4) rubber o-ring; (5) screw guide; (6) band heater; (7) upper heating copper bar; (8) sample charge tube; (9) cell rubber o-ring; (10) lower cooling copper bar; (11) coolant circulation exchanger; (12) coolant circulation ducts (thermocouples in copper bars and distribution of thermocouples are shown in Fig. 3)

enced data are those reported by Wang and Xu [10].

Although the transient hot-wire method for the measurement of the effective thermal conductivity of nanofluids has been widely used, a number of questions have arisen regarding the accuracy of this methodology and whether convective currents or other parameters might impact or affect the measured results. For instance, Vadasz et al. [11] stated that the unusually high effective thermal conductivity of nanofluids obtained using the hot-wire method could be the result of the thermal wave effect of hyperbolic heat conduction used in the temperature change calculation. In the current investigation, results obtained using a transient hot-wire method and a steady-state method are compared to better understand the accuracy of the two methods and determine the relative values.

The steady-state measurement system employed utilizes a cut-bar apparatus to measure the effective thermal conductivity of nanoparticle suspensions. This apparatus and procedure have been used previously by Peterson and Fletcher [12] to measure the thermal conductivity of both saturated and unsaturated dispersed ceramics [13,14], the contact resistance of various interfacial materials [15], and more recently, to measure the effective thermal conductivity of nanofluids [16–19]. Using identical samples, the results are then compared to those obtained by the hot-wire method.

Experimental Test Facility and Procedure

The steady-state experimental facility, which was first described by Miller and Fletcher [20], is illustrated in Figs. 1(*a*) and 1(*b*), and consisted of a pair of 2.54 cm diameter copper rods, separated by an o-ring to form the test cell; a vertical support, an electrical heat source, a coolant heat sink, and two sample charge tubes. A ceramic plate was placed between the electrical heat source and the load screw jack on the vertical support to act as an insulating layer to prevent heat loss from the heat source. In addition, a similar insulating plate was placed between the vertical support and the coolant heat sink.

A total of nine thermocouples were placed in each of the copper bars, as illustrated in Fig. 2. Six of these were used to measure the surface temperatures, two each located in the center, and the other four located radially, halfway between the center of the test sample and the outer surface. The remaining thermocouples were located along the centerline at 1.15 cm intervals.

Neglecting the convective and radiation losses, the steady-state effective thermal conductivity of the fluid or nanoparticle suspensions can be modeled, as shown in Fig. 3. The heat flows down from the upper copper bar, passes through the test cell and sample fluid, and then flows along the lower copper bar to the heat sink.

The heat flux in a traditional cut-bar apparatus can be determined by measuring the temperature differences in the upper and lower copper bars as indicated in Eq. (1) and then averaging the computed heat fluxes.

$$q = k_{\text{copper}} A_{\text{bar}} \frac{\nabla T_{\text{bar}}}{\nabla Z_{\text{bar}}} \tag{3}$$

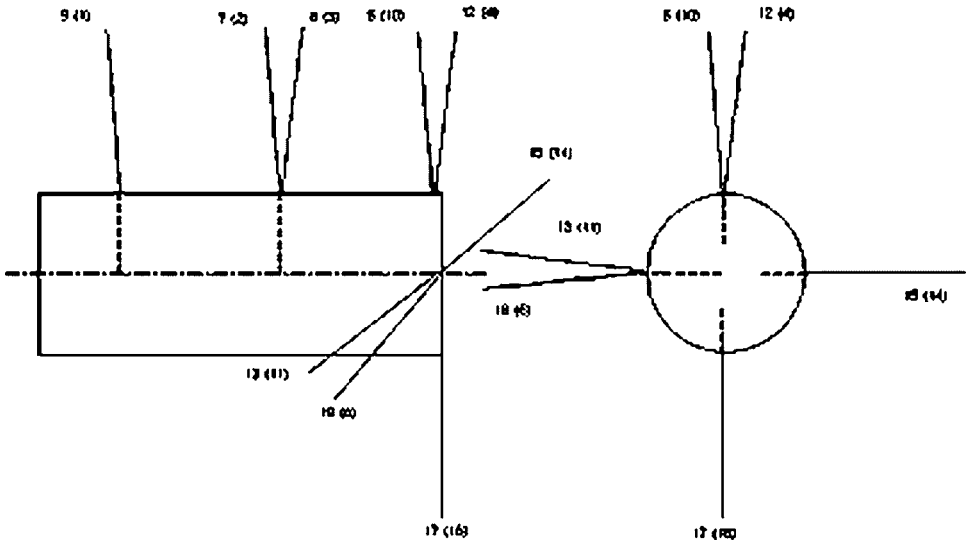

Fig. 2 The distribution of thermocouples in the upper and lower copper bars. Thermocouples 1, 2, 3, 4, and 6 reach the centerline of the upper copper bar (the heating side); Thermocouples 9, 7, 8, 5, and 18 reach the center line of the lower copper bar (the cooling side); Thermocouples 12, 17, 15, and 13, and 10, 16, 15 are located radially halfway between the centerline and the outer surface of the copper bar, respectively [17].

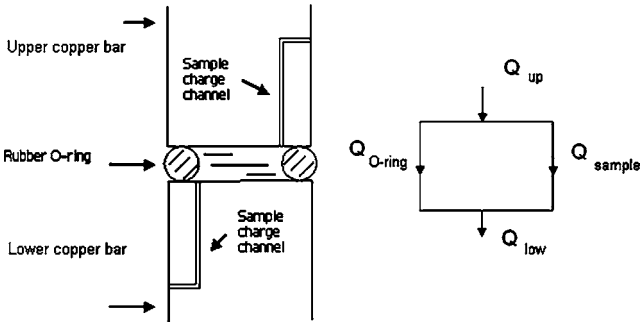

Fig. 3 Diagrams of sample cell and the heat flux [17]

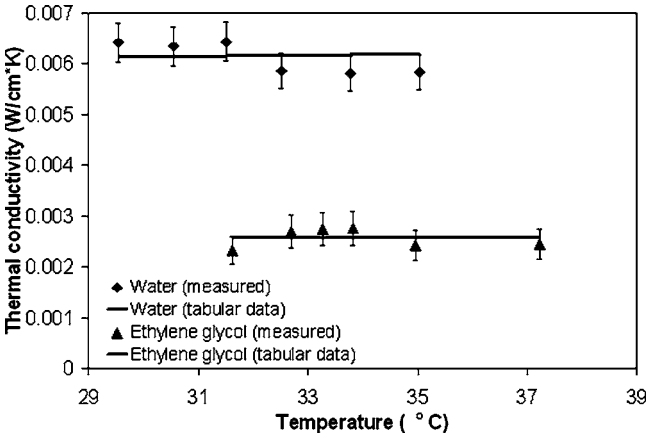

Fig. 4 Results of the tests facility calibration for distilled water and ethylene glycol as a function of temperature [17]

Using this calculated heat flux as q from Eq. (3) and the surface temperatures, determined by averaging the six thermocouples located at the surface of the upper and lower bars, the effective thermal conductivity of the fluid or the nanoparticle suspension sample inside the test cell can be calculated as

$$k_{\text{eff}} = \left(q \frac{\nabla Z_{\text{cell}}}{\nabla T_{\text{cell}}} - k_{\text{o ring}} A_{\text{o ring}} \right) / A_{\text{cell}} \tag{4}$$

Prior to initiating the tests, the two copper bars were carefully aligned vertically, and a load was applied using the load screw to ensure good contact between the copper surfaces and the o-ring and hence, an airtight seal and form a sealed sample cell inside. The sample was charged into the test cell by entering the lower sample change inlet, completely filling the test cell, and then exiting through the upper charge outlet, as shown in Fig. 3. Both sample charge channels were 1 mm diameter inside the copper bars. During this process, care was taken to ensure that no air was trapped in the test cell and that it was completely full of the test fluid.

The objective of the current investigation was to measure the effective thermal conductivity of nanoparticle suspensions using this apparatus and to compare them to the transient hot-wire method to determine the consistency and therefore the validity of the measured results. Based on previous investigations, the enhancements were anticipated to be in the range from 10% to 40%. Because these values are relatively small, it is critical that the experimental test facility be as accurate as possible.

Special limit of error (SLE) thermocouples, Omega number KMQXL-020G-6 were used in the current investigation. Each and every thermocouple was calibrated and the accuracy of each was obtained by measuring the temperature of water within the range of the experimental process. This resulted in a maximum uncertainty of less than 0.15 °C and an average uncertainty of less than 0.6%. Following the calibration of the thermocouples, it was necessary to determine the heat flux transferred through the o-ring as a function of temperature. To accomplish this, the heat flux through the o-ring and the o-ring thermal conductivity were measured as a function of temperatures with a vacuum in the test cell. The entire test apparatus was then calibrated in separate tests in which the test cell was filled with pure distilled water and pure ethylene-glycol. The calibration tests were conducted at steady state in a vacuum of less than 0.15 Torr and over a temperature range of 18.4–51 °C. Steady state was determined when the temperature variation of all of the thermocouples was less than 0.1 °C over a period of 30 min. Data were recorded using an Agilent 34970A data acquisition system, and all measurements were averaged using at least 100 data points.

The results of these calibration tests are illustrated in Fig. 4. As shown, the experimental results are compared with tabular data available in the literature for both ethylene glycol and distilled water [21], and indicate an overall experimental variation between the measured and tabular data of well within ±2.5%.

Pure distilled water (de-ionized (DI) water) was tested with this steady-state cut-bar method system immediately before, and again after, the nanoparticle samples were tested, and the results were compared with the tabular values [21]. As shown in Fig. 5 [22], the relationship between the measured and tabular data available in the literature is well within the overall experimental uncertainty of less than ±2.5%.

The transient hot-wire method has been used by a number of investigators to measure the effective thermal conductivity of nanofluids [2–9]. Some investigators utilized a Wheatstone bridge to measure the voltage changes due to the temperature variation of the test wire by comparing the voltages of the test wire to that of the reference wire, and then to use this value to calculate the thermal conductivity of the test fluid, while others measured the voltage change directly.

The transient hot-wire (THW) experimental facility employed here is the one described by Williams [23] and also in Rusconi et al. [24]. The THW is essentially made from a fine wire placed in a cell, as shown in Fig. 6, consisting mainly of a platinum/Isonel-coated wire (ρ=21.45 g/cm^3, k=71.6 W/m K, c_p=0.1325 J/g K) with a bare diameter of 25 μm (28 μm with the insulating coating). The length of the wire used is variable between 25 mm and 40 mm. The supporting leads are two tantalum rods to keep the wire straight and to connect it to the electrical system; these rods are also electrically insulated. The electrical system is composed of a current source (Keithley 6221) and a nanovoltmeter (Keithley

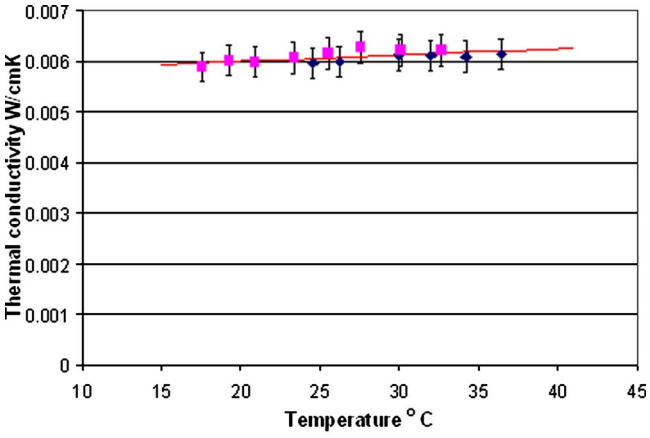

Fig. 5 The steady-state cut-bar method experimental data of DI water (the square represents the first test data set, the diamond the second test data, and the line is the tablular value [20])

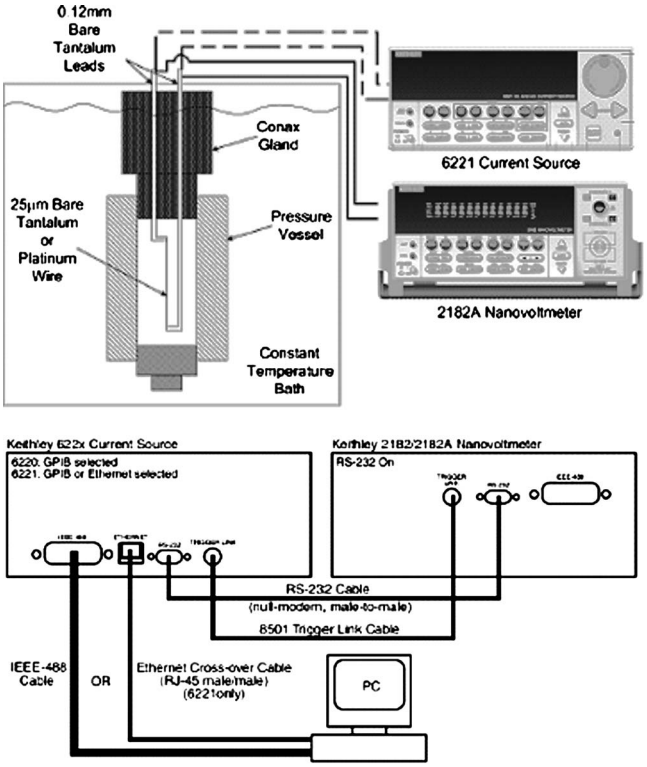

Fig. 6 Schematic of transient hot-wire test setup [22]

2182A) to collect the voltage data: using these instruments is a key factor in the development of this facility, because the variations in the resistance of the wire are usually quite small (less than millivolts), making it extremely important to have a voltage meter with a very high degree of sensitivity. The vessel is made of stainless steel with an external diameter of approximately 2.5 cm and it is placed in a larger container that can be used to circulate water from a thermostatic bath in order to control the temperature at which the experiments are performed. The current source and the voltmeter provide the possibility of using a remote control via a general purpose interface bus (GPIB) port utilizing a MATLAB code to interface the instruments with a personal computer (PC). One parameter of particular importance is the data acquisition rate, because it is important to have very rapid measurements to prevent the onset of convection. The range of acquisition rates for these instruments should go from 0.01 NPLC to 60 NPLC, where NPLC means "number of power line cycles" and 1 NPLC is equal to 16.7 ms. In the measurements, NPLC=0.1 is used, which corresponds to an acquisition rate of about 17 ms. Each measurement takes around 20 s, in this partition. In the first 5 s, the system acquires the voltage signal at a very low input current (usually 1 mA) in order to measure the resistance of the wire before the heating (R_0): In this way, using the resistance-temperature relationship, Fig. 7, the temperature of the sample is known and compared to the thermostatic bath. In the last 15 s, the input current switches to higher values (in the range of 50–100 mA) and the wire starts heating; at the end, the current source is turned off and the collected data are transferred to the software. So the modus operandi is performing a series of runs and taking the average for different input currents (from 50 mA to 100 mA) [23].

In Fig. 8, measurements of thermal conductivity of water and ethylene glycol at 25°C are plotted. It should be noted that the experimental data are linear (in a log scale) throughout almost the entire measurement time as expected except for the very end of the process, where the variation is the result of turning off the power.

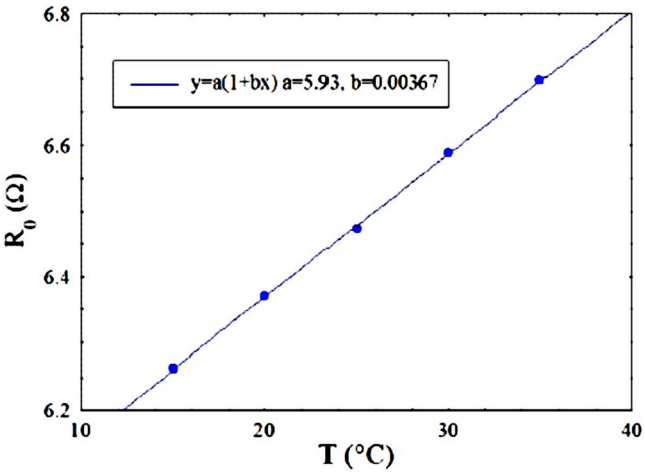

Fig. 7 Resistance-temperature relationship for the platinum wire [22]

In Fig. 9, the temperature dependence of the experimental results for the thermal conductivity of water is illustrated and shows very good agreement with the data available in literature [21].

This preliminary calibration test would indicate that this simplified transient hot wire is effective for the measurement of thermal conductivity in liquids. The simplification of the system through removal of the Wheatstone bridge and the shrinking of the axial dimensions of the wire allow for ease in setup. Wheatstone bridges were typically used to measure the wire resistance; however, the Keithley instrumentation allows for direct measurement of the resistance. The smaller dimensions of the wire are beneficial in the reduction of the sample size, which is of importance, to the desired future application of this method.

The Al_2O_3/DI-water nanofluid test samples were produced by first blending the 47 nm diameter spherical Al_2O_3 nanoparticle powder (Nanophase Inc., IL) with degassed distilled water (DI water) and ultrasonically oscillating it for 90 min. A set of different volume fraction Al_2O_3/DI-water nanofluids is generated through 0.5, 2, 4, to 6%, and their effective thermal conductivity was tested with both methods described above. In the previous reports, the stabilization of nanofluids was achieved either by adding surfactants to the nanofluids or changing the pH value of the nanofluids. While without adding extra materials, the nanofluids could also keep stable for a substantial period of time as reported

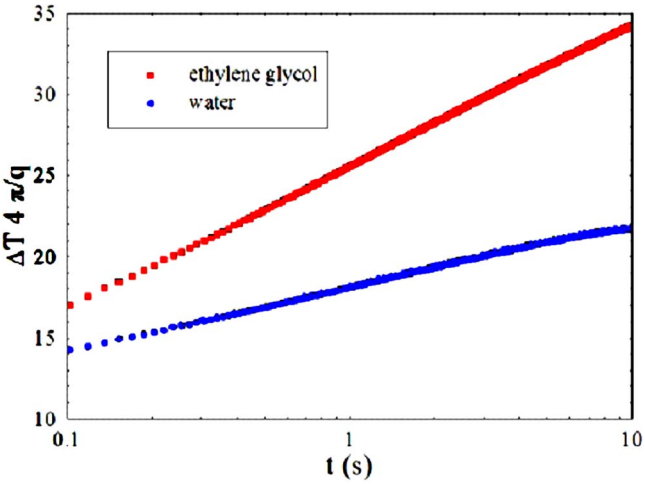

Fig. 8 Measurements of thermal conductivity of water and ethylene glycol [22]

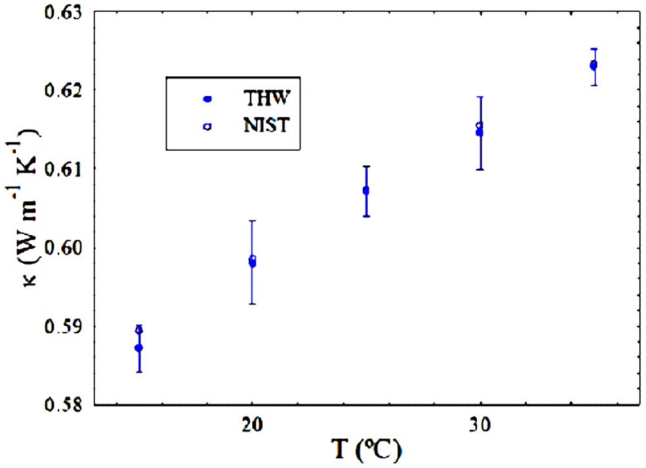

Fig. 9 Measurements of thermal conductivity of water at different temperatures, compared to the tabulated values (NIST) [22]

due to the mechanism of the nanoparticle halos [25,26]. Moreover, adding surfactant and/or changing the pH value may have some influence on the effective thermal conductivity of the nanofluids [8]. In this investigation, no surfactant or pH changes were utilized and the stability of the nanofluids was carefully examined and shown to be very good for a period of at least 48 hours.

Results and Discussions

The effective thermal conductivity of different volume fractions of Al_2O_3/DI-water nanofluids are presented in Fig. 10, and the normalized enhancement of effective thermal conductivity of the nanofluids are compared to pure DI water in Fig. 11, both at room temperature 27.5°C. First, the differences between the data measured by the cut-bar method and the hot-wire method are all within the uncertainty except for the 4% volume fraction. The measured enhancements via the hot-wire method seem to have a linear relationship with the volume fraction at room temperature, similar to what has been reported previously for investigations utilizing hot-wire methods [4,5]. In both figures, at a volume fraction of 4%, the measured value of the hot-wire method is lower than the value measured by the cut-bar method, while at volume fractions of 2% and 6%, the value measured by the hot-wire method is slightly higher. However, as addressed previously, the differences in each pair values are still well within the uncertainty of both methods, with the only exception being the volume fraction of 4%. This difference, however, may be the result of other factors of the testing techniques. The average of the repeated tests

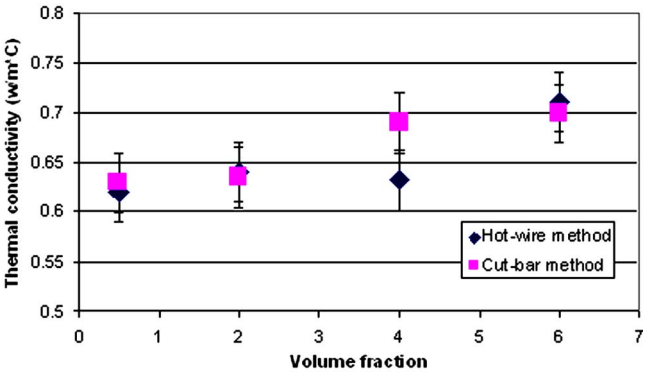

Fig. 10 The comparison of the absolute values measured by the transient method and steady-state method

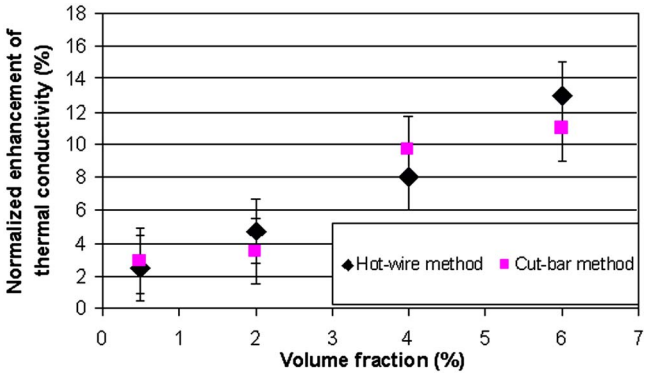

Fig. 11 The comparison of the normalized enhancement measured by the transient method and steady-state method

could eliminate this difference. This distribution also illustrates that there is almost no difference between the two methods regarding the time or technique used to measure the effective thermal conductivity of nanofluids. Because the samples were prepared identically, the effects of the ultrasonic vibration time, the size distribution of the nanoparticles, any possible multibody interactions, nanoparticle shape, and the interfacial phenomena or other thermal property effects that might contribute to the effective thermal conductivity of the nanofluids were minimized.

As shown in Fig. 12, it is apparent that the increase in the effective thermal conductivity of nanofluids (Lee et al., 28 nm diameter Al_2O_3/DI water nanofluids [4], Eastman et al., 33 nm diameter Al_2O_3/DI water nanofluids [5], and Xu and Wang, 28 nm diameter Al_2O_3/DI water nanofluids [10]) does not always assume a linear relationship with the volume fraction, which is not consistent with the predictions of either Maxwell's model (Eq. (5)) [27], Jeffery's model (Eq. (6)) [28], Davis' model (Eq. (7)) [29], or the Hamilton and Crosser model (Eq. (8)) [30], which is the same as Maxwell's for the case where the particle is spherical. This deviation of the experimental data from the theoretical predictions may be due to lack of particle size parameters in the above mentioned models. Moreover, as will be illustrated in Fig. 13, the effective thermal conductivity of each volume fraction nanofluid will increase with an increase in temperature, while the models do not incorporate the effects of different bulk temperatures. The recently introduced new models, namely, Jang and Choi's (Eq. (9)), [31], Prasher's (Eq. (10)), [32], Kumar et al. (Eq. (11)), [34], and Chon et al. (Eq. (12)) [35], all yield much larger predictions of the enhancement of the effective thermal conduc-

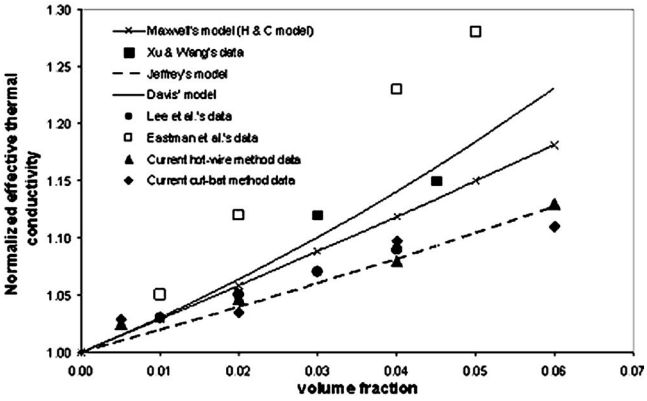

Fig. 12 The comparison of the normalized enhancement measured by the transient method and steady-state method, and other available experimental data and theoretical predictions

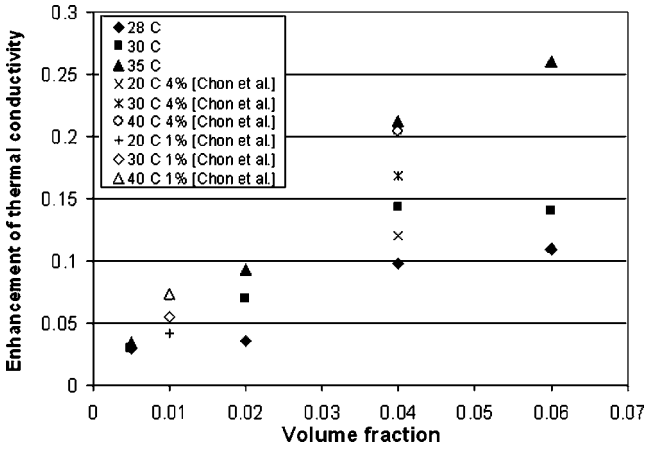

Fig. 13 The comparison of thermal conductivity enhancement of current data and previous report on 47 nm diameter nanofluids [21]

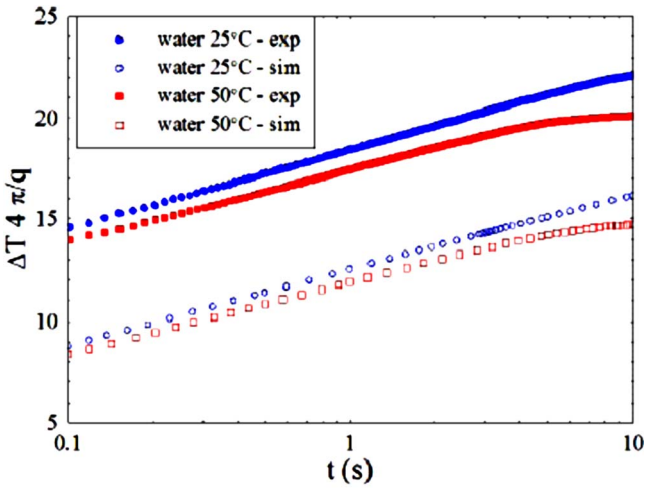

Fig. 14 Comparison between the measurements and numerical simulations for water at 25°C and 50°C [33]

tivity of nanofluids. As a result, a new model, which includes the particle size effect and other parameters, is necessary.

$$\frac{k_{\text{eff}}}{k_1} = 1 + \frac{3(\alpha-1)\phi}{(\alpha+2)-(\alpha-1)\phi} \tag{5}$$

where k_{eff}, is the effective thermal conductivity of the suspension, k_1 is the thermal conductivity of the base fluid, α is the ratio of the thermal conductivities of the nanoparticle and base fluid, and ϕ is the volume fraction of the nanoparticle suspension. In this equation, Maxwell assumed that the potentials at the interface were continuous and equal, thus the current passing through the interface of the two media would be the same [27]. However, the interfacial thermal resistance is not negligible in the nanoscale, and the current passing through will be severely affected.

$$k/k_1 = 1 + 3\beta\phi + 3\beta\phi^2\left(\beta + \sum_{p=6}^{\infty}\frac{B_p - 3A_p}{(p-3)2^{p-3}}\right) \tag{6}$$

where $\beta=(\alpha-1)/(\alpha-2)$, volume fraction $\phi=4/3\pi a^3 n$, a is the radius of the particle, $\alpha=k_2/k_1$, P is the probability density for a second sphere located at r from the center of the reference sphere, and A_p and B_p are known coefficients. Jeffrey considered the interactions between the various pairs of spheres using a second order expression of the volume ratio between the particles and the fluid [28].

$$k_{\text{eff}}/k_1 = 1 + \frac{3(\alpha-1)}{[\alpha+2-(\alpha-1)\phi]}\{\phi + f(\alpha)\phi^2 + 0(\phi^3)\} \tag{7}$$

where $f(\alpha)=\Sigma_{p=6}^{\infty}\{(B_p-3A_p)/[(p-3)2^{p-3}]\}$ was used to represent the decaying temperature field. By developing this equation, Davis, fully aware of the difficulty of integral convergence encountered in earlier investigations, considered a situation where inside the composite material, the undisturbed temperature gradient varied inversely with the square of the distance from the heated body [29].

$$k = k_1\left[\frac{k_2 + (n-1)k_1 - (n-1)\phi(k_1-k_2)}{k_2 + (n-1)k_1 + \phi(k_1-k_2)}\right] \tag{8}$$

where k_2 is the thermal conductivity of the nanoparticle, $n=3/\psi$ for spherical particles, $n=3/\psi^2$ for prolated ellipsoids, and $n=3/\psi^{1.5}$ for oblate ellipsoids. In this model, Hamilton and Crosser further developed Maxwell's equation by including the shape factor [30].

$$k_{\text{eff}} = k_1(1-\phi) + k_2\phi + 3C_1\frac{d_{\text{BF}}}{d_{\text{nano}}}k_1\,\text{Re}_{\text{dnano}}^2\,\text{Pr}\,\phi \tag{9}$$

where C_1 is the constant, f is the volume fraction, d_{BF} and d_{nano} are the diameter of the base fluid molecule and nanoparticle, respectively, Re_{dnano} is the Reynolds number based on the diameter of the nanoparticle, and Pr is the Prandtl number. In this model, the adorption layer of fluid molecules was considered by Jang and Choi [31].

$$\frac{k_{\text{eff}}}{k_1} = (1 + A\,\text{Re}^m\,\text{Pr}^{0.333}\,\phi)\left[\frac{(1+2\alpha)+2\phi(1-\alpha)}{(1+2\alpha)-\phi(1-\alpha)}\right] \tag{10}$$

where m is a constant. Prasher et al. [32] developed this equation based on the model of heat convection between particle and surrounding fluid by Acrivos and Taylor [33].

$$\frac{k_{\text{eff}}}{k_1} - 1 = c\cdot\bar{u}_p\frac{\phi r_m}{k_1(1-\phi)r_p} \tag{11}$$

where c is a constant, $\bar{u}_p$ is the velocity of the nanoparticle, and r_m and r_p are the radius of the base fluid molecule and nanoparticle. This equation was developed by Kumar et al. [34].

$$k_{\text{eff}}/k_1 = 1 + \text{const}(1/d_p)^{0.369}(T^{1.2321}/10^{2.4642B/(T-C)}) \tag{12}$$

where T is absolute temperature, and B and C are constants. This model was an empirical model, which was based on the hot-wire method experimental data by Chon et al. [35].

Finally, although the effective thermal conductivities at higher temperatures were not measured using the transient hot-wire method, the comparison of the normalized effective thermal conductivities between the steady-state cut-bar method and previous report of transient hot-wire method was conducted [30]. In both sets of measurements, the Al_2O_3 nanoparticles used were purchased from a commercial source and were all the same 47 nm diameter spherical shape and had the same γ crystal phase. Hence the validity of this comparison is quite reasonable.

As illustrated in Fig. 13, at the higher temperature, the values of the normalized effective thermal conductivities at the same volume fraction tested by the transient hot-wire method are much higher than the corresponding values tested by steady-state cut-bar method. One possible explanation for this is that the onset of natural convection as explained by Fig. 14 [24], which pointed out that in both cases at temperatures of 25°C and 50°C, the trend is slightly affected by the buoyancy at 25°C, and even more so at 50°C. This effect is much more evident at the higher temperatures and the simulation model presented above correctly predicts this change and the onset of convection.

Conclusions

The comparison between the measured values of the sample set of Al_2O_3/DI-water nanofluids samples shows good agreement between the transient hot-wire method and steady-state cut-bar method at room temperatures. The results confirm that the observed enhancement of the thermal conductivity of Al_2O_3/water nanofluids exists and is independent of the measurement technique. In addition, the existing models have been expanded to incorporate a method by which the effect of the temperature on the effective thermal conductivity can be incorporated. These expanded models need then to be verified and improved to accurately represent the effect of temperature on the effective thermal conductivity Al_2O_3/water nanofluids at different volume fractions.

Acknowledgment

The authors acknowledge the support of the Office of the National Science Foundation through Grant No. CTS-0312848 and Idaho National Laboratory through Grant No. 063, Release 18, and Department of Energy through "Innovations in Nuclear Infrastructure and Education" Grant No. DOE-FG07-02ID14420.

References

[1] Nagasaka, Y., and Nagashima, A., 1981, "Absolute Measurement of the Thermal Conductivity of Electrically Conducting Liquids by the Transient Hot-Wire Method," J. Phys. E, **4**, pp. 1435–1439.

[2] Choi, S. U. S., 1995, "Enhancing Thermal Conductivity of Fluids With Nanoparticles," *Developments and Applications of Non-Newtonian Flows*, D. A. Siginer and H. P. Wang, eds. ASME, New York.

[3] Eastman, J. A., Choi, S. U. S., Li, S., Thompson, L. J., and Lee, S., 1997, "Enhanced Thermal Conductivity Through the Development of Nanofluids," *Nanophase and Nanocomposite Material II*, S. Komarneni, J. C. Parker, and H. J. Wollenberger, eds., Mater. Res. Soc. Symp. Proc., Warrendale, PA, 457, pp. 9–10.

[4] Lee, S., Choi, S. U. S., Li, S., and Eastman, J. A., 1999, "Measuring Thermal Conductivity of Fluids Containing Oxide Nanoparticles," ASME J. Heat Transfer, **121**, pp. 280–289.

[5] Eastman, J. A., Choi, S. U. S., Li, S., Yu, W., and Thompson, L. J., 2001, "Anomalously Increased Effective Thermal Conductivities of Ethylene Glycol-Based Nanofluids Containing Copper Nanoparticles," Appl. Phys. Lett., **78**(6), pp. 718–720.

[6] Xuan, Y., and Li, Q., 2000, "Heat Transfer Enhancement of Nanofluids," Russ. J. Eng. Thermophys., **20**(4), pp. 465–470 (in Chinese).

[7] Xuan, Y., and Li, Q., 2000, "Heat Transfer Enhancement of Nanofluids," Int. J. Heat Fluid Flow, **21**, pp. 58–64.

[8] Xie, H., Wang, J., Xi, T., Liu, Y., and Ai, F., 2002, "Dependence of the Thermal Conductivity of Nanoparticle-Fluid Mixture on the Base Fluid," J. Mater. Sci. Lett., **21**, pp. 1469–1471.

[9] Xie, H., Wang, J., Xi, T., Liu, Y., and Ai, F., 2002, "Thermal Conductivity Enhancement of Suspensions Containing Nanosized Alumina Particles," J. Appl. Phys., **91**(7), pp. 4568–4572.

[10] Wang, X., Xu, X., and Choi, S. U., 1999, "Thermal Conductivity of Nanoparticle-Fluid Mixture," J. Thermophys. Heat Transfer, **13**(4), pp. 474–480.

[11] Vadasz, J. J., Govender, S., and Vadasz, P., 2005, "Heat Transfer Enhancement in Nano-Fluids Suspensions: Possible Mechanisms and Explanations," Int. J. Heat Mass Transfer, **48**(13), pp. 2673–2683.

[12] Peterson, G. P., and Fletcher, L. S., 1987, "Effective Thermal Conductivity of Sintered Heat Pipe Wicks," Int. J. Thermophys., **1**(4), pp. 343–347.

[13] Peterson, G. P., and Fletcher, L. S., 1988, "Thermal Contact Conductance of Packed Beds in Contact With a Flat Surface," ASME J. Heat Transfer, **110**(1), pp. 38–41.

[14] Peterson, G. P., and Fletcher, L. S., 1989, "On the Thermal Conductivity of Dispersed Ceramics," ASME J. Heat Transfer, **111**, pp. 824–829.

[15] Duncan, A. B., Peterson, G. P., and Fletcher, L. S., 1989, "Effective Thermal Conductivity Within Packed Beds of Spherical Particles," ASME J. Heat Transfer, **111**(4), pp. 830–836.

[16] Miller, R. G., and Fletcher, L. S., 1974, "A Facility for the Measurement of Thermal Contact Conductance," *Proceedings of the Tenth Southeastern Seminar on Thermal Sciences*, New Orleans, LA, pp. 263–285.

[17] Kim, B. H., and Peterson, G. P., 2007, "Effect of Morphology of Carbon Nanotubes on Thermal Conductivity Enhancement of Aqueous Nanofluids," J. Thermophys. Heat Transfer, **21**, pp. 451–459.

[18] Li, C. H., and Peterson, G. P., 2006, "Experimental Investigation of Temperature and Volume Fraction Variations on the Effective Thermal Conductivity of Nanoparticle Suspensions," J. Appl. Phys., **99**, p. 084314.

[19] Peterson, G. P., and Li, H. C., 2005, *Advances in Heat Transfer*, Vol. 39, J. P. Hartnett and T. F. Irvine, eds., Pergamon, New York, pp. 261–392.

[20] Miller, R. G., and Fletcher, L. S., 1974, "A Facility for the Measurement of Thermal Contact Conductance," *Proceedings of the Tenth Southeastern Seminar on Thermal Sciences*, New Orleans, LA, pp. 263–285.

[21] Yaws, C. L., 1999, *Chemical Property Handbook, Physical, Thermodynamic, Environmental, Transport, Safety, and Health Related Properties for Organic and Inorganic Chemicals*, 1st ed., McGraw-Hill, New York, p. 1311.

[22] Li, H. C., and Peterson, G. P., 2007, "Size Effect on the Effective Thermal Conductivity of Al_2O_3/Di Water Nanofluids," J. Appl. Phys., **101**, p. 044312.

[23] Williams, W. C., 2006, "Experimental and Theoretical Investigation of Transport Phenomena in Nanoparticle Colloids (Nanofluids)," Doctoral dissertation, the Department of Nuclear Science and Engineering, Massachusetts Institute of Technology.

[24] Rusconi, R., Williams, W. C., Buongiorno, J. Piazza, R., and Hu, L. W., 2007, "Numerical Analysis of Convective Instabilities in a Transient Short-Hot-Wire Setup for Measurement of Liquid Thermal Conductivity," Int. J. Theor. Phys., in press.

[25] Tohver, V., Chan, A., Sakurada, O., and Lewis, J. A., 2001, "Nanoparticle Engineering of Complex Fluid Behavior," Langmuir, **17**, pp. 8414–8421.

[26] Tohver, V., Smay, J. E., Braem, A., Braun, P. V., and Lewis, J. A., 2001, "Nanoparticle Halos: A New Colloid Stabilization Mechanism," Proc. Natl. Acad. Sci. U.S.A., **98**, pp. 8950–8954.

[27] Maxwell, J. C., 1892, *A Treatise on Electricity and Magnetism*, Vol. I, 3rd ed., Oxford University Press, New York.

[28] Jeffrey, D. J., 1973, Proc. R. Soc. London, Ser. A, **335**, pp. 355–367.

[29] Davis, R. H., 1986, "The Effective Thermal Conductivity of a Composite Material With Spherical Inclusions," Int. J. Thermophys., **7**, pp. 609–620.

[30] Hamilton, R. L., and Crosser, O. K., 1962, "Thermal Conductivity of Heterogeneous Two-Component Systems," Ind. Eng. Chem. Fundam., **1**(3), pp. 187–191.

[31] Jang, S. P., and Choi, S. U. S., 2004, "Role of Brownian Motion in the Enhanced Thermal Conductivity of Nanofluids," Appl. Phys. Lett., **84**, pp. 4316–4318.

[32] Prasher, R., Bhattacharya, P., and Phelan, P. E., 2005, "Thermal Conductivity of Nanoscale Colloidal Solutions (Nanofluids)," Phys. Rev. Lett., **94**, p. 025901.

[33] Acrivos, A., and Taylor, T. D., 1962, "Heat and Mass Transfer From Single Spheres in Stokes Flow," Phys. Fluids, **5**, pp. 387–394.

[34] Kumar, D. H., Patel, H. E., Kumar, V. R. R., Sundararajan, T., Pradeep, T., and Das, S. K., 2004, "Model for Heat Conduction in Nanofluids," Phys. Rev. Lett., **93**, p. 144301.

[35] Chon, C. H., Kim, K. D., Lee, S. P., and Choi, S. U. S., 2005, "Empirical Correlation Finding the Role of Temperature and Particle Size for Nanofluid (Al_2O_3) Thermal Conductivity Enhancement," Appl. Phys. Lett., **87**, p. 153107.

Thermal Conductivity Equations Based on Brownian Motion in Suspensions of Nanoparticles (Nanofluids)

Bao Yang
e-mail: baoyang@umd.edu
Nanoscale Heat Transfer and Energy Conversion Laboratory,
Mechanical Engineering Department,
University of Maryland,
College Park, MD 20742

Thermal conductivity equations for the suspension of nanoparticles (nanofluids) have been derived from the kinetic theory of particles under relaxation time approximations. These equations, which take into account the microconvection caused by the particle Brownian motion, can be used to evaluate the contribution of particle Brownian motion to thermal transport in nanofluids. The relaxation time of the particle Brownian motion is found to be significantly affected by the long-time tail in Brownian motion, which indicates a surprising persistence of particle velocity. The long-time tail in Brownian motion could play a significant role in the enhanced thermal conductivity in nanofluids, as suggested by the comparison between the theoretical results and the experimental data for the Al_2O_3*-in-water nanofluids.* [DOI: 10.1115/1.2789721]

Keywords: nanofluids, thermal conductivity, Brownian motion, relaxation time, nanoparticles

Nanofluids are suspensions of high thermal conductivity nanoparticles that offer the potential to surpass the performance of conventional heat transfer fluids [1–10]. Unusually high thermal conductivity enhancement has been experimentally reported in various nanofluid systems [2–8]. A strong dependence of conductivity enhancement on temperature has also been observed. However, existing theories have difficulties explaining these observed abnormal behaviors. Traditional thermal conductivity theories for composites, such as the effective medium theory (EMT), were initially developed by Maxwell in 1873 [11]. According to the EMT, thermal conductivity of nanofluids containing a low volume fraction of high thermal conductivity spherical particles is [11,12]

$$k_{\text{diff}} = k_f\left(1 + 3\Phi\frac{\alpha - 1}{\alpha + 2}\right) \tag{1}$$

where k_f is the thermal conductivity of the base fluids, Φ the volume fraction of the particles, and $\alpha = r_p/R_b k_f$, r_p is the particle radius and R_b is the thermal resistance per unit area of the particle/fluid interface. Equation (1) has been successfully applied to explain thermal conductivity of solid-solid composites in which heat is transported by diffusive conduction, but cannot explain by itself the abnormal conductivity enhancement in nanofluids.

Recently, a number of theoretical studies have been published to explain the thermal conductivity enhancement of nanofluids, but the mechanisms of the thermal conductivity enhancement are still under hot debate [9,10,13–18]. In this paper, thermal conductivity equations in nanofluids are derived based on the kinetic theory of particles dispersed in the fluids. These equations take into account fluid convective heat transfer caused by the Brownian movement of nanoparticles. It is also found that the relaxation time of particle Brownian motion could be significantly affected by the long-time tail in Brownian motion, which indicates a surprising persistence of particle velocity.

Contributed by the Heat Transfer Division of ASME for publication in the JOURNAL OF HEAT TRANSFER. Manuscript received January 24, 2007; final manuscript received March 4, 2007; published online March 18, 2008. Review conducted by Christopher Dames. Paper presented at the ASME 2006 Energy Nanotechnology International Conference (ENIC2006), Boston, MA, June 26–28, 2006.

Nanoparticles in the fluids are small enough to be affected by Brownian motion due to collisions with surrounding thermal molecules [19]. The particle motion may cause fluid convection to promote heat transfer in nanofluids. To evaluate the contribution of such fluid convection on thermal transport in nanofluids, a thermal conductivity equation will be derived, starting by making the following assumptions.

1. Heat is transported in nanofluids primarily by two parallel paths: one is by diffusive conduction of the fluids and the nanoparticles, the other is by fluid convection caused by the particle Brownian motion. The overall heat transfer rate in nanofluids, q_{tot}, can be expressed as $q_{\text{tot}} = q_{\text{diff}} + q_B$, where subscripts diff and B denote the contributions from the diffusive heat conduction and the particle Brownian motion, respectively. Consequently, the effective thermal conductivity of the nanofluids, k_{tot}, is

$$k_{\text{tot}} = k_{\text{diff}} + k_B \tag{2}$$

   where k_{diff} can be evaluated from Eq. (1).
2. The nanoparticles are distinguishable from one another and can be treated as classical particles.
3. Each single particle executes a movement, which is independent of the movement of all other particles. Due to this assumption, the thermal conductivity equations derived below are applicable to nanofluids with low volume fractions of particles.
4. In the absence of external forces (gravity can be neglected), there is no preferred position for a nanoparticle, and there is no preferred direction for the velocity.
5. Nanoparticles in suspensions are small enough to be affected by Brownian motion, but still large enough for the fluid to be treated as a continuum.

Let us consider a nanofluid in an imaginary cylindrical container with each end wall having area A. A stationary coordinate system (X, Y, Z) is defined so that the origin is positioned in an arbitrary plane between the two end walls, and the Z axis is along the cylinder, as illustrated in Fig. 1. In addition, a local coordinate

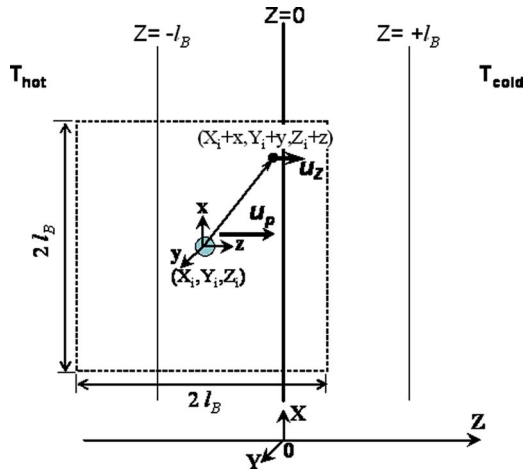

Fig. 1 A nanoparticle with coordinates (X_i, Y_i, Z_i) moves at velocity u_p toward the $Z=0$ plane. The origin of the local coordinate system (x, y, z) is at the center of the moving particle. The hydrodynamic layer thickness is l_B.

system (x,y,z) is defined with its origin at the center of a moving particle (for example, particle i in Fig. 1) and x, y, and z axes are parallel to X, Y, and Z axes, respectively. A temperature gradient, dT/dZ, exists along the Z axis, so heat transports in the $+Z$ direction. The nanofluid has a particle number density of n.

Heat that is transported through the $Z=0$ plane by fluid convection caused by the particle Brownian motion will be examined to determine the k_B. Consider a nanoparticle i located in (X_i, Y_i, Z_i) and moving at a velocity of u_p in the $+Z$ direction, as shown in Fig. 1. According to the equipartition theorem, the mean squared velocity of a Brownian particle can be defined as [19,20]

$$u_p^2 = \frac{3K_BT}{m_p} \tag{3}$$

where K_B is the Boltzmann constant, T the temperature in Kelvin, and m_p the particle mass. As a result of the particle movement, fluid flow near the particle is developed. The fluid flow is characterized by two distinct regions: the hydrodynamic boundary layer and a region outside the boundary layer in which the fluid motion is negligible. The boundary layer thickness l_B is typically defined as the value of r for which $u(r)=0.01u_p$ [21]. In general, l_B is much larger than the mean free path of a Brownian particle, τu_p, since τu_p is of the order of the particle size [19,20]. Here, τ is the relaxation time of the particle, providing a measure of the time required for a particle to forget its initial velocity. A steady fluid flow during the time interval τ is assumed for simplicity in evaluating the heat transfer rate by the fluid flow.

Given the fluid velocity field $u(x,y,z)$ around the particle i, as illustrated in Fig. 1, the amount of thermal energy across the $Z=0$ plane during the time interval τ that is carried with the fluid flow is

$$Q_i(Z_i) = \int_{x=-l_B}^{l_B}\int_{y=-l_B}^{l_B} C_f T(Z=-\tau u_z) u_z(x,y,z=-\tau u_z - Z_i)\,\tau dxdy \tag{4}$$

where C_f is the heat capacity per unit volume of the fluid, $T(Z)$ the fluid temperature, and u_z the Z component of the fluid velocity. Q_i varies with the particle coordinate Z_i, i.e., the distance between the particle and the $Z=0$ plane, but does not depend on its X or Y coordinates.

If particles move in the $\pm X$ and $\pm Y$ directions, it can be assumed that they have negligible contribution to heat transport in the Z direction because the fluid temperature varies only in the Z direction. Since particles move randomly in all directions, 1/6 of the total particles, on the average, move in the $+Z$ direction, and an equal number in the reverse direction [22,23]. The number of particles that travel in the $+Z$ direction and are located between the $Z=-l_B-\tau u_p$ and $Z=l_B-\tau u_p$ planes is $nAl_B/3$. These $nAl_B/3$ particles will stimulate fluid flow passing across the $Z=0$ plane in the $+Z$ direction during the time interval τ. Therefore, the total thermal energy that is transported through the $Z=0$ plane in the $+Z$ direction during time interval τ by the stimulated fluid flow is

$$\begin{aligned} Q_+ &= \sum_{i=1}^{nAl_B/3} Q_i(Z_i) = \sum_{i=1}^{nAl_B/3} \int_{x=-l_B}^{l_B}\int_{y=-l_B}^{l_B} C_f T(-\tau u_z) \\ &\quad \times u_z(x,y,z=-\tau u_z - Z_i)\,\tau dxdy \\ &= \frac{nA}{6} C_f \tau \int_{Z=-l_B-\tau u_p}^{l_B-\tau u_p}\int_{x=-l_B}^{l_B}\int_{y=-l_B}^{l_B} T(-\tau u_z) \\ &\quad \times u_z(x,y,z=-\tau u_z - Z)dxdydZ \end{aligned} \tag{5}$$

where the summation over i can be replaced by integration over Z when the particle number density is not extremely low, i.e., $n \gg 1/Al_B$. Similarly, the thermal energy transported in the $-Z$ direction is

$$\begin{aligned} Q_- &= \frac{nA}{6} C_f \tau \int_{Z=-l_B-\tau u_p}^{l_B-\tau u_p}\int_{x=-l_B}^{l_B}\int_{y=-l_B}^{l_B} T(\tau u_z) u_z \\ &\quad (x,y,z=-\tau u_z - Z)dxdydZ \end{aligned} \tag{6}$$

Although an equal amount of mass flow (fluid) passes through the $Z=0$ plane in the $-Z$ direction, it carries lower thermal energy than those in the $+Z$ direction because the temperature T decreases with increasing Z. Hence, the net heat transfer is

$$\begin{aligned} Q_{\text{net}} &= Q_+ - Q_- \\ &= -\frac{nA}{3} C_f \tau^2 \frac{dT}{dZ} \\ &\quad \times \int_{Z=-l_B-\tau u_p}^{l_B-\tau u_p}\int_{x=-l_B}^{l_B}\int_{y=-l_B}^{l_B} u_z^2(x,y,z=-\tau u_z - Z)dxdydZ \end{aligned} \tag{7}$$

Recalling that $l_B \gg \tau u_p$, the Q_{net} can be written as

$$Q_{\text{net}} = -\frac{nA}{3} C_f \tau^2 \frac{dT}{dZ} \iiint_{V_B} u_z^2(x,y,z)dxdydz \tag{8}$$

where the squared velocity is integrated over the hydrodynamic boundary layer. Comparison of Eq. (8) with Fourier's law of heat conduction leads to the following expression for the k_B:

$$k_B = \frac{1}{3} n C_f \tau \iiint_{V_B} u_z^2(x,y,z)dxdydz \tag{9}$$

where u_z is the Z component of the fluid velocity. Equation (9) is the general form of the thermal conductivity equation that describes the contribution of fluid convection caused by the particle Brownian motion to heat transport in nanofluids. It is interesting that this expression is similar to the thermal conductivity equation for solids $k=Cu^2\tau/3$. According to Eq. (9), k_B is proportional to n, C_f, and τ, and depends on the integration of the square of the fluid velocity over the entire boundary layer.

The flow velocity can be obtained in theory by solving the integral momentum and kinetic energy equations. The Reynolds number based on u_p given by Eq. (3) can be written as $\text{Re}=2r_p u_p \rho_f/\mu_f$, where μ is the dynamic viscosity, ρ is the mass density, and subscripts p and f denote the particles and the fluids, respectively. For the Brownian particles in the fluid, Re is inversely proportional to $\sqrt{r_p}$. For example, the Re for 40 nm Al_2O_3

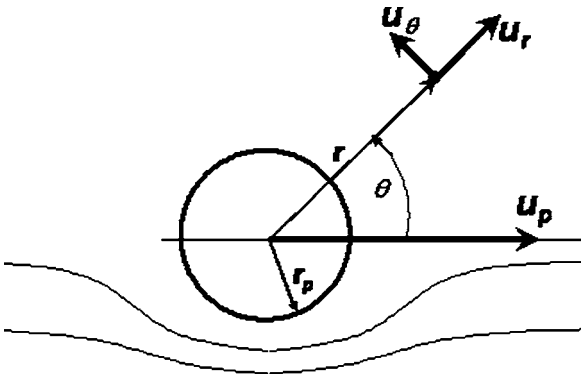

Fig. 2 Stokes flow around a spherical particle moving at u_p in the fluid. The origin of the local spherical coordinate system is at the center of the particle.

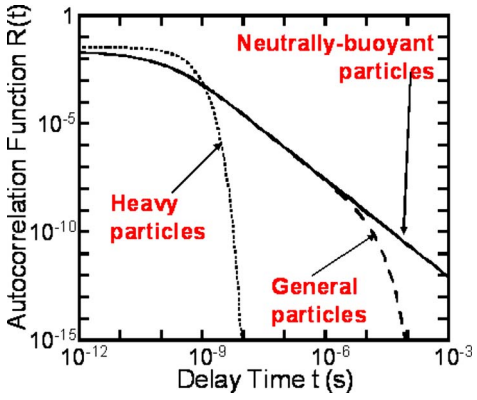

Fig. 3 The velocity autocorrelation function $R(t)$ evaluated using Eq. (13) (heavy particle approximation), Eq. (15) (neutrally buoyant particle approximation), and Eq. (16) (general particle, $M=0.999967$). $\rho_p=3.9$ g/cm^3 (alumina), $\rho_f=1.0$ g/cm^3 (water), and $a=23.5$ nm.

particles in water, Re=0.058, is very small and therefore the convective flow falls in the Stokes regime. The Stokes flow caused by a moving sphere is illustrated in Fig. 2. Assuming an incompressible fluid, the integral momentum and kinetic energy equations for the Stokes flow around a moving sphere can be solved analytically [21]:

$$u_r = u_p \cos\theta\left[\frac{3}{2}\left(\frac{r_p}{r}\right) - \frac{1}{2}\left(\frac{r_p}{r}\right)^3\right],$$

$$u_\theta = u_p \sin\theta\left[-\frac{3}{4}\left(\frac{r_p}{r}\right) - \frac{1}{4}\left(\frac{r_p}{r}\right)^3\right] \tag{10}$$

Substituting Eq. (10) to Eq. (9) and performing some straightforward but tedious integration, we obtain the thermal conductivity equation for spherical particles:

$$k_B = 157.5\Phi C_f u_p^2 \tau \tag{11}$$

where $\Phi=((4/3)\pi r_p^3)n$ is the volume fraction of the particles, C_f is the heat capacity per unit volume of the fluid (not the particles), u_p is the Brownian velocity of the particle, and τ is the particle relaxation time. Please note that the proportionality 157.5 is not a fitting constant, but is strictly obtained from the analytical integration of the fluid velocity over the hydrodynamic boundary layer around the Brownian particle. This thermal conduction equation (Eq. (11)) in nanofluids is virtually parameter free, and reveals how the k_B in nanofluids depends on the fundamental properties of the particles and the fluids. C_f, u_p, and Φ can be obtained relatively easily, but the particle relaxation time τ is difficult to be determined both experimentally and theoretically.

The relaxation time of particle Brownian motion must be related to the velocity correlation function $R(t)$ that is defined as $R(t)=\langle u(t_0)u(t_0+t)\rangle$ [20]. If $R(t)$ is given, τ could be evaluated as

$$\tau = \frac{\int_0^\infty tR(t)dt}{\int_0^\infty R(t)dt} \tag{12}$$

If the $R(t)$ has an exponential form, $\exp(-t/\tau_0)$, $\tau=\tau_0$ according to Eq. (12).

The Langevin equation, in which the random fluctuating force is balanced with the particle inertia and the pseudosteady Stokes drag, is often used to calculate the velocity autocorrelation $R(t)$. The solution to the Langevin equation leads to [20]

$$R_{\text{hp}}(t) = \frac{K_B T}{m_p}\exp\left(-\frac{6\pi\mu_f r_p}{m_p}t\right) \tag{13}$$

and

$$\tau = \frac{m_p}{6\pi\mu_f r_p} \tag{14}$$

where the subscript hp denotes heavy particles. The Langevin equation does not consider the effects of the inertia of the fluid surrounding the particle. Therefore, it can be used to evaluate the velocity autocorrelation only when the mass density of particles is much larger than the fluid density, i.e., $\rho_p/\rho_f\to\infty$. For general particles, a long-time tail in the velocity autocorrelation function $R(t)$, i.e., a surprising persistence of the particle velocity, has been observed both theoretically and experimentally [24,25]. The long-time tail in Brownian motion should have a significant effect on the relaxation time of the Brownian particles. The Langevin equation fails to describe this phenomenon. Unfortunately, there is no analytic solution to the velocity autocorrelation function $R(t)$ of general particles when the fluid inertia is considered. For neutrally buoyant particles, i.e., $\rho_p/\rho_f=1$, several different approaches were pursued to take into account the fluid inertia in literature and the following expression was obtained [26,27]:

$$R_{\text{np}}(t) = \frac{2}{3}\frac{K_B T}{m_p}\text{Im}\left\{(\sqrt{3}+I)\exp\left[(\sqrt{3}+I)^2\frac{3\mu_f}{4r_p^2\rho_f}t\right]\times\text{erfc}\left[(\sqrt{3}+I)\sqrt{\frac{3\mu_f}{4r_p^2\rho_f}t}\right]\right\} \tag{15}$$

where Im[z] gives the imaginary part of the complex number z and I is an imaginary unit. In general cases, the particle mass density falls in between the two extreme cases of $\rho_p/\rho_f=1$ and $\rho_p/\rho_f\to\infty$. In this work, a weighted average of the velocity autocorrelation function is used for the τ evaluation,

$$R(t) = R_{\text{np}}^M(t)R_{\text{hp}}^{1-M}(t) \tag{16}$$

where M is a weighting parameter and should lie between 0 and 1. The M is treated as a fitting parameter here since there is no simple way to calculate it. For very large particles or very viscous fluids, τ goes to zero according to Eqs. (12)–(16), and thus Eq. (2) reduces to the EMT.

The velocity autocorrelation function versus delay time is plotted in Fig. 3 for Brownian particles using each of the above formulations (Eqs. (13), (15), and (16)). In short-time limit, $R_{\text{np}}(0^+)$ is smaller than $R_{\text{hp}}(0^+)$ due to the added mass from the fluid to the particle. In long-time limit, R_{np} has a long tail, rather than decay-

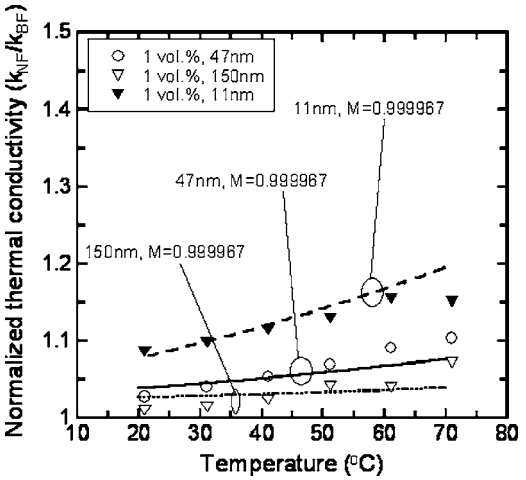

Fig. 4 Comparison of the thermal conductivity equations with experimental data for nanofluids consisting of Al_2O_3 nanoparticles dispersed in water, for varying temperatures and particle diameters. Experimental data are from Ref. 5.

ing exponentially as R_{hp}. The weighted average of $R(t)$ lies in between R_{np} and R_{np}. It is clear from Fig. 3 that (1) different expressions for the velocity autocorrelation function will lead to very different relaxation time, and (2) the Langevin equation might significantly underestimate the relaxation time of Brownian particles.

As an example, the derived thermal conductivity equations and the formula for evaluating the relaxation time are applied to an Al_2O_3-in-water nanofluid system, as shown in Fig. 4. It can be seen in Fig. 4 that these equations could explain the thermal conductivity enhancement observed in Al_2O_3-in-water nanofluids by assuming $M=0.999967$ for all fluid temperatures and particle diameters. Most importantly, the basic trends observed experimentally are captured by these equations, that is, the thermal conductivity enhancement in nanofluids increases with increasing temperature and with decreasing nanoparticle size. The dynamic viscosity of the fluid μ_f and the Brownian velocity of the particle u_p would be primarily responsible for the experimentally observed strong temperature dependence of the conductivity enhancement in nanofluids.

Please note that the weighting parameter M used in the evaluation of the particle relaxation time depends on the ratio of mass density of the particles and the fluid, as shown in Eq. (15), $M=0$ for $\rho_p/\rho_f \to \infty$ and $M=1$ for $\rho_p/\rho_f=1$. To fit the experimental data in the Al_2O_3-in-water nanofluids, M is chosen to be 0.999967. $M=0.999967$ might not be necessarily inconsistent with the fact that $\rho_p \sim 4\rho_f$ since M represents the average of $\rho_p \to \infty$ and $\rho_p=\rho_f$. In the end, however, the real value of M and also the relaxation time need to be determined experimentally. If the fitting value of M is larger than its real value, it implies that the contribution of particle Brownian is overestimated and other mechanisms such as particle aggregation should be considered.

In comparison with the derived thermal conductivity equations, the EMT (Eq. (1)) predicts that, assuming $R_b=7.7 \times 10^{-9}$ K m^2/W [15], the thermal conductivity enhancements in Al_2O_3-in-water nanofluids are 0.2%, 1.7%, and 2.5% for $d_p=11$ nm, 47 nm, and 150 nm, respectively. The predicted conductivity enhancement shows little dependence on the fluid temperature. When compared to the experimental data shown in Fig. 4, the EMT underpredicts the data and completely fails to explain dependence of the thermal conductivity enhancement on the fluid temperature and the particle size.

In summary, thermal conductivity equations have been established to evaluate the contribution of Brownian motion of nanoparticles dispersed in fluids. These equations are derived from the kinetic theory of particles in the fluids under relaxation time approximations, taking into account the convective heat transfer that is caused by the particle Brownian motion. The long-time tail in Brownian motion, i.e., the surprising persistence of particle velocity due to the fluid inertia, could play a significant role in thermal transport in nanofluids. Future experiments are needed to assess the effects of the long-time tail in Brownian motion on the relaxation time of nanoparticles in fluids.

Acknowledgment

The author acknowledges the support of the Department of Energy (DOE) and National Science Foundation (NSF).

This paper was presented at First Energy Nanotechnology International Conference, June 26–28, 2006, Cambridge, MA, and selected for possible publication in the special JHT issue on Energy Nanotechnology. During the review process of this paper, a paper entitled "Stochastic Thermal Transport Of Nanoparticle Suspensions" by Xuan et al. was published in Journal of Applied Physics, Vol. 100, August 21, 2006.

References

[1] Masuda, H., Ebata, A., Teramae, K., and Hishinuma, N., 1993, "Alteration of Thermal Conductivity and Viscosity of Liquid by Dispersing Ultra-Fine Particles (Dispersion of γ-Al_2O_3, SiO_2 and TiO_2 Ultra-Fine Particles)," Netsu Bussei, **4**, pp. 227–233.

[2] Eastman, J. A., Choi, S. U. S., Li, S., Yu, W., and Thompson, L. J., 2001, "Anomalously Increased Effective Thermal Conductivities of Ethylene Glycol-Based Nanofluids Containing Copper Nanoparticles," Appl. Phys. Lett., **78**, pp. 718–720.

[3] Das, S. K., Putra, N., Thiesen, P., and Roetzel, W., 2003, "Temperature Dependence of Thermal Conductivity Enhancement for Nanofluids," ASME J. Heat Transfer, **125**, pp. 567–574.

[4] Patel, H. E., Das, S. K., Sundararajan, T., Sreekumaran Nair, A., George, B., and Pradeep, T., 2003, "Thermal Conductivities of Naked and Monolayer Protected Metal Nanoparticle Based Nanofluids: Manifestation of Anomalous Enhancement and Chemical Effects," Appl. Phys. Lett., **83**, pp. 2931–2933.

[5] Chon, C. H. K., Khim, K. D., Lee, S. P., and Choi, S. U. S., 2005, "Empirical Correlation Finding the Role of Temperature and Particle Size for Nanofluid (Al_2O_3) Thermal Conductivity Enhancement," Appl. Phys. Lett., **87**, p. 153107.

[6] Yang, B., and Han, Z. H., 2006, "Thermal Conductivity Enhancement in Water-in-FC72 Nanoemulsion Fluids," Appl. Phys. Lett., **88**, p. 261914; also selected for the July 11, 2006 issue of the Virtual Journal of Nanoscale Science and Technology, http://www.vjnano.org.

[7] Yang, B., and Han, Z. H., 2006, "Temperature-Dependent Thermal Conductivity of Nanorods-Based Nanofluids," Appl. Phys. Lett., **89**, p. 083111; also selected for the September 4, 2006 issue of the Virtual Journal of Nanoscale Science and Technology, http://www.vjnano.org.

[8] Han, Z. H., Yang, B., Kim, S. H., and Zachariah, M. R., 2007, "Application of Hybrid Sphere/Carbon Nanotube Particles in Nanofluids," Nanotechnology, **18**, p. 105701.

[9] Buongiorno, J., 2006, "Convective Transport in Nanofluids," ASME J. Heat Transfer, **128**, pp. 240–250.

[10] Vadasz, P., 2006, "Heat Conduction in Nanofluid Suspensions," ASME J. Heat Transfer, **128**, pp. 465–477.

[11] Maxwell, J. C., 1904, *A Treatise on Electricity and Magnetism*, 2nd ed., Oxford University Press, Cambridge, UK.

[12] Nan, C. W., Birringer, R., Clarke, D. R., and Gleiter, H., 1997, "Effective Thermal Conductivity of Particulate Composites With Interfacial Thermal Resistance," J. Appl. Phys., **81**, pp. 6692–6699.

[13] Keblinski, P., Phillpot, S. R., Choi, S. U. S., and Eastman, J. A., 2002, "Mechanisms of Heat Flow in Suspensions of Nano-Sized Particles (Nanofluids)," Int. J. Heat Mass Transfer, **45**, pp. 855–863.

[14] Kumar, D. H., Patel, H. E., Kumar, V. R. R., Sundararajan, T., Pradeep, T., and Das, S. K., 2004, "Model for Heat Conduction in Nanofluids," Phys. Rev. Lett., **93**, p. 144301.

[15] Prasher, R., Bhattacharya, P., and Phelan, P. E., 2005, "Thermal Conductivity of Nanoscale Colloidal Solutions (Nanofluids)," Phys. Rev. Lett., **94**, p. 025901.

[16] Koo, J., and Kleinstreuer, C., 2004, "A New Thermal Conductivity Model for Nanofluids," J. Nanopart. Res., **6**, pp. 577–588.

[17] Bastea, S., 2005, "Comment on 'Model for Heat Conduction in Nanofluids'," Phys. Rev. Lett., **95**, p. 019401.

[18] Keblinski, P., and Cahill, D. G., 2005, "Comment on 'Model for Heat Conduction in Nanofluids'," Phys. Rev. Lett., **95**, p. 209401.

[19] Einstein, A., 1956, *Investigations on the Theory of the Brownian Movement*, Dover, New York.

[20] Wilde, R. E., and Singh, S., 1998, *Statistical Mechanics: Fundamentals and Modern Applications*, Wiley, New York.

[21] Panton, R. L., 2005, Incompressible Flow, 3rd ed., Wiley, New York.
[22] Bloch, E., 1930, *The Kinetic Theory of Gases*, 2nd ed., Methuen, London.
[23] Hirschfelder, J. O., Curtiss, C. F., and Bird, R. B., 1964, *Molecular Theory of Gases and Liquids*, Wiley, New York.
[24] Alder, B. J., and Wainwright, T. E., 1970, "Decay of the Velocity Autocorrelation Function," Phys. Rev. A, **1**, pp. 18–21.
[25] Paul, G. L., and Pusey, P. N., 1981, "Observation of a Long-Time Tail in Brownian-Motion," J. Phys. A, **14**, pp. 3301–3327.
[26] Hauge, E. H., and Marin-Lof, A., 1973, "Fluctuating Hydrodynamics and Brownian Motion," J. Stat. Phys., **7**, pp. 259–281.
[27] Hinch, E. J., 1975, "Application of the Langevin Equation to Fluid Suspensions," J. Fluid Mech., **72**, pp. 499–511.

A Photoelectrochemical Model of Proton Exchange Water Electrolysis for Hydrogen Production

Jianhu Nie

Yitung Chen

Robert F. Boehm

Shanthi Katukota

Department of Mechanical Engineering,
University of Nevada, Las Vegas,
Las Vegas, NV 89154

A photoelectrochemical model for hydrogen production from water electrolysis using proton exchange membrane is proposed based on Butler-Volmer kinetics for electrodes and transport resistance in the polymer electrolyte. An equivalent electrical circuit analogy is proposed for the sequential kinetic and transport resistances. The model provides a relation between the applied terminal voltage of electrolysis cell and the current density in terms of Nernst potential, exchange current densities, and conductivity of polymer electrolyte. Effects of temperature on the voltage, power supply, and hydrogen production are examined with the developed model. Increasing temperature will reduce the required power supply and increase the hydrogen production. An increase of about 11% is achieved by varying the temperature from 30°C to 80°C. The required power supply decreases as the illumination intensity becomes greater. The power supply due to the cathode overpotential does not change too much with the illumination intensity. Effects of the illumination intensity can be observed as the current density is relatively small for the examined illumination intensities. [DOI: 10.1115/1.2789722]

Keywords: photoelectrochemical model, electrolysis, PEM, hydrogen production

Introduction

Hydrogen is expected to play an important role as an energy carrier of the future as the quality of human life increasingly depends on the availability of energy resources [1,2]. Hydrogen may be used as fuel in almost every application where fossil fuels are being used today, but almost without harmful emissions. However, hydrogen is not an energy source, and it does not occur in nature in its elemental or molecular form. Several methods have been and are being developed for production of hydrogen from renewable energy sources [3]. One of these methods is to capture the energy that is freely available from sunlight and to directly generate hydrogen. Research of photoelectrochemical systems that produce hydrogen directly from water using sunlight as the energy source has received increasing attention for the past decades [4,5]. Moreover, the advent of nanocrystalline semiconductor systems has rekindled interest in hydrogen production from water electrolysis by visible light [6].

The water electrolyzer cell with proton exchange membrane (PEM) has been utilized in many energy-related fields such as fuel cell, and solar cell systems. Electrolysis of water using the PEM is considered as a promising methodology for producing hydrogen because of its advantages over the classical alkaline process in terms of its simplicity, high energy efficiency, and specific production capacity. Basically, a PEM electrolyzer cell is similar to a PEM fuel cell. It has a polymer membrane, porous electrodes, current collectors and separator plates, and manifolds. In general, the principle of its operation is just reverse of fuel cell operation. On one electrode (anode), water is split into oxygen, protons, and electrons by applying a DC voltage higher than a thermoneutral voltage. Protons pass through the polymer electrolyte membrane and on the other electrode (cathode) combine with electrons to form hydrogen. Passage of protons through the membrane is accompanied by water transport (electro-osmotic drag). Although there are many studies on the theoretical analysis of PEM fuel cells [7–10], not much has been reported on the kinetics and polarization characteristics of the PEM electrolyzer cell. In order to design and use the PEM electrolyzer effectively, analytical and/or numerical models for the device are necessary so that the system may be optimized. Onda et al. [11] provided a voltage-current relation wherein the cell voltage is described as the sum of Nernst voltage, anode and cathode overpotentials, and resistive overpotential. Empirical equations were utilized for the anode and cathode overpotentials as a function of temperature of the electrolytes and current density of the cell. A simple model for electrochemical process in the water electrolysis cell was developed by Choi et al. [12]. However, none of such models, to the authors' knowledge, has been seen in the published literature for the photoelectrochemical PEM electrolysis cell. The present study is motivated by such need to develop a simple but useful first-generation theoretical model to explain the current-potential characteristics of photoelectrochemical PEM electrolysis cell based on the involved charge and mass balances as well as Butler-Volmer kinetics on the electrode surfaces.

Method Descriptions

Electrolysis of water is the dissociation of water molecules into hydrogen and oxygen. A potential is applied across the electrochemical cell to induce electrochemical reactions at both electrodes. A schematic of the water electrolysis cell is shown in Fig. 1. Water is introduced at the anode and dissociated into oxygen, protons, and electrons. For the pure water electrolysis process, the reaction at the anode can be expressed as

$$H_2O \rightleftarrows 2H^+ + 2e^- + 0.5O_2 \quad (1)$$

Under an electric field, the protons are driven through the PEM to the cathode where they combine with the electrons arriving from the external circuit to form hydrogen gas:

$$2H^+ + 2e^- \rightleftarrows H_2 \quad (2)$$

Contributed by the Heat Transfer Division of ASME for publication in the JOURNAL OF HEAT TRANSFER. Manuscript received January 26, 2007; final manuscript received March 28, 2007; published online March 18, 2008. Review conducted by Christopher Dames.

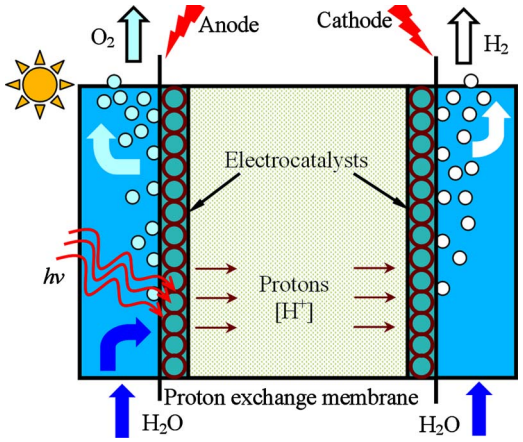

Fig. 1 Schematic of the PEM solar electrolyzer

Therefore, the net reaction in the electrolysis cell can be written as

$$H_2O \rightleftarrows H_2 + 0.5O_2 \tag{3}$$

The membrane-electrode assembly (MEA) is the main part of the PEM water electrolysis cell. The perfluorosulfonic acid polymer such as Nafion® has been widely used as the membrane for water electrolysis because of its intrinsic properties: excellent chemical and mechanical stability, high protonic conductivity, and gas impermeability [13,14]. Because of the highly acidic environment produced by sulfonic acid groups at the membrane surfaces, acid-resistance noble metals or their oxides must be used for electrocatalysts. Platinum provides a significant overpotential and the best performance, and it is commonly used for water electrolysis [14].

Before a detailed analysis of the current distributions in the PEM electrolysis cell, it is important to have a correct description of the constituents of the cell voltage at the macroscopic level. A simplified mathematical model is developed based on appropriate mass balances, transport, and electrochemical kinetics applied to the PEM electrolysis cell, using the similar model development as Ref. [12].

First, the anode chamber is assumed to be well mixed. The mass balances of water and oxygen at the anode and that of hydrogen at the cathode can be written as [15]

$$\dot{N}_{H_2O,in} - \dot{N}_{H_2O,out} = \frac{iA}{2F} \tag{4}$$

$$\dot{N}_{H_2,in} - \dot{N}_{H_2,out} = -\frac{iA}{2F} \tag{5}$$

$$\dot{N}_{O_2,in} - \dot{N}_{O_2,out} = -\frac{iA}{4F} \tag{6}$$

where $\dot{N}$, i, A, and F are the molar flow rates, current density, MEA area, and Faraday constant, respectively.

The potential of the electrode when a net current flows through the electrode ($i \neq 0$) diminished by the equilibrium potential (when $i=0$) is called the overpotential. The overpotential may be regarded as the extra potential necessary to reduce the energy barrier of the rate-determining step to a value such that the electrode reaction proceeds at a desired rate. The stoichiometric number of a reaction is defined as the number of times the rate-determining step takes place for one act of overall reaction. The effect of light on electrode reactions is akin to its effect on chemical reactions (photochemistry). The number of electrons, n_ν, emitted in a second by a metal in a vacuum per unit of incident light energy is given by [16]

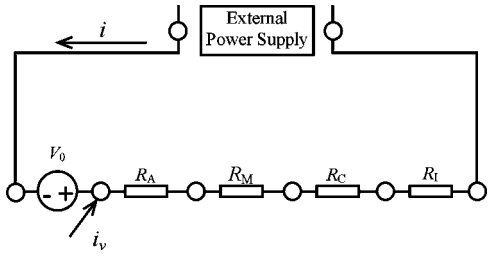

Fig. 2 Equivalent circuit for the solar water electrolysis process

$$n_\nu = \frac{mc^2}{h^2\nu^2}\left(1 - \frac{\phi_M}{h\nu}\right) \tag{7}$$

where m is the mass of electron, c is the velocity of light, ϕ_M is the work function of the metal, and ν is the frequency of light of standard intensity I_0.

It is assumed that there are no transport limitations. The Butler-Volmer expression utilized for the overall electrochemical reaction at the anode and the charge-transfer reaction under illumination can be given as [17]

$$i = i_{A0}\left[\exp\left(\frac{\alpha_A \nu_e^- F \eta_A}{RT}\right) - \exp\left(-\frac{(1-\alpha_A)\nu_e^- F \eta_A}{RT}\right)\right] + F\frac{I_\nu}{I_0}\frac{mc^2}{h^2\nu^2}\left(1 - \frac{\phi_M + \chi}{h\nu}\right) \tag{8}$$

where i_{A0} is the anode exchange current density, ν_e^- is the stoichiometric coefficient of electrons in the anode, α_A is the transfer coefficient, η_A is the anode overpotential, I_υ is the intensity of illumination, R is the universal constant of gases, T is the temperature, and χ is the surface potential difference at the metal-solution surface.

Assuming that the effective transfer coefficient $\alpha_A = 0.5$ and $\nu_e^- = 2$ [18], the anode overpotential can be written in the following form:

$$i = i_{A0}\left[\exp\left(\frac{F\eta_A}{RT}\right) - \exp\left(-\frac{F\eta_A}{RT}\right)\right] + i_\nu \tag{9}$$

$$\eta_A = \frac{RT}{F}\sinh^{-1}\left(\frac{i - i_\nu}{2i_{A0}}\right) \tag{10}$$

where

$$i_\nu = F\frac{I_\nu}{I_0}\frac{mc^2}{h^2\nu^2}\left(1 - \frac{\phi_M + \chi}{h\nu}\right)$$

Similarly, for the cathode, if Butler-Volmer equation is utilized along with $\alpha_C = 0.5$ and $\nu_e^- = -2$, the cathode overpotential can be obtained as

$$\eta_C = -\frac{RT}{F}\sinh^{-1}\left(\frac{i_C}{2i_{C0}}\right) \tag{11}$$

where i_{C0} is the cathode exchange current density. Here, it should be noted that the solutions are assumed to be well mixed in the chambers and thus the surface concentrations do not differ appreciably from the bulk phase.

At steady state, the divergence of current density in the PEM is zero, i.e.,

$$\frac{di}{dz} = 0 \quad \text{and} \quad i = -\sigma\frac{d\phi}{dz} \tag{12}$$

where σ is the conductivity of the electrolyte and ϕ is the potential in the membrane.

Figure 2 shows the equivalent circuit for photoelectrolysis pro-

cess represented by a series of resistances. The overall applied cell potential is thus composed of the cell Nernst potential (V_0), anode (η_A) and cathode (η_C) overpotentials, overpotential due to membrane (η_M), and interfacial resistance (η_I). It can be written as

$$V = V_0 + \eta_A - \eta_C + \eta_M + \eta_I \tag{13}$$

where the interfacial overpotential (η_I) may be written in terms of interfacial resistance R_I and current density as $\eta_I = R_I i$.

The Nernst potential or equilibrium open circuit potential (V_0) is empirically expressed as [19]

$$V_0 = \frac{\Delta G}{2F} + \frac{\Delta S}{2F}(T - T_{\text{ref}}) + \frac{RT}{2F}\left[\ln(P_{\text{H}_2}) + \frac{1}{2}\ln(P_{\text{O}_2})\right] \tag{14}$$

From the reaction as shown in Eqs. (1)–(3), the equilibrium potential can be expressed as

$$V_0 = 1.23 - 0.9 \times 10^{-3}(T - 298) + \frac{RT}{4F}\ln(P_{\text{H}_2}^2 P_{\text{O}_2}) \tag{15}$$

The overpotential due to membrane resistance can be obtained by integrating Eq. (12):

$$\eta_M = \left(\frac{L_M}{\sigma_M}\right) i \tag{16}$$

where L_M is the thickness of the PEM, and σ_M is the conductivity of the electrolyte. The membrane's resistance depends mainly on the temperature and moisture content in the membrane. Conductivity of Nafion® can be described by the following relation [20]:

$$\sigma_M = \sigma_M^{\text{ref}} \exp\left[1268\left(\frac{1}{T_{\text{ref}}} - \frac{1}{T}\right)\right] \tag{17}$$

Therefore, the overall cell voltage-current relation for the electrolysis cell can be obtained by combining the above equations:

$$V = V_0 + \frac{RT}{F}\sinh^{-1}\left[\frac{1}{2}\left(\frac{i - i_\nu}{i_{A0}}\right)\right] + \frac{RT}{F}\sinh^{-1}\left[\frac{1}{2}\left(\frac{i_C}{i_{C0}}\right)\right] + \left(\frac{L_M}{\sigma_M}\right) i + R_I i \tag{18}$$

Then, the required power density can be obtained by $P = Vi$ as

$$P = V_0 i + \frac{RT}{F}\sinh^{-1}\left[\frac{1}{2}\left(\frac{i - i_\nu}{i_{A0}}\right)\right] i + \frac{RT}{F}\sinh^{-1}\left[\frac{1}{2}\left(\frac{i_C}{i_{C0}}\right)\right] i + \left(\frac{L_M}{\sigma_M}\right) i^2 + R_I i^2 \tag{19}$$

The rate of hydrogen production is derived in a way similar to hydrogen usage in the PEM fuel cell, except that there are two moles of electrons to generate a mole of hydrogen, and hence the hydrogen production rate is written as follows:

$$H_{2,\text{production}} = \frac{i}{2F} \tag{20}$$

The electrolysis process has been represented by an equivalent electrical circuit consisting of a series of resistances standing for each individual steps. In analogy to linear Ohm's law, a differential resistance R_d can be defined for an electrolysis cell as [18]

$$R_d = \frac{d(V - V_0)}{di} \tag{21}$$

$$R_d = \frac{d\eta_A}{di} - \frac{d\eta_C}{di} + \frac{d\eta_M}{di} + \frac{d\eta_I}{di} = R_A + R_C + R_M + R_I \tag{22}$$

$$R_A = \frac{RT}{(2Fi_{A0})\sqrt{1 + ((i - i_\nu)/2i_{A0})^2}} \tag{23}$$

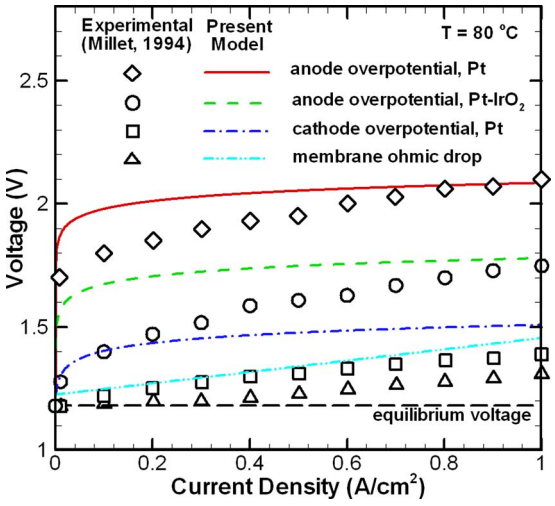

Fig. 3 Comparisons of the computed results with the measured data

$$R_C = \frac{RT}{(2Fi_{C0})\sqrt{1 + (i_C/2i_{C0})^2}} \tag{24}$$

$$R_M = L_M/\sigma_M \tag{25}$$

It should be noted that $i_C = i - i_\nu$.

Results and Discussions

The voltage-current density curves are presented in Fig. 3 for pure water electrolysis (without photocurrent) at the temperature of $T = 80\,^\circ\text{C}$. Values of the physical properties are listed in Table 1. During the present modeling, the conductivity of the electrolyte at the reference state (σ_m^{ref}), which appears in Eq. (17), is determined to be 0.072 S/cm at the reference temperature of $T_{\text{ref}} = 298$ K. In addition, a correction factor of 1.75 from computer optimization is used in Eqs. (8) and (11), because there is a limitation for mass transfer, e.g., oxygen diffusion from catalyst site to gas bubble across a diffusion film near electrodes. Such value is selected as fitting parameter in order to optimize the match with the experimental data, as shown in Fig. 3. The exchange current density, i_0, depends on the temperature at the electrode surface and also the roughness factor, which is defined as the electrochemically determined electrode area divided by the geometric area: $i_0 = \gamma_M \times \exp[-E/R((1/T) - (1/T_{\text{ref}}))] i_0^{\text{ref}}$, where E is the activation energy. It can be seen that comparisons between the computed results and the measured data [13] are in very favorable agreement.

Effects of different temperatures on the voltage-current density curves are shown in Fig. 4. The anode and cathode overpotentials are presented in Fig. 4(*a*) as a function of the current density. It can be seen that the anode and cathode overpotentials become greater as the temperature decreases, as a result of the decreasing exchange current density with the increase of temperature. For the purpose of clarity, the membrane Ohmic drop and the equilibrium voltage are exhibited in Fig. 4(*b*). Both the membrane Ohmic drop and the equilibrium voltage become greater as the temperature decreases.

Figure 5 shows the differential resistances for water electrolysis cell for different temperatures. The membrane differential resis-

Table 1 Model parameters for water electrolysis cell

Parameters	$i_{A0,\text{Pt}}$	$i_{A0,\text{Pt}}$	i_{C0}	L_M	γ_M
Values	10^{-9}	8×10^{-7}	3×10^{-3}	178	150
Dimensions	A/cm^2	A/cm^2	A/cm^2	μm	1

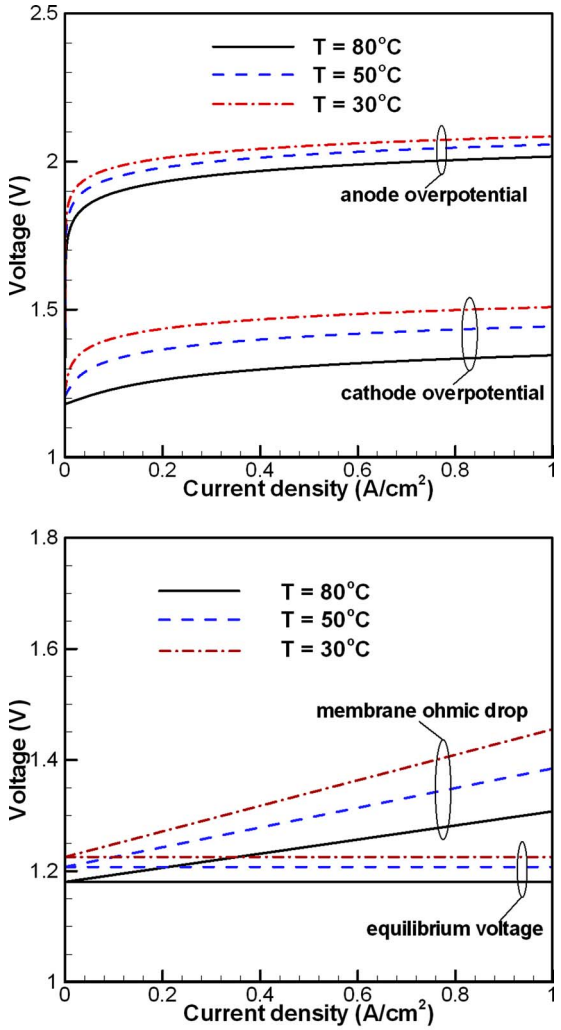

Fig. 4 Effects of temperature on the voltages of the water electrolysis cell

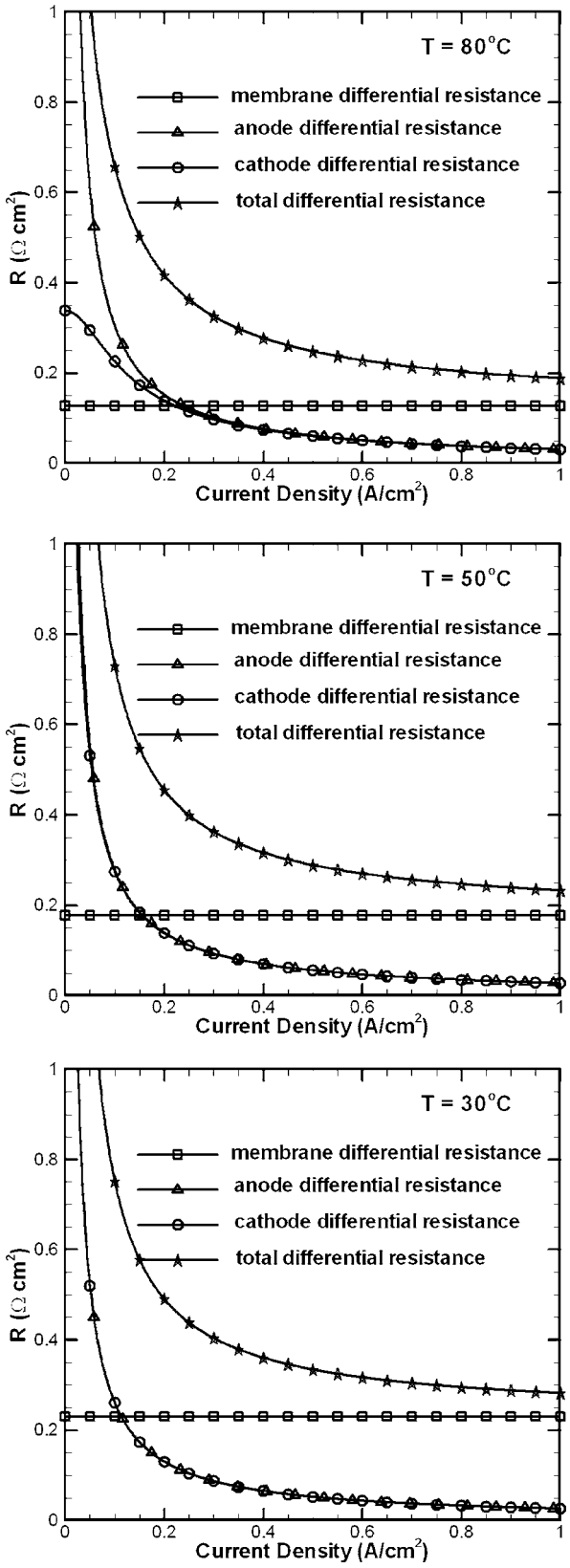

Fig. 5 Effects of temperature on differential resistances for water electrolysis

tance increases with the decrease of temperature. As the temperature becomes smaller (such as $T=50°C$ and $30°C$), the anode and the cathode differential resistances become closer to each other. At $T=30°C$, they almost overlay with each other. Effects of temperature on the power supply are presented in Fig. 6. The minimum power supply in this figure is the required power supply for overcoming the equilibrium open circuit potential. The required power supply increases as the temperature decreases. This can be seen more clearly for the power supply due to anode overpotentials. Hydrogen production rates for different temperatures are exhibited in Fig. 7. For the same power supply, the hydrogen production rate becomes greater with the increase of temperature. For instance, the hydrogen production rate increases by approximately 11% from the temperature of 30°C to 80°C.

Effects of the illumination intensity on the voltage-current density curves are presented in Fig. 8 for $I_\nu/I_0=0$, 0.5, and 1. The temperature is taken as a constant of $T=80°C$. The frequency of the incident light is typically taken as 6.5×10^{15} Hz. The surface potential (χ) is assumed to be 0.1 eV, although different values can be examined without a lot of difficulties. Both the anode and the cathode overpotentials decrease as the illumination intensity increases. This can be seen more clearly as the magnitude of the current density is small. Effects of the illumination intensity become less significant as the current density increases. This is because for the selected illumination intensities, the photocurrent plays a more important role than the electrochemical current. As the current density increases, the electrochemical current becomes more predominant and then effects of the photocurrent become less significant.

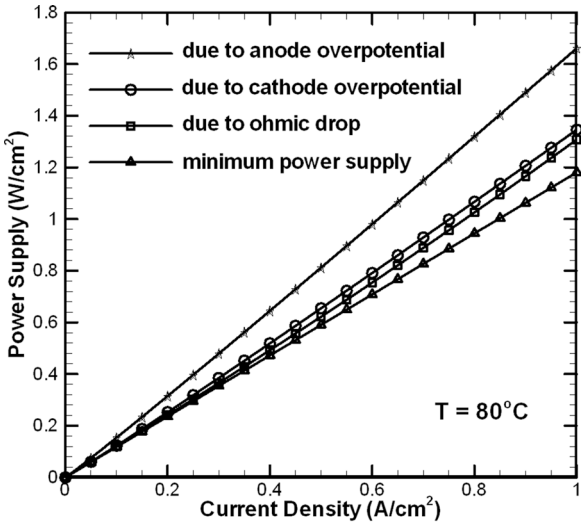

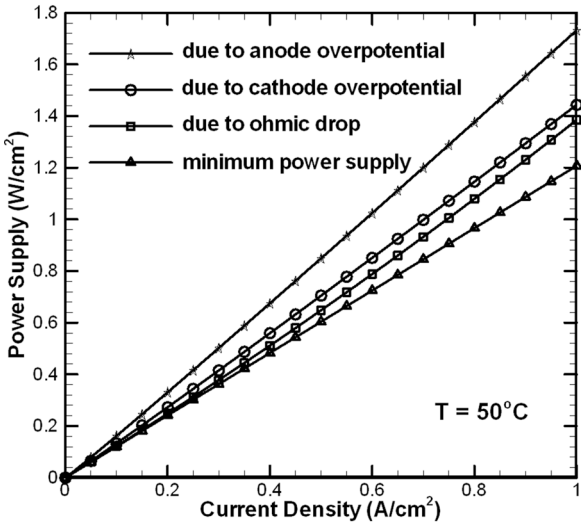

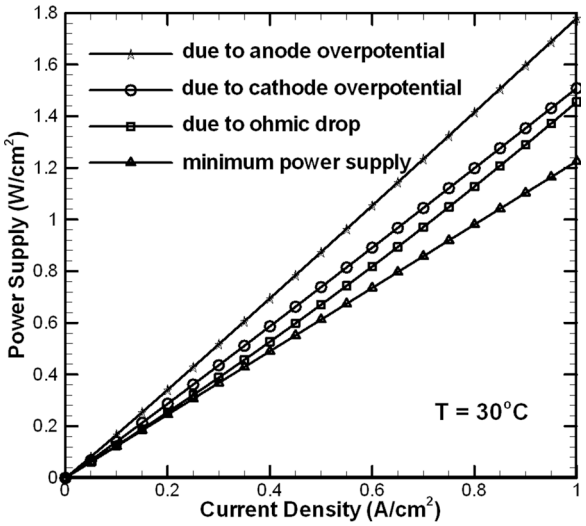

Fig. 6 Effects of temperature on required power supply for water electrolysis

The power supplies due to the anode and cathode overpotentials for different illumination intensities are plotted in Fig. 9. Effects of the illumination intensity can be observed as the current density is relatively small. The required power supply decreases as the illumination intensity becomes greater. The power supply due to the cathode overpotential does not change too much with the illumination intensity. Illumination intensity effects on the hydrogen production are presented in Fig. 10. Effects of the illumination intensity can be observed as the current density is relatively small for the examined illumination intensities.

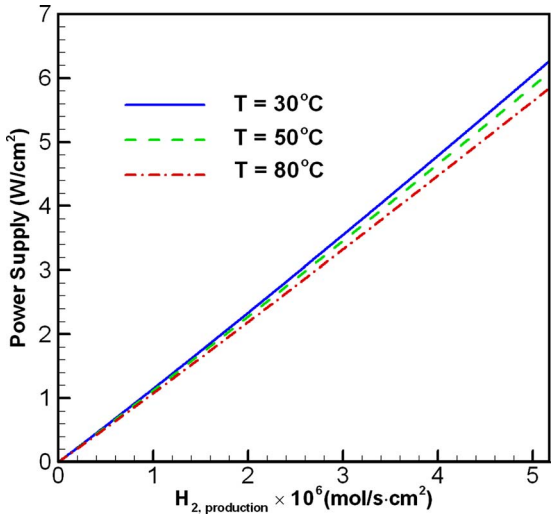

Fig. 7 Effects of temperature on hydrogen production rate

Conclusions

A photoelectrochemical model is developed for the water electrolysis process. Electrolysis process is represented by the equivalent electric circuit. Effects of temperature on the voltage, power supply, and hydrogen production are examined with the developed model. Increasing temperature will decrease the required power supply and increase the hydrogen production. An increase of about 11% is achieved by varying the temperature from 30°C to 80°C. The required power supply decreases as the illumination intensity becomes greater. The power supply due to the cathode overpotential does not change too much with the illumination intensity. Effects of the illumination intensity can be observed as the current density is relatively small for the examined illumination intensities.

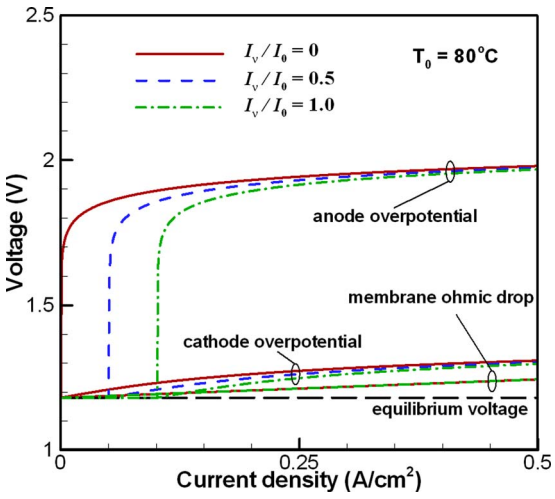

Fig. 8 Effects of illumination intensity on voltage-current density curve

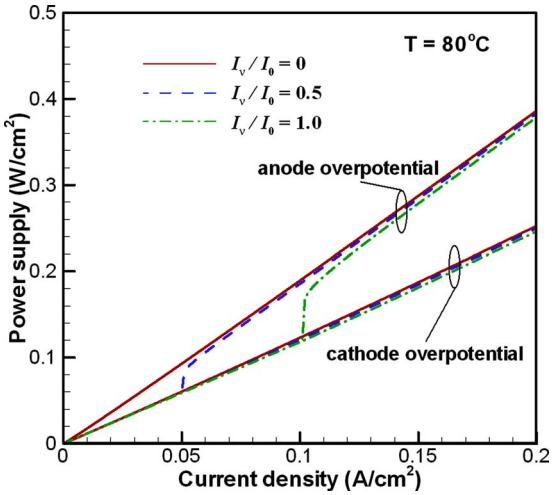

Fig. 9 Effects of illumination intensity on electrode overpotentials

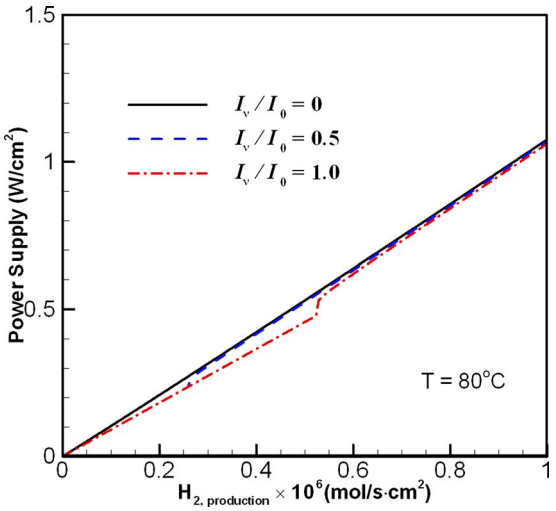

Fig. 10 Effects of illumination intensity on hydrogen production rate

Acknowledgment

This work was supported by US Department of Energy under Grant Nos. DE-FG36-03GO13063 and RF-05-HFS-006. The use of computer resources provided by the National Supercomputing Center for Energy and the Environment is gratefully acknowledged.

Nomenclature

c = speed of light in vacuum = 2.9979×10^8 m/s
E = activation energy
F = Faraday constant = 9.6485×10^4 C/mol
h = Planck constant = 6.626×10^{-34} J s
I_0 = standard intensity of light
i = current density
i_0 = exchange current density
L_B = thickness of the proton exchange membrane
m = mass of electron = 9.1096×10^{-31} kg
$\dot{N}$ = molar flow rate
n = number of electrons transferred in the reaction
P = pressure
R = universal constant of gases = 8.314 J/(mol K)
R_A = anode differential resistance
R_C = cathode differential resistance
R_I = interfacial differential resistance
R_M = membrane differential resistance
T = temperature
T_{ref} = reference temperature
V = voltage
V_0 = equilibrium voltage

Greek Symbols

α = transfer coefficient
χ = surface potential difference at the metal-solution interface
γ_M = roughness factor
σ_B = conductivity of the electrolyte
ϕ_M = work function of the metal
ν = frequency of light
η = overpotential
η_A = anode overpotential
η_C = cathode overpotential
η_I = overpotential due to interfacial resistance
η_M = overpotential due to membrane

References

[1] Adamson, K., 2004, "Hydrogen From Renewable Resources—The Hundred Year Commitment," Energy Policy, **32**(10), pp. 1231–1242.
[2] Ogden, J. M., 2002, "Hydrogen: The Fuel of the Future?" Phys. Today, **55**(4), pp. 69–75.
[3] Barbir, F., 2005, "PEM Electrolysis for Production of Hydrogen From Renewable Energy Sources," Sol. Energy, **78**(5), pp. 661–669.
[4] Nozik, A. J., 1978, "Photoelectrochemistry: Applications to Solar Energy Conversion," Annu. Rev. Phys. Chem., **29**, pp. 189–222.
[5] Grätzel, M., 2001, "Photoelectrochemical Cells," Nature (London), **414**(6861), pp. 338–344.
[6] Grätzel, M., 2005, "Mesoscopic Solar Cells for Electricity and Hydrogen Production From Sunlight," Chem. Lett., **34**(1), pp. 8–13.
[7] Cheddie, D., and Munroe, N., 2005, "Review and Comparison of Approaches to Proton Exchange Membrane Fuel Cell Modeling," J. Power Sources, **147**(1–2), pp. 72–84.
[8] Scott, K., Taama, W., and Cruickshank, J., 1997, "Performance and Modeling of a Direct Methanol Solid Polymer Electrolyte Fuel Cell," J. Power Sources, **65**(1–2), pp. 159–171.
[9] Nguyen, T. V., and White, R. E., 1993, "A Water and Heat Management Model for Proton-Exchange-Membrane Fuel-Cells," J. Electrochem. Soc., **140**(8), pp. 2178–2186.
[10] Larmine, J., and Dicks, A., 2000, *Fuel Cell Systems Explained*, Wiley, New York.
[11] Onda, K., Murakami, T., Hokosaka, T., Kobayashi, M., Notu, R., and Ito, K., 2002, "Performance Analysis of Polymer-Electrolyte Water Electrolysis Cell at a Small-Unit Test Cell and Performance Prediction of Large Stacked Cell," J. Electrochem. Soc., **149**(8), pp. A1069–A1078.
[12] Choi, P., Bessarabov, D. G., and Datta, R., 2004, "A Simple Model for Solid Polymer Electrolyte (SPE) Water Electrolysis," Solid State Ionics, **175**(1–4), pp. 535–539.
[13] Millet, P., 1994, "Water Electrolysis Using EME Technology—Electric-Potential Distribution Inside a Nafion Membrane During Electrolysis," Electrochim. Acta, **39**(17), pp. 2501–2506.
[14] Ioroi, T., Yasuda, K., Siroma, Z., Fujiwara, N., and Miyazaki, Y., 2002, "Thin Film Electrocatalyst Layer for Unitized Regenerative Polymer Electrolyte Fuel Cells," J. Power Sources, **112**(2), pp. 583–587.
[15] Bard, A. J., and Faulkner, L. R., 2001, *Electrochemical Methods: Fundamentals and Applications*, 2nd ed., Wiley, New York.
[16] Wilson, H. A., 1959, *Modern Physics*, 4th ed., Blackie, London, Chap. 4.
[17] Bockris, J. O'M., 1954, *Modern Aspects of Electrochemistry*, Vol. 1, J. O'M. Bockris and B. D. Conway, eds., Butterworth, London, Chap. 4.
[18] Bockris, J. O'M., and Srinivasan, S., 1969, *Fuel Cells: Their Electrochemistry*, McGraw-Hill, New York.
[19] Bernardi, D. M., and Verbrugge, M. W., 1992, "Mathematical Model of the Solid-Polymer-Electrolyte Fuel Cell," J. Electrochem. Soc., **139**(9), pp. 2477–2491.
[20] Beattie, P. D., Basura, V. I., and Holdcroft, S., 1999, "Temperature and Pressure Dependence of O_2 Reduction at Pt | Nafion® 117 and Pt | BAM® 407 Interfaces," J. Electroanal. Chem., **468**(2), pp. 180–192.

Modeling the Thermal Conductivity and Phonon Transport in Nanoparticle Composites Using Monte Carlo Simulation[1]

Ming-Shan Jeng[2]
e-mail: msjeng@itri.org.tw

Ronggui Yang[3]
e-mail: ronggui.yang@colorado.edu

Mechanical Engineering Department,
Massachusetts Institute of Technology,
Cambridge, MA 02139

David Song
Intel Corporation,
Chandler, AZ 85226

Gang Chen
e-mail: gchen2@mit.edu
Mechanical Engineering Department,
Massachusetts Institute of Technology,
Cambridge, MA 02139

This paper presents a Monte Carlo simulation scheme to study the phonon transport and the thermal conductivity of nanocomposites. Special attention has been paid to the implementation of periodic boundary condition in Monte Carlo simulation. The scheme is applied to study the thermal conductivity of silicon germanium (Si–Ge) nanocomposites, which are of great interest for high-efficiency thermoelectric material development. The Monte Carlo simulation was first validated by successfully reproducing the results of (two-dimensional) nanowire composites using the deterministic solution of the phonon Boltzmann transport equation reported earlier and the experimental thermal conductivity of bulk germanium, and then the validated simulation method was used to study (three-dimensional) nanoparticle composites, where Si nanoparticles are embedded in Ge host. The size effects of phonon transport in nanoparticle composites were studied, and the results show that the thermal conductivity of nanoparticle composites can be lower than that of the minimum alloy value, which is of great interest to thermoelectric energy conversion. It was also found that randomly distributed nanopaticles in nanocomposites rendered the thermal conductivity values close to that of periodic aligned patterns. We show that interfacial area per unit volume is a useful parameter to correlate the size effect of thermal conductivity in nanocomposites. The key for the thermal conductivity reduction is to have a high interface density where nanoparticle composites can have a much higher interface density than the simple 1D stacks, such as superlattices. Thus, nanocomposites further benefit the enhancement of thermoelectric performance in terms of thermal conductivity reduction. The thermal conductivity values calculated by this work qualitatively agrees with a recent experimental measurement of Si–Ge nanocomposites. [DOI: 10.1115/1.2818765]

1 Introduction

The advance of nanoengineering in the past decade has enabled researchers to demonstrate enhanced thermoelectric materials through the use of nanostructures [1–8]. The efficiency and energy density of thermoelectric devices is usually determined by the dimensionless figure of merit, $ZT=S^2\sigma T/k$, where S is the Seebeck coefficient, the electrical conductivity, k the thermal conductivity, and T the absolute temperature [9]. These parameters in bulk materials usually have conflicting trends, making it difficult to find high ZT materials. Recently, significantly enhanced ZT values have been reported by different groups using superlattices or quantum-dot superlattices by exploiting phonon thermal conductivity reduction and electron performance enhancement in these structures [3–5]. Nanocomposite materials, in the form of nanoparticles and nanowires embedded in a host matrix material, are proposed as an alternative to realize cost effective large scale production of thermoelectric material with nanostructures [2,10–13].

Although the nanocomposite approach seems promising, currently there is little theoretical or modeling work in the literature regarding electrical and thermal transport in nanocomposites that one can rely on to achieve good design of thermoelectric nanocomposites. The prevailing approach for thermal conductivity modeling is to include the interface thermal resistance, or the Kapitza resistance [14], with the Fourier heat conduction theory [15–22]. However, the Fourier heat conduction theory is based on the diffusion picture and is not applicable when the phonon mean free path (MFP) is longer than the characteristic length of the nanocomposites such as the particle diameter and/or interparticle separation distance. Another approach in the investigation of the nanocomposite thermal conductivity is through the calculation of the phonon dispersion in periodic structures [23]. Due to the short wavelength of the dominant phonon heat carriers, the phonon scattering at interfaces is often diffuse [24]. The diffuse interface scattering inside the nanostructure materials cannot only reduce the phonon MFP but can also destroy the coherence of phonons. The loss of coherence results in the fact that the classical size effect models such as the phonon Boltzmann transport equation (BTE) can be applicable to a wide range of nanostructures. We recently reported our work on thermal conductivity modeling and the analysis of two-dimensional (2D) Si–Ge nanocomposites with Si nanowires embedded in a Ge matrix [12] by the deterministic solution of the phonon BTE [25,26]. Though very much doable,

[1]A brief version of this work first appeared in the Proceedings of ASME InterPack 2005. A poster presentation of this work was then made in ASME ENIC 2006 Conference in Cambridge, MA.

[2]On leave from the Industrial Technology Research Institute, Chutung, Hsinchu, Taiwan 310, R.O.C.

[3]Present address: Department of Mechanical Engineering, University of Colorado, Boulder, CO.

Contributed by the Heat Transfer Division of ASME for publication in the JOURNAL OF HEAT TRANSFER. Manuscript received October 23, 2006; final manuscript received June 4, 2007; published online March 19, 2008. Review conducted by Christopher Dames. Paper presented at the ASME 2006 Energy Nanotechnology International Conference (ENIC2006), Boston, MA, June 26–28, 2006.

extending the 2D BTE simulation to phonon transport in complex three-dimensional (3D) spatial coordinates is very tedious, owing to the complexity in tracking phonon transport deterministically.

The Monte Carlo (MC) simulation solves the BTE in a statistical framework and has been widely used to simulate the radiative transfer equation and the Boltzmann equation for electrons and holes in semiconductors [27–32]. Only few reports of using the MC technique for phonon transport have been published in the past. Peterson [33] employed a MC method to simulate phonon transport in a confined space, while Klitsner et al. [34] performed MC simulations to obtain temperature distributions in a crystal. Mazumder and Majumdar considered phonon dispersion as well as various phonon scattering mechanisms to study heat transport in complex geometries and to predict the thermal conductivities [35]. Song conducted MC simulation to study the size effect of thermal conductivity of porous silicon thin films [36]. During the revision of this manuscript, the authors were aware of a few other attempts using MC simulation for phonon transport in nanostructures [37,38], and our paper in 2004 [12] has generated more interest on modeling phonon thermal conductivity of nanocomposites using the phonon BTE recently [39,40].

This work builds upon previous studies on the phonon transport in nanoscale structures and is the first attempt to use MC methods to study phonon transport in complex 3D nanostructures, i.e., nanocomposites. The objective is to present an algorithm for studying phonon transport in nanocomposites using MC simulation with special attention to the implementation of periodic boundary condition and to the study of the size effect of thermal conductivity in nanoparticle composites. We would like to note that the framework of this paper assumes that the phonon concept is still valid in nanocomposites. This is generally true as long as the nanocomposites form crystalline structures. Though the phonon spectrum in nanostructures can be different from bulk materials, our simulation uses bulk phonon dispersion for constituent materials. This is due to two reasons [24]: (1) The change of phonon spectrum, such as the density of state and the group velocity of phonons in nanostructures, is not the most significant reason for thermal conductivity reduction in nanostructures. (2) Recent experience with superlattices suggests that the idealized phonon dispersion in nanostructures is difficult to realize experimentally because it is difficult to obtain sufficiently smooth and uniform surfaces for coherent interference. In other words, the interface of nanocomposites often induces diffuse scattering, which makes the formation of phonon minibands rather difficult.

2 Monte Carlo Simulation Technique

In a MC solution technique, phonons are drawn and distributed inside the computational domain initially. These phonons are given with velocity and direction, which corresponds to wave vectors in the momentum space in the phonon dispersion relation, and are allowed to move freely. As the phonons move, they engage in various "intrinsic-scattering" events, such as phonon-phonon scattering, phonon-impurity scattering, and phonon-dislocation scattering, and encounter interfaces and boundaries, mimicking the particle picture of phonon transport. If there are enough number of phonons and if the average time is long enough, the averaged transport quantities based on the phonon ensemble should approach the deterministic solution of the phonon Boltzmann equation. The initial selection of phonon positions and directions as well as the subsequent phonon movement must obey the physical laws that determine phonon properties and define phonon dynamics. Though a more comprehensive MC simulation technique—which accounts for phonon dispersion and polarization for scattering events—has been presented before [35], as a first attempt to tackle the 3D phonon transport problem in nanocomposites, we took a simplified gray-media approach that assumes that the frequency-dependent scattering rate in the bulk medium can be approximated by an average phonon MFP. Our past studies on superlattices based on BTE show that by properly taking the average MFP, the modeling results are close to experimental data [41]. Another assumption that has been made is that the phonon wave effect can be excluded. The justification for these assumptions can be found in Refs. [12,41]. In the following sections, we present the details of implementing the gray-media MC technique for solving the phonon transport problem in nanocomposites.

2.1 Gray-Media Approximation. The gray-media approach assumes that phonon properties are frequency independent, i.e., by averaging the frequency-dependent phonon properties over the phonon population. The average phonon properties, which are dependent on temperature only, including average phonon frequency ω_{av} and average phonon group velocity v_{av}, can be calculated as

average frequency:

$$\omega_{\text{av}} = \frac{\sum_{p=1}^{3} \int_0^{\omega_{\text{mp}}} \hbar\omega \langle n \rangle D(\omega) d\omega}{\hbar N} \tag{1}$$

average group velocity:

$$v_{\text{av}} = \frac{1}{N} \sum_{p=1}^{3} \int_0^{\omega_{\text{mp}}} \frac{\partial \omega}{\partial k} \langle n \rangle D(\omega) d\omega \tag{2}$$

where phonon number density is given by

$$N = \sum_{p=1}^{3} \int_0^{\omega_{\text{mp}}} \langle n \rangle D(\omega) d\omega \tag{3}$$

In the above expressions, index p represents the specific branch of polarization, $\hbar = 1.05 \times 10^{-34}$ J s is the Planck's constant divided by 2π, ω is the phonon frequency, ω_{mp} the maximum cutoff phonon frequency for each phonon branch, $k_B = 1.38 \times 10^{-23}$ J/K the Boltzmann constant, and $D(\omega)$ is the phonon density of state for each branch that is given by

$$D(\omega) = -\frac{\mathbf{k}^2}{2\pi^2} \frac{\partial \mathbf{k}}{\partial \omega} \tag{4}$$

where k is the phonon wave vector and $\langle n \rangle$ is the equilibrium distribution function for phonons,

$$\langle n \rangle = \frac{1}{\exp(\hbar\omega / k_B T) - 1} \tag{5}$$

In the above equations (Eqs. (1)–(3)), the summation is only for three polarization branches, one longitudinal and two transverse acoustical phonon branches, since we assume that the contribution of optical phonons to the thermal conductivity is negligible due to their small group velocity in silicon and germanium [41]. We note that there are arguments about the contribution of optical phonons to the thermal conductivity of crystals, which essentially depends on the type of the crystals. Our work emphasizes the average phonon properties, which means that we would be able to accommodate the optical phonon contribution to the thermal conductivity of other crystals in the database of material properties when needed. As a simplification, the phonon dispersion relations are further assumed to be isotropic, and thus only the phonon dispersion in the [100] direction of Si and Ge in literature is taken to calculate the phonon density of state [42,43]. The maximum wave vector k_{max} corresponding to the maximum phonon frequency is determined by $\mathbf{k}_{\text{max}} = \pi / a$, where a is the equivalent atomic distance given by $(\pi(V/6N))^{1/3}$. In this expression, V is the volume and N is the number of atoms in the volume.

The heat capacity of acoustic phonons can be written as

$$C_{\text{ac}} = \frac{\partial E}{\partial T} = \sum_{p=1}^{3} \int_{0}^{\omega_{\text{mp}}} \hbar\omega \frac{\partial \langle n \rangle}{\partial T} D(\omega) d\omega \tag{6}$$

where E is the energy density of acoustic phonons and can be calculated as

$$E = \sum_{p=1}^{3} \int_{0}^{\omega_{\text{mp}}} \hbar\omega \langle n \rangle D(\omega) d\omega \tag{7}$$

With the average acoustic phonon properties and assuming that the contribution from the optical phonons to the thermal conductivity is negligible, the temperature-dependent phonon MFP. Λ can be calculated through the simple kinetic theory

$$\Lambda = \frac{3k_{\text{bulk}}}{v_{\text{av}} C_{ac}} \tag{8}$$

where k_{bulk} is the thermal conductivity of the bulk material and is taken from experimental data in the literature [44]. This estimation leads to a longer MFP than that using the simple kinetic theory expression $k=(1/3)Cv\Lambda$, assuming that C is the heat capacity and v is the sound velocity in the crystal, consistent with existing experiments [45] and theoretical estimations [41].

In the MC simulation, phonons are divided into phonon bundles, and the averaged phonon properties are assigned to the phonon bundles during the simulation. The properties of a phonon bundle do not change while it travels, until it encounters scattering events, either by interface scattering or "intrinsic-phonon" scattering. The number of phonons in a phonon bundle is predetermined before the simulation by considering the computational time and memory requirements, similar to the common practice of statistical simulations [46].

2.2 Computational Domain and Boundary Conditions. The challenge is to simulate the phonon transport in the whole composite structure, as shown in Fig. 1(*a*), with Si nanoparticle embedded in a Ge matrix. The memory and computational time requirements for such a multiscale problem are demanding. Our approach is to apply periodic boundary conditions to a chosen unit cell. A rectangle parallelepiped in the composite material is taken as the computational domain, which is called a unit cell, as shown in Fig. 1(*b*). With the periodic boundary conditions we applied, shown in detail below, the phonon transport in the unit cell represents the phonon transport inside a composite made by repeating the unit cell. The heat is enforced to flow in the x direction. The transport in both the y and z directions are periodic, and thus the specular reflected boundary conditions can be enforced in these boundaries due to the symmetry. However, in the x direction, although the geometry is periodic, the transport and the temperature are not periodic. To address this problem for the deterministic BTE solution, the periodic boundary condition on the deviation of the distribution function was proposed [12]. The periodic boundary conditions are implemented in MC simulation as follows. For specular reflection boundaries at $y=0$, $y=L_y$, $z=0$, and $z=L_z$, the phonon bundles experience mirror reflection when they hit these boundaries, without losing any momentum or energy. The implementation of the periodic boundary condition in the x direction needs more elaboration. First, a certain number of phonon bundles are emitted from the boundaries during each time step so that the net heat flow (phonon energy flow) across the boundaries $x=0$ and $x=L_x$ are identical and equal to a prescribed value. The number of phonon bundles N_{emit} of each boundary emitted into the computational domain in each time step is calculated by

$$N_{\text{emit}} = \frac{\left(\pm Q + S \sum_{n} \hbar\omega_{n,\text{absorb}} \right)}{\hbar\omega_{\text{emit}} S} \tag{9}$$

where Q is the prescribed heat flow, whose sign depends on the boundary emission direction, S the scaling factor representing the number of phonons contained in each bundle, $S\Sigma\hbar\omega_{n,\text{absorb}}$ the total phonon energy leaving the computation domain, and ω_{emit} the average phonon frequency corresponding to the local boundary temperature, which is obtained by extrapolating the temperature profile inside the computational domain to the boundary. When a phonon bundle hits one of the x boundaries, it is considered leaving that boundary. The pattern (velocity, direction, position, and remaining flight time) of phonon emission at one x boundary is assumed to be the same as the pattern of phonon leaving the opposite x boundary. This implementation is realized by maintaining a pool of leaving phonons, recording their velocity, direction, position, and flight time, and determining the properties of each emission phonon by randomly drawing from the pool. The pool is refreshed after each time step.

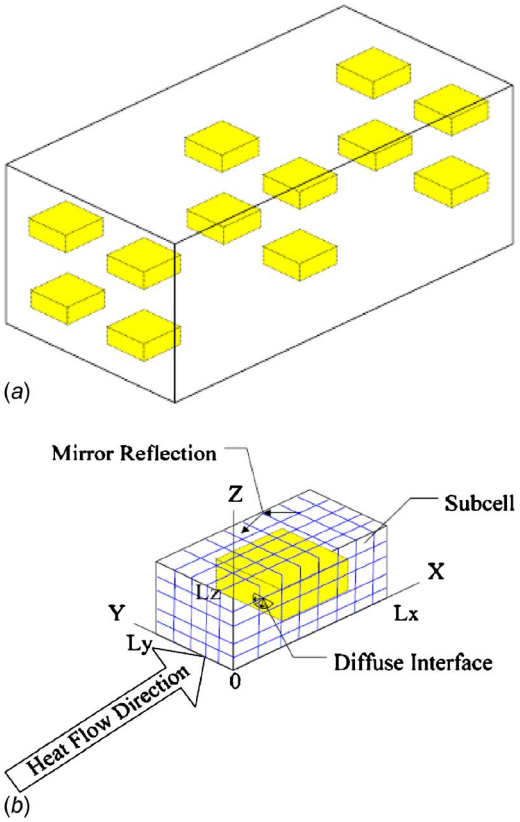

Fig. 1 (*a*) **Periodic nanocomposite with cubic silicon nanoparticles dispersed periodically in a germanium matrix.** (*b*) **With the periodic boundary condition dictated in Sec. 2.2, the MC simulation of phonon transport in the computational domain (unit cell) represents phonon transport in the whole structure shown in (*a*). The unit cell (computational domain) is further divided into subcells.**

The unit cell is further divided into many grids, or "subcell," as shown in Fig. 1(*b*). At the end of each time step, phonon energy inside each subcell is tallied for calculating the temperature of the subcell. With the known temperature, all the averaged phonon properties can be calculated and then assigned to phonon bundles emitting from this local subcell. In the program, a lookup table relating temperature, energy density, and all the other average properties is established before calculation. A significant computational time is saved by searching the lookup table instead of carrying out the integrations shown above for each phonon bundle in each time step. The dimension of the subcell must be selected to maintain a balance between spatial resolution and computation time. In order to obtain statistically stable results in MC simulation, however, there must be a sufficient number of phonon bundles within each subcell: thus, we must set a lower limit on the

subcell dimension. In this work, the smallest subcell dimension that can generate stable results was found to be around 1 nm.

2.3 Phonon Scattering. The dominant scattering event in nanocomposites is particle-host interface scattering. When a phonon encounters an interface, the phonon can experience both specular and diffuse scattering [47,48]. The details depend on the comparison of dominant heat transfer phonon wavelength and the roughness of an interface. Most of earlier experimental results show that diffuse scattering dominates phonon transport in nanostructures. Thus, the phonon scattering at the particle-host matrix interface (Si–Ge) is assumed to be diffuse in this study. By definition, the following relations between energy reflectivity and transmissivity exist for diffuse interfaces [47]:

$$T_{12} = R_{21} = 1 - T_{21} \tag{10}$$

where T_{12} is the energy transmissivity for phonon incident from side 1 toward side 2, R_{21} is the energy reflectivity for phonon incident from side 2 toward side 1, and so on. A detailed balance consideration leads to the following definition of transmissivity for diffuse interface [48],

$$T_{12}(T) = \frac{U_2(T)v_2}{U_1(T)v_1 + U_2(T)v_2} \tag{11}$$

where v and U are the phonon velocity and energy density, respectively. To be consistent with the gray phonon approach adopted here, frequency-averaged velocity and energy density must be used in Eq. (11). In the MC scheme, when a phonon hits an interface, a random number between zero and unity is drawn and compared with the transmissivity. If the random number is larger than the transmissivity, the phonon is transmitted. Otherwise, it is reflected. To comply with the concept of diffuse interface, the phonon direction vector is reset after encountering an interface, either transmitted or reflected, and is given by

$$\hat{\mathbf{s}}_r = \sin\theta\cos\psi\hat{\mathbf{t}}_1 + \sin\theta\sin\psi\hat{\mathbf{t}}_2 + \cos\theta\hat{\mathbf{n}} \tag{12}$$

where $\sin^2\theta = R_1$, $\Psi = 2\pi R_2$, $0 \leqslant R_1 \leqslant 1$ and $0 \leqslant R_2 \leqslant 1$ are independent random numbers, $\hat{\mathbf{n}}$ is the unit surface normal vector at the point of collision, and $\hat{\mathbf{t}}_1$ and $\hat{\mathbf{t}}_2$ are the unit surface tangent vectors that are normal to each other. In order to maintain a continuum of energy density, a transmitted phonon is represented by a new phonon that assumes local properties (velocity, frequency, and MFP) and travels along the new direction that is randomly determined as explained above until finishing the remaining time in the current time step. Because the frequencies at the two sides of the interface are generally different, the phonon energy is not conserved. This is remedied by monitoring the energy deficiency (or surplus) at each side of the interface. When the cumulated energy difference exceeds a certain amount, a new phonon is emitted from the interface (or the current phonon is deleted). This treatment leads to the conservation of energy in the interface scattering process.

In addition to phonon-interface scattering, phonons engage in various intrinsic-scattering events, such as phonon-impurities, phonon-dislocaty, and phonon-phonon scattering, as they move inside a crystalline material. Though it is possible to trace the detailed scattering events using MC simulation, many of the scattering mechanisms are not well understood and existing models are sometimes questionable in addition to tremendous computational time and memory requirements. As a simplified approach, we calculate the scattering probability of a phonon by a lumped MFP,

$$P_S = 1 - \exp(-v_{\mathrm{av}}\Delta t/\Lambda) \tag{13}$$

where Λ is the lumped MFP as calculated by Eq. (8), v_{av} is the phonon group velocity, and Δt is the time step. The assumption is that the intrinsic-scattering events happen similarly in the bulk material as that in nanocomposites. This assumption is valid for most of the cases since the modification of phonon dispersion relation is not important due to the short wavelength of the dominant heat transport phonons, which is around 1 nm. In the current simulation, each phonon is treated for intrinsic-phonon scattering at the end of each time step. A random number is drawn and compared to P_S. The phonon undergoes a scattering when the random number is less than P_S. The scattered phonon assumes local properties of velocity and frequency. Scattered phonon direction is assumed to be isotropic, and the direction vector is given by

$$\hat{\mathbf{s}} = \sin\theta\cos\psi\hat{\mathbf{i}} + \sin\theta\sin\psi\hat{\mathbf{j}} + \cos\theta\hat{\mathbf{k}} \tag{14}$$

where $\cos\theta = 2R_1 - 1$, $\Psi = 2\pi R_2$, and $0 \leqslant R_1 \leqslant 1$ and $0 \leqslant R_2 \leqslant 1$ are independent random numbers. Phonon energy is again not conserved since the phonon frequencies before and after scattering are usually different. The remedy is similar to interface scattering. The energy difference of each subcell that resulted from scattering is monitored, and when the difference exceeds a certain amount, a new phonon is generated (or an existing phonon is deleted). Energy conservation is therefore maintained in the subcell level. Note that the isotropic resetting of phonon direction in the above scheme tends to restore local equilibrium. This physical model is similar to all the relaxation time based phonon BTE simulation without considering the details of momentum conservation of intrinsic-phonon scattering.

2.4 Process Flow. Figure 2 shows the schematic process flow of the MC simulation algorithm. The MC simulation starts with the initialization step, where phonons are created within the unit cell and given frequency, velocity, and direction to represent the initial temperature condition within the unit cell. The initial temperature inside the unit cell is assumed to be uniform. After the initialization step, phonons experience the moving and scattering in each time step. The phonon bundles move one by one in straight lines for a prescribed time step and scatter at the interfaces. The properties of the phonons that leave the unit cell are monitored and stored. The next step is phonon emission at x boundaries using the stored phonon pattern as explained in Sec. 2.2. The total number of emitted phonon is determined by a constant heat flow boundary condition. After moving and emission, the 3D temperature profile of the unit cell is obtained by tallying the internal energy of each subcell. Average phonon properties are then calculated accordingly. Based on the local temperature and MFP values obtained, phonons then undergo intrinsic phonon scattering. This step marks the end of a single time step, and the next time loop starts again from the moving step.

2.5 Convergence and Accuracy. The MC technique is a statistical method, whose accuracy depends largely on the phonon bundle number and the time employed in the calculation. After some initial trials, we adopted a bundle number such that there are on average more than 50 phonon bundles in each subcell. The time step is selected such that within each time step, a phonon travels a distance on the order of the magnitude of the subcell dimension. For example, if the subcell dimension is 1 nm, with phonon group velocity on the order of 10^3 m/s, the appropriate time step would be 10^{-12} s. The simulations usually attain converged thermal conductivity results after 1000 time steps. A typical trend of calculated thermal conductivity with respect to calculation time is shown in Fig. 3. The error after 1 ns, equivalent to 1000 time steps, is within 3% of the final value, while the error after 10 ns is within 0.1% of the final value. Note that due to the statistical nature of the MC method, the results still exhibit a variation, although insignificant, even after a 120 ns calculation. In this study, a calculation time of at least 10 ns, which normally corresponds to 10^4 time steps, is applied to all cases for calculating the thermal conductivity. The results of the last 500 time steps are further averaged to give a representative thermal conductivity value.

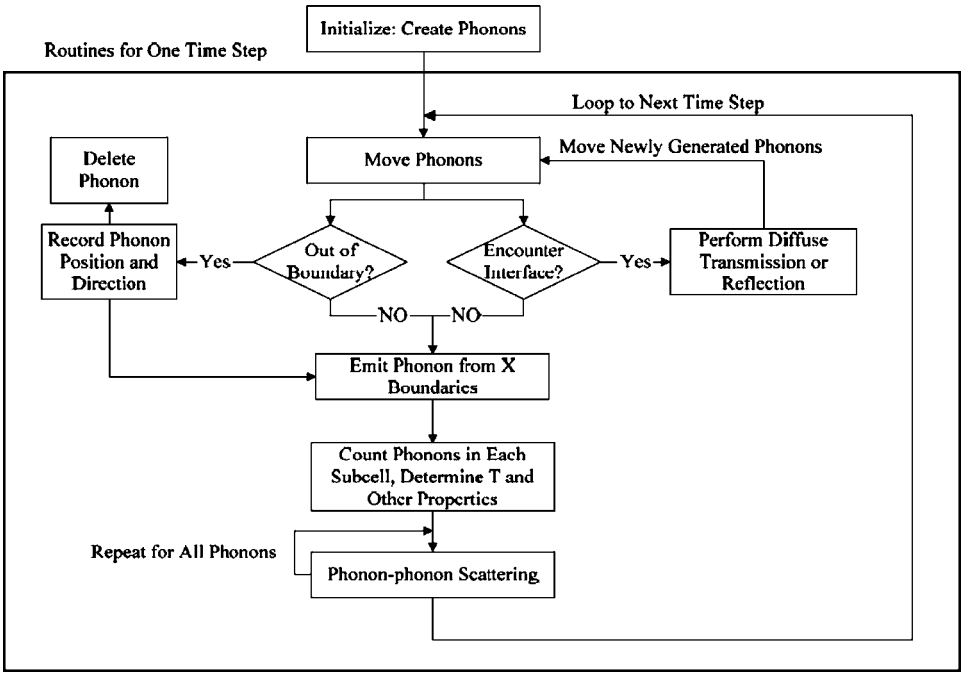

Fig. 2 The schematic process flow of the MC simulation algorithm. The MC simulation starts with the initialization step. After the initialization step, phonons experience the moving and scattering in each time step.

3 Results and Discussions

To validate our MC simulation methodology, we first simulate the phonon transport in a bulk Ge material to compare the thermal conductivity obtained through MC with the experiment data in literature. Then, we conducted MC simulation for phonon transport in 2D nanowire composites and compare the results with those obtained through the deterministic solution of the phonon BTE. After the validation, the code is then used to simulate phonon transport in various 3D Si–Ge nanocomposites to study the size effect of thermal conductivity of nanoparticle composites. Some of the fundamental questions critical for designing highly efficient thermoelectric nanocomposites are addressed, including (a) how the thermal conductivity changes with the size of nanoparticles and atomic composition and (b) what the effect of nonmonosize and the distribution pattern of nanoparticles is on the thermal conductivity reduction in nanoparticle composites. A comparison with the effective medium approach (EMA) based on the Fourier heat conduction theory with the addition of interface thermal resistance is also given. Knowing that the phonon-interface scattering dominates the thermal conductivity reduction for nanocomposites, we suggest using interfacial area per unit volume as a parameter to correlate the size effect of thermal conductivity in nanocomposites. In the end, the temperature dependence of thermal conductivity of nanocomposites is given and compared with recent experimental data.

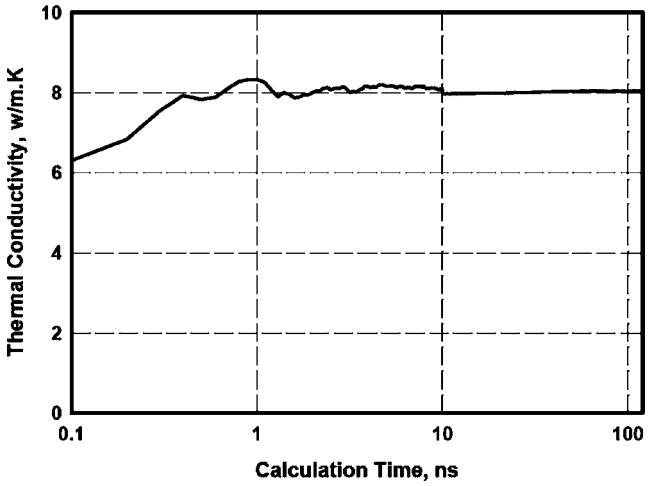

Fig. 3 Typical variation of thermal conductivity values with respect to calculation time. The case shown is a 2D nanocomposite with 10 nm Si nanowire embedded in Ge host. The result is converged after 10 ns simulation, corresponding to 10,000 time steps, with a variation of less than 0.1% afterward.

3.1 Code Validation: Bulk and Two-Dimensional Simulation. Homogeneous bulk Ge material was simulated first, where the computational domain contains no particles and the only scattering mechanism is the intrinsic-phonon scattering. Figure 4 shows the comparison of the thermal conductivity value from the gray-medium MC simulation conducted in this work with the experimental thermal conductivity value of the bulk germanium sample. The experimental Ge value is taken from Ref. 44. The circular symbols indicate the results of simulating a solid bulk material without any particle inside. The square symbol represents the simulation of a "pseudocomposite," with both the "particle" region and the "host material" assumed to be germanium. When the two sides of the interface both have transmissivity values of 1, the simulation should be equal to a solid bulk material without a particle. This pseudocomposite simulation served to validate the MC coding. Though the MC code can be used to simulate temperature-dependent thermal conductivity values of nanocomposites, the rest of this work focuses on the size effect of the thermal conductivity of nanocomposites at room temperature. The simulation results of the thermal conductivity of bulk Ge agree very well with the experimental data, as shown in Fig. 4. The program was then used to study the thermal conductivity of 2D nanowire composites, which were previously studied by simulating phonon transport using the deterministic solution of the phonon BTE [12]. To simulate phonon transport in a 2D nanowire composite, the particle in the unit cell shown in Fig. 1(*b*) is ex-

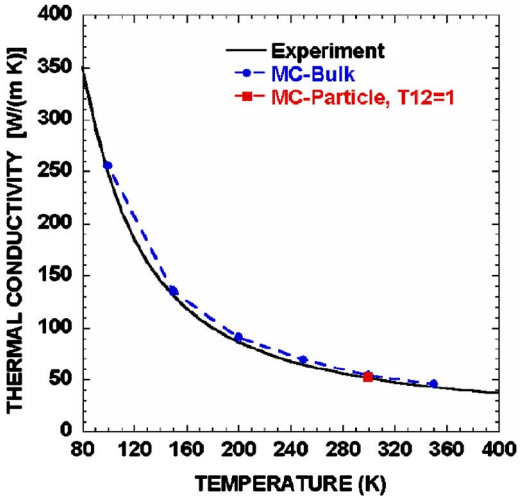

Fig. 4 Comparison of the thermal conductivity value from the gray-medium MC simulation conducted in this work with the experimental thermal conductivity value of a bulk germanium sample. The experimental Ge value is taken from Ref. [44]. The circular symbols indicate the results of simulating a solid bulk material without any particle inside. The triangle symbol represents the simulation of a pseudocomposite when both the particle and the host material are Ge. When the two sides of the interface both have transmissivity values of 1, the simulation should equal that of a solid bulk material without any particles. This pseudocomposite simulation served to validate the MC coding.

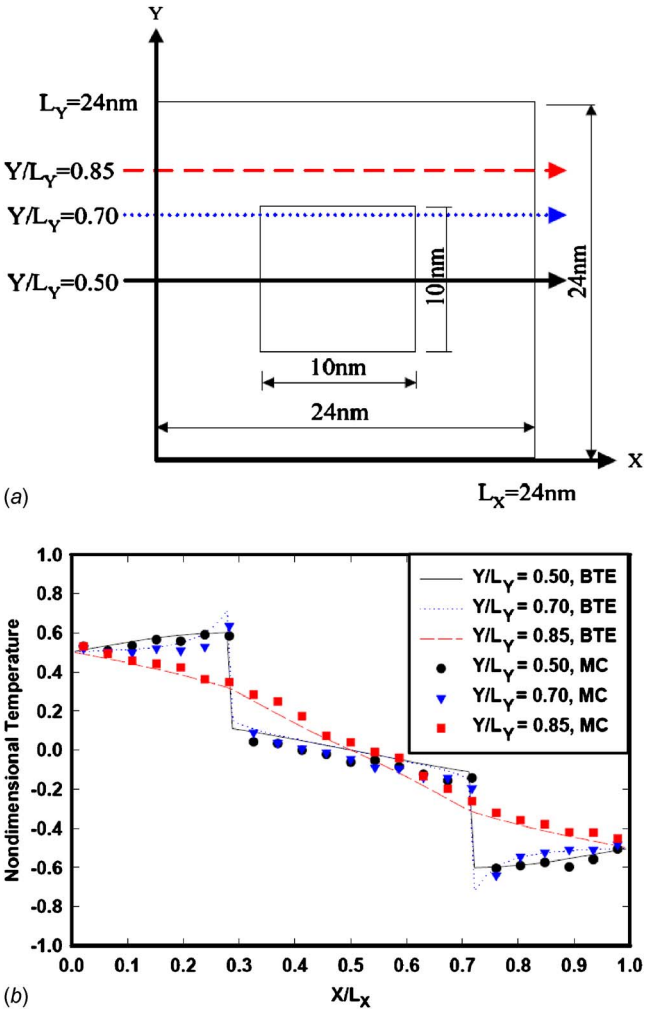

Fig. 5 Comparison of the temperature (energy density) distributions inside a nanowire composite obtained, respectively, by the deterministic solution of the phonon BTE and MC method. (*a*) Geometric dimensions of the unit cell for a $Si_{0.2}-Ge_{0.8}$ nanowire composite with a 10×10 nm^2 nanowire inclusion with *z* along the wire direction. (*b*) Temperature distribution along the *x* direction at various *y* positions assuming heat flows in the *x* direction.

tended to touch the z boundaries. Due to the specular reflection and periodic boundary conditions, this is equivalent to infinitely long nanowires (with a square cross section) embedded in the host material, thus fully reproducing our previous 2D case [12]. The temperature distributions in the middle plane of the unit cell are taken for comparison with that obtained from the deterministic solution of 2D phonon BTE [12]. Figure 5 presents the temperature profile of the $Si_{0.2}-Ge_{0.8}$ nanocomposite, which consists of 10×10 nm^2 cross-section Si nanowires embedded in the Ge host material along the x direction for various y locations. Although the results by MC simulation exhibit a slight asymmetry, which is attributed to the statistical error associated with the MC method, the temperature profiles by the two simulations show a very good agreement. Thermal conductivity values from the MC simulation and those from the deterministic BTE solution also agree with each other, as shown in Fig. 6, for 10 nm and 50 nm nanowires with heat flow in the cross-wire direction. We note that the effective thermal conductivity value of the Si–Ge nanocomposites is counterintuitive, which was explained in detail in Ref. 12. The above comparisons justify the phonon gray-medium-based MC simulation methodology adopted in this study and also validate the program coding.

3.2 Three-Dimensional Periodic Structures. After verifying the MC methodology, the program is used to simulate phonon transport in various nanocomposites with different particle sizes and particle distributions. Figures 7(*a*) and 7(*b*) show the nanoparticles with the monosize particles distributing in aligned and staggered patterns in a periodic 3D nanoparticle composites. The staggered distribution resembles a face centered cubic (fcc) structure, in the crystallography terminology, with particles arranged in a pattern similar to the atomic pattern in a fcc crystal. Likewise, the aligned distribution resembles a simple cubic pattern.

Figure 8 shows the 2D temperature distribution in the middle plane of the unit cell for an aligned pattern. The Si particle has a size of $10\times10\times10$ nm^3 and occupies a 3.7% volume fraction, with the volume of the Si particle divided by the total volume of the unit cell. Similar to the temperature profile shown in Fig. 5 for the 2D nanowire composite, Fig. 8 again shows that the maximum temperature overshoot occurs at the nanoparticle–matrix material interface similar to that observed in Ref. 12. The MC simulation does not show the highest energy density (temperature) region occurring at the corner of the nanoparticle-host interface as those simulated by the deterministic BTE solution. The reason is possibly due to the lower spatial resolution implemented in the MC simulation. As mentioned earlier, the requirement of having sufficient phonon bundles in each subcell largely limits the spatial resolution in MC phonon simulation.

It is also worthwhile at this point to show the effectiveness of the periodic boundary condition implemented in Sec. 2.2, i.e., to verify that the phonon transport simulation in the unit cell can be used to represent the phonon transport in the whole nanocomposites and thus to deduce the effective thermal conductivity of the nanocomposites. Fig. 9(*a*) shows the comparison of heat flux at hot (x=0) and cold (x=Lx) x boundaries in a periodic aligned nanoparticle composite, i.e., with one 10 nm cubic particle inside a 14 nm cubic unit cell. The periodicity in local heat flux in x boundaries clearly demonstrated that the unit cell with a periodic

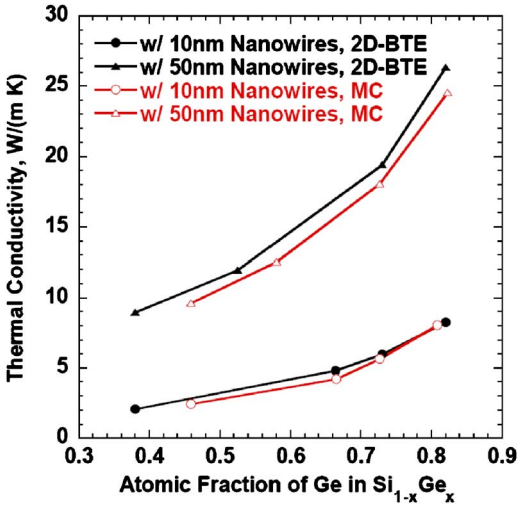

Fig. 6 Comparison of thermal conductivity values for the 2D nanowire composites obtained by a MC simulation and by a deterministic solution of the BTE. The relative percentage deviation is less than 8%.

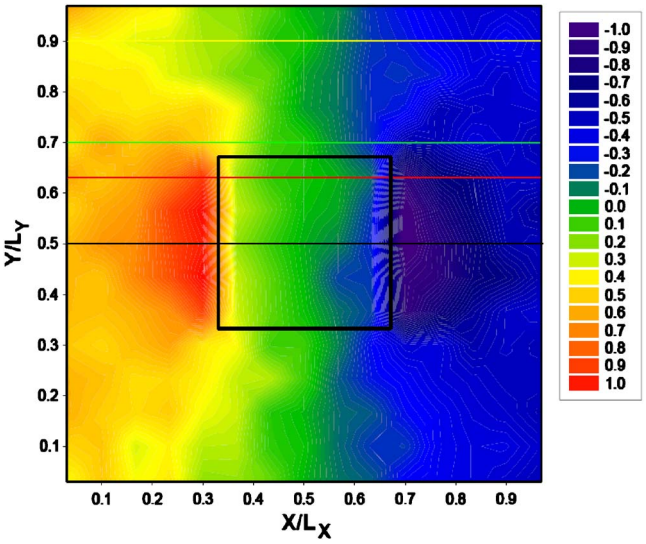

Fig. 8 Temperature distribution inside an aligned periodic nanoparticle composite in the middle plane in the *z* direction. The dimension of the nanoparticle is 10×10×10 nm^3. The volume fraction of Si particles is 3.7%, corresponding to a $Si_{0.04}$–$Ge_{0.96}$ atomic composition.

boundary condition implemented in this work is effective.

Figure 10 shows the size effect on the thermal conductivity of nanoparticle composites. The comparison of the thermal conductivity of the nanoparticle composites with 50 nm silicon particles and 10 nm silicon particles simply aligned in the germanium matrix and that of the SiGe alloy apparently, shown in Fig. 10(*a*), shows that the thermal conductivity decreases as the size of the nanoparticle decreases and the thermal conductivity of nanocomposites with a 10 nm particle can be even lower than that of the alloy value with same constituents. This demonstrates that the nanocomposite can be an effective approach to reduce the thermal conductivity and thus to develop a high-efficiency thermoelectric material. Figure 10(*b*) shows the effect of the particle distribution on the thermal conductivity of nanocomposites with a 10 nm Si particle in the Ge host material. For the same Si/Ge atomic ratio, the lowest thermal conductivity is achieved by organizing well the particles in a staggered pattern (the fcc structure). This phenomenon is within our anticipation as staggered particles effectively block the pathway of ballistic transport and increase the chances of interface scattering. Also shown in Figure 10(*b*) are the thermal conductivity values in the cross-interface direction of the 2D nanocomposite composed of 10 nm nanowires.

As stated in the Introduction, most past studies on the thermal conductivity of nanocomposites were based on the Fourier diffusion theory together with a consideration of the thermal boundary resistance. To examine the validity of such an approach, we compare the effective thermal conductivity obtained from the MC simulation with that of the EMA. The following EMA equation was developed by Nan et al. [18] for spherical particles:

$$\frac{k_e}{k_m} = \frac{k_P(1+2\alpha)+2k_m+2f[k_P(1-\alpha)-k_m]}{k_P(1+2\alpha)+2k_m-f[k_P(1-\alpha)-k_m]} \tag{15}$$

where k_e is the effective composite thermal conductivity, k_m is the host material thermal conductivity, k_P is the particle thermal conductivity, f is the volume fraction of nanoparticle inclusion, and α is a dimensionless parameter defined as $\alpha = a_k/a_p$ for nanoparticle composites. a_p is the radius of nanoparticle inclusions, and a_k

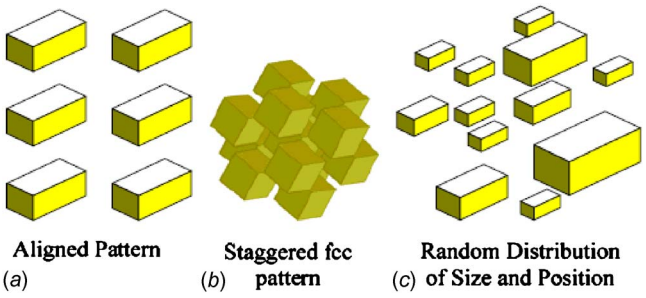

Fig. 7 Sketch of nanoparticle composites with silicon cubic nanoparticles distributed (*a*) in an aligned pattern, (*b*) in a staggered pattern, and, randomly, (*c*) in a germanium matrix for MC simulation conducted in this work. Even in (*c*), the cubic nanoparticles are aligned parallel to each other. The thermal conductivity calculated in this work are all in the direction normal to the cubic nanoparticles.

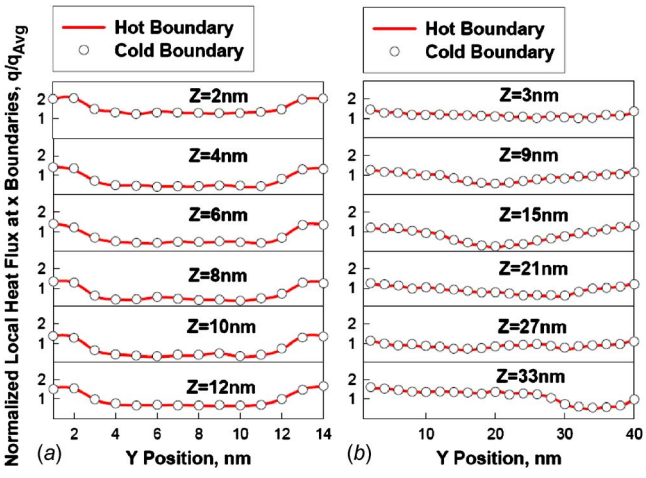

Fig. 9 Comparison of the heat flux at the hot ($x=0$) and cold ($x=L_x$) *x* boundaries in (*a*) A periodic aligned nanoparticle composite, i.e., with one 10 nm cubic particle inside a 14 nm cubic unit cell. (*b*) A random nanoparticle composite, i.e., with ten nanoparticles, each of which is a 10 nm cube randomly distributed inside a 40×40×40 nm^3 unit cell. The comparison demonstrates the periodicity of local heat flux in the *x* direction.

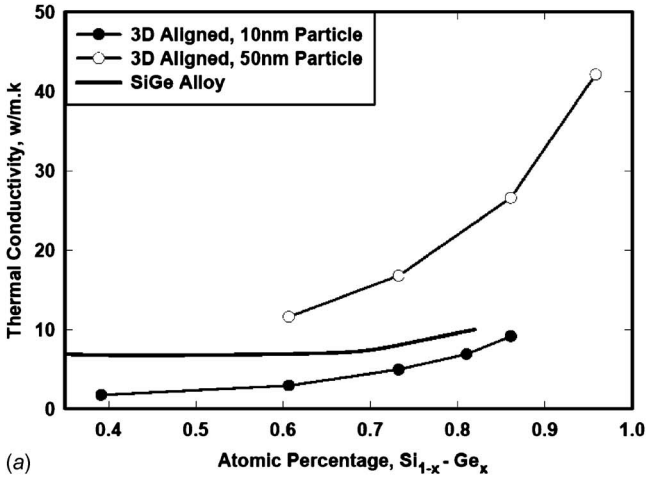

(a)

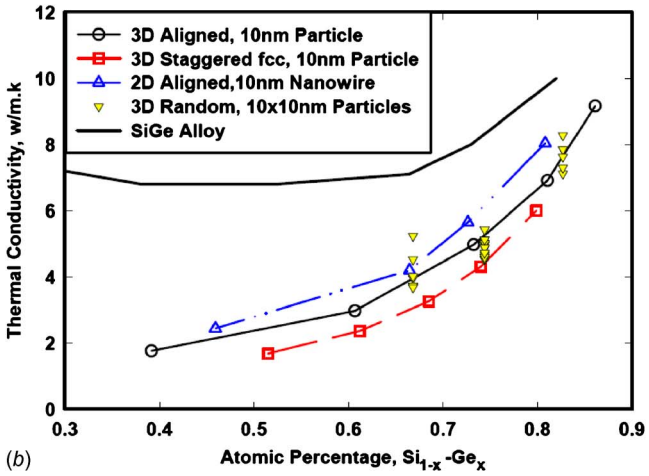

(b)

Fig. 10 The effects of silicon nanoparticle size and distribution on the thermal conductivity of nanoparticle composites: (*a*) Comparison of the thermal conductivity of composites with 10 nm and 50 nm silicon cubic particles distributed in a simple periodic pattern in a germanium host and that of a Si–Ge alloy as a function of atomic composition. (*b*) The effect of the distribution pattern on the thermal conductivity of composites with 10 nm silicon particle inclusions. Also shown in (*b*) is the thermal conductivity of a Si–Ge alloy.

$=Rk_m$, where R is the interface thermal resistance, which can be calculated as [41,48]

$$R = \frac{4}{T_{d12}U_1v_1} = \frac{4(U_1v_1 + U_2v_2)}{U_1v_1U_2v_2} \tag{16}$$

Using the heat capacity and the sound velocity to calculate interface thermal resistance shown in Eq. (16), we obtain $R=1.0\times10^{-9}$ m^2 K/W. Other parameters used in the calculation are k_m(Ge)=51.7 W/(m K), k_p(Si)=150 W/(m K), a_p=5 nm, 25 nm, and 100 nm (for nanoparticle dimensions of 10 nm, 50 nm, and 200 nm). Strictly speaking, Eq. (15) is correct only for composites with spherical particle inclusions, and the present MC simulation is conducted for composites with cubic nanoparticle inclusions, but we expect the difference of the true thermal conductivity values of nanocomposites between cubic and spherical nanoparticle inclusions to be very small. Figure 11 compares the thermal conductivity obtained from the MC simulation and the effective medium approximation. As we can see, the effective medium approach based on incorporating the thermal boundary resistance into the solutions of the Fourier heat conduction law underpredicts the size effects. The EMA results do not predict a thermal conductivity value lower than the bulk SiGe alloy in any case. This conclusion is further supported by a recent experimental work, which shows that the thermal conductivity of the Si–Ge nanocomposite is very close to that of the MC simulation [49,50].

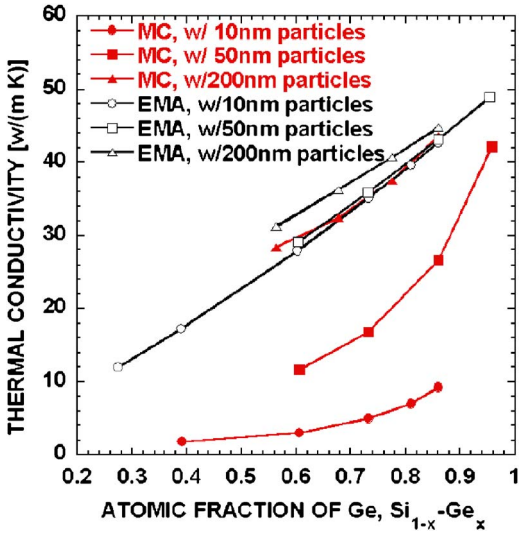

Fig. 11 Thermal conductivity of nanoparticle composites predicted by the MC simulation conducted in this work and that predicted by the EMA proposed by Nan et al. in Ref. [18]. The EMA based on incorporating the thermal boundary resistance into the solutions of the Fourier heat conduction law underpredicts the size effects.

3.3 Effects of Randomness. In the random distribution, the particles are distributed randomly with their positions determined by random numbers. Figure 8(*c*) also shows further randomization on particle size in addition to random position distribution. However, owing to the periodic boundary conditions addressed in Sec. 2.2 the computation is mathematically equal to simulating an infinite material consisting of repeating structures of the computational domain. In other words, the random distribution treated in this paper represents a semirandom semiperiodic pattern (short range random and long range periodic pattern). This argument is solidified by the periodic heat flux shown in Fig. 9(*b*). Figure 9(*b*) shows that the periodicity of heat flux is remarkably well preserved even in the random distribution case. Without a solid proof, we comment that if the computational domain (unit cell) is larger than a few phonon MFPs (or contains enough particles), the simulation results should be converged to the true value of the random nanocomposites. However, it requires much larger computational time and memory since the problem is intrinsically a multiscale problem. Figures 10(*b*) and 12 show the thermal conductivity values of nanocomposites composed of randomly distributed particles. In these figures, each data point for random structures is the result of randomly distributing ten particles in the computational domain. Since the process of distributing particles and selecting particle sizes is purely random and the computational domain is not large enough, the outcomes of the program after each run vary from one another. However, the spreading of these random structure results sheds some light on the possible range of thermal conductivity reduction associated with a nanocomposite sample fabricated through a process like hot pressing. Figure 10(*b*) shows that the random distribution of particle positions generally results in thermal conductivity values very close or even lower than those of aligned distribution. However, a further randomness associated with particle sizes [distribution pattern shown in Fig. 8(*c*)] does not help reduce thermal conductivity, as shown in Fig. 12, which is evidenced by comparing the thermal conductivity values of aligned 50 nm particles and of random 10–100 nm particles.

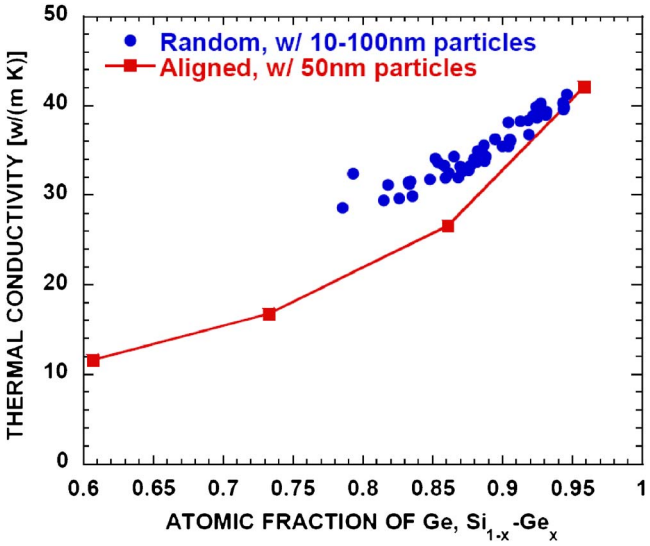

Fig. 12 Comparison of the thermal conductivity of a periodically aligned nanocomposite with 50 nm cubic silicon particles distributed in a germanium matrix and that of a random composite with silicon nanoparticles having a size range from 10 nm to 100 nm distributed randomly in a germanium matrix as a function of germanium atomic composition.

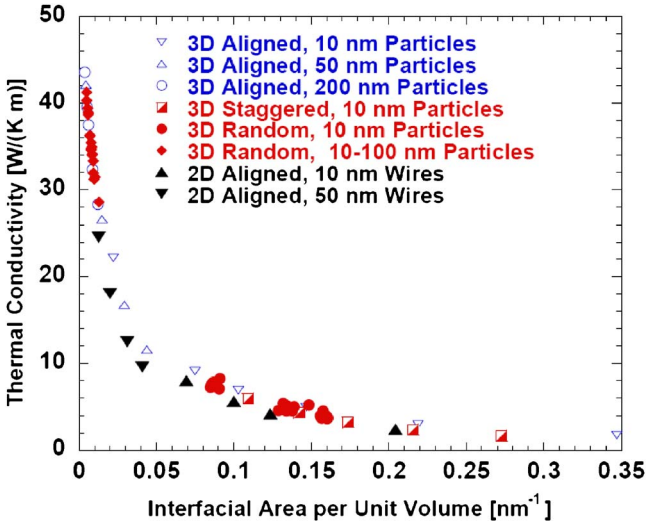

Fig. 13 The thermal conductivity of nanoparticle composites as a function of the interfacial area per unit volume (interface density). The thermal conductivity data of nanoparticle composites falls on to a single curve nicely as a function of interfacial area per unit volume. The randomness either in particle size or position distribution causes slight fluctuations. However, these fluctuations are not a dominant factor for the reduction in the thermal conductivity. The effective thermal conductivity of 2D nanowire composites is lower than that of 3D nanoparticle composites for the same interface area per unit volume since the effectiveness of interface scattering on the thermal conductivity reduction is different when the interface is perpendicular to the applied temperature difference direction and when the interface is parallel to the applied temperature difference direction.

3.4 Interfacial Area Per Unit Volume. Knowing that the phonon-interface scattering dominates the thermal conductivity reduction for nanocomposites, we propose using interfacial area per unit volume as a unified parameter to replace the nanoparticle size and the atomic composition and to correlate the wide spreading thermal conductivity data. Figure 13 shows that the thermal conductivity data of nanoparticle composites follow nicely into one curve as a function of interfacial area per unit volume. The randomness either in particle size or position distribution causes a slight fluctuation but is not a dominant factor for thermal conductivity reduction. Also shown in Fig. 13 are the thermal conductivity values of 2D nanowire composites. Apparently, the effective thermal conductivity of 2D nanowire composites is lower than that of 3D nanoparticle composites for the same interface area per unit volume. The reason is that a 2D nanowire composite contains half of its interfacial area perpendicular to the applied temperature difference direction and the other half parallel to the applied temperature difference direction, while a 3D nanocomposite contains only one-third of its interfacial area perpendicular to the applied temperature difference direction and the rest is parallel to the applied temperature difference direction. All the previous works show that interfaces that are perpendicular to the applied temperature direction are more efficient in scattering phonons and thus in reducing the thermal conductivity [12,41]. This also suggests that one might try to use "effective" interfacial area per unit volume to correlate the thermal conductivity of nanocomposites with different shapes of nanowire/particle inclusions.

3.5 Temperature-Dependent Thermal Conductivity (Comparison With Experiments). The MC code can be used to simulate temperature-dependent thermal conductivity value of nanocomposites. Figure 14(*a*) shows the temperature-dependent thermal conductivity of nanoparticle composites. Boundary scattering results in a very different temperature dependence of the thermal conductivity of nanocomposites compared to their bulk counterpart, where at high temperature the thermal conductivity is dominated by the Umklapp phonon-phonon scattering process. The thermal conductivity of Si-Ge nanocomposites with 10 nm particles in the germanium matrix is almost temperature independent. Figure 14(*b*) shows the comparison of the simulated thermal conductivity with recent experimental results from the Jet Propulsion Laboratory [50]. The "3run 2 HTB A" sample is a Si–Ge nanocomposite with 20–80 nm Si particles embedded in a Ge matrix. The "SGMA05" sample is a ball-milled SiGe alloy nanocomposite with an average particle size of 10 nm. Although the SMGA05 sample cannot be directly compared with the modeling since we did not consider the alloy scattering, both sets of experimental data clearly show that the size effect dominates the thermal conductivity reduction.

4 Conclusions

This work presents a phonon gray medium MC scheme to simulate the phonon transport and thus to study the thermal conductivity in nanocomposites. Special attention has been paid to the implementation of periodic boundary condition in the heat flow direction for MC simulation, which is essential to the study of the thermal conductivity of bulk composites with nanoparticle/nanowire inclusions—an intrinsic multiscale transport problem. With a simplified gray phonon approach, the simulation was able to duplicate our earlier results of deterministically solving BTE. The MC simulation reveals the ballistic feature of phonon transport in nanocomposites, which is consistent with the deterministic solution of the phonon BTE. The size effects of phonon transport in nanoparticle composites were systematically studied, and the results showed that the thermal conductivity of nanoparticle composites can be lower than the alloy value. Several other parameters that could influence the thermal conductivity were also investigated by the MC simulation, including the distribution of the size and position of Si nanoparticles. It was found that randomly distributed nanopaticles in nanocomposites rendered the thermal conductivity values close to that of periodic aligned patterns. On the other hand, a staggered distribution of nanoparticles could result in a much lower thermal conductivity for the same particle volume fraction. The thermal conductivity values calculated by

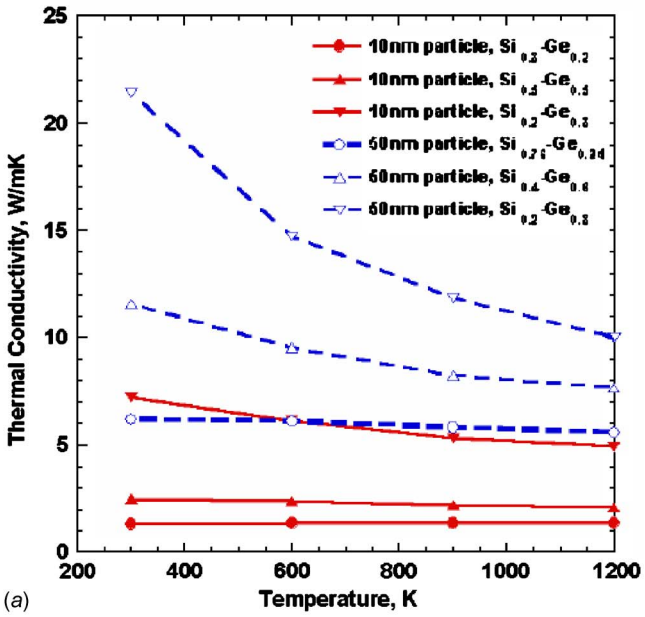

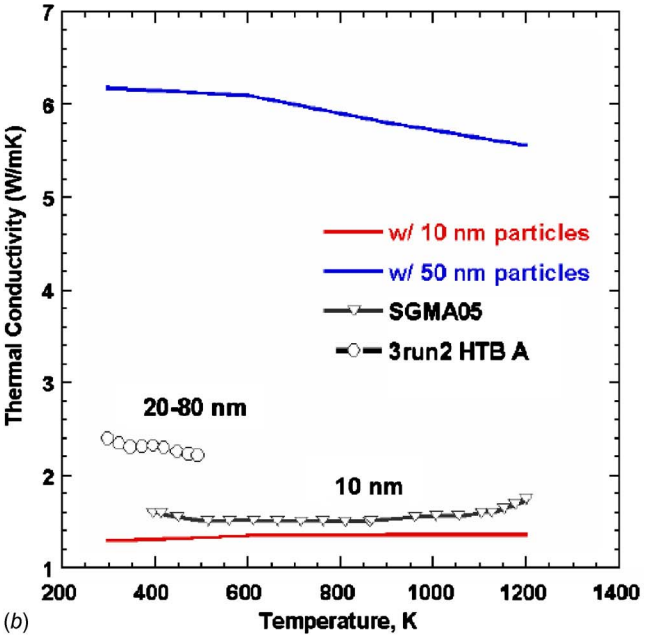

Fig. 14 (*a*) **The temperature-dependent thermal conductivity of nanoparticle composites.** (*b*) **Comparison of the simulated thermal conductivity with recent experimental results from the Jet Propulsion Laboratory [50].**

this work qualitatively agrees with recent experimental measurement in SiGe nanocomposites. This work also suggested using interfacial area per unit volume as a parameter to correlate the size effect of the thermal conductivity of nanocomposites. The key for the thermal conductivity reduction is to have a high interface density where nanoparticle composites can have a much higher interface density than the simple 1D stacks, such as superlattices. Thus, nanocomposites further benefit the enhancement of *ZT* in terms of thermal conductivity reduction.

Acknowledgment

We greatly acknowledge discussions with Professor M. S. Dresselhaus at MIT, Professor Zhifeng Ren at Boston College, and Dr. J. P. Fleurial at JPL/Caltech. This work was supported by NASA Grant No. NNC06GA48G and DoD/AFOSR MURI Grant No. FA9550-06-1-0326. One author's (M.-S.J.) stay at MIT was supported by ITRI.

The follow-up work on this study can be found in Refs. [51–54].

References

[1] Chen, G., Dresselhaus, M. S., Dresselhaus, G., Fleurial, J.-P., and Caillat, T., 2003, "Recent Developments in Thermoelectric Materials," Int. Mater. Rev., **48**, pp. 45–66.
[2] Dresselhaus, M. G., Chen, G., Tang, M. Y., Yang, R. G., Lee, H., Wang, D. Z., Ren, Z. F., Fleurial, J. P., and Gogna, P., 2007, "New Directions for Low-Dimensional Thermoelectric Materials," Adv. Mater. (Weinheim, Ger.), **19**, pp. 1043–1053.
[3] Kim, W., Zide, J., Gossard, A., Klenov, D., Stemmer, S., Shakouri, A., and Majumdar, A., 2006, "Thermal Conductivity Reduction and Thermoelectric Figure of Merit Increase by Embedding Nanoparticles in Crystalline Semiconductors," Phys. Rev. Lett., **96**, pp. 045901.
[4] Harman, T. C., Taylor, P. J., Walsh, M. P., and LaForge, B. E., 2002, "Quantum Dot Superlattice Thermoelectric Materials and Devices," Science, **297**, pp. 2229–2232.
[5] Venkatasubramanian, R., Silvona, E., Colpitts, T., and O'Quinn, B., 2001, "Thin-Film Thermoelectric Devices With High Room-Temperature Figures of Merit," Nature (London), **413**, pp. 597–602.
[6] Hsu, K. F., Loo, S., Guo, F., Chen, W., Dyck, J. S., Uher, C., Hogan, T., Polychroniadis, E. K., and Kanatzidis, M. G., 2004, "Cubic AgPbmSbTe2 +m:Bulk Thermoelectric Materials With High Figure of Merit," Science, **303**, pp. 818–821.
[7] Majumdar, A., 2004, "Thermoelectricity in Semiconductor Nanostructures," Science, **303**, pp. 777–778.
[8] Tritt, T. M., Semicond. Semimetals, Vols. **69–71** (special issues on Recent Developments on Thermoelectrics).
[9] Golsmid, H. J., 1964, *Thermoelectric Refrigeration*, Plenum, New York.
[10] Yang, R. G., and Chen, G., 2005, "Nanostructured Thermoelectric Materials: From Superlattices to Nanocomposites," Materials Integration, **18**, pp. 31–36 (feature issue on "Thermoelectric Materials R&D in the World").
[11] Chen, G., 2001, "Phonon Transport in Low-Dimensional Structures," Semicond. Semimetals, **71**, pp. 203–259.
[12] Yang, R. G., and Chen, G., 2004, "Thermal Conductivity Modeling of Periodic Two-Dimensional Nanocomposites," Phys. Rev. B, **69**, p. 195316.
[13] Zhao, X. B., Ji, X. H., Zhang, Y. H., Zhu, T. J., Tu, J. P., and Zhang, X. B., 2005, "Bismuth Telluride Nanotubes and the Effects on the Thermoelectric Properties of Nanotube-Containing Nanocomposites," Appl. Phys. Lett., **86**, p. 062111.
[14] Kapitza, P. L., 1941, "Heat Tracer and Superfluidity of Helium II," J. Phys. (Moscow), **4**, pp. 181–210; Swartz, E. T., and Pohl, P. P., 1989, "Thermal Boundary Resistance," Rev. Mod. Phys., **61**, pp. 605–668.
[15] Hasselman, D. P. H., and Johnson, L. F., 1987, "Effective Thermal Conductivity of Composites With Interfacial Thermal Barrier Resistance," J. Compos. Mater., **21**, pp. 508–515.
[16] Benvensite, Y., and Miloh, T., 1991, "On the Effective Thermal Conductivity of Coated Short-Fiber Composites," J. Appl. Phys., **69**, pp. 1337–1344.
[17] Every, A. G., Tzou, Y., Hasselman, D. P. H., and Raj, R., 1992, "The Effect of Particle Size on the Thermal Conductivity of ZnS/Diamond Composites," Acta Metall. Mater., **40**, pp. 123–129.
[18] Nan, C.-W., Birringer, R., Clarke, D. R., and Gleiter, H., 1997, "Effective Thermal Conductivity Of Particulate Composites With Interfacial Thermal Resistance," J. Appl. Phys., **81**, pp. 6692–6699.
[19] Felske, J. D., 2004, "Effective Thermal Conductivity of Composite Spheres in a Continuous Medium With Contact Resistance," Int. J. Heat Mass Transfer, **47**, pp. 3453–3461.
[20] Lu, S. Y., and Song, J. L., 1996, "Effect of Interfacial Characteristics on Effective Conductivities of Composites Containing Randomly Distributed Aligned Long Fibers," Chem. Eng. Sci., **51**, pp. 4393–4404.
[21] Graham, S., and McDowell, D. L., 2003, "Numerical Analysis of the Transverse Thermal Conductivity of Composites With Imperfect Interfaces," ASME J. Heat Transfer, **125**, pp. 389–393.
[22] Torquato, S., and Rintoul, M. D., 1995, "Effect of the Interface on the Properties of Composite Media," Phys. Rev. Lett., **75**, pp. 4067–4070.
[23] Lazarenkova, O. L., and Balandin, A. A., 2002, "Electron and Phonon Energy Spectra in a Three-Dimensional Regimented Quantum Dot Superlattice," Phys. Rev. B, **66**, p. 245319.
[24] Yang, B., and Chen, G., 2003, "Partially Coherent Phonon Heat Conduction in Superlattices," Phys. Rev. B, **67**, p. 195311.
[25] Yang, R. G., Chen, G., Laroche, M., and Taur, Y., 2005, "Multidimensional Transient Heat Conduction at Nanoscale Using the Ballistic-Diffusive Equations and the Boltzmann Equation," ASME J. Heat Transfer, **127**, pp. 298–306.
[26] Yang, R. G., Chen, G., and Dresselhaus, M. S., 2005, "Thermal Conductivity of Simple and Tubular Nanowire Composites in the Longitudinal Direction," Phys. Rev. B, **72**, p. 125418.
[27] . Howell, J. R., 1998, "The Monte Carlo Method in Radiative Heat Transfer," ASME J. Heat Transfer, **120**, pp. 547–560.
[28] Moglestue, C., 1982, "Monte-Carlo Particle Modeling of Small Semiconductor Devices," Comput. Methods Appl. Mech. Eng., **30**, pp. 173–208.

[29] Jacoboni, C., and Reggiani, L., 1983, "The Monte-Carlo Method for the Solution of Charge Transport in Semiconductors With Applications to Covalent Materials," Rev. Mod. Phys., **55**, pp. 645–705.
[30] Fischetti, M. V., and Laux, S. E., 1988, "Monte Carlo Analysis of Electron Transport in Small Semiconductor Devices Including Band-Structure and Space-Charge Effects," Phys. Rev. B, **38**, pp. 9721–9745.
[31] . Fischetti, M. V., and Laux, S. E., 1993, "Monte Carlo Study of Electron Transport in Silicon Inversion Layers," Phys. Rev. B, **48**, pp. 2244–2274.
[32] Lugli, P., Bordone, P., Reggiani, L., Rieger, M., Kocevar, P., and Goodnick, S. M., 1989, "Monte Carlo Studies of Nonequilibrium Phonon Effects in Polar Semiconductors and Quantum Wells. I. Laser Photoexcitation," Phys. Rev. B, **39**, pp. 7852–7865.
[33] Peterson, R. B., 1994, "Direct Simulation of Phonon-Mediated Heat Transfer in a Debye Crystal," ASME J. Heat Transfer, **116**, pp. 815–822.
[34] . Klitsner, T., VanCleve, J. E., Fischer, H. E., and Pohl, R. O., 1988, "Phonon Radiative Heat Transfer and Surface Scattering," Phys. Rev. B, **38**, pp. 7576–7594.
[35] Mazumder, S., and Majumdar, A., 2001, "Monte Carlo Study of Phonon Transport in Solid Thin Films Including Dispersion and Polarization," ASME Trans. J. Heat Transfer, **123**, pp. 749–759.
[36] Song, D., 2003, "Phonon Heat Conduction in Nano and Micro-Porous Thin Films," Ph.D. thesis, University of California at Los Angeles, Los Angeles, CA.
[37] Lacroix, D., Joulain, K., and Lemonnier, D., 2005, "Monte Carlo Transient Phonon Transport in Silicon and Germanium at Nanoscales," Phys. Rev. B, **72**, p. 064305.
[38] Chen, Y. F., Li, D. Y., Lukes, J. R., and Majumdar, A., 2005, "Monte Carlo Simulation of Silicon Nanowire Thermal Conductivity," ASME Trans. J. Heat Transfer, **127**, pp. 1129–1138.
[39] Prasher, R., 2006, "Transverse Thermal Conductivity of Porous Materials Made From Aligned Nano- and Microcylindrical Pores," J. Appl. Phys., **100**, p. 064302.
[40] Prasher, R., 2006, "Thermal Conductivity of Composites of Aligned Nanoscale and Microscale Wires and Pores," J. Appl. Phys., **100**, p. 034307.
[41] Chen, G., 1998, "Thermal Conductivity and Ballistic-Phonon Transport in the Cross-Plane Direction of Superlattices," Phys. Rev. B, **57**, pp. 14958–14973.
[42] Brockhouse, B. N., 1959, "Lattice Vibrations in Silicon and Germanium," Phys. Rev. Lett., **2**, pp. 256–258.
[43] Nilsson, G., and Nelin, G., 1971, "Phonon Dispersion Relations in Ge at 80 k," Phys. Rev. B, **3**, pp. 364–369.
[44] The temperature-dependent thermal conductivity of bulk Si and Ge is available at http://www.ioffe.rssi. ru/SVA/NSM/Semicond/
[45] Goodson, K. E., and Ju, Y. S., 1999, "Heat Conduction in Novel Electronic Films," Annu. Rev. Mater. Sci., **29**, pp. 261–293.
[46] Thijssen, J., 2007, *Computational Physics*, 2nd ed. Cambridge University Press, UK.
[47] Swartz, E. T., and Pohl, R. O., 1989, "Thermal Boundary Resistance," Rev. Mod. Phys., **61**, pp. 605–668.
[48] Dames, C., and Chen, G., 2004, "Theoretical Phonon Thermal Conductivity of Si/Ge Superlattice Nanowires," J. Appl. Phys., **95**, pp. 682–693.
[49] Lee, H., 2005, "Experimental Study of Thermal Conductivity Reduction of Silicon-Germanium Nanocomposite for Thermoelectric Application," MS thesis, Massachusetts Institute of Technology, Boston, MA.
[50] Dresselhaus, M. S., Chen, G., Ren, Z. F., Fleurial, J. P., and Gogna, P., 2005, Second Annual Technical Report for NASA Contract No. NAS3-03108.
[51] Tian, W. X., and Yang, R. G., 2007, "Effect of Interface Scattering on Phonon Thermal Conductivity Percolation in Random Nanowire Composites," Appl. Phys. Lett., **90**, p. 263105.
[52] Tian, W. X., and Yang, R. G., 2007, "Thermal Conductivity Modeling of Compacted Nanowire Composites," J. Appl. Phys., **101**, p. 054320.
[53] Tian, W. X., and Yang, R. G., "Phonon Transport and Thermal Conductivity Percolation in Random Nanoparticle Composites," Comput. Model. Eng. Sci.(CMES), in press.
[54] Minnich, A., and Chen, G., 2007, "Modified Effective Medium Formulation for the Thermal Conductivity of Nanocomposites," Appl. Phys. Lett., **91**, p. 073105.

An Atomistic Simulation Study of the Role of Asperities and Indentations on Heterogeneous Bubble Nucleation

Brian R. Novak
Edward J. Maginn
Mark J. McCready

Department of Chemical and Biomolecular Engineering, University of Notre Dame, Notre Dame, IN 46556

Heterogeneous bubble nucleation was studied on surfaces having nanometer scale asperities and indentations as well as different surface-fluid interaction energies. Nonequilibrium molecular dynamics simulations at constant normal stress and either temperature or heat flux were carried out for the Lennard–Jones fluid in contact with a Lennard–Jones solid. When surface defects were of the same size or smaller than the estimated critical nucleus (the smallest nucleus whose growth is energetically favored) size of $1000-2000$ Å^3*, there was no difference between the defected surfaces and atomically smooth surfaces. On the other hand, surfaces with significantly larger indentations had nucleation rates that were about two orders of magnitude higher than the systems with small defects. Moreover, nucleation was localized in the large indentations. This localization was greatest under constant heat flux conditions and when the solid-fluid interactions were weak. The results suggest strategies for enhancing heterogeneous bubble nucleation rates as well as for controlling the location of nucleation events.*
[DOI: 10.1115/1.2818771]

Keywords: heterogeneous bubble nucleation, nonequilibrium molecular dynamics simulations, constant heat flux, constant temperature, geometric defects, surface-fluid interactions

1 Introduction

The understanding of bubble nucleation at surfaces is important for various applications including boiling heat transfer [1–3], formation of carbon dioxide bubbles on the anode of direct methanol fuel cells [4–6], and microfluidic devices such as bubble jet printing heads [7–10]. In boiling heat transfer, the goal is to design a surface to maximize heat loss from a surface through bubble formation and detachment. In methanol fuel cells, carbon dioxide must be removed from the anode through the diffusion layer while minimizing the decrease in the flow of fuel in the other direction. In bubble jet printers, a high heat flux is used to produce vapor whose growth ejects ink from a nozzle. Some issues in surface nucleation include the question of whether nucleation is homogeneous or heterogeneous, the mechanism, and the role preexisting nuclei (PEN) play in the nucleation mechanism.

Experimentally [9,11] it was found that when the heat flux into a surface was very high, the nucleation temperature was equal to the spinodal temperature; this was indicative of homogeneous nucleation. As the heat flux was decreased, a point was reached when the nucleation temperature began to decrease. This indicated that heterogeneous nucleation began to play a role. For relatively low heat flux applications, heterogeneous nucleation should be the dominant mechanism.

PEN theory [12–15] is the idea that vapor can be trapped in crevices when a liquid floods a surface (see Fig. 1). Theofanous et al. [16] performed boiling experiments using water on titanium surfaces with 4 nm surface roughness and found that nucleation required tens of degrees of superheat. In contrast, relations based on PEN theory predict that superheats on the order of hundreds [17] or thousands [14] of degrees would be required for nucleation on such smooth surfaces. Relationships based on PEN between nucleation site density and superheat, and heat flux and superheat [14,17,18] were also found to be different from the experimental results. PEN theory clearly does not work on the nanometer scale. The defects on a surface might promote nucleation regardless of trapped gas on a surface. Recent work has shown that nanobubbles on a surface are seemingly stable even under a shock wave giving a minimum pressure of −6 MPa [19]. Cavitation occurred only at defects.

Molecular dynamics (MD) simulations can be used to study nucleation at high superheats or high heat fluxes on surfaces with nanometer scale geometric defects. For constant heat flux MD simulations, relatively high fluxes on the order of 100 MW/m^2 are required due to time scale limitations. This is greater than typical critical heat fluxes, which are on the order of 1 MW/m^2. However, these fluxes are experimentally accessible using pulse heating. High heat fluxes up to 1.0 GW/m^2 generated using electrical heating [8,9,11,20–26] or a laser [27,28] have been studied.

There have been various molecular simulation studies of heterogeneous nucleation. The ones most similar to this work were the studies of explosive boiling of a variable depth fluid on a hot surface using argon on a platinum surface [29] and water on a gold surface [30]. Maruyama and Kimura [31] studied bubble nucleation in a Lennard–Jones fluid between harmonic platinum walls. The nucleation was induced by moving the upper wall to reduce the pressure. The effect of surface wettability on contact angle was obtained by varying the platinum-fluid energy parameter. Novak et al. [32] used MD simulations to study homogeneous and heterogeneous nucleation using a Lennard–Jones fluid and solid and the effect of surface wettability. Nucleation was induced by ramping up the temperature while keeping the pressure (homogeneous) or the normal stress on a top wall potential (heterogeneous) constant. Yi et al. [33] studied the vaporization of a thin Lennard–Jones argon layer from a harmonic platinum wall.

Contributed by the Heat Transfer Division of ASME for publication in the JOURNAL OF HEAT TRANSFER. Manuscript received February 22, 2007; final manuscript received July 16, 2007; published online March 21, 2008. Review conducted by Satish G. Kandlikar.

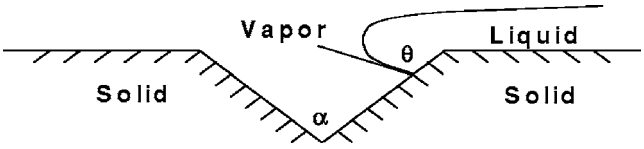

Fig. 1 A necessary condition for trapping vapor in a crevice when a surface is flooded with liquid is that the angle between the liquid-vapor interface, α, is greater than the crevice angle, θ [12].

Neimark and Vishnyakov [34] studied the nucleation of a Lennard–Jones fluid in wetting spherical pores using Monte Carlo simulations.

Theoretical work with defects was performed by Wilt [35]. He calculated nucleation rates for spherical and conical indentations and asperities for solutions supersaturated with carbon dioxide. He found that nucleation was favored in conical and spherical indentations, but not at the corresponding projections. The results showed increasing nucleation rates with decreasing cavity angle.

There have also been relationships developed to predict the size range of active cavities under conditions of constant wall temperature or constant heat flux [36–39]. These relationships relate fluid properties, temperature differences, contact angles, and thermal layer thickness to the minimum and maximum radius of active cavities.

This paper presents the results of a study of bubble nucleation on surfaces using MD simulations of simple Lennard–Jones spheres at constant temperature and normal stress or constant heat flux and normal stress. The goal was to determine the role of the size of nanometer scale geometric defects, the strength of solid-fluid interactions (wettability), and heat flux on the formation and growth of vapor nuclei.

2 Method

2.1 Simulated Systems. The simulations consisted of a fluid sitting above several layers of solid. A representation of a simulation box is shown in Fig. 2. Periodic boundary conditions were used in the x and y directions and walls formed the boundaries in the z direction. In the z direction, a mean field restraining wall potential was used at the top of the simulation cell. In some simulations, a wall potential was also placed below the solid atoms. Alternatively, a fixed layer of solid was used as the bottom boundary for other simulations. The position of the top wall potential

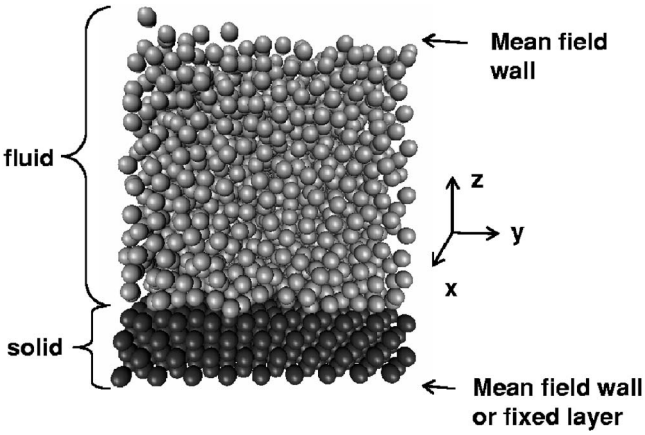

Fig. 2 The configuration of a heterogeneous simulation box. The light colored atoms are the fluid atoms and the dark colored ones are solid. The *z* directions were bounded by wall potentials or a fixed layer of solid, while periodic boundary conditions were used in the *x* and *y* directions.

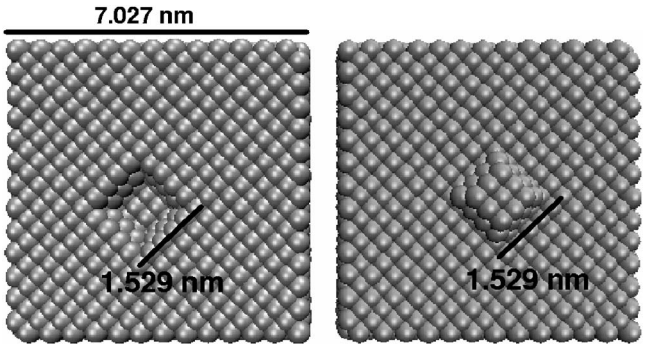

Fig. 3 The defected solids with small defects. The defects were approximately 1.5 nm wide and two layers deep.

was adjusted to maintain a constant normal stress (P_{zz}).

The top wall potential only interacted with the fluid atoms, and the bottom wall potential only interacted with the solid atoms. No truncation of the interactions was used; all of the fluid or solid atoms interacted with the wall potential at all times.

The solid was fcc with the (100) face exposed to the fluid except in the defects, where the (111) face was exposed. Initially, the lattice parameter was 5.405 Å but was compressed slightly in the z direction once the constant normal stress was applied.

Two system sizes were considered. In the small system, nucleation on an atomically smooth surface was compared to surfaces with a square right pyramidal frustum shaped asperity or indentation. The small system size had 4803 fluid atoms on five layers of solid with lateral dimensions of 70.27×70.27 Å^2. The largest base of the defects had sides of approximately 1.5 nm. The defect depth was two layers (see Fig. 3). The boundary on the bottom of the solid was a wall potential. In the large system, a larger square right pyramid shaped indentation was compared to an atomically smooth surface. Since the sides of the pyramid were on the (111) plane, the half angle for the indentation was 35.3 deg. The large system size had 13,132 fluid atoms on five layers of solid with lateral dimensions of 113.51×113.51 Å^2. The indentation had dimensions of approximately $4.5 \times 4.5 \times 3$ nm^3 (650 atoms). For the indented surface, the solid was not flat on the bottom to avoid simulating a large number of solid atoms. (see Fig. 4). The boundary on the bottom of the solid was a fixed layer of atoms.

2.2 Potential Models. A 12-6 Lennard–Jones model was used for all atom-atom interactions. The Lennard–Jones potential as a function of distance between two atoms, r_{ij}, is shown below,

$$\phi_{\mathrm{LJ}}(r_{ij}) = 4\epsilon\left(\left(\frac{\sigma}{r_{ij}}\right)^{12} - \left(\frac{\sigma}{r_{ij}}\right)^{6}\right) \quad r_{ij} \leqslant r_c \tag{1}$$

The cutoff radius r_c was 11.9175 Å for all interactions. A model of argon [40] was used for the fluid-fluid interactions. The value of σ was 3.405 Å for all interactions. The values of ϵ divided by Boltzmann's constant were $\epsilon_{\mathrm{ff}}/k_B = 121.014$ K for the fluid-fluid interactions, $\epsilon_{\mathrm{ss}}/k_B = 1210.14$ K for the solid-solid interactions, and was either $\epsilon_{\mathrm{sf}}/k_B = 60.507$ K or $\epsilon_{\mathrm{sf}}/k_B = 121.014$ K for the solid-fluid interactions. The case with $\epsilon_{\mathrm{ff}} > \epsilon_{\mathrm{sf}}$ will be referred to as the weak case, and the case with $\epsilon_{\mathrm{ff}} = \epsilon_{\mathrm{sf}}$ will be referred to as the neutral case.

A 9-3 potential [32,41,42] was used for the interaction between the mean field wall and a fluid or solid atom. The potential is

$$\phi_{9\text{-}3}(z_i) = \frac{2\pi\rho_w\sigma^3}{3}\epsilon\left[\frac{2}{15}\left(\frac{\sigma}{z_i + \Delta}\right)^9 - \left(\frac{\sigma}{z_i + \Delta}\right)^3\right]$$

$$\Delta = (2/5)^{1/6}\sigma \tag{2}$$

where z_i is the absolute distance of atom i from the wall. The density (ρ_w) of the top wall was 0.02 Å^{-3}, which is near the den-

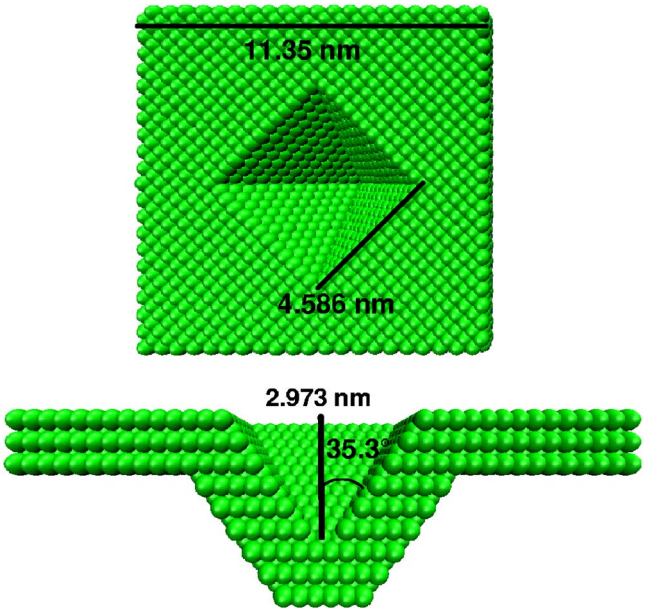

Fig. 4 The solid used in the large indentation simulations. The indentation dimensions were approximately 4.5×4.5×3 nm. The upper picture is a top view and the lower picture is a diagonal cross section.

sity of the liquid at 96.0 K and 4.23 bars. The density of the bottom wall was equal to the initial density of the solid. The Lennard–Jones parameters σ and ϵ in the wall potential were chosen to be the same as for the fluid-fluid and solid-solid interactions for the top and bottom wall, respectively.

2.3 Transient Simulation Types. Two types of transient MD simulation were run with a time step of 2.16 fs. The first was a constant number of atoms, normal stress, and temperature ($NP_{zz}T$ MD). The second was a constant number of atoms, normal stress, and heat flux ($NP_{zz}q$ MD). Constant temperature simulations were run for both small and large size systems. Constant heat flux simulations were only run for the large size system.

Simulations at constant temperature consisted of equilibration for at least 432 ps at 96.0 K and 4.23 bars starting from a random configuration or at least 108 ps starting from an equilibrated configuration with new velocities sampled randomly from the Maxwell–Boltzmann distribution. The set point temperature was then linearly ramped up into the metastable region over 1.67 ps and maintained at the final value until after nucleation occurred. The actual temperature reached the new set point value within 3 ps.

To control the temperature, two Nosé–Hoover thermostats were used [43], one for the solid atoms and one for the fluid atoms. The time constant was 0.05 ps. Two thermostats were required because using only one caused the solid to heat up faster than the fluid when ramping up the temperature, which subsequently led to a temperature gradient in the system.

The normal stress at time step τ, $P_{zz}(\tau)$, was calculated as the sum of the forces per area on the upper wall and was controlled by changing the acceleration (a_w) of the upper wall using a proportional-integral controller. Details are discussed in a previous work [32]. The set point normal stress was 4.23 bars for all simulations.

Nucleation times at constant temperature were obtained from multiple simulations and used to calculate nucleation rates and time lags from a transient nucleation model [44–46],

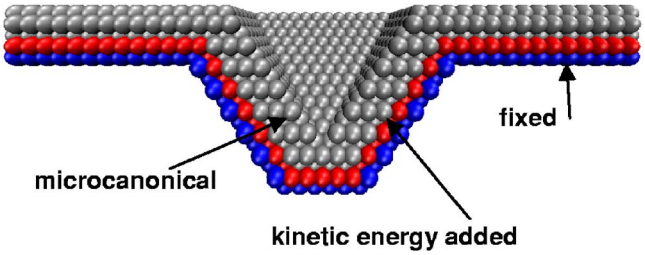

Fig. 5 Diagonal cross section of the solid for the large system with constant heat flux. The bottom layer is fixed, kinetic energy is added to the second to the bottom layer each time step [49], and the other layers have just microcanonical dynamics.

$$t = t_0 + \frac{g}{J_s V_{\text{box}}} - t_0\left(1 - \frac{0.5}{M_R^{2.5}}\right)\exp\left[-1.82 \times \left(\frac{g}{J_s V_{\text{box}} t_0}\right)^{1/2} \Big/ (M_R - 1)^{0.41}\right]$$

$$g = -\ln\left(\frac{N}{N_0}\right) \tag{3}$$

where N_0 is the total number of simulations, N is the number of non-nucleated simulations at time t, t_0 is a lag time, J_s is the steady state nucleation rate, and M_R is the reduced moment, which was set to 1.4 [47,48]. The nucleation times were taken at an average volume of 112% of the average volume of the metastable liquid. At this volume, a critical sized nucleus had already formed and began to grow. The average metastable liquid volume was obtained by averaging the volumes in each simulation at a time of 108 ps after beginning to ramp up the temperature. This was just after the volume reached the metastable liquid value and before the increase in volume due to vapor formation. The nucleation times and N_0 values were fitted to Eq. (3) to get J_s and t_0. The calculation of nucleation rates and errors is discussed in detail in a previous work [32].

Initial configurations for the constant heat flux simulations were obtained in the following manner. First, a randomly generated configuration was subjected to a $NP_{zz}T$ MD relaxation run at 96.0 K and 4.23 bars. Next, the set point temperature was increased linearly over 1.67 ps to bring the system to a metastable state. This temperature was low enough, however, that an additional 324 ps of $NP_{zz}T$ MD could be performed to get an initial "equilibrated" configuration without nucleation occurring. The resulting configuration was used to obtain subsequent ones by reassigning velocities from the Maxwell-Boltzmann distribution, then running $NP_{zz}T$ MD for another 108 ps. From these initial configurations, $NP_{zz}q$ MD was run by turning the temperature control off and adding a constant heat flux to the system.

Constant heat flux was obtained by the addition of kinetic energy to the second from the bottom layer of solid atoms each time step while keeping the bottom most layer immobile. Heat flux (q) is just the amount of kinetic energy added (ΔE_k) divided by the time step (Δt) and area (A) it is added to,

$$q = \frac{\Delta E_k}{\Delta t A} \tag{4}$$

The area used was the box length in the x direction times the box length in the y direction. The algorithm for adding kinetic energy conserves the linear momentum of the atoms it is applied to [49]. The velocity Verlet algorithm was used to integrate the microcanonical equations of motion [50]. Figure 5 shows the status of each solid layer for the constant flux case with the large indentation.

Nucleation times were also determined at constant heat flux, but

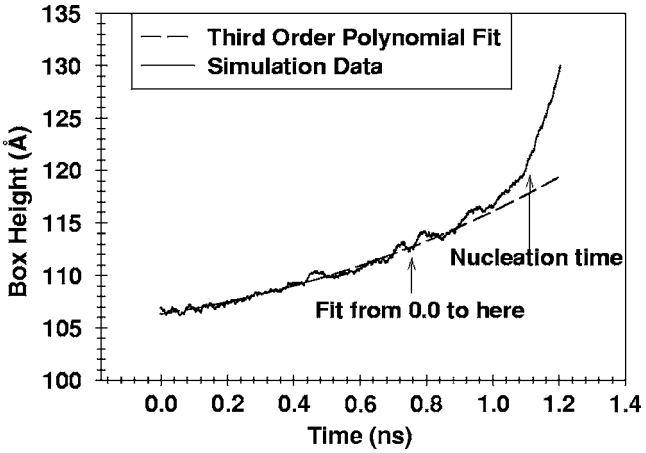

Fig. 6 Box height as a function of time for a simulation of the large indentation with a weak surface using constant heat flux, and the third order polynomial from a fit to the data from 0 to 756 ps. The nucleation time was taken as the first time when the data deviated from the polynomial by more than 3.5 Å.

steady state nucleation rates could not be obtained since the temperature changed during the course of the simulations. However, nucleation times and lag time before any nucleation events occurred could still be compared for the two different surface interactions. Nucleation times were determined by fitting a third order polynomial to the box height as a function of time at short times and then finding the time at which the box height deviated by more than 3.5 Å from the polynomial. Fits were from 0 ps to 756 ps in the weak cases and from 0 ps to 1188 ps in the neutral cases. Although this is a somewhat arbitrary procedure for determining the nucleation time, it was an objective means of locating the approximate time when the box height started increasing due to nucleation instead of just due to the expansion of the liquid. Figure 6 shows an example from a weak surface simulation.

2.4 Void Analysis: Large Indentation and Contact Angles. To characterize the size and structure of voids in the fluid in the large system, the simulation box was divided into small cubes of about 1.3 Å on a side. Cubes were designated as "empty" if their center was greater than 1.2σ from any atom center of mass [31]. To find the voids, the connectivity of these empty cubes was determined via a clustering algorithm similar to the one developed by Sevick et al. [51], with the criterion that cubes were connected if they shared any point(s). This meant that the maximum number of other cubes that any cube was directly connected to was 26. This method is good for finding the extent of bubbles, but underestimates the volume if there are atoms enclosed by the empty cubes since their volume is not counted.

To quantify to what extent void formation was favored in the indentation compared with the flat part of the surface, a void probability was calculated as a function of the x and y directions by averaging over the z direction. The average was also over multiple simulations and over time up until a bubble percolated the simulation box, at which point it contained on the order of a hundred.

To provide a quantitative measure of the wettability of the surfaces, constant volume simulations on flat surfaces were performed at a volume such that a vapor nucleus was stable. The positions of void regions in this nucleus were found using the void analysis every 1000 time steps. These positions were then shifted in the x and y directions by $[x_{cv}/x_{cube}]$ and $[y_{cv}/y_{cube}]$ where $[\ ]$ represents the nearest integer function, x_{cv} and y_{cv} the center of volume positions, and x_{cube} and y_{cube} the cube lengths. This approximately centered all nuclei with the positions of the voids restricted to the grid points. From all of the positions of voids in any configuration, an average shape could be found by only keeping those whose probability of occurrence was greater than some cutoff value. This method is similar to the work of Maruyama and Kimura with a Lennard–Jones vapor bubble on a Lennard–Jones surface [31] and Maruyama et al. with a Lennard–Jones liquid droplet on a Lennard–Jones surface [52].

Table 1 Temperatures (T) and number of simulations (N_0) for the constant temperature simulations

Defect	Surface	T (K)	N_0
Small asperity	Weak	131.0	42
		131.5	42
		132.0	42
		133.0	42
Small asperity	Neutral	134.5	42
Small flat	Weak	131.0	39
		131.5	39
		132.0	41
		133.0	51
Small flat	Neutral	134.5	40
Small indentation	Weak	131.0	44
		131.5	47
		132.0	47
		133.0	48
Small indentation	Neutral	134.5	40
Large indentation	Weak	131.0	44

3 Results

3.1 Contact Angles. For both the neutral and weak cases, a configuration was taken from a constant heat flux simulation, and the velocities were rescaled to get a temperature of 131.0 K. Constant volume and temperature simulations were then ran for

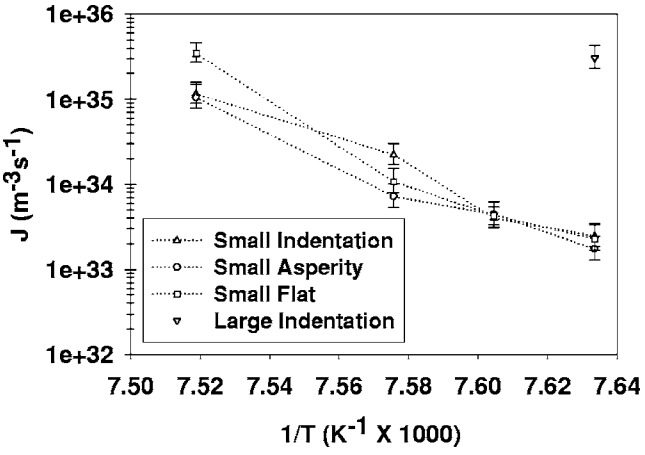

Fig. 7 Nucleation rates ($m^{-3}\,s^{-1}$) versus inverse temperature (K^{-1}) on a weakly attractive solid surface. Dotted lines are to guide the eye. A small indentation, asperity, and a flat surface with the same simulation box size were simulated. A large indentation was also simulated. The nucleation rates were not significantly different when comparing the small defects to a flat surface, but the rate for the large indentation was about two orders of magnitude greater than for the small defects at 131.0 K. The error bars are 68.3% confidence intervals.

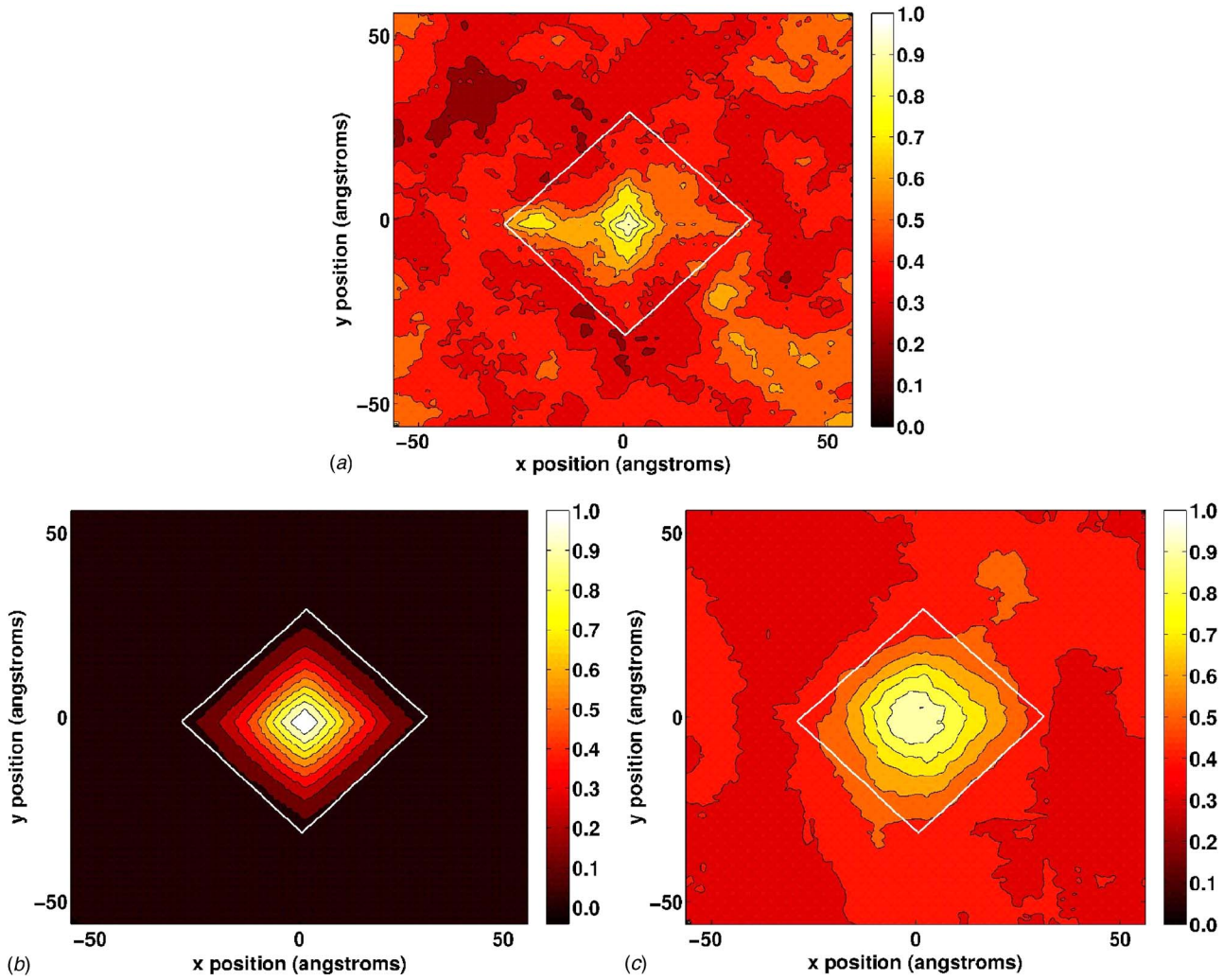

Fig. 8 Relative void probability for the large indentation as a function of x and y averaged over the z direction, over multiple simulations, and over time up until a void percolated the box. The top figure is for the constant temperature case (131.0 K, weak surface, 30 simulations). The bottom left figure is for the constant heat flux case (149 MW/m^2, 122.0 K starting temperature, 39 simulations) with a weak surface. The bottom right figure is for the constant heat flux case (149 MW/m^2, 122.0 K starting temperature, 39 simulations) with a neutral surface. In all three cases, void formation was favored in the indentation whose approximate boundaries are shown by the white line. The dark regions in the lower left and upper right corners are due to the fact that one point in those corners was set to either 0 or 1 to get the scale correct.

100,000 time steps to get a persistent vapor nucleus. An additional 200,000 time steps in the neutral case and 100,000 in the weak case were performed to get the average shape. The cutoff probability was chosen so that the number of void positions in the nucleus was about 0.7 times the maximum number in any snapshot. For the weak and neutral cases, these probabilities were 0.13 and 0.19, respectively.

To estimate the contact angle, the effective radius of the bottom two complete layers of void positions was used, assuming they were circular. Bottom layers with only a few voids were not considered. The contact angle (β) in radians was then estimated from

$$\beta = \pi/2 - \tan^{-1}(r_{12}/z_{12}) \tag{5}$$

for the neutral case and from

$$\beta = \pi - \tan^{-1}(z_{12}/r_{12}) \tag{6}$$

for the weak case. In these equations, r_{12} is the absolute difference in effective radii between the bottom and second to the bottom layer of void positions, and z_{12} is the absolute distance between layers. For the neutral and weak cases, the contact angle was estimated to be 22 deg and 129 deg, respectively. The neutral surface was wetting and the weak surface was nonwetting.

The contact angle was also estimated by using the data of Maruyama and Kimura,[31] relating the ratio of the well depth of the integrated potential for one layer of the solid to the well depth of the fluid to the cosine of the contact angle. They used a (111) surface, so the well depth of the integrated potential for our case was modified for the (100) surface,

$$\epsilon_{\text{surf}} = \left(\frac{12\pi}{5}\right)\left(\frac{\sigma_{\text{fs}}}{a_0}\right)^2 \epsilon_{\text{fs}} \tag{7}$$

The potential parameters (σ_{fs} and ϵ_{fs}) are for the solid-fluid interaction and a_0 is the lattice parameter of the solid. Maruyama et al. plotted the values for argon drops [52] and drew a straight line through them, and also plotted values for argon bubbles at 100 K and 110 K, which differ from the temperature we used, but contact angle is not a strong function of temperature and pressure. The values of the contact angles from this line were 50 deg and 124 deg for the neutral and weak cases, respectively. Our value for the neutral case falls in between their points for bubbles that

are well above the line for small contact angles, so there is a good agreement with our calculation.

3.2 Small Defects: Constant Temperature. Table 1 shows the temperatures and number of simulations used in each case and Fig. 7 shows a plot of nucleation rate versus inverse temperature for the weak case with small defects. The percentage differences in nucleation rates between the neutral surfaces were comparable or smaller than the differences between the weak surfaces, so they are not plotted. Figure 7 shows that the nucleation rates for the three surfaces are not significantly different from each other. This is likely due to the fact that the defects were smaller than the critical nucleus volumes determined from previous simulations [32] at these temperatures. In these previous simulations, it was found that critical nuclei of about 1000–2000 $Å^3$ were required for the bubbles to continue to grow on an atomically smooth surface. The current result indicates that surface defects smaller than the critical nucleus size do not change nucleation rates when compared to atomically smooth surfaces.

3.3 Large Indentation: Constant Temperature. An indentation significantly larger than the critical size having a volume of about 25,000 $Å^3$ or more than ten times the critical volume was simulated. The box size was chosen so that the distance between the edge of the indentation and its images was approximately the same as this distance in the system with the small indentation.

A temperature of 131.0 K and 44 simulations were used with a weak surface to compare with the smaller indentation. The nucleation rate is plotted in Fig. 7. The nucleation rate was $3.0(2.31,4.26)\times10^{35}$ m^{-3} s^{-1} compared with $1.7(1.30,2.46)\times10^{33}$ m^{-3} s^{-1}, $2.3(1.69,3.33)\times10^{33}$ m^{-3} s^{-1}, and $2.5(1.87,3.44)\times10^{33}$ m^{-3} s^{-1} for the small system with an asperity, flat surface, and indentation, respectively. The numbers in parentheses are the 68.3% confidence intervals. The large indentation increased the nucleation rate by two orders of magnitude over the small defects. Finite size effects due to the larger simulation box in the large indentation case cannot explain this. Previous work with even smaller systems showed a small *decrease* in the nucleation rate with increasing system size [32]. The presence of an indentation larger than the critical size clearly enhanced nucleation at constant temperature. This is in qualitative agreement with work on boiling in microchannels, which found that superheats required for nucleation were larger than in an unconfined space [53,54]. Indentations cannot enhance nucleation if critical nuclei cannot form there.

Figure 8(*a*) shows a contour plot of relative void probability for the constant temperature case. This figure shows that void formation was favored in the indentation. This enhancement can be explained by the fact that a void formed in an indentation can collapse from fewer directions than one formed on the flat surface, so it will last longer on average and have a greater probability of growing to critical size. For the same critical radius and with the contact angle for this case, the critical volume in an indentation is also smaller, making it easier to form a critical nucleus. This qualitative picture of void collapse is shown in Fig. 9.

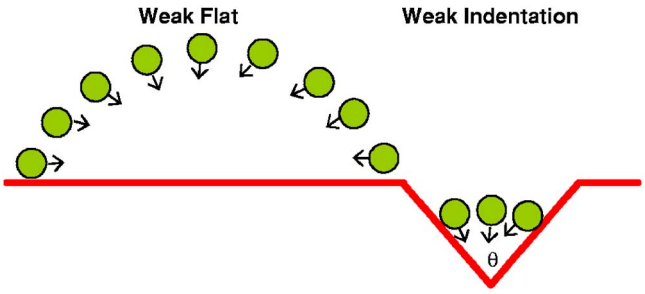

Fig. 9 These figures represent the ways in which atoms can collapse into a 2-D void on a weakly attractive surface. Fluid atoms are represented as circles, and the solid surface as a line. The arrows point into the void. The arc length that can collapse into a void of the same radius and contact angle is smaller in the indentation (right) compared with the flat part of the surface (left). The volume of a critical nucleus in the indentation is also smaller for a given critical radius.

3.4 Large Indentation: Constant Heat Flux. In the constant heat flux cases, nucleation was further enhanced by localized heating in the indentation. Figure 10 is a plot of the time and simulation average of local temperature minus bulk fluid temperature as a function of height perpendicular to the flat surface. The average was taken over 39 simulations until the maximum sized void in a simulation was larger than 1000 $Å^3$. Two separate regions were considered, above the indentation and above the flat part of the surface. The temperature in the indentation was considerably higher than in the rest of the fluid, increasing the probability of formation of a critical sized nucleus there. This occurred because heating occurred from multiple sides of the indentation, not just from below.

Figure 11 shows the nucleation times for indented and flat solids for the weak and neutral cases. The nucleation times in the neutral cases are longer than in the weak cases because adsorbed fluid layers in these cases had to be heated up before nucleation could occur above them. In the weak cases, nucleation occurred right above the surface. Due to the focused heating in the indentation, the indented surface might be expected to have a smaller time lag. This was not the case, and there were several contributions to this. The first was that surface area of solid exposed to the fluid in the indented case was about 11.95% higher than in the flat case, but the same amount of energy was added each time step. The heat flux was based on the cross sectional area, not on the surface area, so there was a lower "effective" heat flux for the indented case. The second was that although the indentation heated up faster, the fluid outside of it was still relatively cold, which inhibited bubble growth. In the neutral case, the adsorbed fluid volume was larger in the indented case than in the flat case, so the lag time was slightly longer than in the flat case.

Figures 8(*b*) and 8(*c*) show contour plots of relative void probability for the constant heat flux case for a weak and neutral surface, respectively. For a weak surface, it was seen in visualizations that a void formed in and grew from the indentation every time. This gives the nearly perfect rings in Fig. 8(*b*). In the case of a neutral surface, nucleation still occurred preferentially in the indentation, but a void large enough to continue to grow would occasionally form away from the indentation. Sometimes a void formed on the flat surface entirely, and sometimes it formed with one side attached to the indentation.

The increased frequency of bubble nucleation away from the indentation was due to the presence of adsorbed fluid layers on the solid in the neutral case. The local pressure and spinodal temperature in high density adsorbed layers are higher than in the bulk fluid [55]. This makes this region inaccessible to vapor nuclei formation. The effective size of the indentation in the neutral case was reduced relative to the weak case, so forming a critical sized bubble there was less favorable. Further increasing the fluid-solid attraction would increase the thickness of adsorbed layers and decrease the effective size of the indentation, making the indentation region even less favorable relative to the flat part of the surface. Atoms below a void in the indentation in the adsorbed layers could also collapse into the void, but collapse was less likely from the bottom due to lower mobility of the adsorbed layers (see Fig. 12). Void formation was favored in the indentation for both cases more than in the constant temperature case.

Void probabilities were also calculated for flat surfaces and for the weak case with a starting temperature of 128.0 K instead of 122.0 K. The flat cases were used to check the analysis and, of course, showed that nucleation occurred with equal probability at all points on the surface. The simulations started at a higher temperature gave a void probability plot that was nearly identical to

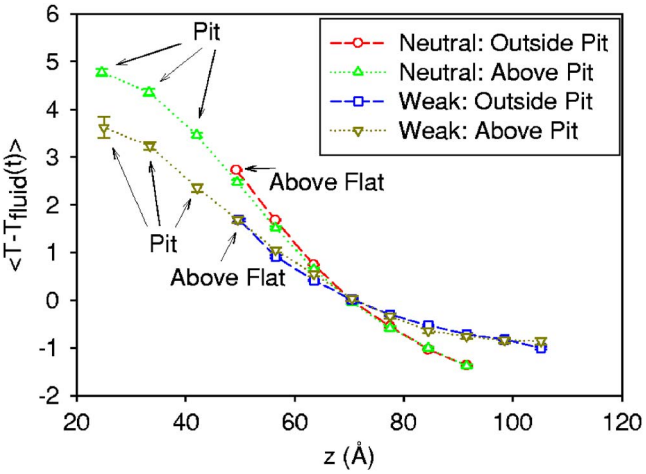

Fig. 10 Time average until a void had a volume greater than 1000 Å^3 and simulation average over 39 simulations of local temperature (T) minus bulk fluid temperature (T_{fluid}) as a function of z position for the large indentation with constant heat flux. Two separate regions were considered, above the indentation and above the flat part of the surface. In both the neutral and weak cases, the temperature in the indentation was considerably higher than in the rest of the fluid.

Fig. 8(*b*), so the starting temperature had no effect on the result that void formation was localized in the indentation.

3.5 Predicted Wall Temperatures. To test the criterion for active cavity size, we used the relation of Davis and Anderson [38] to calculate the wall temperatures (T_w) under constant heat

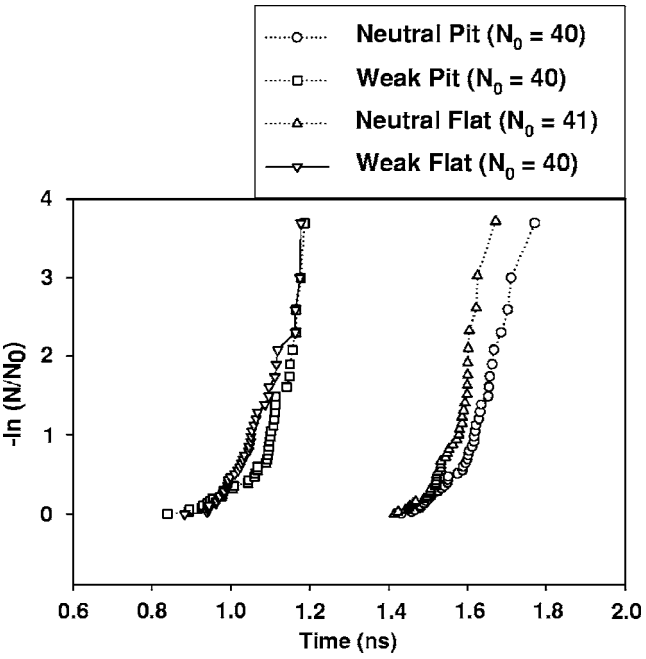

Fig. 11 Nucleation times as a function of the negative logarithm of the ratio of non-nucleated (N) to total simulations (N_0) for all constant heat flux cases. The times for the neutral cases were longer because the adsorbed layers had to be heated up before nucleation could occur. Nucleation was slightly faster for the flat surface compared to the indented one for the neutral case and there was little difference for the weak case.

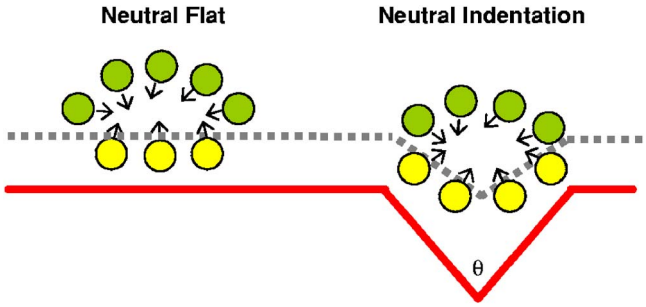

Fig. 12 These figures represent the ways in which atoms can collapse into a 2-D void on a neutral surface. Fluid atoms are represented as light gray (yellow) and dark gray (green) circles, and the solid surface as a solid line. The "edge" of the adsorbed fluid layers is the dashed line. The arrows point into the void. Nucleation cannot occur in the adsorbed fluid layers between the solid line and the dashed line. These layers effectively reduce the the size of the indentation and make the nucleation more like homogeneous nucleation, since the light gray (yellow) atoms in the adsorbed fluid layers can collapse into the void, but are not as likely to collapse as the dark gray (green) bulk fluid atoms since they are not as mobile.

flux conditions that would be required to get a minimum cavity radius ($r_{c,\min}$) equal to the hydraulic radius of the large indentation,

$$r_{c,\min} = \frac{\delta_t \sin\beta}{2(1+\cos\beta)}\left(\frac{\theta_w}{\theta_w+\theta_{\text{sub}}}\right)\left[1-\sqrt{1-\frac{8\sigma T_{\text{sat}}(\theta_w+\theta_{\text{sub}})}{\rho_v h_{lv}\delta_t\theta_w^2}}\right]$$

$$\delta_t = k/h$$

$$h = q/(T_w - T_\infty)$$

$$\theta_w = T_w - T_{\text{sat}}$$

$$\theta_{\text{sub}} = T_{\text{sat}} - T_\infty \tag{8}$$

We used adjusted experimental parameters for argon for the surface tension (σ=5.790×10^{-3} N/m) [32,56], heat of vaporization (h_{lv}=5392 J/mol) [57], and thermal conductivity (k=90 mW/(m K)) [58]. We used the Lennard–Jones equation of state to get the saturation temperature and vapor density (T_{sat}=106.7 K, ρ_v=519.1 mol/m^3) [59], and used the contact angles (β) calculated for the flat surface. We did not know the heat flux (q) into the liquid, so we varied it from 5% up to 100% of the flux added to the solid, giving a range of wall temperatures of 10–15 K. The calculated wall temperatures for the neutral and weak cases were around 155 K and 510 K. The maximum wall temperatures seen in the simulations were 140–145 K. For the neutral case, this is probably within the error of the calculated value. In the weak case, the calculated value is clearly too high.

4 Conclusions

Nonequilibrium MD simulations of bubble nucleation were run for a Lennard–Jones fluid on a Lennard–Jones solid. The solid had various geometric defects (small asperities and small and large indentations). The solid-fluid energy parameter (ϵ_{sf}) was also varied. It was either less than the fluid-fluid value (weak) or equal to the fluid-fluid value (neutral). Two types of simulations were run, constant temperature and constant normal stress or constant heat flux into the bottom of the solid and constant normal stress.

It was shown that some level of control over the rate and location of heterogeneous bubble nucleation could be accomplished with the right surface topology and chemistry even at the nanometer scale. Defects of about the same size as the critical nucleus (1000–2000 Å^3) had no effect on nucleation rate, while an inden-

tation much larger than the critical nucleus increased the nucleation rate by approximately two orders of magnitude over a flat surface at constant temperature. Void formation was favored in the large indentation over the flat part of the surface in all cases due in part to the stabilizing effect of the solid and the smaller critical volume for an indentation compared with a flat surface. In the constant heat flux cases, concentrated heating in the indentation further increased the probability of forming a void there. In the weak case with constant heat flux, a void formed and grew from the indentation every time. In the neutral case, the spatial control was not as good due to adsorbed fluid layers on the solid surface in which nucleation could not easily occur. These layers are partially filled in the indentation and could not stabilize voids as well as the solid.

These results show that dissolved gas is not required to enhance nucleation at the nanometer scale, in qualitative agreement with the work of Theofanous et al., [16] who found that PEN theory did not apply for nanometer scale defects. Dissolved gas might have an additional effect, which could be explored in further work.

Acknowledgment

This work was partially supported by the U.S. Army CERDEC through agreement No. DAAB07-03-3-K414. It was also partially supported through funding from the Indiana 21st Century Technology and Research Fund. Computational resources for this work were partially provided by the Notre Dame Center for Research Computing. Figures 2–5 were made using Visual Molecular Dynamics (VMD) [60].

References

[1] Dhir, V. K., 1998, "Boiling Heat Transfer," Annu. Rev. Fluid Mech., **30**, pp. 365–401.
[2] Webb, R. L., 2004, "Odyssey of the Enhanced Boiling Surface," ASME J. Heat Transfer, **126**, pp. 1051–1059.
[3] Dhir, V. K., 2006, "Mechanistic Prediction of Nucleate Boiling Heat Transfer: Achievable or a Hopeless Task?," ASME J. Heat Transfer, **128**, pp. 1–12.
[4] Argyropoulos, P., Scott, K., and Taama, W. M., 1999, "Carbon Dioxide Evolution Patterns in Direct Methanol Fuel Cells," Electrochim. Acta, **44**, pp. 3575–3584.
[5] Argyropoulos, P., Scott, K., and Taama, W. M., 1999, "Gas Evolution and Power Performance in Direct Methanol Fuel Cells," J. Appl. Electrochem., **29**, pp. 661–669.
[6] Scott, K., Argyropoulos, P., Yiannopoulos, P., and Taama, W. M., 2001, "Electrochemical and Gas Evolution Characteristics of Direct Methanol Fuel Cells With Stainless Steel Mesh Flow Beds," J. Appl. Electrochem., **31**, pp. 823–832.
[7] Asai, A., 1989, "Application of Nucleation Theory to the Design of Bubble Jet Printers," Jpn. J. Appl. Phys., Part 1, **28**(5), pp. 909–915.
[8] Hong, Y., Ashgriz, N., and Andrews, J., 2004, "Experimental Study of Bubble Dynamics on a Micro Heater Induced by Pulse Heating," ASME J. Heat Transfer, **126**, pp. 259–271.
[9] Avedisian, C. T., Osborne, W. S., McLeod, F. D., and Curley, C. M., 1999, "Measuring Bubble Bucleation Temperature on the Surface of a Rapidly Heated Thermal Ink-Jet Heater Immersed in a Pool of Water," Proc. R. Soc. London, Ser. A, **455**, pp. 3875–3899.
[10] Hong, Y., Ashgriz, N., Andrews, J., and Parizi, H., 2004, "Numerical Simulation of Growth and Collapse of a Bubble Induced by a Pulsed Microheater," J. Microelectromech. Syst., **13**(5), pp. 857–869.
[11] Glod, S., Poulikakos, D., Zhao, Z., and Yadigaroglu, G., 2002, "An Investigation of Microscale Explosive Vaporization of Water on an Ultrathin Pt Wire," Int. J. Heat Mass Transfer, **45**, pp. 367–379.
[12] Bankoff, S. G., 1958, "Entrapment of Gas in the Spreading of a Liquid Over a Rough Surface," AIChE J., **4**(1), pp. 24–26.
[13] Corry, C., and Foust, A., 1955, "Surface Variables in Nucleate Boiling," Chem. Eng. Prog., Symp. Ser., **51**(17), pp. 1–12.
[14] Griffith, P., and Wallis, J. D., 1960, "The Role of Surface Conditions in Nucleate Boiling," Chem. Eng. Prog., Symp. Ser., **56**, pp. 49–62.
[15] Cornwell, K., 1977, "Naturally Formed Boiling Site Cavities," Lett. Heat Mass Transfer, **4**, pp. 63–72.
[16] Theofanous, T. G., Tu, J. P., Dinh, A. T., and Dinh, T. N., 2002, "The Boiling Crisis Phenomenon Part I: Nucleation and Nucleate Boiling Heat Transfer," Exp. Therm. Fluid Sci., **26**, pp. 775–792.
[17] Kocamustafaogullari, G., and Ishii, M., 1983, "Interfacial Area and Nucleation Site Density in Boiling Systems," Int. J. Heat Mass Transfer, **26**(9), pp. 1377–1387.
[18] Gaertner, R. F., and Westwater, J. W., 1960, "Population of Active Sites in Nucleate Boiling Heat Transfer," Chem. Eng. Prog., Symp. Ser., **56**(30), pp. 39–48.
[19] Borkent, B. M., Dammer, S. M., Schönherr, H., Vancso, G. J., and Lohse, D., 2007, "Superstability of Surface Nanobubbles," Phys. Rev. Lett., **98**, p. 204502.
[20] Yin, Z., Prosperetti, A., and Kim, J., 2004, "Bubble Growth on an Impulsively Powered Microheater," Int. J. Heat Mass Transfer, **47**, pp. 1053–1067.
[21] Okuyama, K., Takehara, R., Iida, Y., and Kim, J.-H., 2006, "Pumping Action by Boiling Propagation in a Microchannel," Microscale Thermophys. Eng., **9**, pp. 119–135.
[22] Thomas, O. C., Cavicchi, R. E., and Tarlov, M. J., 2003, "Effect of Surface Wettability on Fast Transient Microboiling Behavior," Langmuir, **19**, pp. 6168–6177.
[23] Avedisian, C. T., Cavicchi, R. E., and Tarlov, M. J., 2006, "New Technique for Visualizing Microboiling Phenomena and Its Application to Water Pulse Heated by a Thin Metal Film," Rev. Sci. Instrum., **77**, p. 063706.
[24] Balss, K. M., Avedisian, C. T., Cavicchi, R. E., and Tarlov, M. J., 2005, "Nanosecond Imaging of Microboiling Behavior on Pulsed-Heated Au Films Modified With Hydrophilic and Hydrophobic Self-Assembled Monolayers," Langmuir, **21**, pp. 10459–10467.
[25] Zhao, Z., Glod, S., and Poulikakos, D., 2000, "Pressure and Power Generation During Explosive Vaporization on a Thin-Film Microheater," Int. J. Heat Mass Transfer, **43**, pp. 281–296.
[26] Chen, T., Klausner, J. F., Garimella, S. V., and Chung, J. N., 2006, "Subcooled Boiling Incipience on a Highly Smooth Microheater," Int. J. Heat Mass Transfer, **49**, pp. 4399–4406.
[27] Lang, F., and Leiderer, P., 2006, "Liquid Vapour Phase Transitions at Interfaces: Sub-Nanosecond Investigations by Monitoring the Ejection of Thin Liquid Films," New J. Phys., **8**, p. 14.
[28] Yavas, O., Leiderer, P., Park, H. K., Grigoropoulos, C. P., Poon, C. C., Leung, W. P., Do, N., and Tam, A. C., 1993, "Optical Reflectance and Scattering Studies of Nucleation and Growth of Bubbles at a Liquid-Solid Interface Induced by Pulsed Laser Heating," Phys. Rev. Lett., **70**(12), pp. 1830–1833.
[29] Gu, X., and Urbassek, H. M., 2005, "Atomic Dynamics of Explosive Boiling of Liquid-Argon Films," Appl. Phys. B: Lasers Opt., **81**, pp. 675–679.
[30] Dou, Y., Zhigilei, L. V., Winograd, N., and Garrison, B. J., 2001, "Explosive Boiling of Water Films Adjacent to Heated Surfaces: A Microscopic Description," J. Phys. Chem. A, **105**, pp. 2748–2755.
[31] Maruyama, S., and Kimura, T., 2000, "A Molecular Dynamics Simulation of a Bubble Nucleation on Solid Surface," Heat Technol., **18** (Suppl. 1) pp. 69–74.
[32] Novak, B. R., Maginn, E. J., and McCready, M. J., 2007, "Comparison of Heterogeneous and Homogeneous Bubble Nucleation Using Molecular Simulations," Phys. Rev. B, **75**(8), p. 085413.
[33] Yi, P., Poulikakos, D., Walther, J., and Yadigaroglu, G., 2002, "Molecular Dynamics Simulation of Vaporization of an Ultra-Thin Liquid Argon Layer on a Surface," Int. J. Heat Mass Transfer, **45**, pp. 2087–2100.
[34] Neimark, A. V., and Vishnyakov, A., 2005, "The Birth of a Bubble: A Molecular Simulation Study," J. Chem. Phys., **122**, p. 054707.
[35] Wilt, P. M., 1986, "Nucleation Rates and Bubble Stability in Water-Carbon Dioxide Solutions," J. Colloid Interface Sci., **112**(2), pp. 530–538.
[36] Sato, T., and Matsumura, H., 1964, "On the Conditions of Incipient Subcooled Boiling With Forced Convection," Bull. JSME, **7**(26), pp. 392–398.
[37] Hsu, Y. Y., 1962, "On the Size Range of Active Nucleation Cavities on a Heating Surface," ASME J. Heat Transfer, **84**, pp. 207–216.
[38] Davis, E. J., and Anderson, G. H., 1966, "The Incipience of Nucleate Boiling in Forced Convection Flow," AIChE J., **12**(4), pp. 774–780.
[39] Kandlikar, S. G., 2006, "Nucleation Characteristics and Stability Considerations During Flow Boiling in Microchannels," Exp. Therm. Fluid Sci., **30**, pp. 441–447.
[40] Wu, Y. W., and Pan, C., 2003, "A Molecular Dynamics Simulation of Bubble Nucleation in Homogeneous Liquid Under Heating With Constant Mean Negative Pressure," Microscale Thermophys. Eng., **7**, pp. 137–151.
[41] Toxvaerd, S., 2002, "Molecular Dynamics Simulation of Heterogeneous Nucleation at a Structureless Solid Surface," J. Chem. Phys., **117**(22), pp. 10303–10310.
[42] Hill, T. L., 1952, "Theory of Physical Adsorption," Adv. Catal., **4**, pp. 211–258.
[43] Martyna, G. J., Tuckerman, M. E., Tobias, D. J., and Klein, M. L., 1996, "Explicit Reversible Integrators for Extended Systems Dynamics," Mol. Phys., **87**(5), pp. 1117–1157.
[44] Bartell, L. S., 2002, "Analyses of Nucleation Rates From Molecular Dynamics Simulations," J. Phys. Chem. A, **106**(45), pp. 10893–10897.
[45] Jacob, E. J., and Bartell, L. S., 2003, "Analyses of Nucleation Rates From Molecular Dynamics Simulations. II. Weight Functions, Generation of Stochastic Times, and Realistic Uncertainties," J. Phys. Chem. A, **107**(11), pp. 1859–1866.
[46] Wu, D. T., 1997, "Nucleation Theory," Solid State Phys., **50**, pp. 37–187.
[47] Kashchiev, D., 1969, "Solution of the Non-Steady State Problem in Nucleation Kinetics," Surf. Sci., **14**, pp. 209–220.
[48] Kashchiev, D., 2005, "Moments of the Rate of Nonstationary Nucleation," J. Chem. Phys., **122**, p. 114506.
[49] Ikeshoji, T., and Hafskjold, B., 1994, "Non-Equilibrium Molecular Dynamics Calculation of Heat Conduction in Liquid and Through Liquid-Gas Interface," Mol. Phys., **81**(2), pp. 251–261.
[50] Allen, M. P., and Tildesley, D. J., 1987, *Computer Simulation of Liquids*, Oxford Science, Oxford.
[51] Sevick, E. M., Monson, P. A., and Ottino, J. M., 1988, "Monte Carlo Calculations of Cluster Statistics in Continuum Models of Composite Morphology,"

J. Chem. Phys., **88**(2), pp. 1198–1206.
[52] Maruyama, S., Kurashige, T., Matsumoto, S., Yamaguchi, Y., and Kimura, T., 1998, "Liquid Droplet in Contact With a Wolid Surface," Microscale Thermophys. Eng., **2**, pp. 49–62.
[53] Peng, X. F., Tian, Y., and Lee, D. J., 2002, "Arguments on Microscale Boiling Dynamics," Microscale Thermophys. Eng., **6**, pp. 75–83.
[54] Peng, X. F., Tien, Y., and Lee, D. J., 2001, "Bubble Bucleation in Microchannels: Statistical Mechanics Approach," Int. J. Heat Mass Transfer, **44**, pp. 2957–2964.
[55] Carey, V. P., and Wemhoff, A. P., 2005, "Thermodynamic Analysis of Near-Wall Effects on Phase Stability and Homogeneous Nucleation During Rapid Surface Heating," Int. J. Heat Mass Transfer, **48**, pp. 5431–5445.
[56] Daubert, T., and Danner, R., 1983, *Physical and Thermodynamic Properties of Pure Chemicals: Data Complilation*, Hemisphere, UK.
[57] 1995, *CRC Handbook of Chemistry and Physics*, 76th ed., D. R. Lide, ed., CRC, Boca Raton, FL.
[58] Younglove, B. A., and Hanley, H. J. M., 1986, "The Viscosity and Thermal Conductivity Coefficients of Gaseous and Liquid Argon," J. Phys. Chem. Ref. Data, **15**(4), pp. 1323–1337.
[59] Johnson, J. K., Zellweg, J. A., and Gubbins, K. E., 1993, "The Lennard-Jones Equation of State Revisited," Mol. Phys., **78**(3), pp. 591–618.
[60] Humphrey, W., Dalke, A., and Schulten, K., 1996, "VMD—Visual Molecular Dynamics," J. Mol. Graphics, **14**(1), pp. 33–38.

Experimental Investigation of Turbulent Convective Heat Transfer and Pressure Loss of Alumina/Water and Zirconia/Water Nanoparticle Colloids (Nanofluids) in Horizontal Tubes

Wesley Williams

Jacopo Buongiorno

Department of Nuclear Science and Engineering,
Massachusetts Institute of Technology,
Cambridge, MA 02139

Lin-Wen Hu

Nuclear Reactor Laboratory,
Massachusetts Institute of Technology,
Cambridge, MA 02139

The turbulent convective heat transfer behavior of alumina (Al_2O_3) *and zirconia* (ZrO_2) *nanoparticle dispersions in water is investigated experimentally in a flow loop with a horizontal tube test section at various flow rates* ($9000 < Re < 63{,}000$), *temperatures* ($21–76\,^{\circ}C$), *heat fluxes (up to* $\sim 190\ kW/m^2$*), and particle concentrations (*0.9–3.6 vol % *and* 0.2–0.9 vol % *for* Al_2O_3 *and* ZrO_2*, respectively). The experimental data are compared to predictions made using the traditional single-phase convective heat transfer and viscous pressure loss correlations for fully developed turbulent flow, Dittus–Boelter, and Blasius/MacAdams, respectively. It is shown that if the measured temperature- and loading-dependent thermal conductivities and viscosities of the nanofluids are used in calculating the Reynolds, Prandtl, and Nusselt numbers, the existing correlations accurately reproduce the convective heat transfer and viscous pressure loss behavior in tubes. Therefore, no abnormal heat transfer enhancement was observed in this study.*
[DOI: 10.1115/1.2818775]

Keywords: nanofluids, convective heat transfer, enhancement, thermal conductivity

1 Introduction

Modification of the thermophysical properties of a system through heterogenization is an age-old practice, a phenomenon readily visible in the lowered thermal conductivity of fibrous-air mixtures found in most insulation. Historically, a scientific understanding of the thermophysical properties of such mixtures of materials stemmed from the works of Maxwell [1] and Maxwell-Garnett [2] on electrical conductivity of heterogeneous solids. Unlike the chemical, rheological, and optical properties of colloids (solid-liquid mixtures), which have been vastly studied, an understanding of the thermal properties of such systems has been somewhat neglected. The works of Masuda et al., [3] Choi [4], Eastman et al., [5] Choi et al., [6] Assael et al., [7] among others, have generated great interest in the thermophysical properties of nanofluids, i.e., colloidal dispersions of nanoparticles in a base fluid, and their potential for heat transfer enhancement.

Convective heat transfer enhancement through the addition of particulates has been proposed in various places in the literature; one early and thorough study by Ahuja [8] showed the ability of micron sized polystyrene particles to enhance laminar convective heat transfer in tubes. Ahuja [8] concluded that the enhancement was due to shear-induced rotation of the particles and particle-particle interactions. However, the engineering applicability of microparticle colloids is generally hindered by particle settling, channel erosion, and clogging. The recent development of stable nanoparticulate colloids reopened the idea of enhancement of convective heat transfer through the addition of particles. Despite this, there are few experimental works to be found in the literature. Wen and Ding [9–11] have studied nanofluid laminar flow convective heat transfer in the entry region. Pak and Cho [12] explored alumina and titania in water nanofluids in turbulent convective heat transfer in tubes. Xuan and Li [13] investigated turbulent convective heat transfer and flow features of copper oxide in water nanofluids. Xuan and Roetzel [14] considered a heat transfer correlation for nanofluids to capture the effect of energy transport by particle "dispersion." Buongiorno [15] investigated nanofluids through nondimensional groups and determined that other than possible diffusion effects in the boundary layer, nanofluids should behave like equivalent single-phase fluids. All the above researchers have concluded or assumed that nanofluids provide heat transfer enhancement with respect to their respective base fluids. However, assessment of what constitutes an enhancement in turbulent convective heat transfer is somewhat arbitrary. The convective heat transfer coefficient h depends heavily on the fluid properties via the Reynolds, Prandtl, and Nusselt numbers, as per the classic Dittus–Boelter correlation:

$$\mathrm{Nu} = 0.023\,\mathrm{Re}^{0.8}\,\mathrm{Pr}^{0.3}$$
$$h = 0.023\,\mathrm{Re}^{0.8}\,\frac{c^{0.3}\lambda^{0.7}\mu^{0.3}}{D} = 0.023\frac{c^{0.3}\lambda^{0.7}\rho^{0.8}V^{0.8}}{\mu^{0.5}D^{0.2}} \tag{1}$$

As nanofluids typically have higher thermal conductivity and viscosity than their base fluids, Eq. (1) suggests that, for a fixed Reynolds number, they will also have a higher heat transfer coefficient. On the other hand, for a fixed velocity, the nanofluid heat

Contributed by the Heat Transfer Division of ASME for publication in the JOURNAL OF HEAT TRANSFER. Manuscript received March 23, 2007; final manuscript received May 30, 2007; published online March 21, 2008. Review conducted by Peter Vadasz.

transfer coefficient could be either higher or lower than that of the base fluids, depending on the magnitude of the thermal conductivity and viscosity increase. These trends are expected and their explanation does not necessitate invoking any special physical phenomena occurring in nanofluids. So, what constitutes an *interesting* heat transfer enhancement in nanofluids? It is proposed in this paper that an increase in the measured heat transfer coefficient substantially above that predicted by the traditional single-phase fluid correlation (e.g., Dittus–Boelter) utilizing the nanofluid thermophysical properties can be considered as an unexpected heat transfer enhancement and thus worthy of study. Therefore, to assess the merits of nanofluids, their thermophysical properties must be known accurately. The density of the nanofluids is by definition

$$\rho = \phi\rho_p + (1-\phi)\rho_b \tag{2}$$

Assuming thermal equilibrium between the particles and the surrounding fluid, the specific heat is immediately estimated as follows:

$$c = \frac{\phi\rho_p c_p + (1-\phi)\rho_b c_b}{\rho} \tag{3}$$

On the other hand, the thermal conductivity and viscosity of nanofluids have exhibited abnormal behavior and therefore must be measured, as functions of loading and temperature, for every different nanofluids used in the experiments. Unfortunately, none of the above referenced studies uses nanofluids fully characterized in this strict sense. This is the starting point of our paper, which investigates two water-based nanofluids, with alumina and zirconia nanoparticles, for their potential to enhance the convective heat transfer coefficient in a heated tube. Full characterization of the fluids colloidal and thermophysical properties is done experimentally (Sec. 2), including measurement of the temperature- and loading-dependent thermal conductivities and viscosities. The flow loop is described in Sec. 3. Measurements are done for two nanoparticle/base fluid combinations at various particle loadings and flow conditions and the results are analyzed using the measured properties and traditional single-phase correlations (Secs. 4 and 5).

2 Nanofluids and Their Properties

The nanofluids used in this experiment were colloidal alumina AL20SD at 20 wt % and colloidal zirconia Zr50/15 at 15 wt %, purchased from Nyacol® Nano Technologies, Inc. These colloids were used as received except for dilution using de-ionized water. Characterization was done to assure the specifications of the colloids are as stated by the manufacturer. Inductively coupled plasma (ICP) spectroscopy found there to be only the primary components specified, aluminum and zirconium, in each respective fluid. Only trace amounts of other chemicals were found. Thermogravimetric analysis (TGA) was done to determine the weight loading of the compounds and were found to be as specified by the manufacturer. TGA was also used to determine the exact loading of the diluted samples before and after the flow experiments to assure there was no settling in the loop. The conversion between weight and volume fraction (ϕ) was done through the bulk density of alumina ($\sim$3920 kg/m^3) and zirconia ($\sim$5500 kg/m^3).

Particle sizing was done using dynamic light scattering (DLS) in combination with transmission electron microscopy (TEM); the methodologies are described elsewhere [16]. It is noted that DLS determines only the equivalent spherical hydrodynamic diameter of the particles. Likewise the TEM can be used only on particles dried out of the colloidal state and hence could have agglomerations, which may not be present in the colloidal state. The DLS results showed that the average particle size for the alumina is about 46 nm and the zirconia is about 60 nm. There is a distribution of size around these averages and the zirconia had small amounts of agglomerations averaging around 200 nm. TEM images confirmed these results are reasonable.

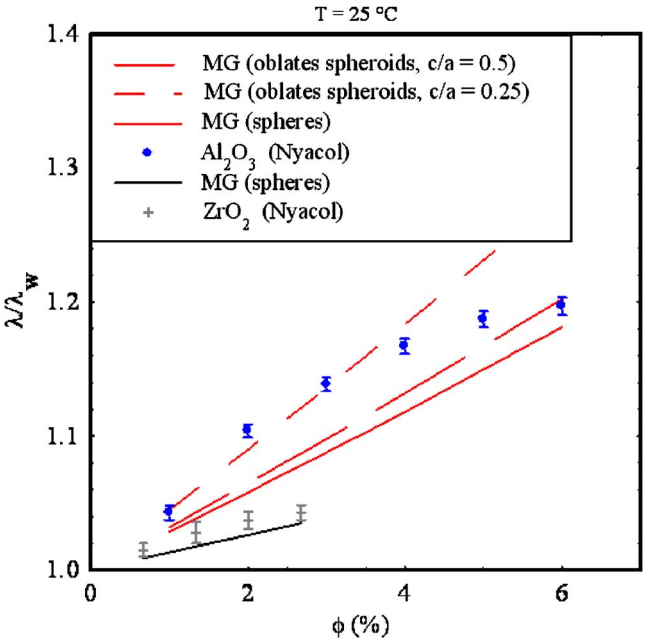

Fig. 1 Loading-dependent thermal conductivity

The temperature- and loading-dependent thermal conductivities were measured with a short transient hot wire apparatus, which was validated with various fluids at different temperatures and found to have $\pm 2\%$ accuracy [17]. The transient hot wire apparatus made use of a Teflon-coated platinum wire to prevent the occurrence of parasitic currents in the test fluid. The dependence of thermal conductivity on loading was measured for each fluid from zero to the maximum loading, 20 wt % and 15 wt % for alumina and zirconia, respectively. Temperature dependence of the conductivity was measured from 20°C to 80°C, which encompasses the anticipated in-loop conditions. The results are shown in Figs. 1 and 2, where the nanofluid thermal conductivity is λ, the thermal conductivity of water is λ_w, and MG refers to the modified Maxwell-Garnett model [2], applied here to two values of the spheroidal aspect ratio c/a, which captures the shapes of our nanoparticles, as per the TEM observations. The measurements show that the loading dependence of thermal conductivity is bracketed by the MG model, while the temperature dependence is the same as that of water. This latter fact is contrary to the findings of Das et al. [18], who reported an abnormally large increase of thermal conductivity in nanofluids and attributed it to Brownian motion of the nanoparticles.

Viscosity was measured by means of a capillary viscometer submerged in a controlled-temperature bath. The viscometer was benchmarked with water at various temperatures and its accuracy was found to be within 0.5%. The alumina and zirconia nanofluid viscosities are shown in Figs. 3 and 4, respectively. Note the rapid viscosity increase with particle loading and the independence of the μ/μ_w ratio on temperature. Curve fits were created for the thermal conductivity and viscosity experimental data to be used in the interpretation of the convective heat transfer data.

Alumina nanofluids,

$$\lambda(\phi,T) = \lambda_w(T)(1 + 4.5503\phi) \tag{4}$$

$$\mu(\phi,T) = \mu_w(T)\exp[4.91\phi/(0.2092-\phi)] \tag{5}$$

Zirconia nanofluids,

$$\lambda(\phi,T) = \lambda_w(T)(1 + 2.4505\phi - 29.867\phi^2) \tag{6}$$

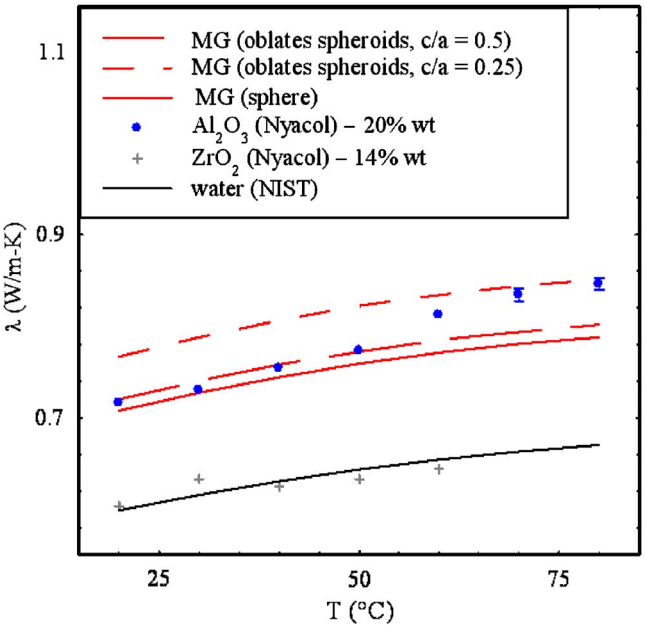

Fig. 2 Temperature-dependent thermal conductivity

$$\mu(\phi,T) = \mu_w(T)\exp[11.19\phi/(0.1960-\phi)] \quad (7)$$

Equations (4)–(7) apply to our nanofluids and are not of general validity.

3 Description of the Flow Loop

A flow loop facility was constructed to conduct the convective heat transfer coefficient and pressure loss experiments. A schematic of the loop is shown in Fig. 5. The test section is a smooth horizontal tube, made of stainless steel, with 1.27 cm outside diameter (o.d.) (0.5 in.) and 1.65 mm thickness (0.065 in.), resistively heated by a dc power supply from Lambda America, providing a maximum power of 24 kW. Fourteen T-type thermocouples axially spaced by 0.2 m measure the outer wall temperature. The inner wall temperature is calculated assuming radial heat conduction within the tube wall. There are also two T-type thermocouples submerged in the flow channel at the inlet and outlet of the heated section to measure the bulk temperature of the fluid. The flow is provided by a 1 HP Berkeley SS1XS1-1 pump with a frequency speed controller. The flow is measured by

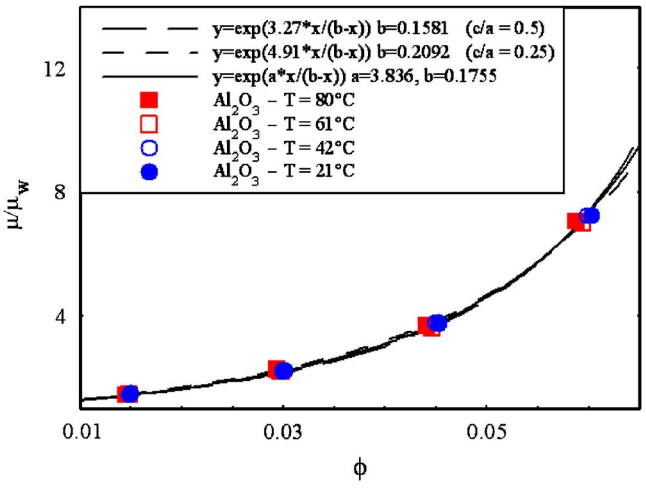

Fig. 3 Viscosity of alumina nanofluids

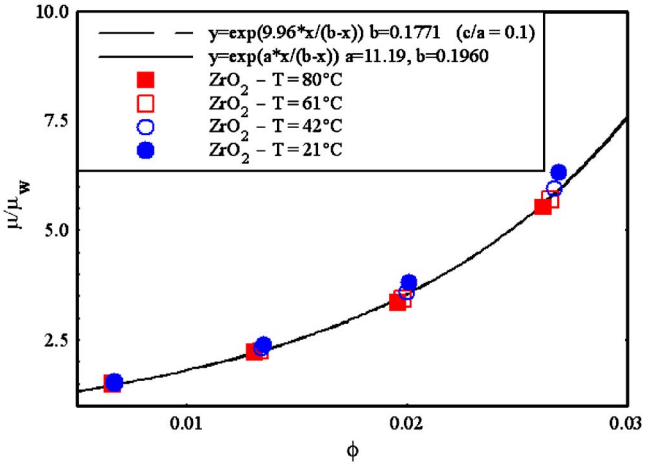

Fig. 4 Viscosity of zirconia nanofluids

a turbine flow meter, which was calibrated to ±0.5% accuracy. The data are acquired by an HP3852A data acquisition unit. The heat is removed by a McMaster Carr 35185K55, stainless steel shell-and-tube heat exchanger. Various valves are included in the system for loading, flow control, and discharge of the test fluid. The heat transfer coefficient is calculated from knowledge of the heat flux and the calculated wall and bulk temperatures at the different axial locations. The viscous pressure loss is measured directly by a differential pressure transducer Omega PX293-030D5V, operating over a range of 0–207 kPa (0–30 psid) with accuracy to within 0.5%, as calibrated by the manufacturer. Because the test section is very long ($L/D \sim 300$), entry region effects on heat transfer and pressure loss are negligible. More details about the design and operation of the loop can be found in Ref. [16].

4 Heat Transfer Coefficient Measurement

The local heat transfer coefficient was measured for both water, as a base case, and each nanofluid under turbulent fully developed conditions. The results were compared against the predictions of the Dittus–Boelter correlation (Eq. (1)), using the temperature- and loading-dependent measured properties of the specific fluid. The benchmark for water at various Reynolds numbers is shown in Fig. 6 and can be seen that the experimental data agree well (within ±10%) with the predictions of the correlation.

Alumina nanofluid was measured at three different volumetric loadings (0.9%, 1.8%, and 3.6%), as shown in Fig. 7, and zirconia nanofluid at three volumetric loadings (0.2%, 0.5%, and 0.9%), as shown in Fig. 8. The data are also reported in Table 1. It can be seen that the Nusselt number is predicted by the Dittus–Boelter correlation to within ±10%, if the nanofluid mixture properties are utilized. No effect of the heat flux on the heat transfer coefficient was observed, as is expected in single-phase forced convection. Water was retested between nanofluid runs in order to assure that there was no significant fouling due to the particles and, in fact, none was found.

5 Viscous Pressure Loss and Friction Factor Measurement

The viscous pressure drop was measured for both water, as a benchmark, and each nanofluid under turbulent fully developed conditions in both the heated and nonheated sections of the loop. The heated-tube case was included to explore the effect of thermal gradients on the pressure loss in nanofluids. The results were compared against the predictions of theory for pressure drop as

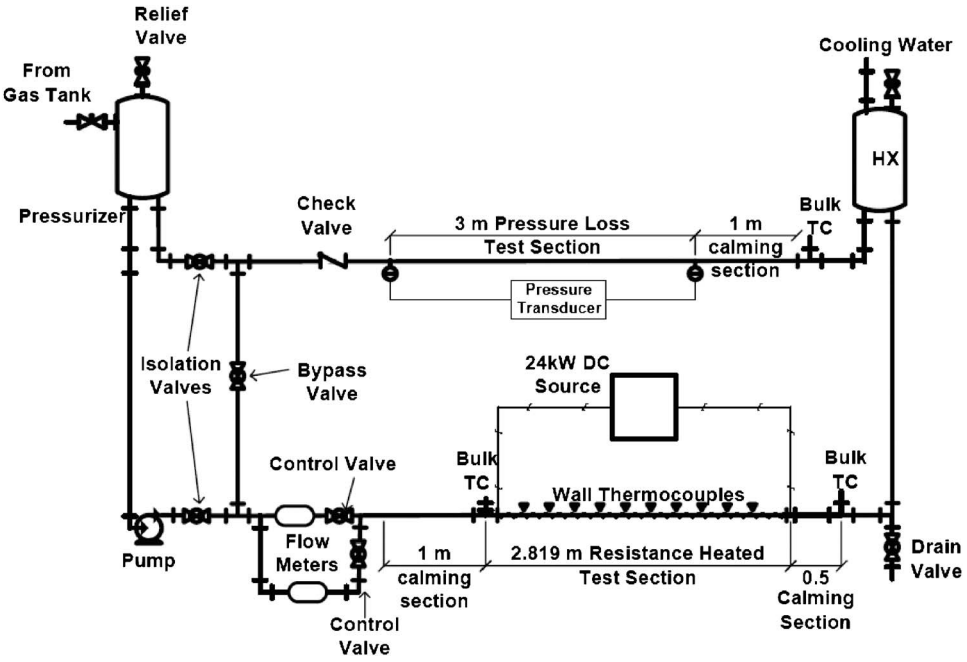

Fig. 5 Schematic of convective loop experimental facility

$$\Delta P = f\frac{L}{D}\frac{\rho V^2}{2} \tag{8}$$

where the friction factor is determined from either the Blasius relation

$$f = 0.316\,\mathrm{Re}^{-0.25} \tag{9}$$

for $\mathrm{Re} < 30{,}000$ or the McAdams relation

$$f = 0.184\,\mathrm{Re}^{-0.2} \tag{10}$$

for $\mathrm{Re} > 30{,}000$ using the temperature- and loading-dependent measured properties of the specific fluid. The benchmark of pressure loss for water at various Reynolds numbers is shown in Fig. 9 and can be seen that the experimental data agree well with the theoretical predictions.

Alumina nanofluid was tested at three different volumetric loadings (0.9%, 1.8%, and 3.6%), as shown in Fig. 10, and zirconia nanofluid also at three volumetric loadings (0.2%, 0.5%, and 0.9%), as shown in Fig. 11. The pressure loss data are also reported in Table 1. It can be seen that the viscous pressure losses are predicted by the theory to within ±20%, if the nanofluid mixture properties are utilized. A post-test characterization of the nanofluids verified that the particle size and loadings had not changed in the loop.

6 Conclusions

The most interesting finding of this paper is that the convective heat transfer and pressure loss behavior of the alumina/water and zirconia/water nanofluids tested in fully developed turbulent flow can be predicted by means of the traditional correlations and models, as long as the effective nanofluid properties are used in calculating the dimensionless numbers. That is, no abnormal heat transfer enhancement was observed. As such, the merits of nanofluids as enhanced coolants depend largely on the trade-off be-

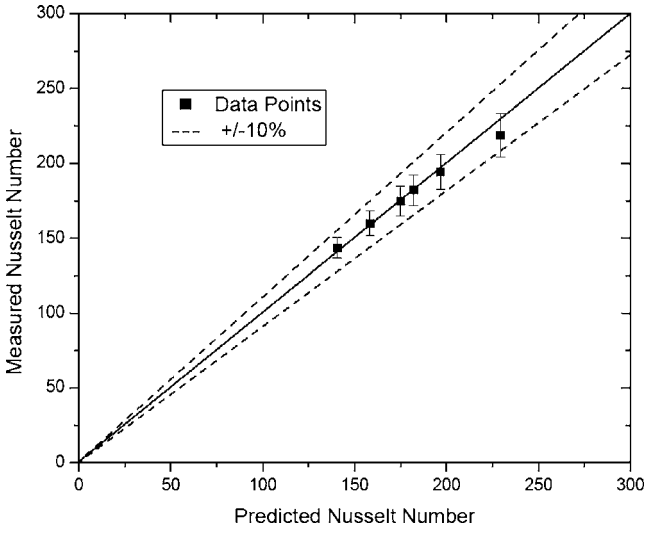

Fig. 6 Tube averaged Nusselt number for water tests

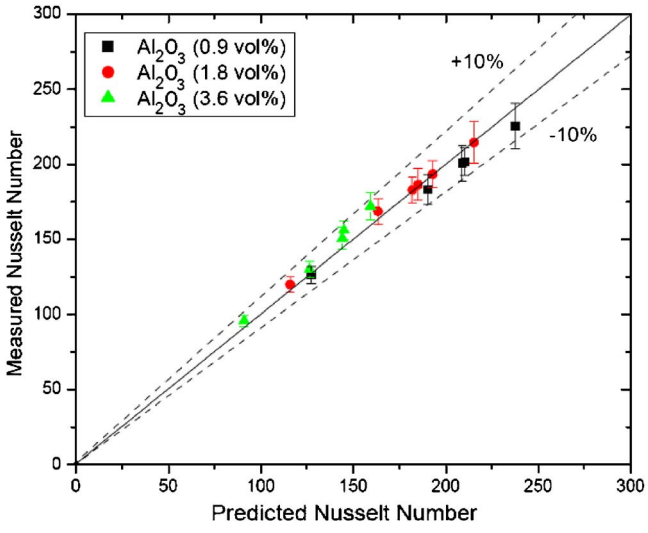

Fig. 7 Tube averaged Nusselt number for alumina nanofluid tests

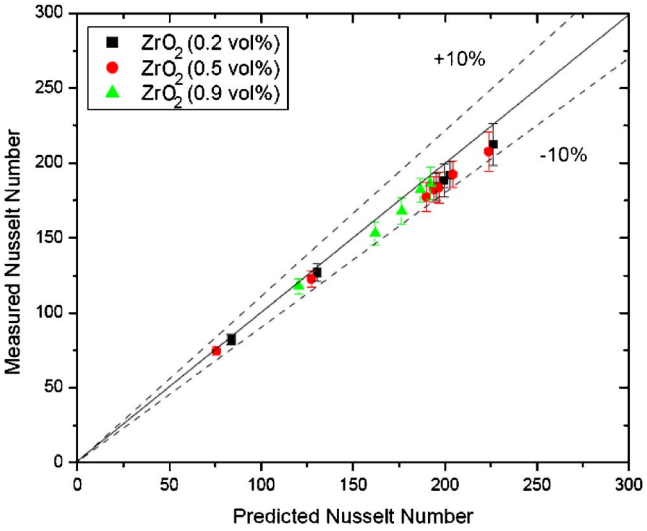

Fig. 8 Tube averaged Nusselt number for zirconia nanofluid tests

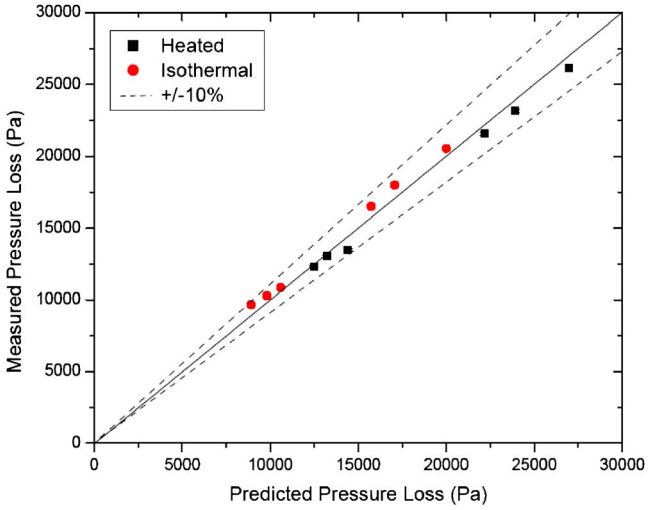

Fig. 9 Viscous pressure losses for water tests

Table 1 Experimental data for convective heat transfer and pressure loss in water and nanofluids

ϕ Water	Flow rate (gpm)	Voltage (V)	Current (A)	T_{in} (°C)	T_{out} (°C)	ΔP_{iso} (psi)	ΔP_{heat} (psi)	P (psi)	h_{ave} (kW/m^2 K)
0	3.0049	18.6728	464.9508	64.9897	75.6521	2.3948	3.1299	5.8560	16.9
0	2.1733	18.6539	464.9247	60.5061	75.0787	1.4016	1.7898	4.4559	12.9
0	3.0627	17.9173	465.0416	22.642	32.6221	2.9806	3.7977	3.2521	12.9
0	2.1388	18.0241	464.9816	24.304	38.8204	1.576	1.9522	3.1228	10.1
0	2.9704	18.1881	464.9652	37.7	48.166	2.6123	3.3636	3.6603	14.3
0	2.1639	18.327	464.9612	41.7497	56.2337	1.4912	1.891	3.3370	11.6
Alumina nanofluids									
0.009	2.147081	18.0176	464.1053	22.82405	38.17461	1.547489	1.881898	3.020074	9.6
0.009	3.715541	17.86031	464.1133	21.43268	30.08651	4.108022	5.151524	3.794503	14.2
0.009	3.851073	24.30109	620.27	27.8986	43.2501	4.204298	5.136252	4.492296	16.5
0.009	3.596595	18.17254	464.1121	38.78505	47.87099	3.553072	4.520337	4.335136	16.3
0.009	3.574315	18.61698	464.0545	63.8074	73.13351	3.164858	4.123959	6.104082	19.1
0.018	2.111757	18.08459	464.1162	25.91971	41.28559	1.664668	2.021926	3.168925	8.9
0.018	3.486365	17.87957	464.1384	21.40127	30.25747	4.348929	5.408708	3.913946	12.0
0.018	3.71442	20.86823	535.851	27.78721	39.45859	4.379486	5.42377	5.197161	14.3
0.018	3.756194	24.45356	620.2195	33.40115	49.18956	4.30093	5.254686	5.534782	15.8
0.018	3.605431	18.12009	464.1094	35.52497	44.43941	4.037124	5.103306	4.625466	14.5
0.018	3.669152	18.55121	464.0947	60.26876	69.26843	3.696665	4.772949	6.703416	17.6
0.036	2.138405	18.10837	464.1348	23.68641	38.62886	2.208656	2.619751	3.216397	6.7
0.036	3.280033	18.02803	465.1244	24.24426	34.05324	4.510882	5.534656	4.106527	9.4
0.036	3.348142	24.70353	620.2382	39.0955	56.74525	4.336269	5.195003	5.186453	12.0
0.036	3.367383	18.3139	465.0778	41.51349	51.24416	4.275407	5.364995	4.956857	11.5
0.036	3.388538	18.61091	465.1196	59.234	68.89603	4.062228	5.170971	6.486388	13.2
Zirconia nanofluids									
0.002	1.052563	18.4147	463.6993	30.17757	61.00621	0.452303	0.51691	3.951985	5.9
0.002	1.973989	18.11652	463.7125	28.4696	44.46611	1.360026	1.693065	4.504671	9.1
0.002	3.238005	20.90897	534.5986	31.30535	44.19403	3.211092	4.03379	5.459796	13.7
0.002	3.177872	24.58308	620.2432	37.23694	55.14627	3.022197	3.759854	5.601450	14.5
0.002	3.141638	18.20885	463.7295	40.20654	50.15454	2.925374	3.77284	5.417549	14.0
0.002	3.164751	18.60896	463.7192	63.09067	73.0723	2.736606	3.62162	7.289336	16.1
0.005	1.015151	18.44775	463.7133	29.14622	61.32544	0.445873	0.497301	3.782135	5.4
0.005	2.06217	18.18333	464.5749	30.09272	45.76818	1.481579	1.846512	4.566293	9.1
0.005	3.557445	18.01022	464.5957	28.23168	37.15283	3.942201	5.012364	5.858727	13.3
0.005	3.47117	21.13534	539.6111	32.60267	45.068	3.697729	4.633149	5.894043	13.9
0.005	3.461399	24.57022	619.1973	39.19982	55.91998	3.552015	4.420837	6.099345	15.1
0.005	3.382455	18.2276	464.5565	39.6313	49.13828	3.370069	4.323706	5.467187	14.2
0.005	3.471451	18.57643	464.5376	59.91715	69.31236	3.231422	4.241396	7.682759	16.6
0.009	2.037224	18.33887	464.5479	38.50456	53.45984	1.73875	2.175113	4.035102	7.9
0.009	3.185502	18.18921	466.6289	31.62775	41.16436	3.944558	4.97116	4.028946	10.3
0.009	3.242367	18.38691	466.5541	43.27367	52.75307	3.814665	4.880184	4.971594	11.6
0.009	3.218808	24.91002	620.2104	50.74531	67.85979	3.708972	4.622206	5.911190	12.8
0.009	3.227561	18.67422	466.5752	59.8875	69.43956	3.558802	4.618606	6.315442	13.0

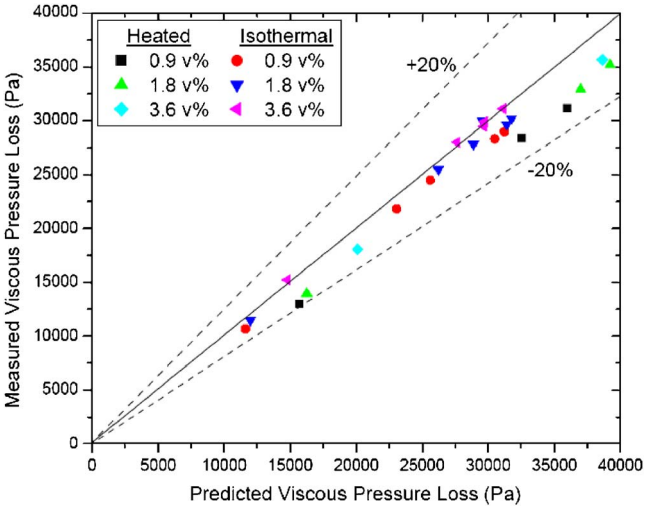

Fig. 10 Viscous pressure losses for alumina nanofluid tests

tween increase in thermal conductivity (determining the desired heat transfer enhancement) and increase in viscosity (determining an undesirable increase in pumping power). A quantitative analysis for our alumina/water and zirconia/water nanofluids has shown that the ratio of heat transfer rate to pumping power for nanofluids is lower than for water [19], because of the dominant effect of the viscosity rise. This is consistent with Pak and Cho's conclusion about their nanofluids [12]. Future research should be directed toward selection of nanoparticle materials, shape, and size that would boost the thermal conductivity increase and reduce the viscosity increase. Nanofluids remain suitable for applications in which an increase in pumping power is not of great concern, e.g., thermal management of high-power electronics. Also, the potential for boiling heat transfer enhancement in nanofluids is truly exciting, as shown by You et al. [20] and confirmed in our laboratory [21] among others.

Acknowledgment

This work was supported by the Idaho National Laboratory through Grant No. 063, Release 18 and the DOE Innovations in Nuclear Infrastructure and Education Grant (DOE-FG07-02ID14420).

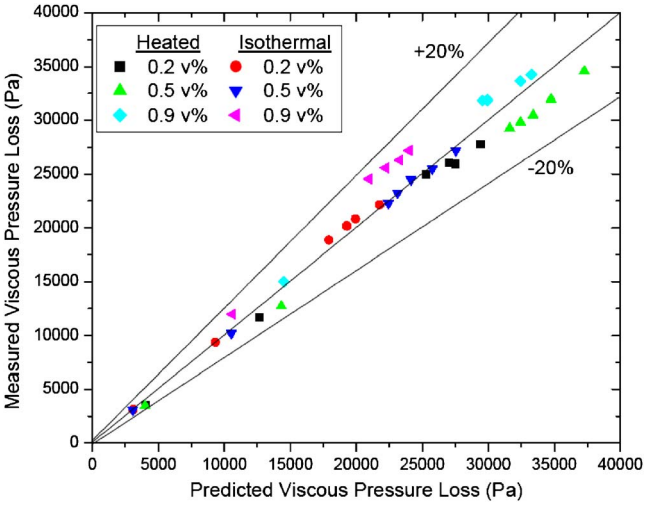

Fig. 11 Viscous pressure losses for zirconia nanofluid tests

Nomenclature

c = specific heat, J/kg K
c/a = ratio of axes for oblate spheroids
D = channel diameter, m
f = friction factor
h = heat transfer coefficient, W/m^2 K
L = channel length, m
Nu = Nusselt number
P = pressure, Pa
Pr = Prandtl number
q = heat flux, W/m^2
Re = Reynolds number
T = temperature, K
V = mean velocity, m/s

Greek

ΔP = pressure loss, Pa
ϕ = nanoparticle volumetric fraction
λ = thermal conductivity, W/m K
μ = viscosity, Pa s
ρ = density, kg/m^3

Subscripts

ave = average
b = base fluid
heat = heated
in = inlet
iso = isothermal
out = outlet
p = nanoparticle
w = water

References

[1] Maxwell, J. C., 1954, *Treatise on Electricity and Magnetism*, Dover, New York.
[2] Maxwell-Garnett, J. C., 1904, "Colours in Metal Glasses and in Metallic Films," Philos. Trans. R. Soc. London, Ser. A, **203**, pp. 385–420.
[3] Masuda, H., Ebata, A., Teramae, K., and Hishinuma, N., 1993, "Alteration of Thermal Conductivity and Viscosity of Liquid by Dispersing Ultra-Fine Particles (Dispersion of Al_2O_3, SiO_2, and TiO_2 Ultra-Fine Particles)," Netsu Bussei, **4**(4), pp. 227–235.
[4] Choi, S. U. S., 1995, "Enhancing Thermal Conductivity of Fluids With Nanoparticles," *Developments and Applications of Non-Newtonian Flows*, D. A. Siginer and H. P. Wang, eds., American Society of Mechanical Engineers, New York.
[5] Eastman, J., Choi, S. U. S., Li, S., Yu, W., and Thompson, L. J., 2001, "Anomalously Increased Effective Thermal Conductivities of Ethylene-Glycol-Based Nanofluids Containing Copper Nanoparticles," Appl. Phys. Lett., **78**(6), pp. 718–720.
[6] Choi, S. U. S., Zhang, Z. G., Yu, W., Lockwood, F. E., and Grulke, E. A., 2001, "Anomalous Thermal Conductivity Enhancement in Nanotube Suspensions," Appl. Phys. Lett., **79**, pp. 2252–2254.
[7] Assael, M. J., Chen, C.-F., Metaxa, I., and Wakeham, W. A., 2004, "Thermal Conductivity of Suspensions of Carbon Nanotubes in Water," Int. J. Thermophys., **25**, pp. 971–985.
[8] Ahuja, A. S., 1975, "Augmentation of Heat Transport in Laminar Flow of Polystyrene Suspensions," J. Appl. Phys., **46**, pp. 3408–3416.
[9] Wen, D., and Ding, Y., 2004, "Experimental Investigation Into Convective Heat Transfer of Nanofluids at the Entrance Region Under Laminar Flow Conditions," Int. J. Heat Mass Transfer, **47**(24), pp. 5181–5188.
[10] Wen, D., and Ding, Y., 2004, "Effective Thermal Conductivity of Aqueous Suspensions of Carbon Nanotubes (Carbon Nanotube Nanofluids)," J. Thermophys. Heat Transfer, **18**(4), pp. 481–485.
[11] Wen, D., and Ding, Y., 2005 "Effect of Particle Migration on Heat Transfer in Suspensions of Nanoparticles Flowing Through Minichannels," Microfluid. Nanofluid., **1**(2), pp. 183–189.
[12] Pak, B. C., and Cho, Y. I., 1998, "Hydrodynamic and Heat Transfer Study of Dispersed Fluids With Submicron Metallic Oxide Particles," Exp. Heat Transfer, **11**(2), pp. 151–170.
[13] Xuan, Y., and Li, Q., 2003, "Investigation on Convective Heat Transfer and Flow Features of Nanofluids," ASME J. Heat Transfer, **125**(1), pp. 151–155.
[14] Xuan, Y., and Roetzel, W., 2000, "Conceptions for Heat Transfer Correlation of Nanofluids," Int. J. Heat Mass Transfer, **43**(19), pp. 3701–3707.
[15] Buongiorno, J., 2006, "Convective Transport in Nanofluids," ASME J. Heat Transfer, **128**, pp. 240–250.
[16] Williams, W. C., 2007, "Experimental and Theoretical Investigation of Transport Phenomena in Nanoparticle Colloids (Nanofluids)," Ph.D. thesis, Massachusetts Institute of Technology, Cambridge, MA.

[17] Rusconi, R., Williams, W. C., Buongiorno, J., Piazza, R., and Hu, L. W., 2007, "Numerical Analysis of Convective Instabilities in a Transient Short-Hot-Wire Setup for Measurement of Liquid Thermal Conductivity," Int. J. Thermophys., **28**(4), pp. 1131–1146.
[18] Das, S. K., Putra, N., Thiesen, P., and Roetzel, W., 2003, "Temperature Dependence of Thermal Conductivity Enhancement for Nanofluids," ASME J. Heat Transfer, **125**(4), pp. 567–574.
[19] Williams, W. C., Buongiorno, J., and Hu, L. W., 2007, "The Efficacy of Nanofluids as Convective Heat Transfer Enhancing Coolants for Nuclear Reactor Applications," *Proceedings of the 2007 ANS Meeting*, Boston, Jun. 24–28.
[20] You, S. M., Kim, J., and Kim, K. H., 2003, "Effect of Nanoparticles on Critical Heat Flux of Water in Pool Boiling Heat Transfer," Appl. Phys. Lett., **83**(16), pp. 3374–3376.
[21] Kim, S. J., Bang, I. C., Buongiorno, J., and Hu, L. W., 2007, "Surface Wettability Change during Pool Boiling of Nanofluids and Its Effect on Critical Heat Flux," Int. J. Heat Mass Transfer, **50**, pp. 4105–4116.

Shin-ichi Satake
Mem. ASME

Takafumi Anraku

Hiroyuki Kanamori

Department of Applied Electronics,
Tokyo University of Science,
2641 Yamazaki,
Noda, Chiba 278-8510, Japan

Tomoaki Kunugi
Department of Nuclear Engineering,
Graduate School of Engineering,
Kyoto University,
Yoshida,
Sakyo, Kyoto 606-8501, Japan

Kazuho Sato
Toyota Industries Corporation,
2-1 Toyoda cyou,
Kariya, Aichi 448-8671, Japan

Tomoyoshi Ito
Japan Science and Technology Agency (JST),
Chiba University,
1-33 Yayoi,
Inage-ku, Chiba 263-8522, Japan
and
Department of Electronics and Mechanical Engineering,
Chiba University,
1-33 Yayoi,
Inage-ku, Chiba 263-8522, Japan

Measurements of Three-Dimensional Flow in Microchannel With Complex Shape by Micro-Digital-Holographic Particle-Tracking Velocimetry

High time-resolution flow field measurement in two microchannels with a complex shape is performed by a micro-digital-holographic particle-tracking velocimetry (micro-DHPTV). The first microchannel has a Y junction that combines the flow of fluid from two inlets into one outlet. In this case, two laminar velocity profiles from the inlet regions merge into one laminar velocity profile. The second microchannel has a convergence region from where a fluid flows into a divergence region. At this region, two recirculation regions appear. Consequently, approximately 250 velocity vectors in both cases can be obtained instantaneously. For a microchannel with the convergence region, the two recirculation regions that appear at the divergence point are captured from a three-dimensional vector field, with which the axes of recircular vortices have some alignment. The reason why we can observe this phenomenon is that a three-dimensional velocity, including the depth direction, can be obtained by micro-DHPTV.
[DOI: 10.1115/1.2818783]

Keywords: digital holography, microfluidics, three-dimensional flow, complex flow

1 Introduction

Noncontact measurement with three-dimensional real time for flow fluid phenomena in microchannel is important to elucidate a mechanism of heat transfer such as in microreactor, red blood flow, etc. For example, from a spatial aspect, there are fundamental components such as cells and red blood cells that exist and function within regions of the order of submicrometer to submillimeter, where the previous micromeasurement techniques could address only the steady state phenomena and that was also limited to 2D observation [1,2]. Therefore, those techniques cannot be applied in the capture of the primary three-dimensional phenomena such as blood motion. A micro-digital-holographic particle-tracking velocimetry (micro-DHPTV) method [3,4] has been developed for high time resolution capable of measuring 3D unsteady flow at microscale by using a digital hologram technique. We have already taken high time-resolution measurements of straight microchannel and pipe flows. In this study, a high time-resolution flow field measurement in two microchannels with complex shape is performed by the technique mentioned above. Both channels are conventional microchannels. The first one has a *Y* junction, which combines the flow from two inlet regions to one outlet region. Here, two laminar velocity profiles from the inlet regions merge into one laminar velocity profile. The second microchannel has only one inlet and one outlet, with a convergence and a divergence region somewhere in the middle part of the microchannel.

2 Optical Setup

Figure 1 shows an optical setup of our experiment. A high-resolution digital charge coupled design (CCD) camera (1024 $\times$1024 resolution with 16 μm/pixel) takes fringe images of the particles using an objective lens (Nikon, 40$\times$, numerical aperture (NA)=0.55). The particles are illuminated by a Nd:YLF (yttrium lithium fluoride) laser (Photonics Industries DS20-527, λ =527 nm). The laser gives out a pair of pulses at a repetition rate of 1 kHz with a pulse length of 58 ns and a pulse delay of 100 μs. This setup records 2000 holograms over a 2 s period to obtain 1000 vector fields. The camera and the laser are synchronized by a pulse generator unit. The test involves the use of nylon spherical particles with 1 μm diameter and a specific gravity of 1.05. In this setup, a syringe pump is used to introduce pressurized water into the microchannel where a fixed mass flow rate is maintained by

Contributed by the Heat Transfer Division of ASME for publication in the JOURNAL OF HEAT TRANSFER. Manuscript received June 21, 2007; final manuscript received July 6, 2007; published online March 21, 2008. Review conducted by Christopher Dames. Paper presented at the ASME 2006 Energy Nanotechnology International Conference (ENIC2006), Boston, MA, June 26–28, 2006.

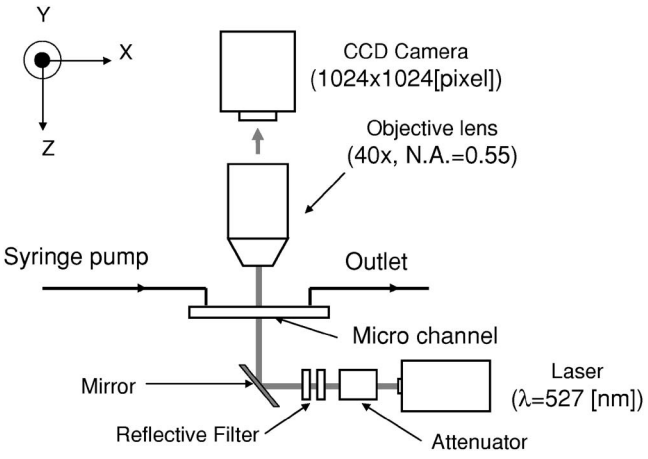

Fig. 1 Optical setup

using a controller. The nylon particles are suspended in the water and are used to track the flow of water in the microchannel.

Figures 2(*a*)–2(*c*) show a schematic illustration of a microchip that was fabricated in the form of a *Y* junction between two inlets and one outlet. The width of the microchannel is 100 μm, and its depth at the deepest point is 40 μm, as is illustrated by a semicircular cross section in Fig. 2(*c*). Water was introduced into the two inlets by two micropumps. Both flow rates were set to 0.5 ml/h.

Figures 3(*a*)–3(*c*) show a schematic illustration of a microchip that was fabricated in the form of a convergence region between one inlet and one outlet with a microchannel of 198.8 μm width, and its depth at the deepest point is 90 μm, as illustrated by a semicircular cross section in Fig. 3(*c*). Both flow rates were set at 4.0 ml/h.

3 Reconstruction Method

Reconstructions of the particle positions from the fringe images in the *x* and *y* directions are done by a fast Fourier transform (FFT) technique with the Fresnel diffraction equation [4,5]. The FFT technique was used for the following transform:

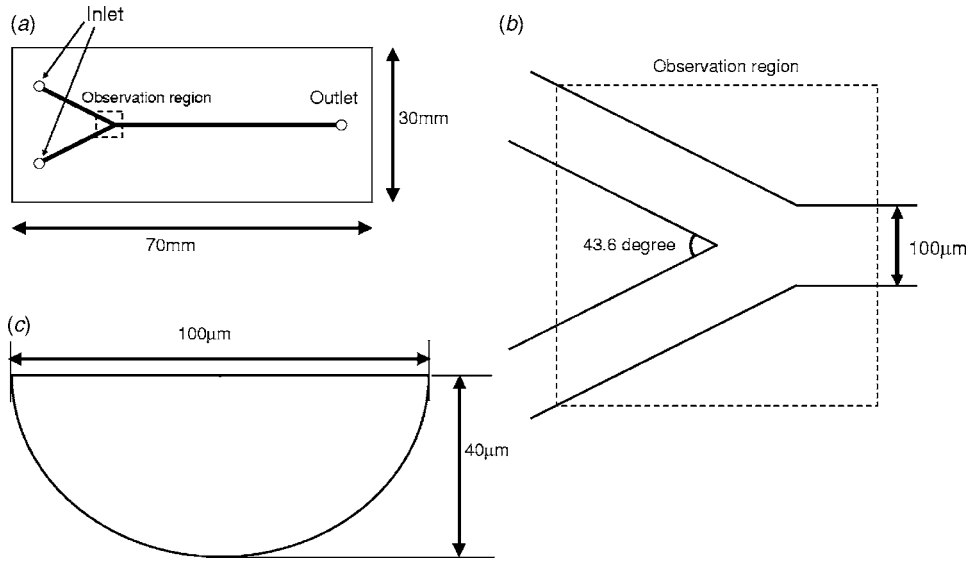

Fig. 2 Schematic of the *Y*-junction microchip: (*a*) microchip, (*b*) *Y* junction, and (*c*) cross section of the microchannel

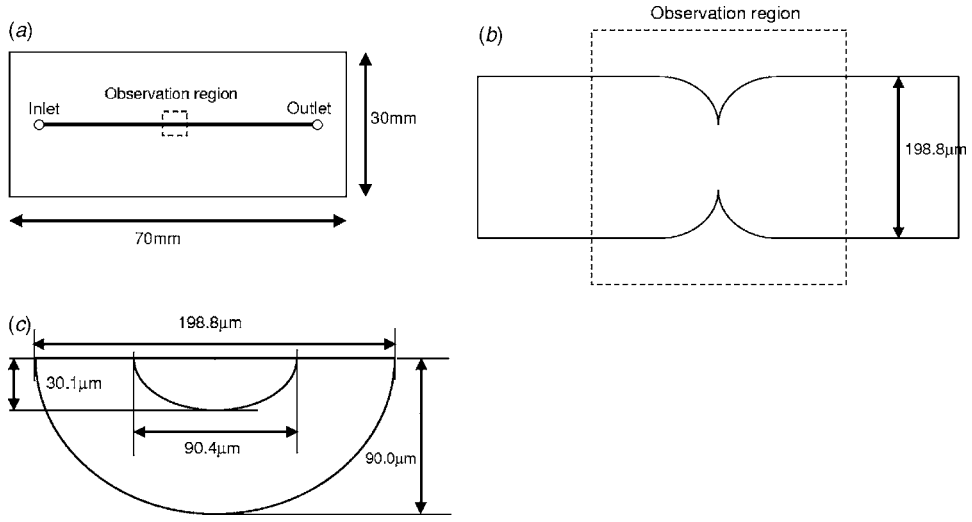

Fig. 3 Schematic of the microchip with a convergence region: (*a*) microchip, (*b*) a convergence region, (*c*) cross section of the microchannel

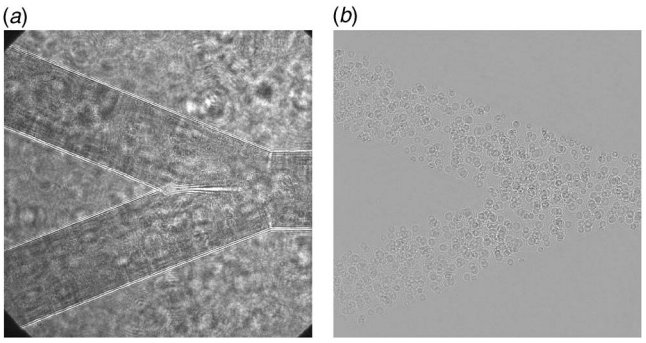

Fig. 4 Fringe image of the microchannel with a *Y* junction: (*a*) Real image. (*b*) This image is the deducted background image from the real image.

$$\Phi(I,J) = \int_{-N1/2}^{N1/2} \int_{-N2/2}^{N2/2} I(x,y)G(I,J)e^{-2\pi i(Ix+Jy)}dxdy = \hat{I}(I,J)G(I,J)$$

where, $\Phi(I,J)$, $\Phi(x,y)$, and $\hat{I}(IJ)$ are the reconstruction image in Fourier space, hologram image, and hologram image in Fourier space, respectively. (I,J) is a transform function using the Fresnel approximation and including the reconstructed depth in the Z direction.

The reconstructed depth is determined by the flow channel depth. In the microchannel with a Y junction, the reconstructed depth is 40 μm, and in the microchannel with a convergence area, the reconstruction depths is 90 μm. To achieve a resolution in the Z direction at approximately 0.2 μm, the microchannel with a Y

Table 1 Uncertainties of the 3D position measurement of the tracer particle.

Error sources		Bias limit (μm)	Precision index (μm)	Degrees of freedom
Traverse of particles on plate	x	± 0	± 0	>30
	y	± 0	± 0	>30
	z	± 0.025	± 0.05	>30
Reconstruction of hologram	x	± 0.080	± 0.040	>30
	y	± 0.067	± 0.033	>30
	z	± 0.0059	± 0.349	11

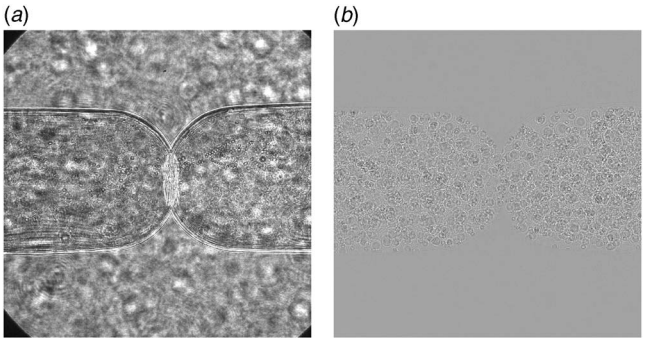

Fig. 5 Fringe image of the microchannel with a convergence region: (*a*) Real image. (*b*) This image is the deducted background image from the real image.

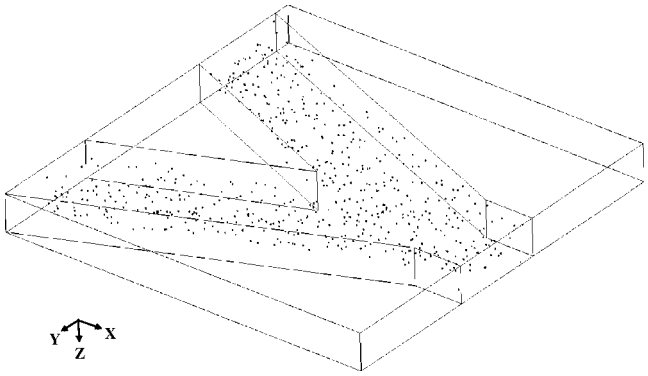

Fig. 6 Reconstruction of particles in the microchannel with the *Y* junction

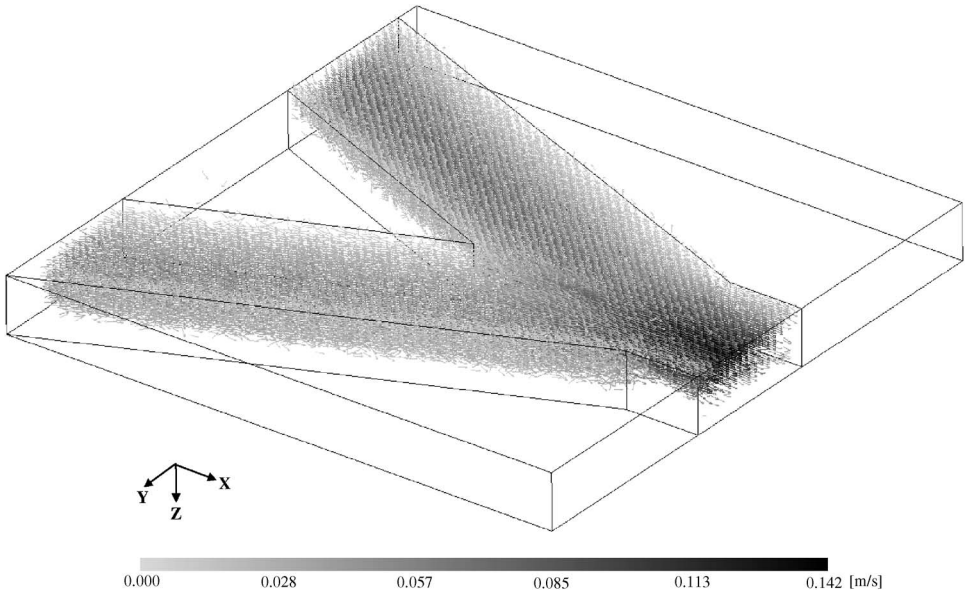

Fig. 7 3D velocity vectors in the microchannel with the *Y* junction

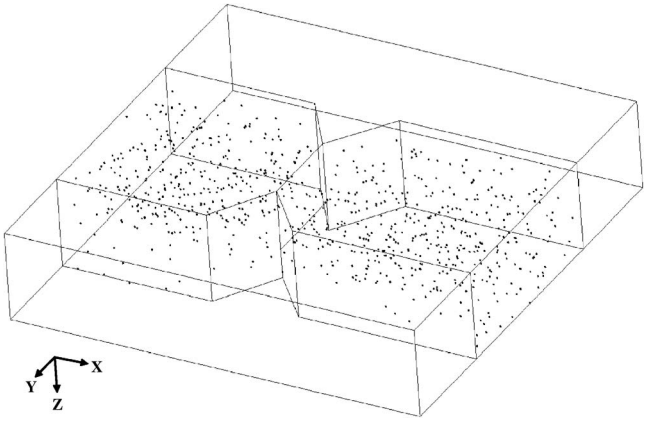

Fig. 8 Reconstruction of particles in the microchannel with a convergence region

junction is divided into 200 sections in the Z direction, and the microchannel with a convergence area pipe is divided into 445 sections. The locations of the particles along the Z direction were calculated in terms of the peak of the reconstructed particle distribution [5]. 3D tracking of the reconstructed particle positions was performed over two frames as a function of time. Since the pulse interval was short, the tracking of particles for this interval was sufficient. The reconstruction and tracking took 65 h for 2000 frames using four processors (AMD Opteron 850, 2.4 GHz).

A fringe image of particles from the observation region is shown in Fig. 4(a). The measurement area is 410×410 μm^2 with a 100 μm wide microchannel at the Y junction near the center. The movement of the particle flow is from left to right. It is believed that the stationary fringes were from the particles stuck to the glass side. For noise reduction, an image averaged from 2000 images was defined as the background. The image in Fig. 4(b) shows the result of subtracting the background image from a real image. The same process is done in the microchannel with a convergence region (Figs. 5(a) and 5(b). After the process, 3D coordinates of particles are reconstructed in each frame. The coordinates of a particle are moved by a distance (flow velocity (mm/s) $\times$ time between frames (s)). In the next frame, the moved coordinates are assumed to be at the center of a circle and where particles are searched within this region defined by the circle. If there is one particle in the region, it is judged to be the same particle as in the previous frame and is used for calculating the velocity.

If there are two or more particles, no velocities are calculated because it is impossible to associate particles. These processes are repeated in each frame, and then mean velocities in 3D coordinates are obtained.

4 Uncertainly Analysis

To obtain the error in the measurement system, uncertainty analysis using a test target was done [5]. Instead of a microchannel in Fig. 1, a glass plate was used. Nylon spherical particles, with 1 μm diameter (Duke Scientific 4010A), were put on the glass plate. The plate was traversed (moved upward or downward along the optical axis (z axis) of the setup by a piezo actuator (Chuo Precision Industrial Co., Ltd, NPS-347-S1) with a resolution of 10 nm. The respective traverse value was detected by a laser displacement sensor (KEYENCE Japan, LK-G35) with a resolution of 50 nm.

Starting from the point of best focus, the hologram pictures were taken at different distances in 1 μm steps. The maximum distance from the point of the best focus, where the picture was taken, was 100 μm in either direction. From all these pictures, we arbitrarily chose 30 particle images. These images were then run through the computer generated hologram (hereafter called CGH) program.

Through the reconstruction processing by CGH, the following parameters were obtained: (a) the change in the z direction where the light intensity value became the maximum and (b) the amount of the average movement of the particle.

The uncertainty of this technique was analyzed by using the result of the amount of the movement of the obtained particle. It was thought that the error margin of the particle coordinates was caused when the hologram was reproduced, which had an error margin of its own. The error margin in this hologram reproduction operation was caused when the elemental error resources were

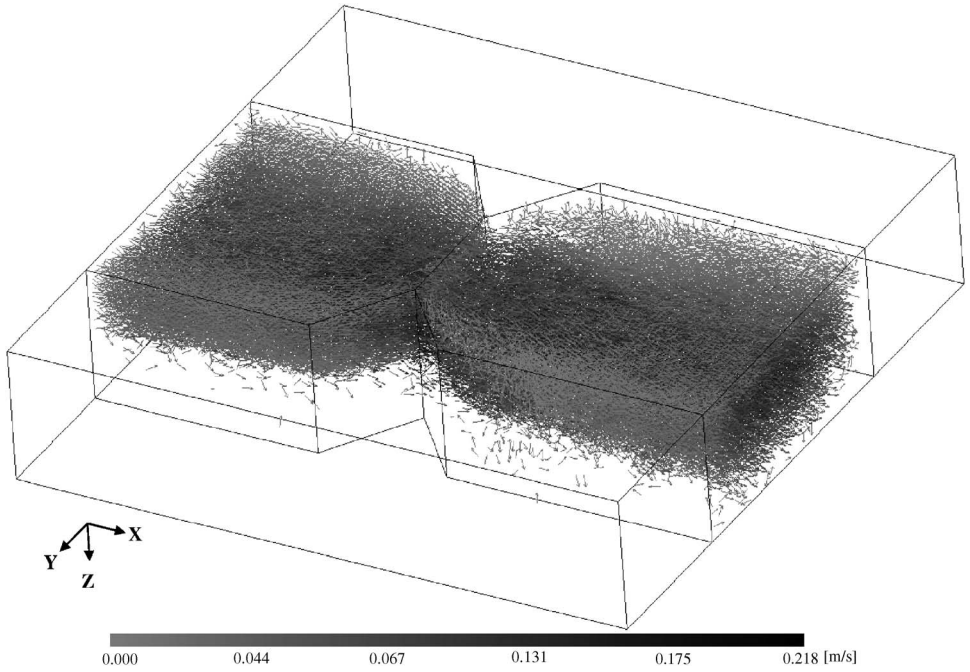

Fig. 9 3D velocity vectors in the microchannel with a convergence region

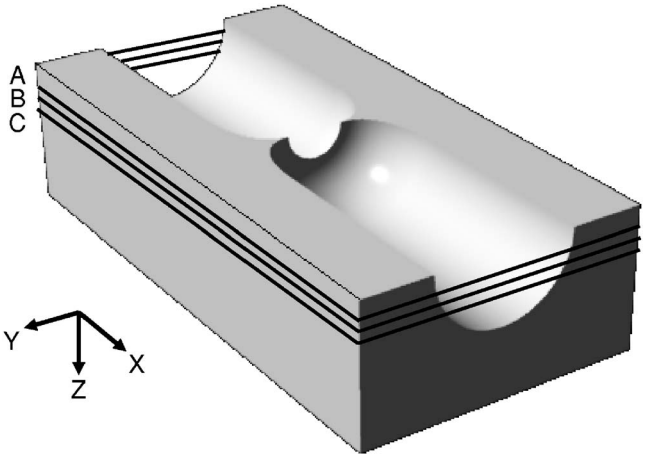

Fig. 10 Schematic viewgraph of the microchannel with a convergence region: Line *A* is defined by $Z=28.2$ μm located from the upper wall of the microchannel. Line *B* is defined by $Z=39.3$ μm located from the upper wall of the microchannel. Line *C* is defined by $Z=50.4$ μm located from the upper wall of the microchannel.

roughly divided among the error margins from the proofreading, data collection, and data processing. Moreover, it also traversed here as an error margin because of data collection and data processing

The measurement was in the form of a laminar flow, but because the interval of time was very short, we disregarded these factors. However, we did take into consideration the error margins because of a straight line approximation of the movement of the flow of the tracer particle in the fluid and the tracer particle in PTV. The elemental error resources are summarized in Table 1. When each error was integrated and the uncertainty of each velocity component was obtained for 95% confidence level, then we came up with the following calculated values of U_{RSS}:

$$U_{\mathrm{RSS},X} = \pm 1.600 \quad [\mathrm{mm/s}]$$

$$U_{\mathrm{RSS},Y} = \pm 1.333 \quad [\mathrm{mm/s}]$$

$$U_{\mathrm{RSS},Z} = \pm 9.916 \quad [\mathrm{mm/s}]$$

The uncertainty becomes 11.03% of the average flow velocity in the microchannel with a *Y* junction (the average flow velocity is 89.87 mm/s), and it becomes 13.42% in the microchannel with a convergence region (the average flow velocity is 73.88 mm/s).

5 Results and Discussion

5.1 Microchannel With *Y* Junctions. The hologram image excepted from the background image was reconstructed into 200 sections in the *Z* direction, and it obtained average 291 particles in the microchannel. 3D particle images in the microchannel with a *Y* junction are shown in Fig. 6. 3D particle tracking was performed over two frames as a function of time, and approximately 291 velocity vectors were obtained in the full region of the microchannel (Fig. 7). The velocity was accelerated at the *Y* junction area. The velocity value at the center region was highest at the cross section.

5.2 Microchannel With Convergence Region. The hologram image excepted from the background image was reconstructed into 445 sections in the *Z* direction and obtained an average of 293 particles in the microchannel. 3D particle images in the microchannel with a convergence region are shown in Fig. 8. 3D particle tracking was performed over two frames as a function of time, and approximately 293 velocity vectors were obtained in the full region of the microchannel (Fig. 9). The velocity in Fig. 10 was accelerated at the convergence area. The velocity value at the center region was highest on the crosssection.

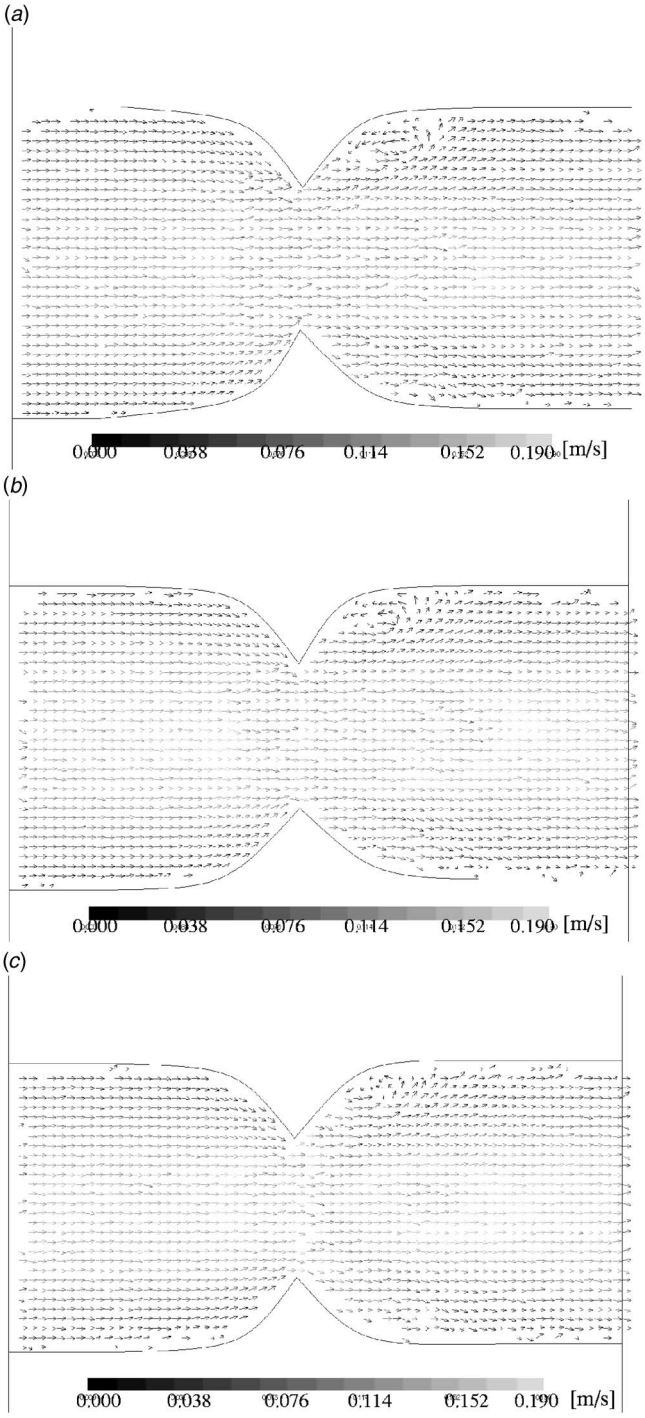

Fig. 11 Time averaged velocity profile in 2 s calculated at lines *A*, *B*, and *C*: (*a*) two-dimensional velocity vectors on line *A* in Fig. 10 at the *x-y* plane, (*b*) two-dimensional velocity vectors on line *B* in Fig. 10 at the *x-y* plane, and (*c*) two-dimensional velocity vectors on line *C* in Fig. 10 at the *x-y* plane

To examine a three-dimensional vortex, we introduce a two-dimensional velocity field at the cross section. Figure 10 shows a schematic viewgraph of the microchannel with a convergence region: Line *A* is defined by $Z=28.2$ μm located from the upper wall of the microchannel. Line *B* is defined by $Z=39.3$ μm located from the upper wall of the microchannel. Line *C* is defined

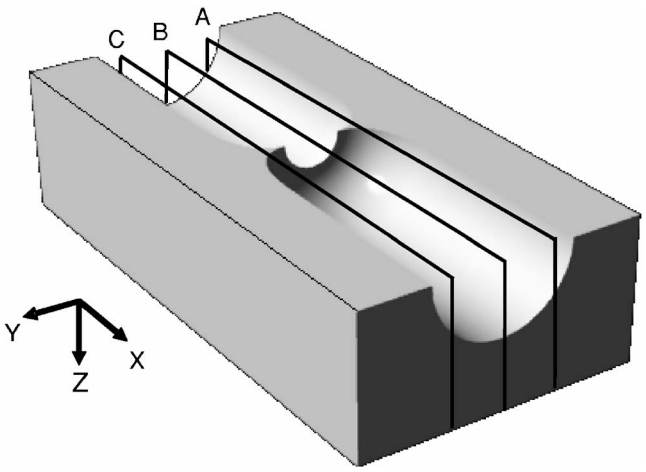

Fig. 12 Schematic viewgraph of the microchannel with a convergence region: Line *A* is defined by *Y*=133.4 μm located from the upper side of the observation area. Line *B* is defined by *Y*=203.8 μm located from the upper side of the observation area. Line *C* is defined by *Y*=304.2 μm located from the upper side of the observation area.

by $Z=50.4$ μm located from the upper wall of the microchannel. Figure 11 showing a time averaged velocity profile over a period of 2 s is calculated at lines A, B, and C: (a) two-dimensional velocity vectors on line A in Fig. 10 at the x-y plane, (b) two-dimensional velocity vectors on line B in Fig. 10 at the x-y plane, and (c) two-dimensional velocity vectors on line C in Fig. 10 at the x-y plane. Two recirculation regions at divergence point were captured from the 2D vector field, with which the axes of recircular vortices have some alignment because the location of the vortex center slightly shifted toward the wall. The reason why we can observe this phenomenon is that a three-dimensional velocity, including the depth direction, can be obtained by micro-DHPTV. Figure 12 shows schematic viewgraph of the microchannel with a convergence region: Line A is defined by $Y=133.4$ μm located from the upper side of the observation area. Line B is defined by $Y=203.8$ μm located from the upper side of the observation area. Line C is defined by $Y=304.2$ μm located from the upper side of the observation area. Figure 13 shows a time averaged velocity profile in a duration of 2 s calculated at lines A, B, and C: (a) two-dimensional velocity vectors on line A in Fig. 12 at the y-z plane, (b) two-dimensional velocity vectors on line B in Fig. 12 at the y-z plane, and (c) two-dimensional velocity vectors on line C in Fig. 12 at the y-z plane. At the channel center in Fig 13(b), the flow state is stable; the flow is along the concavity. On the other hand, near the position for the side wall (see Fig. 13(c)), the flow state is complicated: the tendency appears strongly at the downstream region rather than the upstream one.

6 Conclusions

The measurement of a microchannel and a micropipe flow is performed using a single high-speed camera and a high frequency double pulsed laser by a micro-DHPTV system. One thousand frames of velocity fields in a microchannel with Y junction and convergence region were visualized with a time resolution of 100 μs and repetition rate of 1 kHz in a 3D measurement volume of $409.6\times92\times92$ μm^3. The system can take 291 vectors from 588 particles per frame reconstructed in the microchannel with Y junction, and 293 vectors from 762 particles per frame reconstructed in the microchannel with a convergence area. For the microchannel with the convergence area, two recirculation regions at divergence point were captured from the 2D vector field, with which the axes of recircular vortices have some alignment because the location of the vortex center slightly shifted toward the wall. The reason why we can observe this phenomenon is that a three-dimensional velocity including the depth direction can be obtained by micro-DHPTV. We intend to investigate the limitations of this technique by studying cells, blood red cells.

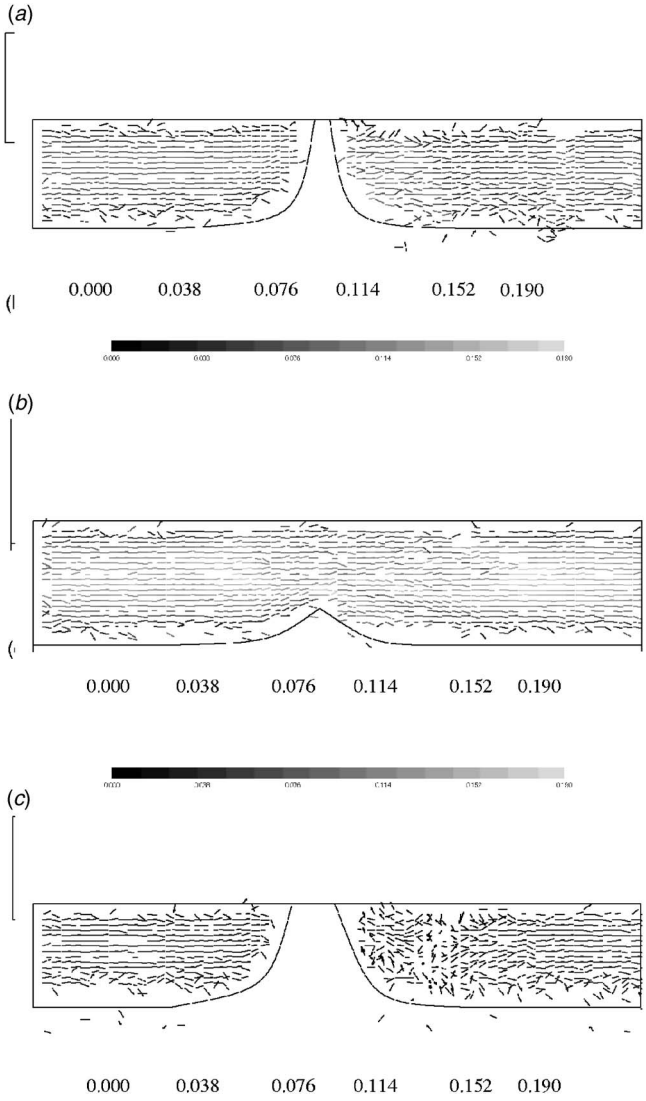

Fig. 13 Time averaged velocity profile in two 2 s calculated at lines *A*, *B*, and *C*: (*a*) two-dimensional velocity vectors on line *A* in Fig. 12 at the *y-z* plane, (*b*) two-dimensional velocity vectors on line *B* in Fig. 12 at the *y-z* plane, (*c*) two-dimensional velocity vectors on line *C* in Fig. 12 at the *y-z* plane

Acknowledgment

This research was partially supported by the Ministry of Education, Science, Sports and Culture Grant-in-Aid for Young Scientists (B) (17760173, 2005-2006).

Nomenclature

G = transform function using the Fresnel approximation
H = hologram image
$\hat{H}$ = hologram image in Fourier space
I = division number of the X direction
i = imaginary number
J = division number of the Y direction
N1 = total division number of the X direction

N2 = total division number of the Y direction

Greek

Φ = reconstruction image in Fourier space
λ = wavelength of laser (nm)

References

[1] Santiago, J. G., Wereley, S. T., Meinhart, C. D., Beebe, D. J., and Adrian, R. J., 1998, "A Particle Image Velocimetry System for Microfluidics," Exp. Fluids, **25**, pp. 316–319.

[2] Meinhart, C. D., Wereley, S. T., and Santiago, J. G., 1999, "PIV Measurements of a Microchannel Flow," Exp. Fluids, **27**, pp. 414–419.

[3] Satake, S., Kunugi, T., Sato, K., Ito, T., and Taniguchi, J., 2005, "Three-Dimensional Flow Tracking in a Micro Channel With High Time Resolution Using Micro Digital-Holographic Particle-Tracking Velocimetry," Opt. Rev., **12**(6), pp. 442–444.

[4] Masuda, N., Kayama, K., Kono, H., Ito, T., Satake, S., Kunugi, T., and Sato, K., 2006, "Special Purpose Computer for Digital Holographic Particle Tracking Velocimetry," Opt. Express, **14**, pp. 587–592.

[5] Satake, S., Kunugi, T., Sato, K., Ito, T., Kanamori, H., and Taniguchi, J., 2006, "Measurements of 3D Flow in Micro Pipe Via Micro Digital Holographic Particle Tracking Velocimetry," Meas. Sci. Technol., **17**, pp. 1647–1651.

Alumina Nanoparticles Enhance the Flow Boiling Critical Heat Flux of Water at Low Pressure

Sung Joong Kim

Thomas McKrell

Jacopo Buongiorno
e-mail: jacopo@mit.edu

Nuclear Science and Engineering Department,
Massachusetts Institute of Technology,
Cambridge, MA 02139

Lin-Wen Hu
Nuclear Reactor Laboratory,
Massachusetts Institute of Technology,
Cambridge, MA 02139

Many studies have shown that addition of nanosized particles to water enhances the critical heat flux (CHF) in pool boiling. The resulting colloidal dispersions are known in the literature as nanofluids. However, for most potential applications of nanofluids the situation of interest is flow boiling. This technical note presents first-of-a-kind data for flow boiling CHF in nanofluids. It is shown that a significant CHF enhancement (up to ~30%) can be achieved with as little as 0.01% by volume concentration of alumina nanoparticles in flow experiments at atmospheric pressure, low subcooling ($<20°C$)*, and relatively high mass flux* ($\geq 1000\ kg/m^2\ s$). [DOI: 10.1115/1.2818787]

Keywords: nanofluids, flow boiling, critical heat flux, colloids

1 Introduction

Nanofluids are colloidal dispersions of solid nanoparticles in a base fluid, e.g., water or refrigerant. Many studies have reported very significant enhancement of the critical heat flux (CHF) in pool boiling of nanofluids [1–5]. These observations have generated considerable interest in nanofluids as potential coolants for more compact and efficient thermal management systems. At MIT we are studying, in collaboration with AREVA, the application of nanofluids to nuclear reactors. However, the situation of interest in most of these practical applications is flow boiling, for which no nanofluid data have been reported so far. This technical note shows for the first time the potential of nanofluids to enhance CHF in flow boiling.

2 Nanofluids Preparation

We have selected nanofluids with alumina (Al_2O_3) nanoparticles for their colloidal stability and wide use in previous pool boiling experiments. A concentrated water-based dispersion of alumina nanoparticles was purchased from Nyacol. The vendor-specified concentration was 20% by weight, which we verified with thermogravitometric analyses. No abnormal impurities were found in the sample, as shown by inductive coupled plasma and neutron activation analyses. The as-purchased dispersion was then diluted with de-ionized water to the low concentration of interest for the CHF experiments, i.e., 0.01% by volume. The size (effective diameter) of the nanoparticles in the diluted nanofluids was measured with the dynamic light scattering technique and ranged from 40 nm to 50 nm. Various parameters relevant to two-phase heat transfer were also measured including boiling point, surface tension, thermal conductivity, and viscosity, and were found virtually identical to those of pure water, which was expected for such dilute nanofluids. All diluted nanofluids used in our experiments were found to be colloidally stable (i.e., did not sediment) with no surfactant addition or pH control after dilution. More information on the nanofluids used in this study can be found in Ref [6].

3 Description of the Experimental Apparatus and Procedure

CHF has been measured in the MIT nanofluid flow loop, which consists essentially of a heated test-section assembly, a cooler, a pump, and an accumulator. This facility has a design pressure of 1 MPa with a maximum flow rate of about ~0.15 kg/s. The loop is constructed with 25.4 mm outside diameter (o.d.) (1 in.) stainless steel tubing. The test section (Fig. 1) consists of a tube made of stainless steel grade 316 (purchased from All-Stainless Inc.) with 9.52 mm o.d. (3/8 in.), 0.41 mm (0.016 in.) thickness, and 240 mm length, through which the test fluid flows. The tube is electrically heated using two identical 30 V, 600 A dc power supplies operating in parallel and connected to the tube ends by copper electrodes. The electric power supplied to the test section is measured with a calibrated voltmeter and ammeter with an uncertainty <2%. With this setup, the heat flux in the test section was verified to be axially uniform by direct voltage measurement at 12 equidistant voltage taps along the tube length. The heat flux delivered to the fluid in the test section q'' is calculated as

$$q'' = \frac{VI}{\pi DL} \tag{1}$$

where V and I are the measured voltage and current, respectively, and D and L are the test-section inner diameter and length, respectively. Twelve K-type thermocouples (TCs) of nominal uncertainty $<1.1°C$ are clamped to the outer surface of the tube, to measure the wall temperature. Since these TCs are used to detect the large temperature excursion associated with CHF, a greater accuracy is not required. The loop is equipped with a stainless steel shell-and-tube cooler to reject the heat and control the test-section inlet subcooling. Pressure is maintained by an accumulator and regulated nitrogen overpressure. However, for the experiments presented here the pressure was always atmospheric. Also, the accumulator is used to purge noncondensable gases at the beginning of each run. The flow rate in the loop is controlled with a constant-displacement pump (modulated with a variable-frequency drive), and measured with a flow meter of $<\pm 5\%$ uncertainty. Two submerged TCs measure the fluid bulk temperatures at the inlet and exit of the test section, respectively.

The experimental procedure is as follows. The loop is filled with the test fluid and is run at 80°C for 1 h to deaerate. Then, the desired flow rate is established and a stepwise power escalation is initiated. Each power step lasts a few minutes until a new steady state is achieved (Fig. 2). The flow rate, test-section current and voltage, pressure, wall, and bulk temperatures are monitored and recorded at each power step. The heat losses are less than 3% in this loop, as estimated from the comparison of the electric power and the heat rate supplied to the fluid in the test section, which is measured by the bulk temperature TCs:

Contributed by the Heat Transfer Division of ASME for publication in the JOURNAL OF HEAT TRANSFER. Manuscript received January 9, 2007; final manuscript received April 2, 2007; published online March 18, 2008. Review conducted by Satish G. Kandlikar.

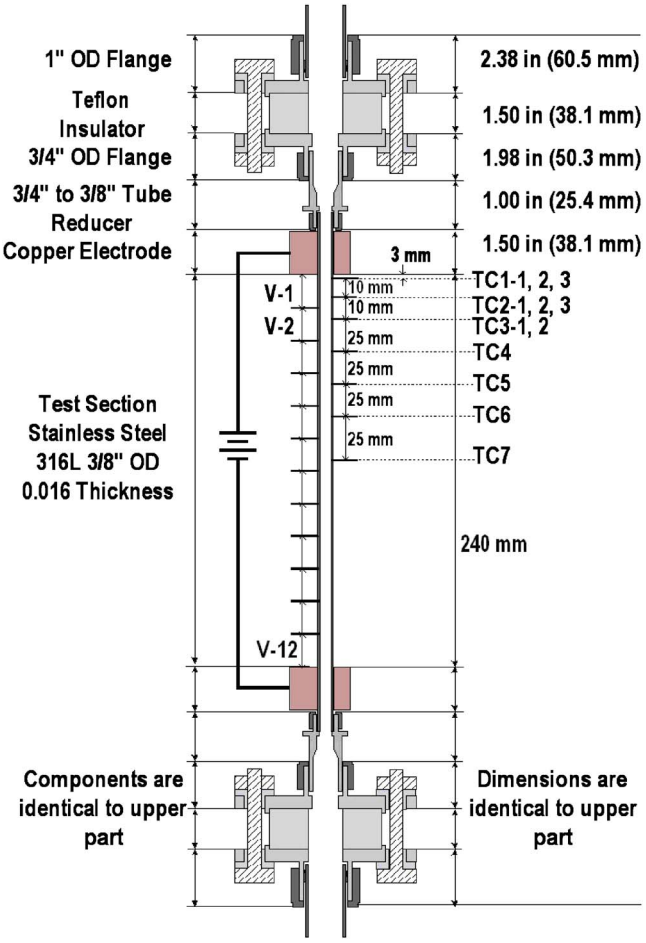

Fig. 1 The flow loop test section

$$\frac{VI - \dot{m}c_p(T_e - T_i)}{VI} < 0.03 \tag{2}$$

where $\dot{m}$ is the mass flow rate, T_e and T_i are the exit and inlet temperatures, respectively, and c_p is the average specific heat of water between T_i and T_e. Since the heat flux is axially uniform, CHF occurs at the test-section exit and can be detected from the temperature excursion measured by the TCs near the exit. In other words, the heat flux value at which the wall temperature excursion occurs is the CHF. The control system automatically shuts down the power supply as soon as any wall TC detects a runaway temperature excursion. Therefore, the experiment is arrested within 1–2 s of CHF occurrence. The test-section tube typically experiences burnout at the location of CHF (i.e., the exit), so it has to be replaced after every run. Prior to its use the inner surface of every new tube is cleaned with acetone to remove any dust, grease, or other contaminants that could affect CHF.

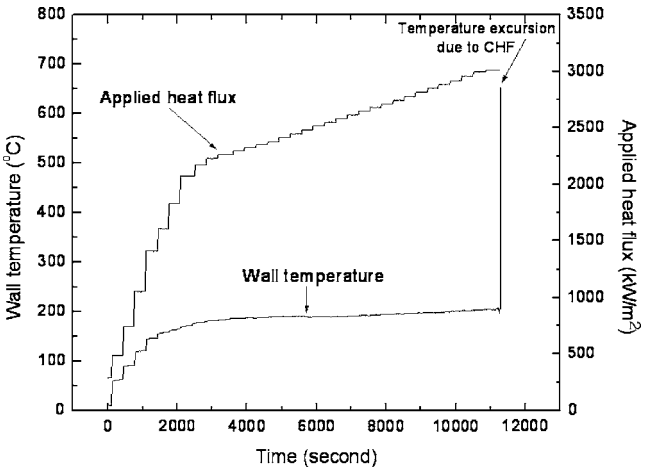

Fig. 2 Wall temperature and heat flux history in a typical CHF run. Note the rapid temperature excursion at CHF.

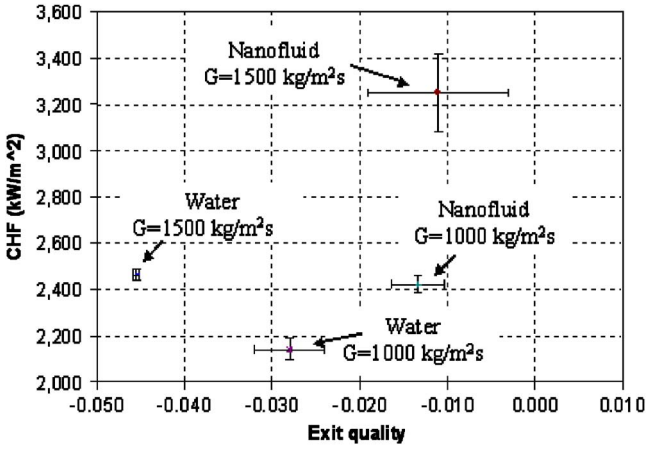

Fig. 3 Measured values of the CHF for water and 0.01% by volume alumina nanofluid at atmospheric pressure.

4 Results

About a dozen CHF runs were performed, of which half for water and half for nanofluids, including multiple runs at the same conditions to ensure repeatability of the results. The exit conditions were subcooled in all runs, so the CHF mechanism of interest here is departure from nucleate boiling. The exit equilibrium quality x_e is calculated as follows:

$$x_e = \frac{c_p(T_e - T_{\text{sat}})}{h_{\text{fg}}} \tag{3}$$

where T_{sat} and h_{fg} are the saturation temperature and heat of evaporation at atmospheric pressure, respectively. The CHF results are summarized in Fig. 3, where the CHF is displayed as a function of the exit equilibrium quality for two values of the mass flux (G). It can be seen that for a given mass flux the nanofluids exhibit a higher CHF, i.e., about +10% at $G=1000$ kg/m^2 s and +30% at $G=1500$ kg/m^2 s, well beyond the estimated experimental uncertainty. Because in our experiments the *inlet* subcooling is held constant, the nanofluids, which have higher CHF, tend to have also higher *exit* quality. Since it is well known that CHF decreases with increasing quality, it is logical to hypothesize that, for the same exit quality, the nanofluid CHF enhancement would be even higher than is shown in Fig. 3.

Explaining the CHF enhancement mechanism in nanofluids is beyond the scope of this technical note; however, it should be reported that, remarkably, the mode of burnout in the water and nanofluid runs can be different. Extensive burnout with complete azimuthal failure always occurs in the water runs (Fig. 4(*a*)), while localized burnout with a pinhole-type failure was observed in several nanofluid runs (Fig. 4(*b*)). In a previous paper [7], we have shown that nucleate boiling of nanofluids causes deposition of a layer of nanoparticles on the heater surface[1], and that such layer significantly improves the surface wettability. When CHF

[1]In our laboratory, we ran single-phase convective heat transfer experiments with electrically heated wires and found no deposition of nanoparticles on the wire surface. Therefore, nanoparticle deposition is caused by boiling.

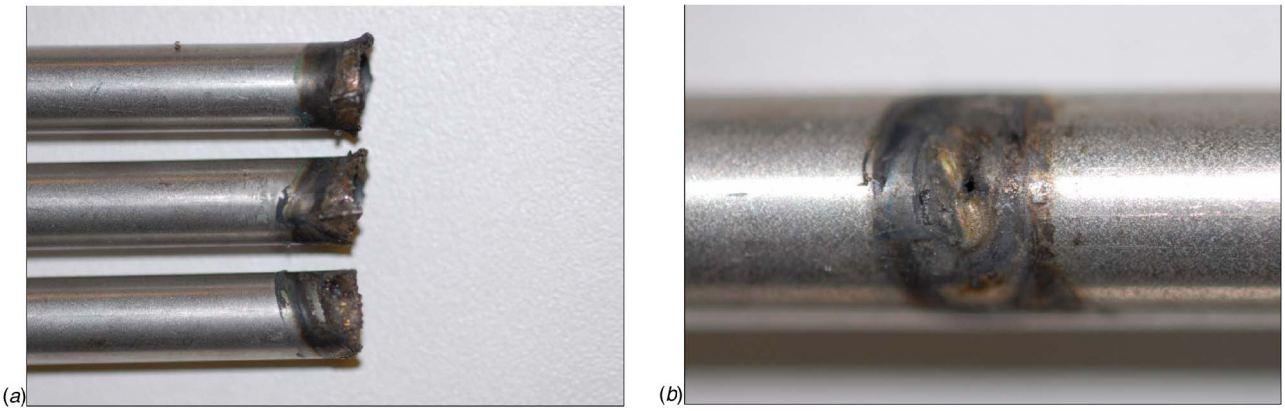

Fig. 4 Test-section burnout due to CHF in water (*a*) and nanofluid (*b*).

occurs, high surface wettability mitigates the propagation of the hot spot, which could explain why burnout tends to be more localized in the nanofluid runs than in the water runs.

Finally, the CHF values in our experiments are significantly lower than those calculated from the 1995 CHF lookup table [8] for the pressure, quality, and mass flux of interest. We suspect that this may be due to the onset of a two-phase flow instability in our test section at the high heat flux. This aspect warrants further investigation. However, given the comparative nature of the present study and the identical operating procedures and conditions of the water and nanofluid runs, any offset from the tabulated values should not invalidate the conclusion that nanofluids exhibit higher CHF than water.

5 Conclusions

Experiments of subcooled flow boiling at atmospheric pressure have revealed that small additions of alumina nanoparticles to water can enhance the CHF by as much as 30%. The presence of the nanoparticles seems to have an effect on the burnout mode, making it more localized. A more systematic study of the effect of mass flux, quality, and nanoparticle concentration on the CHF enhancement is underway in our laboratory and the results will be reported in a full paper in the near future.

Acknowledgment

The nanofluid program at MIT is sponsored by AREVA, the Idaho National Laboratory, the Nuclear Regulatory Commission, and the DOE Innovation in Nuclear Infrastructure and Education Program. The Korea Science and Engineering Foundation is also gratefully acknowledged for Mr. Kim's doctoral fellowship.

References

[1] You, S. M., Kim, J., and Kim, K. H., 2003, "Effect of Nanoparticles on Critical Heat Flux of Water in Pool Boiling Heat Transfer," Appl. Phys. Lett., **83**(16), pp. 3374–3376.
[2] Vassallo, P., Kumar, R., and D'Amico, S., 2004, "Pool Boiling Heat Transfer Experiments in Silica-Water Nano-Fluids," Int. J. Heat Mass Transfer, **47**, pp. 407–411.
[3] Bang, I. C., and Chang, S. H., 2005, "Boiling Heat Transfer Performance and Phenomena of Al_2O_3-Water Nano-fluids From a Plain Surface in a Pool," Int. J. Heat Mass Transfer, **48**, pp. 2407–2419.
[4] Kim, H., Kim, J., and Kim, M., 2006, "Experimental Study on CHF Characteristics of Water-TiO_2 Nano-Fluids," Nuclear Engineering and Technology, 38(1), pp. 61–68.
[5] Kim, S. J., Bang, I. C., Buongiorno, J., and Hu, L. W., 2007, "Surface Wettability Change During Pool Boiling of Nanofluids and its Effect on Critical Heat Flux," Int. J. Heat Mass Transfer, **50**, pp. 4105–4116.
[6] Williams, W. C., 2007, "Experimental and Theoretical Investigation of Transport Phenomena in Nanoparticle Colloids (Nanofluids)," Ph.D. thesis, Massachusetts Institute of Technology.
[7] Kim, S. J., Bang, I. C., Buongiorno, J., and Hu, L. W., 2006, "Effects of Nanoparticle Deposition on Surface Wettability Influencing Boiling Heat Transfer in Nanofluids," Appl. Phys. Lett., **89**(15), p. 153107.
[8] Groeneveld, D. C., Leung, L. K. H., Kirillov, P. L., Bobkov, V. P., Smogalev, I. P., Vinogradov, V. N., Huang X. C., and Royer, E., 1996, "The 1995 Look-up Table for Critical Heat Flux in Tubes," Nucl. Eng. Des., **163**, pp. 1–23.

A Generic Approach to Coat Carbon Nanotubes With Nanoparticles for Potential Energy Applications

Liying Zhu

Ganhua Lu

Junhong Chen[1]
e-mail: jhchen@uwm.edu

Department of Mechanical Engineering,
University of Wisconsin-Milwaukee,
3200 North Cramer Street,
Milwaukee, Wisconsin 53211

A generic and material-independent dry route based on electrostatic force directed assembly (ESFDA) is used to assemble various nanoparticles onto multiwalled carbon nanotubes (CNTs). Charged and nonagglomerated aerosol nanocrystals are first produced using a mini-arc plasma source and then delivered in an inert carrier gas to electrically biased CNTs. The electric field near the CNT is significantly enhanced, and the aerosol nanoparticles are attracted to the external surface of CNTs. For the first time, CNTs have been sequentially coated with nanoparticles of multiple materials to realize the multicomponent coating. High resolution transmission electron microscopy images show that the nonagglomerated entity of nanoparticles and the crystallinity of both nanoparticles and CNTs are preserved during the assembly. The ESFDA technique enables unique hybrid nanostructures attractive for various energy applications.
[DOI: 10.1115/1.2787026]

Keywords: carbon nanotubes, nanoparticles, electrostatic force directed assembly, coating, size selection, fuel cells, solar cells

Introduction

Energy has become the most important problem facing humanity [1]. Nanoscience and nanotechnology are promising in introducing scientific breakthroughs and revolutionary developments for addressing the grand energy challenge [2]. Nanoparticles with sizes between 1 nm and 100 nm have attracted considerable interest because of their unique electronic, optical, magnetic, mechanical, and chemical properties [3,4]. The discovery of carbon nanotubes (CNTs) [5,6] has generated unprecedented large-scale research activities in nanotechnology. CNTs coated with nanoparticles form a new class of hybrid nanomaterials that could potentially display both the unique properties of nanoparticles [7,8] and those of nanotubes [9–11]. These hybrid nanomaterials have recently been shown to be promising for various energy applications including solar cells [12,13], fuel cells [14,15], Li-ion batteries [16], and hydrogen storage [17,18].

In fuel cells, the catalytic activity of catalyst nanoparticles for the electro-oxidation of fuel molecules depends on the size of nanoparticles [19], the type of catalyst support [20], and the method of catalyst preparation [21]. CNTs are considered as strong candidates for catalyst support because of their high surface-to-volume ratio, stability, and unique mechanical properties [22–24]. Nanoparticles with uniform size loaded onto CNTs have been proven effective for catalyzing redox reactions [25]. CNTs coated with nanoparticles of CdSe and CdS have been demonstrated for potential solar cell applications [12,13], in which semiconductor nanocrystals are photoreceptors and CNTs are interconnects for conducting electrons from the photoexcitation of the semiconductor nanocrystals. Finally, metal catalyst nanoparticles dispersed onto CNTs can be used for hydrogen storage [17,18].

Various methods have been developed to obtain nanoparticle-CNT hybrid structures. Popular wet-chemistry methods typically consist of two steps in solutions—chemical prefunctionalization of the CNT surface followed by the attachment of nanoparticles onto CNTs via covalent [26], noncovalent [27], or electrostatic [28,29] interactions. Only single-component nanoparticles have been assembled onto CNTs using wet-chemistry methods. Our group has recently developed a convenient, efficient, and material-independent dry route to coat both multiwalled CNTs (MWCNTs) and single-walled CNTs (SWCNTs) with aerosol nanoparticles based on electrostatic force directed assembly (ESFDA) [30]. We have previously reported the successful assembly of single-component Ag and SnO_2 nanoparticles onto CNTs. Here, we demonstrate that this generic method can be used to coat the same CNT with multicomponent nanocrystals (Ag and SnO_2), which offers new opportunities to tailor properties of product hybrid nanostructures.

Experimental Method

Aerosol nanoparticles were generated through physical vaporization of solid precursor materials using a mini-arc plasma source sustained between a tungsten cathode and a graphite anode [31]. High purity metal wires (gold, silver, and tin) used for precursors were purchased from ESPI. To produce oxide nanoparticles, an additional air flow was mixed with the metallic nanoparticle flow at the exit of the mini-arc plasma reactor. Most nanoparticles as prepared were nonagglomerated and crystalline. Typical sizes of nanoparticles ranged from a few to tens of nanometers. A fraction of as-prepared nanoparticles were charged possibly by the arc plasma or through thermionic emission of electrons from the particle surface [32].

The product nanoparticles were carried by an inert carrier gas (Ar/N_2) and delivered into an electrode gap to form a stagnation flow. One of the electrodes was the grounded metal tubing that introduced the nanoaerosol. The other electrode was a dc-biased (−2 kV) copper grid dispersed with MWCNTs purchased from Alfa Aesar [30]. A 2 mm electrode gap was maintained by a precision-machined ceramic spacer. The electric field near CNTs was significantly enhanced due to their small diameters, and charged aerosol nanoparticles were attracted to the external surface of CNTs. The ESFDA was accomplished at room temperature and 1 atm pressure with a typical assembly time of 3–10 min. To produce multicomponent nanoparticle-CNT hybrid structures, the same CNTs were coated sequentially with one nanoparticle material at a time.

A Hitachi H 9000 NAR transmission electron microscope (TEM) was used to analyze the resulted nanoparticle-CNT hybrid nanostructures. The TEM has a point resolution of 0.18 nm at 300 kV in the phase contrast high resolution TEM (HRTEM) imaging mode. Both low-magnification bright field (BF) TEM and HRTEM images were obtained for each sample.

Results and Discussion

The successful assembly of nanoparticles onto CNTs is confirmed by low-magnification TEM and HRTEM images. As a comparison, Fig. 1(*a*) shows the TEM image of MWCNTs before assembly with a diameter of about 20–40 nm and a length of

Contributed by the Heat Transfer Division of ASME for publication in the JOURNAL OF HEAT TRANSFER. Manuscript received August 6, 2006; final manuscript received February 23, 2007; published online March 20, 2008. Review conducted by Christopher Dames. Paper presented at the ASME 2006 Energy Nanotechnology International Conference (ENIC2006), Boston, MA, June 26–28, 2006.
[1]Correspondence author.

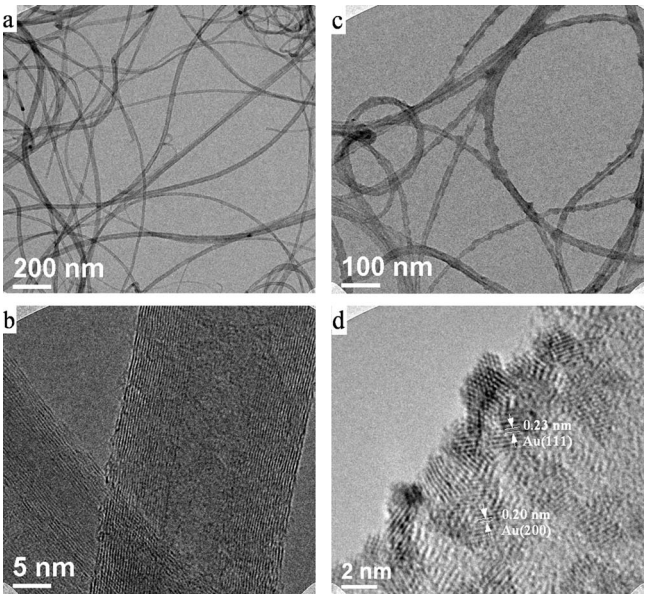

Fig. 1 Low-magnification TEM and HRTEM images of ((*a*) and (*b*)) MWCNTs before assembly and ((*c*) and (*d*)) MWCNTs coated with Au nanoparticles

several micrometers. It is obvious that the MWCNT surface is very smooth, which can be further confirmed by the corresponding HRTEM image shown in Fig. 1(*b*).

Nanoparticles of Au have been coated onto individual MWCNTs to form single-component nanoparticle-CNT hybrid structures. Figure 1(*c*) shows MWCNTs coated with small Au nanocrystals, which have been demonstrated with high catalytic activity [33] and are hence attractive for catalysis applications, for example, in fuel cells. It is difficult to discern Au nanocrystals on MWCNTs due to their very small sizes. However, CNT surfaces covered with gold nanocrytals are much rougher than those before assembly (Fig. 1(*a*)). The HRTEM image shown in Fig. 1(*d*) confirms the presence of localized gold nanocrystals with sizes around 1–2 nm. The lattice fringes of 0.23 nm and 0.20 nm of gold correspond to (111) and (200) crystal planes, respectively. In principle, uncapped metal nanoparticles tend to agglomerate even at room temperature. The nonagglomerated entity of nanoparticles preserved during the assembly is likely attributed to the predominant unipolar charges carried by these nanoparticles before reaching CNTs. The unipolar charges effectively prevent the nanoparticles from agglomeration.

Most importantly, the ESFDA technique provides a unique opportunity to assemble multicomponent nanoparticles onto CNTs, which is quite difficult to realize using the wet-chemistry method. As an example, MWCNTs have been sequentially coated with semiconductor SnO_2 and metallic Ag nanocrystals, in which Ag nanoparticles have been shown to catalyze the gas sensing process of SnO_2 nanoparticles [34]. Figure 2(*a*) shows the TEM image of the double-component nanoparticle-coated MWCNTs. The uniformity of the nanoparticle coverage is not as good as that in the single-component nanoparticle-CNT sample. The HRTEM image in Fig. 2(*b*) provides more detailed information of the interesting hybrid structure. The lattice fringes of Ag and SnO_2 nanocrystals are simultaneously seen on the same MWCNT. The lattice fringe of 0.23 nm corresponds to the (111) plane of Ag nanoparticles. Lattice fringes of 0.33 nm and 0.26 nm correspond to (110) and (101) planes of rutile SnO_2 nanoparticles, with the zone axis of a SnO_2 nanoparticle identified as [111].

The capability to coat the same CNT with multicomponent nanoparticles is attractive for energy applications. Catalytic systems of current interest generally involve alloys or intermetallic

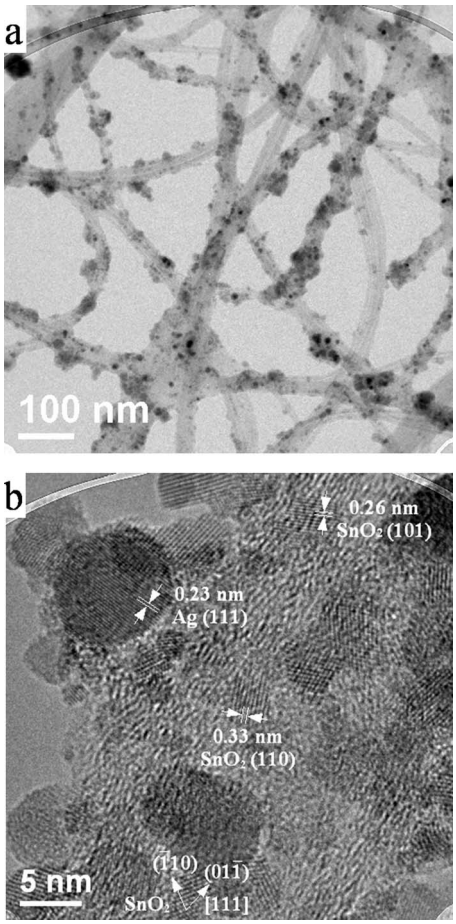

Fig. 2 MWCNTs coated with both Ag and SnO_2 nanocrystals: (*a*) low-magnification TEM image and (*b*) HRTEM image

compounds composed of Pt, Au, or Ag and a post-transition metal Sn, Bi, or Pb [35]. Therefore, the ESFDA technique can be used to produce nanocatalysts of multiple materials supported on CNTs for fuel cells and hydrogen storage. Semiconductor nanoparticles with varying energy band gaps assembled onto CNTs can expand the absorption bandwidth and hence increase the efficiency of solar cells. A solar cell that can absorb the full solar spectrum may be fabricated by coating the same CNTs with nanocrystals of various materials and sizes.

Nanoparticle sizes are critical to all applications discussed above. The optimum Au particle size in a catalyst system is around 3 nm [36]. The nanoparticle size in solar cells can be used to tailor the energy band gap of the nanoparticle material. An important feature of the ESFDA technique is its intrinsic nanoparticle size selection through the electrical mobility of nanoparticles, which results in a smaller mean size and a narrower distribution of nanoparticles on CNTs [30]. The electrical mobility of nanoparticles increases with reducing particle size, assuming that all particles carry the same number of elementary charges. Only smaller nanoparticles with sufficient electrical mobility can be assembled onto CNTs for a given electric field strength and flow residence time. Larger nanoparticles with smaller electrical mobility remain in the stagnation flow and are carried away by the flow. The size selection mechanism also suggests that the ESFDA technique can control the final nanoparticle size distribution on CNTs through electric field and flow residence time.

The binding mechanism between nanoparticles and nanotubes is critical to the properties of the hybrid nanostructures. It is well known that some transition metals may chemically bond to carbon atoms due to their unfilled *d* orbitals. Since Au and Ag atoms have

no *d* vacancy orbitals, they have very weak affinity with carbon atoms [37]. As a result, Ag and Au nanoparticles are most likely attached to CNTs through the van der Waals force instead of through chemical bonds [38], considering the room-temperature assembly process in the inert carrier gas. The unique properties of the catalyst nanoparticles and CNTs should be preserved with the noncovalent coating, which is very important for catalysis applications. For tin oxide nanoparticles, the situation may be different due to the ubiquitous bonding between C and O. Experiments are being carried out to unveil the attachment mechanism for various nanoparticles.

Conclusions

The ESFDA process provides a unique route to assemble nanoparticles onto CNTs. In particular, interesting multicomponent (Ag and SnO_2) nanocrystal-CNT hybrid structures, which are otherwise difficult to realize with wet-chemistry methods, have been obtained using this new route. The uniform coating of CNTs has been confirmed with low-magnification TEM and HRTEM images. The unique intrinsic size selection during the assembly enables a fine tuning of the properties of hybrid nanostructures. The ESFDA technique can be used to coat CNTs with small nanoparticles of a narrow size distribution desirable for energy applications. Since the method is generic and material independent, hybrid nanostructures with arbitrary composition can be produced for intended applications.

Acknowledgment

We thank Marija Gajdardziska-Josifovska for providing TEM access and Donald Robertson for technical support with TEM analyses. The financial support for this study was provided by National Science Foundation through a SGER grant (Combustion, Fire, and Plasma Systems Program, Grant No. 0604079, Dr. Phillip R. Westmoreland, Program Director) and a NER grant (NER Program, Grant No. 0609059, Dr. Charalabos H. Doumanidis, Program Director).

References

[1] Smalley, R. E., 2005, "Future Global Energy Prosperity: The Terawatt Challenge," MRS Bull., **30**(6), pp. 412–417.
[2] Nanoscale Science, Engineering, and Technology (NSET) Subcommittee of the National Science and Technology Council's Committee on Technology, 2004, *Nanoscience Research for Energy Needs, The National Nanotechnology Initiative Workshop*.
[3] Siegel, R. W., 1993, "Synthesis and Properties of Nanophase Materials," Mater. Sci. Eng., A, **168**(2), pp. 189–197.
[4] Alivisatos, A. P., 1996, "Semiconductor Clusters, Nanocrystals, and Quantum Dots," Science, **271**(5251), pp. 933–937.
[5] Iijima, S., and Ichihashi, T., 1993, "Single-Shell Carbon Nanotubes of 1-nm Diameter," Nature (London), **363**(6430), pp. 603–605.
[6] Iijima, S., 1991, "Helical Microtubules of Graphitic Carbon," Nature (London), **354**(6348), pp. 56–58.
[7] Scher, E. C., Manna, L., and Alivisatos, A. P., 2003, "Shape Control and Applications of Nanocrystals," Philos. Trans. R. Soc. London, Ser. A, **361**(1803), pp. 241–255.
[8] Fissan, H., Kennedy, M. K., Krinke, T. J., and Kruis, F. E., 2003, "Nanoparticles from the Gas Phase as Building Blocks for Electrical Devices," J. Nanopart. Res., **5**(3–4), pp. 299–310.
[9] Dresselhaus, M. S., and Dai, H. J., 2004, "Carbon Nanotubes: Continued Innovations and Challenges," MRS Bull., **29**(4), pp. 237–239.
[10] de Heer, W. A., 2004, "Nanotubes and the Pursuit of Applications," MRS Bull., **29**(4), pp. 281–285.
[11] Dresselhaus, M. S., Dresselhaus, G., and Avouris, P., 2001, *Carbon Nanotubes: Synthesis, Structure, Properties and Applications*, Springer-Verlag, Berlin.
[12] Landi, B. J., Castro, S. L., Ruf, H. J., Evans, C. M., Bailey, S. G., and Raffaelle, R. P., 2005, "Cdse Quantum Dot-Single Wall Carbon Nanotube Complexes for Polymeric Solar Cells," Sol. Energy Mater. Sol. Cells, **87**(1–4), pp. 733–746.
[13] Robel, I., Bunker, B., and Kamat, P. V., 2005, "SWCNT-Cds Nanocomposite as Light Harvesting Assembly: Photoinduced Charge Transfer Interactions," Adv. Mater. (Weinheim, Ger.), **17**(20), pp. 2458–2463.
[14] Santhosh, P., Gopalan, A., and Lee, K. P., 2006, "Gold Nanoparticles Dispersed Polyaniline Grafted Multiwall Carbon Nanotubes as Newer Electrocatalysts: Preparation and Performances for Methanol Oxidation," J. Catal., **238**(1), pp. 177–185.
[15] Robel, I., Girishkumar, G., Bunker, B. A., Kamat, P. V., and Vinodgopal, K., 2006, "Structural Changes and Catalytic Activity of Platinum Nanoparticles Supported on C-60 and Carbon Nanotube Films During the Operation of Direct Methanol Fuel Cells," Appl. Phys. Lett., **88**(7), p. 073113.
[16] Zhang, Y., Zhang, X. G., Zhang, H. L., Zhao, Z. G., Li, F., Liu, C., and Cheng, H. M., 2006, "Composite Anode Material of Silicon/Graphite/Carbon Nanotubes for Li-Ion Batteries," Electrochim. Acta, **51**(23), pp. 4994–5000.
[17] Yildirim, T., and Ciraci, S., 2005, "Titanium-Decorated Carbon Nanotubes as a Potential High-Capacity Hydrogen Storage Medium," Phys. Rev. Lett., **94**(17), p. 175501.
[18] Anson, A., Lafuente, E., Urriolabeitia, E., Navarro, R., Benito, A. M., Maser, W. K., and Martinez, M. T., 2006, "Hydrogen Capacity of Palladium-Loaded Carbon Materials," J. Phys. Chem. B, **110**(13), pp. 6643–6648.
[19] Valden, M., Lai, X., and Goodman, D. W., 1998, "Onset of Catalytic Activity of Gold Clusters on Titania With the Appearance of Nonmetallic Properties," Science, **281**(5383), pp. 1647–1650.
[20] Wolf, A., and Schuth, F., 2002, "A Systematic Study of the Synthesis Conditions for the Preparation of Highly Active Gold Catalysts," Appl. Catal., A, **226**(1–2), pp. 1–13.
[21] Liu, H., Kozlov, A. I., Kozlova, A. P., Shido, T., Asakura, K., and Iwasawa, Y., 1999, "Active Oxygen Species and Mechanism for Low-Temperature CO Oxidation Reaction on a TiO_2-Supported Au Catalyst Prepared From Au(PPh3)(NO_3) and As-Precipitated Titanium Hydroxide," J. Catal., **185**(2), pp. 252–264.
[22] Saito, R., Dresselhaus, G., and Dresselhaus, M. S., 1998, *Physical Properties of Carbon Nanotubes*, Imperial College, London.
[23] Treacy, M. M. J., Ebbesen, T. W., and Gibson, J. M., 1996, "Exceptionally High Young'S Modulus Observed for Individual Carbon Nanotubes," Nature (London), **381**(6584), pp. 678–680.
[24] Yu, M. F., Lourie, O., Dyer, M. J., Moloni, K., Kelly, T. F., and Ruoff, R. S., 2000, "Strength and Breaking Mechanism of Multiwalled Carbon Nanotubes Under Tensile Load," Science, **287**(5453), pp. 637–640.
[25] Joo, S. H., Choi, S. J., Oh, I., Kwak, J., Liu, Z., Terasaki, O., and Ryoo, R., 2001, "Ordered Nanoporous Arrays of Carbon Supporting High Dispersions of Platinum Nanoparticles," Nature (London), **412**(6843), pp. 169–172.
[26] Zamudio, A., Elias, A. L., Rodriguez-Manzo, J. A., Lope-Urias, F., Rodriguez-Gattorno, G., Lupo, F., Ruhle, M., Smith, D. J., Terrones, H., Diaz, D., and Terrones, M., 2006, "Efficient Anchoring of Silver Nanoparticles on N-Doped Carbon Nanotubes," Small, **2**(3), pp. 346–350.
[27] Hu, X. G., Wang, T., Qu, X. H., and Dong, S. J., 2006, "In Situ Synthesis and Characterization of Multiwalled Carbon Nanotube/Au Nanoparticle Composite Materials," J. Phys. Chem. B, **110**(2), pp. 853–857.
[28] Xing, Y. C., 2004, "Synthesis and Electrochemical Characterization of Uniformly-Dispersed High Loading Pt Nanoparticles on Sonochemically-Treated Carbon Nanotubes," J. Phys. Chem. B, **108**(50), pp. 19255–19259.
[29] Kim, B., and Sigmund, W. M., 2004, "Functionalized Multiwall Carbon Nanotube/Gold Nanoparticle Composites," Langmuir, **20**(19), pp. 8239–8242.
[30] Chen, J. H., and Lu, G. H., 2006, "Controlled Decoration of Carbon Nanotubes With Nanoparticles," Nanotechnology, **17**(12), pp. 2891–2894.
[31] Chen, J. H., Lu, G. H., Zhu, L. Y., and Flagan, R. C., 2007, "A Simple and Versatile Mini-Arc Plasma Source for Nanocrystal Synthesis," J. Nanopart. Res., **9**(2), pp. 203–213.
[32] Wang, X., Hafiz, J., Mukherjee, R., Renault, T., Heberlein, J., Girshick, S. L., and McMurry, P. H., 2005, "System for In Situ Characterization of Nanoparticles Synthesized in a Thermal Plasma Process," Plasma Chem. Plasma Process., **25**(5), pp. 439–453.
[33] Atwan, M. H., Macdonald, C. L. B., Northwood, D. O., and Gyenge, E. L., 2006, "Colloidal Au and Au-Alloy Catalysts for Direct Borohydride Fuel Cells: Electrocatalysis and Fuel Cell Performance," J. Power Sources, **158**(1), pp. 36–44.
[34] Joshi, R. K., and Kruis, F. E., 2006, "Influence of Ag Particle Size on Ethanol Sensing of $SnO_{1.8}$:Ag Nanoparticle Films: A Method to Develop Parts Per Billion Level Gas Sensors," Appl. Phys. Lett., **89**(15), pp. 153116.
[35] Mann, J., Yao, N., and Bocarsly, A. B., 2006, "Characterization and Analysis of New Catalysts for a Direct Ethanol Fuel Cell," Langmuir, **22**(25), pp. 10432–10436.
[36] Jia, J. F., Haraki, K., Kondo, J. N., Domen, K., and Tamaru, K., 2000, "Selective Hydrogenation of Acetylene Over Au/Al_2O_3 Catalyst," J. Phys. Chem. B, **104**(47), pp. 11153–11156.
[37] Durgun, E., Dag, S., Bagci, V. M. K., Gulseren, O., Yildirim, T., and Ciraci, S., 2003, "Systematic Study of Adsorption of Single Atoms on a Carbon Nanotube," Phys. Rev. B, **67**(20), pp. 201401.
[38] Zhang, Y., and Dai, H. J., 2000, "Formation of Metal Nanowires on Suspended Single-Walled Carbon Nanotubes," Appl. Phys. Lett., **77**(19), pp. 3015–3017.

Practical Considerations for Waveguide-Ballistic Thermal Energy Conversion

Michael Wieckowski
Department of Electrical Engineering
and Computer Science,
University of Michigan,
Ann Arbor, MI 48105
e-mail: wieckows@umich.edu

Martin Margala
Electrical and Computer Engineering Department,
University of Massachusetts Lowell,
Lowell, MA 01854
e-mail: martin_margala@uml.edu

The potential of converting heat energy into electrical energy using a previously reported waveguide-ballistic device is presented. The interactions between incident electromagnetic waves and free electrons in a metal waveguide are analyzed with respect to their transport through a high-frequency ballistic rectifier using finite element method simulation. It was determined that the resulting conversion efficiency to a dc potential is approximately 6%, yielding a power density on the order of 30 W/m^2.
[DOI: 10.1115/1.2818784]

Keywords: thermoelectric conversion, ballistic rectification

1 Introduction

A rough framework for the development of a thermal energy conversion device was previously presented in Refs. [1,2]. The device was based on the premise that radiated heat energy (low infrared) could be coupled into a metal waveguide and the resulting surface currents on the walls of the guide be rectified to provide a dc potential voltage. In this work, the same structure is analyzed in more detail to determine whether it is genuinely realizable, particularly at higher temperatures around 400–500°C. This choice of temperature range is based on the need expressed by the automotive industry for energy recovery in vehicle exhaust systems. For such an application, this work considers in more detail the characteristics of the thermal energy, the construction of the waveguides, the field distributions within the guides, the operation of the rectifiers, and the overall efficiency of the conversion process.

2 Background

A body at 723 K is assumed as the primary source of energy for conversion, whose maximum emissive power occurs at 4.0 μm (74.9 THz) when it is resting in air/vacuum, and whose total emitted power density is 15,493 W/m^2. It is also assumed for the sake of simplicity that the temperatures of the environment and of the converter itself have reached static equilibriums at 27°C. Since the waveguide of the energy converter is sized to operate at a specified frequency, one must only consider the power emitted over a certain spectral bandwidth. It is known from simulation that the converter bandwidth is approximately 30 THz and as such, the energy source under consideration will radiate 3984 W/m^2 of power convertible by the waveguide-ballistic device.

2.1 Waveguide Interaction. It is well known that electromagnetic radiation propagating in a metal waveguide induces currents on the surfaces of its walls. The principle behind the thermal energy converter as explained in Refs. [1,2] is to rectify these ac currents into a dc potential. As such, one must consider the effects of partitioning the guide walls for the insertion of the rectification devices. Essentially, one of the walls must be modified to force the surface currents into the rectifier. This modification to the wall structure of the guide is considered in this work with respect to the effect it has on the field distribution, and hence the surface current distribution within the guide itself.

2.2 Ballistic Rectification. Of the hurdles to overcome in developing the proposed device, one of the most challenging is the construction of an electrical rectifier operating at such high frequencies. To this end, ballistic electron transport is considered as a solution where the carrier distance traveled is less than the carrier scattering length. At this scale, traditional notions of device physics must be reconsidered. In a ballistic rectifier, the channel structure is defined as shown in Fig. 1 where the dark areas are etched away and the light area is a 2D electron gas. The central triangular antidot creates an asymmetry between the top and bottom half of the device resulting in a nonlinear response yielding rectification. Simply stated, any carriers entering the channel from S or D will be deflected toward L resulting in a potential difference between U and L [3].

The transmission coefficient of carriers into the device is mainly a function of the carrier ejection angle. Carriers ejected from S at a small angle (relative to the channel conduction axis) will deflect into the lower channel L, while carriers ejected with a larger angle will simply move into the upper channel U. It is reasonable to suggest that the ejection angle will be a function of the current, I_s or I_d, into the rectifier. A larger current effectively prevents dispersion of the projection beam around the antidot due to the higher carrier velocity. The four terminal resistance of such a structure is derived in Refs. [3–6] as in Eqs. (1)–(3).

$$R_{SD,LU} = \frac{V_{LU}}{I_{SD}} = \left(\frac{h}{2e^2 D_t}\right)\left[T_{S\to L}(I_s)T_{U\to D}(I_U) - T_{L\to D}(I_L)T_{S\to U}(I_S)\right] \tag{1}$$

$$D_t = N_{SD}^2\left[N_{LU}\left(1 - \frac{W_t}{W_{LU}}\right) - \frac{1}{2}N_{SD}(1 - \sin\theta_0)^2\right] \tag{2}$$

$$W_t \approx \tfrac{2}{3}W_{LU} \tag{3}$$

It is assumed that $I_L = I_U = 0$, N_{SD} is the number of propagating modes in the S and D channels of width W_{SD}, and wave number k_F, and $N_{SD} = k_F W_{SD}/\pi$. Similar expressions apply for N_{LU}. θ_0 is the angle relative to the channel at which the probability of an electron deflecting into L or U is 50%. This angle is typically $\pi/4$ and is based solely on physical geometry. The efficiency when I_{SD} is small is then approximately equal to Eq. (4).

$$\frac{V_{LU}}{I_{SD}} \approx -\frac{h}{e^2}\frac{3\hbar}{4eE_F N_{SD}}\frac{\sin 2\theta_0 I_{SD}}{2N_{LU} - 3N_{SD}(1 - \sin\theta_0)^2} \tag{4}$$

From this result, two important observations must be noted. The first is that the effective efficiency of the rectifier can be altered by geometrical means as expressed by the dependence on θ_0. Thus, an optimal geometry can be created to increase efficiency. The second is that the efficiency is also dependent on the current through the device. This is a peculiar phenomenon related to the coherence of the injected carriers, but directly implies that a larger current results in a higher efficiency. The proposed converter must

Contributed by the Heat Transfer Division of ASME for publication in the JOURNAL OF HEAT TRANSFER. Manuscript received July 3, 2007; final manuscript received August 14, 2007; published online March 21, 2008. Review conducted by Christopher Dames. Paper presented at the ASME 2006 Energy Nanotechnology International Conference (ENIC2006), Boston, MA, June 26–28, 2006.

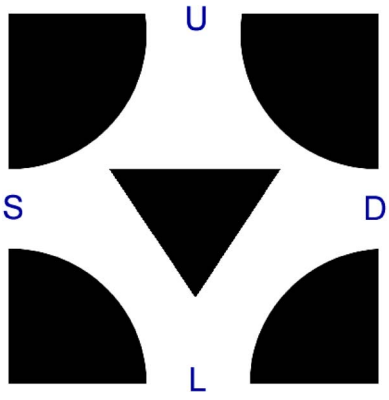

Fig. 1 Simplified ballistic rectifier structure

therefore be designed to maximize the current injected into each rectifier along the waveguide wall. This will yield the greatest voltage across the rectifier as specified by the four terminal resistance in Eq. (1) and, in turn, increase the overall power efficiency of the converter.

3 Simulation Model

A simplified converter structure is shown in Fig. 2 as a series of stacked waveguides, each one composed of three metal walls and one InGaAs/InP wall containing the fabricated rectifier structure. The stacked guides form a thin sheet that would then be positioned normal to the radiating body.

To begin characterizing the potential effectiveness of the thermal energy converter, a 3D model was created to demonstrate the operation of the rectifiers in a single waveguide. Using FEMLAB, a guide was modeled and geometric partitions were added in the walls at the theoretically calculated locations of maximal current density. Example partition structures are shown in Fig. 3, where the shaded areas represent deposited metal on the rectifier substrate forming one wall of the guide. Since the rectifiers themselves are fabricated using semiconductor heterostructures, it is assumed that they will only be inserted into one wall of the waveguide, and the other three walls will be of the standard metal type.

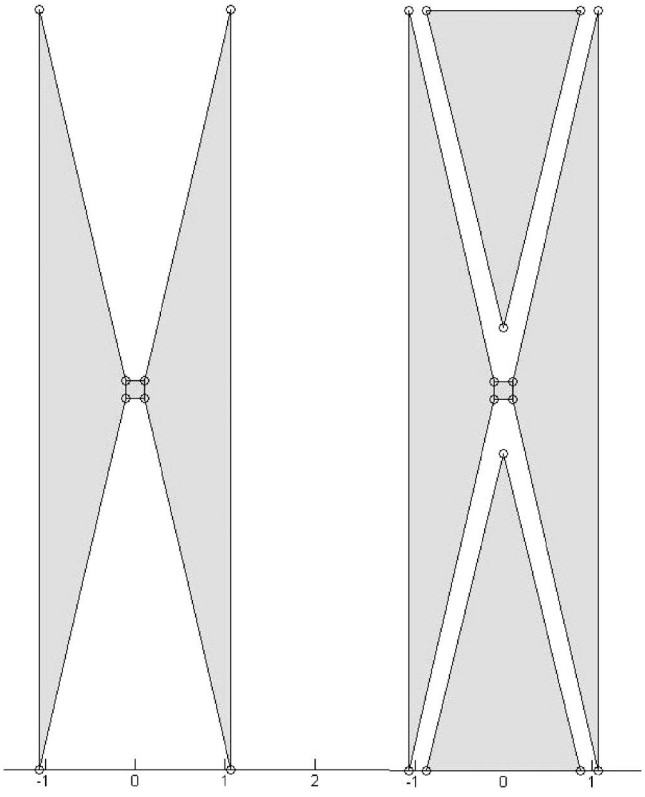

Fig. 3 Example guide wall partitions

The modified wall partitions serve as the locations for rectifier insertion and are also shown in Fig. 4 where the resulting field distribution is shown from simulation with and without rectifying structures.

Two important results are immediately apparent. The first is that the device is still guiding in both cases, even with the modified wall geometry. The second is that the field in Fig. 4(*b*) has been compressed along the axis of the guide such that the partitions no longer coincide with the current density extrema. This

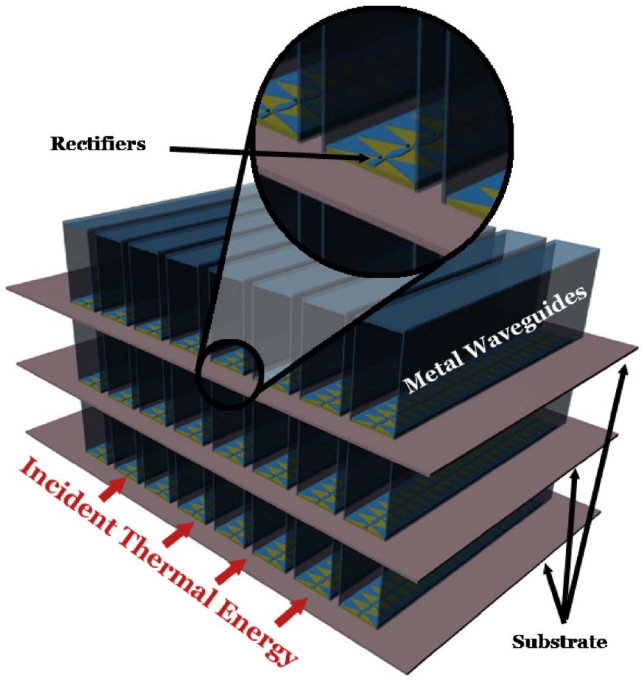

Fig. 2 Simplified energy converter structure

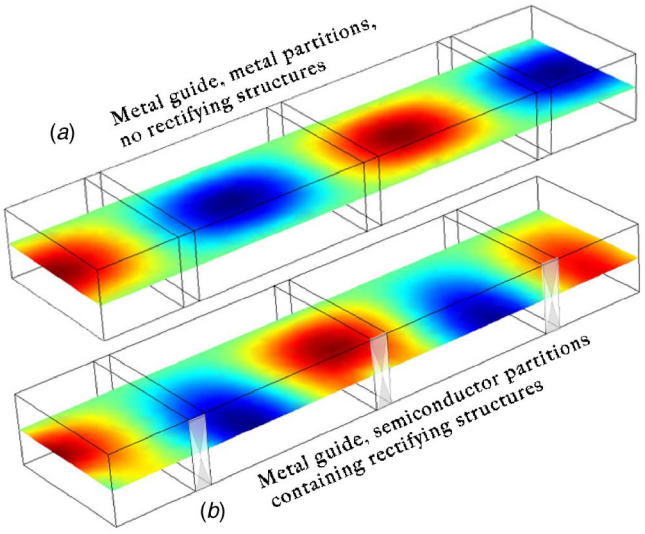

Fig. 4 Simulated field distributions demonstrating the compression that results from rectifier insertion

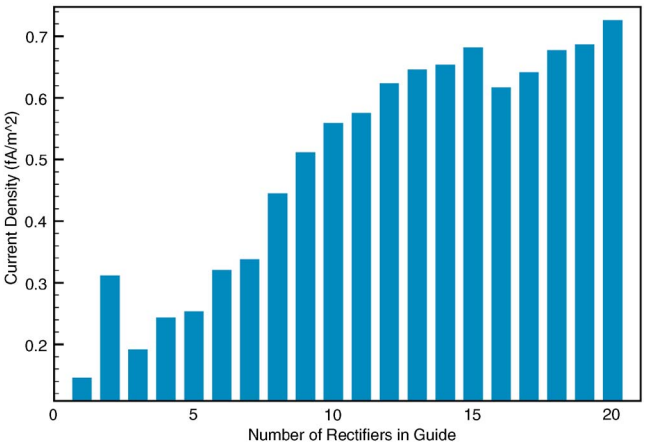

Fig. 5 Relation between average rectifier current density and total number of rectifiers

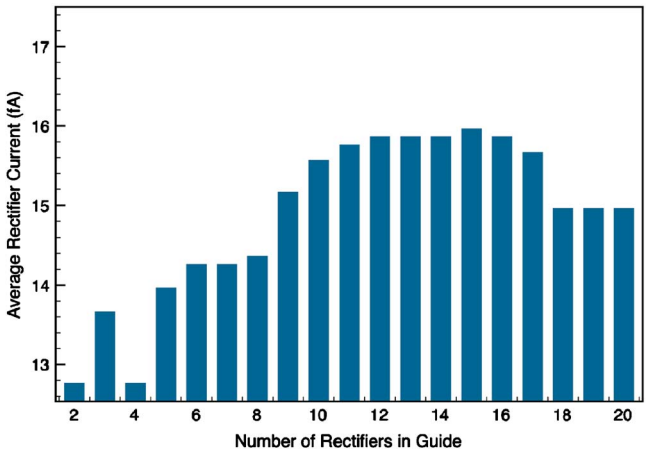

Fig. 6 Results from electrical current optimization

implies that for a maximally efficient energy converter, the rectifier partitions should be relocated to positions of high current density, since the efficiency of the rectifiers increases with the current through them, as shown in Eq. (4). The solution can be expressed as a ratio of the spacing based on an ideal field distribution to the spacing based on a distorted field distribution, and is henceforth referred to as the "compression factor" for the guide.

The rectifiers themselves are modeled as the small square in the middle of the partitions in Fig. 3. For simulation purposes, they are represented as an equivalent circuit impeding the current flow along the guide wall. Such a circuit was determined in Refs. [7,8] by analyzing the step response of a ballistic rectifier using a Monte Carlo simulator. In that work, the rectifier channel is based on an AlInAs/InGaAs structure 100 nm wide $\times$ 250 nm long at 300 K. The resulting equivalent circuit is a series *RL* network, where $R=1.36\times10^{-3}$ Ω m and $L=3.29\times10^{-17}$ H m. As the feature size of the guide is decreased, L will also decrease and the cutoff frequency will increase. In addition, due to the limited number of modes in the channel, conductance saturation will begin to play a critical role [9]. Thus, the limiting factor in the rectifier operation for the proposed converter application is mainly feature size. Without developing a Monte Carlo or other simulator to determine the equivalent values at 74.9 THz, it must be assumed that the contact resistance remains constant while the inductance decreases linearly when scaled. The equivalent impedance at 74.9 THz is then approximately 7.9 k Ω.

4 Optimization Algorithm

Two variables were considered when generating the maximally efficient converter: the number of rectifiers in the guide and the spacing between them (compression factor). By simulating guides with different numbers of rectifiers, the resulting average electrical current density was determined, as shown in Fig. 5.

This result suggests an almost linear dependence of rectifier current on the number of rectifiers in the guide. This does not, however, consider the relationship between rectifier placement and field distortion. To properly maximize efficiency, each guide in the simulation should be adjusted by means of the compression factor to maximize the average current density in each rectifier element separately. An iterative algorithm was used to generate many guides, each with a different number of rectifiers and each with a compression factor that maximizes its respective average rectifier current density. Each guide was then evaluated for current density to determine an optimal design.

5 Results

By using the aforementioned algorithm to determine the average current and power through the rectifiers when maximized for their compression factor, an optimized guide structure was determined. Shown in Fig. 6, the results indicate that the optimal number of rectifiers is approximately 10–17. This will yield the highest rectifier efficiency as specified by the four terminal resistance equation. The compression factor for this range was approximately 80%. This implies that having the rectifiers close together improves the phase dependence, and limiting the total number of rectifiers forces more current into each one.

Using the optimized guide structure, the average power was then measured for different incident frequencies to determine the effective bandwidth of the converter based on a falloff factor of $2^{-1/2}$. The result is shown in Fig. 7, and the resulting bandwidth of 30 THz was used in determining the total fraction of thermal energy "convertible" by the guide.

As a visual example of the conversion process, an optimized guide was simulated with 15 optimally compressed rectifiers inside. Figure 8 shows the current density inside the guide and Fig. 9 shows the power available to each rectifier along the length of the guide. The majority of the conversion process occurs within the first four rectifiers, which helps to mitigate interference and reemission effects.

Table 1 presents the results for the optimized converter operating with a source body at 450°C. As stated before, it is assumed that the body will radiate 15,034 W/m^2 of thermal energy but that only a fraction (3984 W/m^2) of that energy can be coupled into the guide based on the conversion bandwidth. Through simulation incorporating guide losses and geometry, the power available to the rectifiers for conversion was determined. Using a previously determined rectifier conversion efficiency of 14%, the power area density of the converter can be calculated with a guide opening area of 2.5×1.25 μm$=3.125$ μm^2 [1,2].

Since the radiant energy will contain waves of all frequencies and polarizations, one cannot assume that all 3984 W/m^2 in the converter bandwidth will be coupled into the guide. If one assumes a material emissivity of $\frac{1}{2}$, and a simplified polarization distribution where $\frac{1}{4}$ of the radiated photons are TE mode, then only 498 W/m^2 will be available for conversion. This value will be further reduced when considering coupling mismatches. Simulations for various incident densities are shown in Table 1, and the converter linearly converts approximately 6% of any energy available. This is comparable to many other thermoelectric based converters [10]. As an estimate, it is reasonable to predict a conversion power density on the order of 250 W/m^2 for the ideal case but closer to 30 W/m^2 for a realistic application.

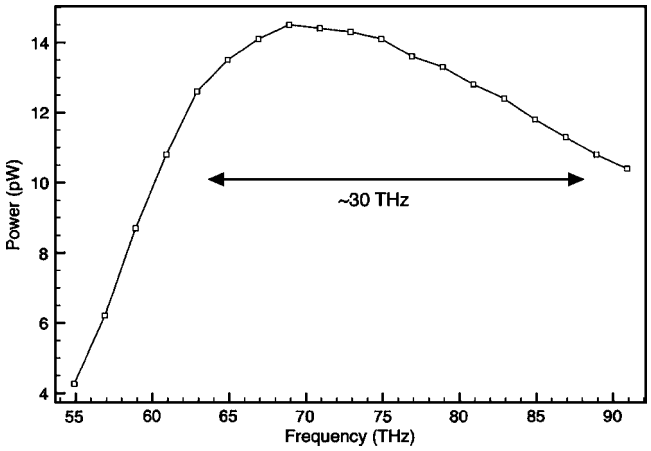

Fig. 7 Bandwidth of an optimized converter

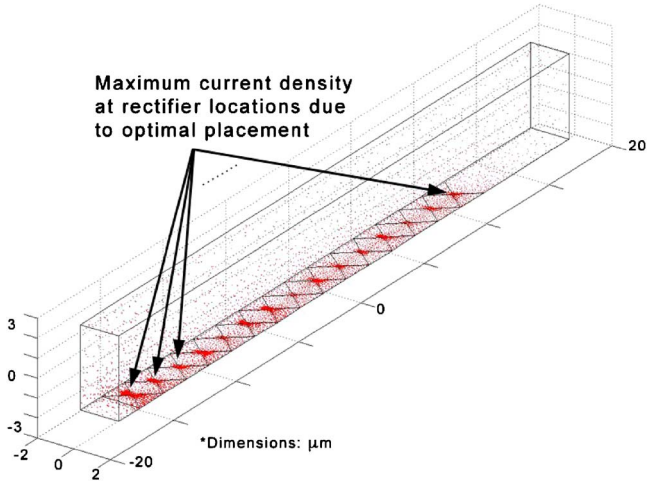

Fig. 8 Current density in converter with 15 rectifiers

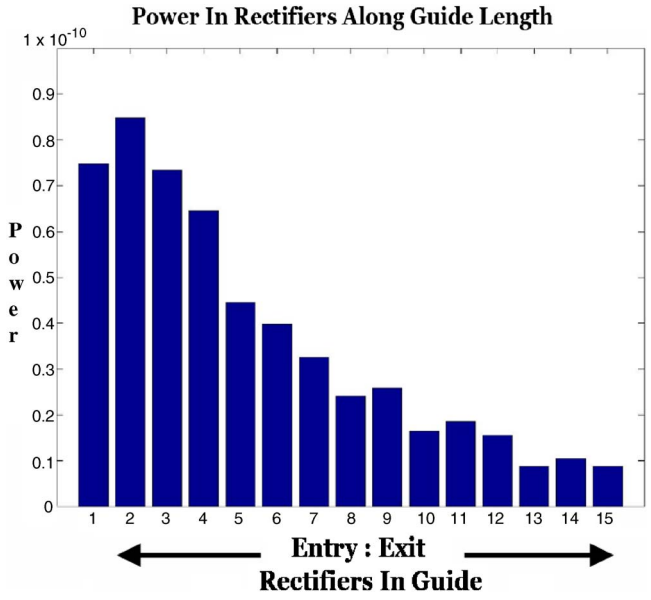

Fig. 9 Power per rectifier along the length of the guide

Table 1 Power densities for simulated converters

Coupled power density (W/m^2)	Power to rectifiers (W)	Converted power density (W/m^2)
3984	5.68×10^{-9}	254.46
1992	2.79×10^{-9}	124.99
996	1.396×10^{-9}	62.54
498	7.06×10^{-10}	31.63
249	3.548×10^{-10}	15.90

6 Conclusions

The simulated power area density recovered by the converter in this work is significantly lower than previously suspected [1,2]. This is due to several factors including modeling accuracy and simplifying assumptions. Parasitic effects surrounding the thermal properties of the system materials and mechanisms should also be considered, especially with respect to the scale of the proposed device [11]. The overall efficiency of the device, however, is not necessarily a function of conversion capability. It was proposed in Ref. [10] that capturing only 10% of the waste energy in automotive systems would result in a 20% increase in fuel efficiency. The fundamental question is therefore one of economy—is the cost in fabrication and implementation worth the return? The answer to this can only be ascertained with further investigation into construction techniques, rectifier mass production, material cost, etc. In conclusion, the results in this work have demonstrated with greater accuracy the theoretical operation of the energy converter along with several merits and downfalls, but much research is still required to determine its practical applications.

Acknowledgment

This work was performed at the Department of Electrical and Computer Engineering, University of Rochester, Rochester, NY 14627.

References

[1] Diduck, Q., and Margala, M., 2003, "The Viability of Thermal Energy Conversion Utilizing Black Body Radiation," *22nd International Conference on Thermoelectrics*, pp. 447–451.
[2] Diduck, Q., and Margala, M., 2004, "Nanotechnology Based Energy Generation From Thermal Radiation," *Canadian Conference on Electrical and Computer Engineering*, Vol. 3, pp. 1597–1600.
[3] Song, A. M., Omling, P., Samuelson, L., Seifert, W., Shorubalko, I., and Zirath, H., 2001, "Operation of InGaAs/InP-Based Ballistic Rectifiers at Room Temperature and Frequencies up to 50 GHz," Jpn. J. Appl. Phys., Part 2, **40**, pp. L909–L911.
[4] Song, A. M., 1999, "Formalism of Nonlinear Transport in Mesoscopic Conductors," Phys. Rev. B, **59**, pp. 9806–9809.
[5] Song, A. M., 2004, *Room-Temperature Ballistic Nanodevices*, Encyclopedia of Nanoscience and Nanotechnology, Vol. 9, pp. 371–389.
[6] Song, A. M., Lorke, A., Kriele, A., Kotthaus, J. P., Wegscheider, W., and Bichler, M., 1998, "Nonlinear Electron Transport in an Asymmetric Microjunction: A Ballistic Rectifier," Phys. Rev. Lett., **80**, pp. 3831–3834.
[7] Mateos, J., Vasallo, B. G., Pardo, D., Gonzalez, T., Galloo, J. S., Bollaert, S., Roelens, Y., and Cappy, A., 2003, "Microscopic Modeling of Nonlinear Transport in Ballistic Nanodevices," IEEE Trans. Electron Devices, **50**, pp. 1897–1905.
[8] Vasallo, B. G., González, T., Pardo, D., and Mateos, J., 2004, "Monte Carlo Analysis of Four-Terminal Ballistic Rectifiers," Nanotechnology, **15**, pp. S250–S253.
[9] Bulusu, A., and Walker, D. G., 2007, "Modeling of Thermoelectric Properties of Semi-Conductor Thin Films With Quantum and Scattering Effects," ASME J. Heat Transfer, **129**, pp. 492–499.
[10] Yang, J., 2005, "Potential Applications of Thermoelectric Waste Heat Recovery in the Automotive Industry," *International Conference on Thermoelectrics*, pp. 170–174.
[11] Miner, A., 2007, "The Compatibility of Thin Films and Nanostructures in Thermoelectric Cooling Systems," ASME J. Heat Transfer **129**, pp. 805–812.